

# **On droplet interactions and suspension flows**

by

Zhouyang Ge

March 2020  
Technical Reports  
Royal Institute of Technology  
Department of Mechanics  
SE-100 44 Stockholm, Sweden

Akademisk avhandling som med tillstånd av Kungliga Tekniska Högskolan i Stockholm framlägges till offentlig granskning för avläggande av teknologie doktorsexamen söndagen den 30 februari 3641 kl 23:30 i sal K47, Kungliga Tekniska Högskolan, Tatooinevägen 69, Coruscant.

TRITA-SCI-FOU 3641:01  
ISBN 978-91-7942-634-9

*Cover:* schematics of a thermal exhaust port of the Death Star.

©Zhouyang Ge 2020  
Universitetsservice US-AB, Stockholm 2020

*If the scientist had an infinity of time at his disposal, it would be sufficient to say to him, “Look, and look carefully.”*

Henri Poincaré



# **On droplet interactions and suspension flows**

**Zhouyang Ge**

Linné FLOW Centre, KTH Royal Institute of Technology, Department of Mechanics  
SE-100 44 Stockholm, Sweden

## **Abstract**

Access points must work. In fact, few cryptographers would disagree with the emulation of robots, which embodies the technical principles of complexity theory. Hyp, our new application for lossless information, is the solution to all of these challenges.

**Key words:** super-lasers, space-stations, The Force, cookies.

## På stabiliteten i en galax långt, långt borta

**Zhouyang Ge**

Linné FLOW Centre, Kungliga Tekniska högskolan, Institutionen för Mekanik  
SE-100 44 Stockholm, Sverige

### Sammanfattning

Åtkomstpunkter måste arbeta. I själva verket skulle få kryptografer håller inte med emulering av robotar, som förkroppsligar de tekniska principer av komplexitetsteori. Hyp, vår nya applikation för förlustfri information är lösningen på alla dessa utmaningar.

**Nyckelord:** super-lasrar, rymdstationer, Kraften, kakor.

## Preface

This thesis summarizes a selection of studies on droplet interactions and suspension flows that are relevant to applications in microfluidics, soft matter, and rheology. A brief introduction of some basic physical concepts and numerical methods is presented in the first part, followed by eight journal articles or preprints listed below. For consistency, the papers have been reformatte to fit with the style of the thesis; their contents have obviously not been altered.

**Paper 1.** Z. GE, J-CH. LOISEAU, O. TAMMISOLA, L. BRANDT, 2018. *An efficient mass-preserving interface-correction level set/ghost fluid method for droplet suspensions under depletion forces.* *J. Comput. Phys.* **353**, 435–459.

**Paper 2.** I. FOUXON, Z. GE, L. BRANDT, A. LESHANSKY, 2017. *Integral representation of channel flow with interacting particles.* *Phys. Rev. E.* **96** (063110).

**Paper 3.** Z. GE, O. TAMMISOLA, L. BRANDT, 2019. *Flow-assisted droplet assembly in a 3D microfluidic channel.* *Soft Matter.* **15**, 3451–3460.

**Paper 4.** I. FOUXON, B. RUBINSTEIN, Z. GE, L. BRANDT, A. LESHANSKY. *The theory of hydrodynamic interaction of two spheres in wall-bounded shear flow.* Under review for *Phys. Rev. Fluids*.

**Paper 5.** M.E. ROSTI, Z. GE, S.S. JAIN, M.S. DODD, L. BRANDT, 2019. *Droplets in homogeneous shear turbulence.* *J. Fluid Mech.* **876**, 962–984.

**Paper 6.** Z. GE, H. HOLMGREN, M. KRONBICHLER, L. BRANDT, G. KREISS, 2018. *Effective slip over partially filled microcavities and its possible failure.* *Phys. Rev. Fluids.* **3** (054201).

**Paper 7.** Z. GE, R. MARTONE, C. CAROTENUTO, R. RADHAKRISHNAN, L. BRANDT, M. MINALE. *Anomalous frequency dependence of the complex viscosity of a dense noncolloidal particle suspension.* To be submitted.

**Paper 8.** Z. GE, O. TAMMISOLA, L. BRANDT. *A discrete-element lubrication/contact dynamics model for simulation of dense particle suspensions in shear flows.* Technical Report.

March 2020, Stockholm  
Zhouyang Ge

## **Division of work between authors**

The main thesis advisor is Professor Luca Brandt (LB). Associate Professor Outi Tammisola (OT) acts as the co-advisor.

**Paper 1.** LB directed the research. Z. Ge (ZG) and J-Ch. Loiseau developed, implemented, and validated the methods. OT oversaw the entire project. ZG wrote the paper with input from the rest of the authors.

**Paper 2.** A. Leshansky (AL) directed the research. I. Fouxon (IF) developed the theory. ZG performed the simulation. IF wrote the paper with input from the rest of the authors.

**Paper 3.** All authors were involved in the discussion of the research. ZG developed the idea, performed the simulation, and wrote the paper with input from the rest of the authors.

**Paper 4.** AL directed the research. IF constructed the theory. B. Rubinstein performed the multipole expansion simulation. ZG performed the Navier-Stokes simulation. IF wrote the paper with input from the rest of the authors.

**Paper 5.** LB conceived the project. M.E. Rosti (MER) implemented the method and performed the simulation. ZG performed the droplet statistics and scaling analysis. S.S. Jain performed the droplet rendering. M.S. Dodd performed the turbulent kinetic budget analysis. MER wrote the paper with input from the rest of the authors.

**Paper 6.** G. Kreiss initiated the project. H. Holmgren implemented the code and performed part of the Stokes simulation. M. Kronbichler performed the phase field simulation. ZG performed part of the Stokes simulation, and wrote the paper with input from the rest of the authors.

**Paper 7.** M. Minale and LB directed the research. R. Martone and C. Carotenuto performed the experiment. ZG performed the simulation with help from R. Radhakrishnan, and wrote the paper with input from the rest of the authors.

**Paper 8.** LB led the research. ZG developed and implemented the method, with input from OT. ZG wrote the paper.

## **Conferences**

Part of the work in this thesis has been presented at the following international conferences. The presenting author is underlined.

**ANAKIN SKYWALKER, DARTH VADER & ADMIRAL MOTTI.** *Effects on breathing of underestimation of the power of The Force.* Intergalactic Conference on Weapons and Peace. Kamino, 3639.

# Contents

<b>Abstract</b>	v
<b>Sammanfattning</b>	vi
<b>Preface</b>	vii
 <b>Part I - Overview and summary</b>	
<b>Chapter 1. Introduction</b>	1
1.1. Our Contribution	1
<b>Chapter 2. Principles</b>	2
2.1. Stochastic Technology	2
<b>Chapter 3. Evaluation</b>	3
3.1. Hardware and Software Configuration	3
3.2. Experimental Results	3
<b>Chapter 4. Related Work</b>	6
<b>Chapter 5. Conclusions and outlook</b>	7
<b>Chapter 6. Test chapter, a very very very long title to test the table of contents</b>	8
<b>Acknowledgements</b>	10
<b>Bibliography</b>	11

## **Part II - Papers**

<b>Summary of the papers</b>	<b>15</b>
<b>Paper 1.</b> An efficient mass-preserving interface-correction level set/ghost fluid method for droplet suspensions under depletion forces	17
<b>Paper 2.</b> Integral representation of channel flow with interacting particles	61
<b>Paper 3.</b> Flow-assisted droplet assembly in a 3D microfluidic channel	97
<b>Paper 4.</b> The theory of hydrodynamic interaction of two spheres in wall-bounded shear flow	123
<b>Paper 5.</b> Droplets in homogeneous shear turbulence	127
<b>Paper 6.</b> Effective slip over partially filled microcavities and its possible failure	159
<b>Paper 7.</b> Anomalous frequency dependence of the complex viscosity of a dense noncolloidal particle suspension	185
<b>Paper 8.</b> A discrete-element lubrication/contact dynamics model for simulation of dense particle suspensions in shear flows	189

# **Part I**

## **Overview and summary**



## CHAPTER 1

# Introduction

### 1.1. Our Contribution

Our contributions are as follows. We validate that the foremost wireless algorithm for the understanding of the lookaside buffer by O. Moore Stallman (1996) is maximally efficient. Further, we explore new real-time methodologies (Hyp), which we use to show that the little-known knowledge-based algorithm for the exploration of the Turing machine by Taylor et al. Stallman (1996) runs in

$$\Omega(\log \log \log n^{\log \log n}) \quad (1.1)$$

time. This outcome might seem unexpected but has ample historical precedence.

The rest of this paper is organized as follows. Primarily, we motivate the need for DNS. On a similar note, we disprove the refinement of 2 bit architectures. We place our work in context with the existing work in this area. Ultimately, we conclude.

**Thesis structure.** Add here a brief description of the structure of the thesis.

## CHAPTER 2

# Principles

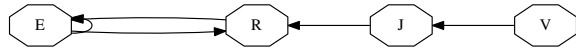


Figure 2.1: The relationship between our heuristic and the robust unification of local-area networks and congestion control.

$$\mathcal{N} = \nabla \cdot \mathbf{u} \quad (2.1)$$

### 2.1. Stochastic Technology

## CHAPTER 3

# Evaluation

### 3.1. Hardware and Software Configuration

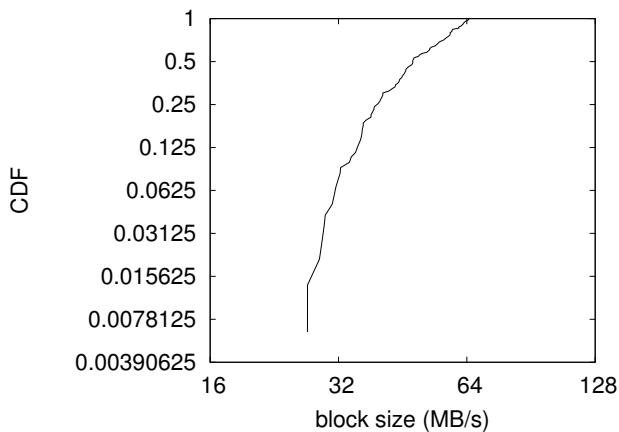


Figure 3.1: The median throughput of Hyp, as a function of bandwidth.

### 3.2. Experimental Results

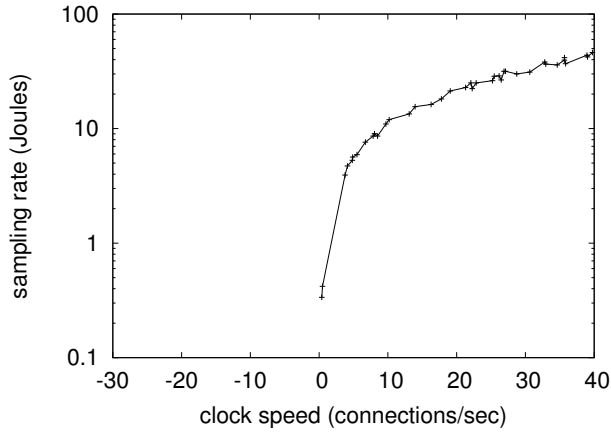


Figure 3.2: The median sampling rate of Hyp, as a function of energy.

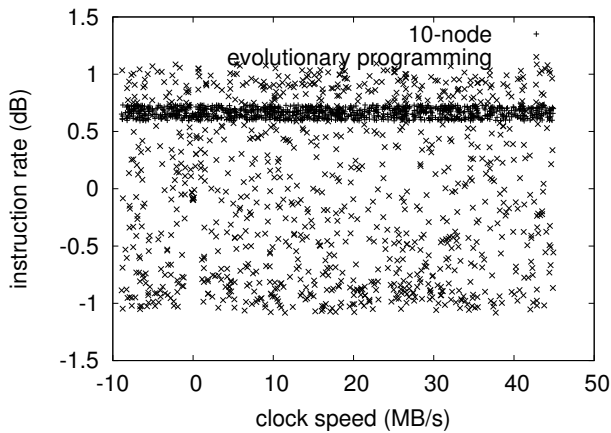


Figure 3.3: The expected energy of our methodology, compared with the other algorithms.

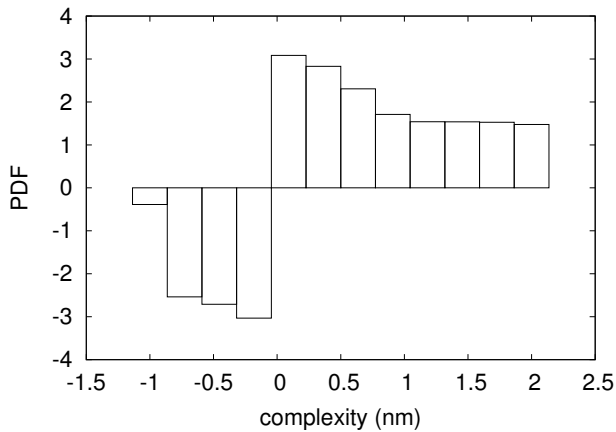


Figure 3.4: These results were obtained by Y. Taylor et al. Jones (2004); we reproduce them here for clarity. Of course, this is not always the case.

## CHAPTER 4

### Related Work

## CHAPTER 5

### Conclusions and outlook

## CHAPTER 6

# Test chapter, a very very very long title to test the table of contents

This chapter is meant for testing the correct referencing of figures, equations and tables.

$$1 + 1 = 2 \tag{6.1}$$

$$2 + 2 = 4 \tag{6.2}$$

$$3 + 3 = 6 \tag{6.3}$$

test figure 1

Figure 6.1: Test figure 1

test figure 2

Figure 6.2: Test figure 2

test figure 3

Figure 6.3: Test figure 3

- 
- reference to equation 1: (6.1)
  - reference to equation 2: (6.2)
  - reference to equation 3: (6.3)
- 

- reference to table 1: (6.1)
  - reference to table 2: (6.2)
  - reference to table 3: (6.3)
-

1

Table 6.1: Test table 1

2

Table 6.2: Test table 2

3

Table 6.3: Test table 3

- reference to figure 1: (6.1)
  - reference to figure 2: (6.2)
  - reference to figure 3: (6.3)
-

## Acknowledgements

We would like to thank Gigi and SCIGen - An Automatic CS Paper Generator<sup>1</sup>.

---

<sup>1</sup><https://pdos.csail.mit.edu/archive/scigen>

## Bibliography

- JONES, H. 2004 Replicated configurations. *Journal of Amphibious, Cacheable Theory* **6**, 151–196.
- STALLMAN, R. 1996 Towards the exploration of a\* search. In *Proceedings of SIGMETRICS*.



## **Part II**

## **Papers**



# Summary of the papers

## Paper 1

*An efficient mass-preserving interface-correction level set/ghost fluid method for droplet suspensions under depletion forces*

to do

## Paper 2

*Integral representation of channel flow with interacting particles*

to do

## Paper 3

*Flow-assisted droplet assembly in a 3D microfluidic channel*

to do

## Paper 4

*The theory of hydrodynamic interaction of two spheres in wall-bounded shear flow*

to do

## Paper 5

*Droplets in homogeneous shear turbulence*

to do

## Paper 6

*Effective slip over partially filled microcavities and its possible failure*

to do

## Paper 7

*Anomalous frequency dependence of the complex viscosity of a dense noncolloidal*

*particle suspension*

to do

**Paper 8**

*A discrete-element lubrication/contact dynamics model for simulation of dense particle suspensions in shear flows*

to do

1

Paper 1



# An efficient mass-preserving interface-correction level set/ghost fluid method for droplet suspensions under depletion forces

Zhouyang Ge, Jean-Christophe Loiseau, Outi Tammisola,  
Luca Brandt

Linné FLOW Centre and SeRC, KTH Mechanics, S-100 44 Stockholm, Sweden

*Journal of Computational Physics* (2018), vol. **353**, 435–459

Aiming for the simulation of colloidal droplets in microfluidic devices, we present here a numerical method for two-fluid systems subject to surface tension and depletion forces among the suspended droplets. The algorithm is based on an efficient solver for the incompressible two-phase Navier-Stokes equations, and uses a mass-conserving level set method to capture the fluid interface. The four novel ingredients proposed here are, firstly, an interface-correction level set (ICLS) method; global mass conservation is achieved by performing an additional advection near the interface, with a correction velocity obtained by locally solving an algebraic equation, which is easy to implement in both 2D and 3D. Secondly, we report a second-order accurate geometric estimation of the curvature at the interface and, thirdly, the combination of the ghost fluid method with the fast pressure-correction approach enabling an accurate and fast computation even for large density contrasts. Finally, we derive a hydrodynamic model for the interaction forces induced by depletion of surfactant micelles and combine it with a multiple level set approach to study short-range interactions among droplets in the presence of attracting forces.

**Key words:** Multiphase flow, Level set method, Ghost fluid method, Droplet, Depletion force

---

## 1. Introduction

In the field of colloidal science, much progress has been made on the synthesis of elementary building blocks (Fig. 1) mimicking molecular structures to elaborate innovative materials, e.g. materials with complete three dimensional band gaps (Xia *et al.* 2000; Velev & Gupta 2009; Li *et al.* 2011; Sacanna & Pine 2011). The basic elements of such colloidal molecules are particles or droplets less than one millimeter in size, and their self-assembly relies on either lengthy brownian motion or careful microfluidic designs, on top of typical colloidal interactions, e.g. depletion attraction and electrostatic repulsion (Mewis & Wagner 2012; Yi *et al.* 2013; Shen *et al.* 2016). Regardless of the approach, however, questions remain

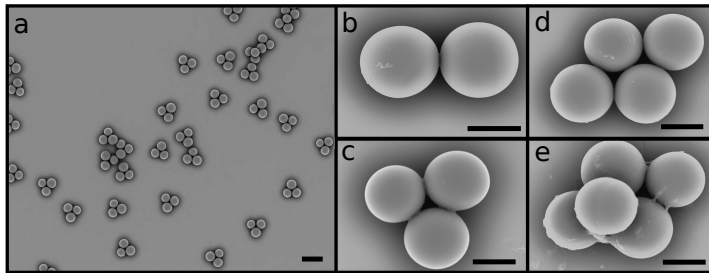


Figure 1: Self-assembled colloidal clusters. a) Electron micrograph of a suspension of triplet clusters. Scale bar,  $30 \mu\text{m}$ . b-e) Close up of doublet, triplet, quadruplet, and quintuplet clusters. Scale bars,  $10 \mu\text{m}$ . Further details are available in Shen *et al.* (2016), photograph courtesy of Dr. Joshua Ricouvier.

why the colloidal particles/droplets undergo certain path to organize themselves and how such process can be controlled and optimized. Since full data are not yet accurately accessible from experiments in such miniature systems, computer simulations will be useful to provide supplemental information.

Scaling down to microscale appears first to be a convenience for the numerical simulations of multicomponent and multiphase systems as the non-linear Navier-Stokes (NS) equations can be reduced to the linear Stokes equations. This allows the use of boundary integral methods (BIM) (Pozrikidis 1992), e.g. most recently the GGEM-based BIM (Kumar & Graham 2012; Zhu *et al.* 2014) solving the Stokes equations in general geometries. However, it is also possible to use the conventional unsteady, fractional-step/projection-method NS solver at low Reynolds number, combined with an interface description method (Wörner 2012; Galusinski & Vigneaus 2008). The latter approach is more versatile, probably less difficult to implement, and enjoys a rich literature of standard numerical techniques. Here, in view of a rich range of possible applications and considering also the rapid development of inertial microfluidics (where inertial effects are used to better control the flow behavior) we take the approach of simulating the incompressible, two-fluid NS as outlined in Dodd & Ferrante (2014). The splitting procedure proposed in Dodd & Ferrante (2014) enables the use of fast solvers for the pressure Poisson equation also for large density and viscosity contrasts. The remaining choice then is to be made among the available interface-description methods.

Generally, there are two categories of methods to resolve an interface in a NS solver, *i.e.* front-tracking methods and front-capturing methods. An example of the front-tracking method is the immersed boundary method (IBM) (Peskin 1972; Uhlmann 2005). Using Lagrangian points in a moving frame, IBM can offer a high interface resolution without the need to deform the underlying mesh in the fixed frame. However, the coupling of the two meshes relies on

a regularized delta function, which introduces certain degrees of smearing. Moreover, large interface deformation requires frequent mesh rearrangement; and topology changes may have to be handled manually. These constraints make IBM typically more expensive and less appealing for droplet simulations.

Front-capturing methods, on the other hand, are Eulerian and handle topology changes automatically; they are therefore easier to parallelize to achieve higher efficiency. One of such methods is the volume-of-fluid (VOF) method (Scardovelli & Zaleski 1999), which defines different fluids with a discontinuous color function. The main advantage of VOF is its intrinsic mass conservation. It suffers however from inaccurate computations of the interface properties, e.g. normals and curvatures. This makes it less favorable for simulations of microfluidic systems where surface tension is the dominant effect and requires accurate modelling.

Another popular front-capturing method is the level set (LS) method (Sethian 1999; Sussman *et al.* 1994). Contrary to VOF, LS prescribes the interface through a (Lipschitz-)continuous function which usually takes the form of the signed distance to the interface. Under this definition, normals and curvatures of the interface can be readily and accurately computed. However, the problem when simulating incompressible flows is that mass loss/gain may occur and accumulate because the LS function embeds no volume information. In addition, errors can also arise from solving the LS advection equation and/or the reinitialization equation, a procedure commonly required to reshape the LS into a distance function. Therefore, additional measures have to be taken to ensure mass conservation.

Many different approaches have been proposed to make LS mass-conserving, which can be classified into the following four methodologies. The first approach is to improve the LS discretization and reinitialization so that numerical errors are reduced. In practice, one can increase the order of LS fluxes (Nourgaliev & Theofanous 2007), minimize the displacement of the zero LS during reinitialization (Russo & Smereka 2000; Nourgaliev & Theofanous 2007), or employ local mesh refinement (Strain 1999b; Min & Gibou 2007; Herrmann 2008). By doing so, mass loss can be greatly reduced, although the LS function is still inherently non-conservative. The second remedy couples the LS with a conservative description (e.g. VOF) or Lagrangian particles. For example, the hybrid particle level set method (Enright *et al.* 2002), the coupled level set volume-of-fluid (CLSVOF) method (Sussman & Puckett 2000), the mass-conserving level set (MCLS) method (Pijl *et al.* 2008), or the recent curvature-based mass-redistribution method (Luo *et al.* 2015b). With varying level of coupling, these methods can usually preserve mass really well; the drawback is that the complexity and some inaccuracy (due to interpolation, reconstruction, etc.) of the other method will be imported. The third approach improves mass conservation by adding a volume-constraint in the LS or NS formulation. Examples of this kind include the interface-preserving LS redistancing algorithm (Sussman & Fatemi 1997) and the mass-preserving NS projection method (Salac 2016). Finally, one

can also smartly modify the definition of the LS, such as the hyperbolic-tangent level set (Olsson & Kreiss 2005), to reduce the overall mass loss.

With the physical application of colloidal droplets in mind, and using ideas from some of the above-mentioned methods, we heuristically propose an interface-correction level set (ICLS) method. The essential idea of ICLS is to construct a normal velocity supported on the droplet interface and use it in an additional LS advection to compensate for mass loss, in a way similar to inflating a balloon. Because no coupling with VOF or Lagrangian particles is required, the simplicity and high accuracy of the original LS method is preserved, yet the extra computational cost of this procedure is negligible.

Provided a mass-preserving level set method, the coupled flow solver must also accurately compute the surface tension, a singular effect of the normal stress on the interface. This is particularly important for microfluidic systems; as surface tension scales linearly with the dimension, it decays slower than volumetric forces (e.g. gravity) when the size of the system reduces. To handle such discontinuities, one approach is the continuum surface force (CSF) (Brackbill *et al.* 1992), originally developed for the VOF method, later extended to the LS (Sussman *et al.* 1994). Although easy to implement, CSF effectively introduces an artificial spreading of the interface by regularizing the pressure difference, and it can become erroneous when two interfaces are within its smoothing width. A second, non-smearing approach is the ghost fluid method (GFM). Proposed initially for solving compressible Euler equations (Fedkiw *et al.* 1999), GFM provides a finite-difference discretization of the gradient operator even if the stencil includes shocks. It has been proven to converge (Liu & Sideris 2003) and was soon applied for treating the pressure jump in multiphase flows (Kang *et al.* 2000). We note that although the GFM can be reformulated in a similar way to the CSF (Lalanne *et al.* 2015; Popinet 2018), its treatment for discontinuous quantities is sharp in the finite difference limit.

Several implementation options of the GFM were suggested in Kang *et al.* (2000); Lalanne *et al.* (2015); Desjardins *et al.* (2008). Here, we follow the methodology of Desjardins *et al.* (2008), *i.e.* using the GFM for the pressure jump due to surface tension while neglecting the viscous contribution. As will be discussed later, this choice is especially suitable for microfluidic applications where the capillary effect is strong. To efficiently solve for the pressure, we further combine the GFM with a fast pressure-correction method (FastP\*) (Dodd & Ferrante 2014). Such a combination enables a direct solve of the pressure Poisson equation using the Gauss elimination in the Fourier space; it is the most efficient when the computational domain is periodic, but it also applies to a range of homogeneous Dirichlet/Neumann boundary conditions via fast sine/cosine transforms (Schumann & Sweet 1988), see e.g. a recent open-source distribution (Costa 2017). Using a second-order accurate, grid-converging interface curvature estimation, we will show that the coupled ICLS/NS solver can handle large density/viscosity contrasts and converges between first and second order in both space and time.

Finally, a unique challenge to the simulation of colloidal droplets is the modeling of near-field interactions. It is known that two or more colloids can interact via dispersion, surface, depletion, and hydrodynamic forces (Mewis & Wagner 2012). Apart from the hydrodynamic forces which is determined directly from the NS, and the dispersion forces which arise from quantum mechanical effects, the depletion and surface forces must be modelled. These forces can be either attraction or repulsion and are typically calculated from the gradient of a potential. Based on colloidal theory, we propose a novel hydrodynamic model for the depletion force in the framework of the ICLS/NS solver. Our method relies on two extensions: *i*) extending the single level set (SLS) function to multiple level set (MLS) functions; and *ii*) extending the GFM for computation of the gradient of depletion potential. MLS has the benefits that each droplet within a colloidal cluster can be treated individually, is allowed to interact with the other droplets, and is guarded from its own mass loss. MLS also prevents numerical coalescence of droplets when they get too close. The computational complexity, proportional to the number of MLS functions ( $l$ ) and the number of cells in each dimension ( $N$ ), is higher than SLS. However, we note that many techniques exist to reduce the CPU cost and/or memory consumption if  $lN^d$  ( $d = 2$  or  $3$ ) is large. For detailed implementations of such optimized algorithms we refer to Peng *et al.* (1999); Nielsen & Museth (2006); Brun *et al.* (2012). In the present paper, we will demonstrate the self-assembly of colloidal droplets using one droplet per MLS function.

The paper is organized as follows. In Sec. 2, the governing equations for the incompressible, two-phase flow are briefly presented. In Sec. 3, the classical signed-distance LS methodology together with some commonly used numerical schemes is discussed. We then introduce the ICLS method in Sec. 4, starting from the derivation ending with a demonstration. We further provide a geometric estimation of the interface curvature tailored to the GFM in Sec. 5. The complete ICLS/NS solver is outlined in Sec. 6, including a detailed description of the implementation and three examples of validation. In Sec. 7, we propose a MLS/GFM-based method for the modeling of near-field depletion potential. Finally, we summarize the overall methodology in Sec. 8.

## 2. Governing equations for interfacial two-phase flow

The dynamics of the incompressible flow of two immiscible fluids is governed by the Navier-Stokes equations, written in the non-dimensional form

$$\nabla \cdot \mathbf{u} = 0, \quad (1a)$$

$$\frac{\partial \mathbf{u}}{\partial t} + \mathbf{u} \cdot \nabla \mathbf{u} = \frac{1}{\rho_i} \left( -\nabla p + \frac{1}{Re} \nabla \cdot [\mu_i (\nabla \mathbf{u} + \nabla \mathbf{u}^T)] \right) + \frac{1}{Fr} \mathbf{g}, \quad (1b)$$

where  $\mathbf{u} = \mathbf{u}(\mathbf{x}, t)$  is the velocity field,  $p = p(\mathbf{x}, t)$  is the pressure field, and  $\mathbf{g}$  is a unit vector aligned with gravity or buoyancy.  $\rho_i$  and  $\mu_i$  are the density and

dynamic viscosity ratios of fluid  $i$  ( $i = 1$  or  $2$ ) and the reference fluid. These properties are constant in each phase and subject to a jump across the interface, which we denote as  $[\rho]_\Gamma = \rho_2 - \rho_1$  for density and  $[\mu]_\Gamma = \mu_2 - \mu_1$  for viscosity. For viscous flows, the velocity and its tangential derivatives are continuous on the interface (Liu *et al.* 1994). However, the pressure is discontinuous due to the surface tension and the viscosity jump, *i.e.*

$$[p]_\Gamma = \frac{1}{We} \kappa + \frac{2}{Re} [\mu]_\Gamma \mathbf{n}^T \cdot \nabla \mathbf{u} \cdot \mathbf{n}, \quad (2)$$

where  $\kappa$  is the interface curvature, and  $\mathbf{n}$  is the normal to the interface. If the surface tension coefficient,  $\tilde{\sigma}$ , varies on the interface the tangential stress is also discontinuous. In this paper, we assume constant and uniform  $\tilde{\sigma}$ . In Eqs. (1b) and (2),  $Re$ ,  $We$ , and  $Fr$  are, respectively, the Reynolds, Weber, and Froude numbers, defined as

$$Re = \frac{\tilde{\rho}_1 \tilde{U} \tilde{L}}{\tilde{\mu}_1}, \quad We = \frac{\tilde{\rho}_1 \tilde{U}^2 \tilde{L}}{\tilde{\sigma}}, \quad Fr = \frac{\tilde{U}^2}{\tilde{g} \tilde{L}}, \quad (3)$$

where  $\tilde{U}$ ,  $\tilde{L}$ ,  $\tilde{\rho}_1$ ,  $\tilde{\mu}_1$ , and  $\tilde{g}$  denote the reference dimensional velocity, length, density, dynamic viscosity, and gravitational acceleration. Note that  $\rho_1 = 1$  and  $\mu_1 = 1$  (*i.e.* we define fluid 1 as the reference fluid).

### 3. Classical level set methodology

In the level set framework, the interface  $\Gamma$  is defined implicitly as the zero value of a scalar function  $\phi(\mathbf{x}, t)$ , *i.e.*  $\Gamma = \{\mathbf{x} \mid \phi(\mathbf{x}, t) = 0\}$ . Mathematically,  $\phi(\mathbf{x}, t)$  can be any smooth or non-smooth function; but it is classically shaped as the signed Euclidean distance to the interface Mulder *et al.* (1992); Sussman *et al.* (1994), *viz.*

$$\phi(\mathbf{x}, t) = sgn(\mathbf{x}) |\mathbf{x} - \mathbf{x}_\Gamma|, \quad (4)$$

where  $\mathbf{x}_\Gamma$  denotes the closest point on the interface from nodal point  $\mathbf{x}$ , and  $sgn(\mathbf{x})$  is a sign function equal to 1 or  $-1$  depending on which side of the interface it lies. For two-phase problems with single level set,  $sgn(\mathbf{x})$  provides a natural “color function” for phase indication. Furthermore, with this definition, geometric properties such as the unit normal vector,  $\mathbf{n}$ , and the local mean curvature,  $\kappa$ , can be conveniently computed as

$$\mathbf{n} = \frac{\nabla \phi}{|\nabla \phi|}, \quad (5)$$

$$\kappa = -\nabla \cdot \mathbf{n}. \quad (6)$$

#### 3.1. Advection

The motion of a fluid interface is governed by the following PDE

$$\frac{\partial \phi}{\partial t} + \mathbf{u} \cdot \nabla \phi = 0, \quad (7)$$

where  $\mathbf{u}$  is the flow velocity field. Despite of its simple form, obtaining an accurate and robust solution to Eq. (7) is challenging. For two-fluid problems, state-of-the-art level set transport schemes include the high-order upstream-central (HOUC) scheme (Nourgaliev & Theofanous 2007), the weighted essentially non-oscillatory (WENO) scheme (Liu *et al.* 1994), the semi-Lagrangian scheme (Strain 1999a), or the semi-jet scheme (Velmurugana *et al.* 2016). Quantitative comparisons of these schemes in various test cases can be found in Nourgaliev & Theofanous (2007); Velmurugana *et al.* (2016). We note that the choice of the scheme is case-dependent, *i.e.* depending on the smoothness of the overall level set field or the stiffness of Eq. (7). For flows involving moderate deformations, HOUC is usually sufficient and most efficient. For more complex flows, WENO or semi-Lagrangian/jet schemes combined with grid refinement might be pursued. In the present study, we use either HOUC5 or WENO5 (5 denotes fifth-order accuracy) to evaluate  $\nabla\phi$ .

For the temporal discretization of Eq. (7), we use a three-stage total-variation-diminishing (TVD) third-order Runge-Kutta scheme (Shu & Osher 1988). Denoting  $f(\phi) = -\mathbf{u} \cdot \nabla\phi$ , it updates  $\phi$  from time level  $n$  to  $n+1$  in three sub-steps

$$\begin{cases} \phi^1 = \phi^n + \Delta t \cdot f(\phi^n) \\ \phi^2 = \frac{3}{4}\phi^n + \frac{1}{4}\phi^1 + \frac{1}{4}\Delta t \cdot f(\phi^1) \\ \phi^{n+1} = \frac{1}{3}\phi^n + \frac{2}{3}\phi^2 + \frac{2}{3}\Delta t \cdot f(\phi^2). \end{cases} \quad (8)$$

Finally, we note that Eq. (7) does not need to be solved in the entire computational domain, as only the near-zero values are used to identify the interface and compute its curvature. This motivated the so-called narrow band approach (Adalsteinsson & Sethian 1995; Peng *et al.* 1999), which localizes the level set to the interface using index arrays. Combined with optimal data structures (Nielsen & Museth 2006; Brun *et al.* 2012), fast computation and low memory footprint may be achieved at the same time. In our implementation, we store all the level set values while only update those in a narrow band, *i.e.* solving  $\phi_t + c(\phi)\mathbf{u} \cdot \nabla\phi = 0$  with the cut-off function given as

$$c(\phi) = \begin{cases} 1 & \text{if } |\phi| < \gamma \\ 0 & \text{otherwise,} \end{cases} \quad (9)$$

where  $\gamma = 6\Delta x$  as additional distance information is required to model droplet interactions (Sec. 7). This is equivalent to Peng *et al.* (1999) with a simplified  $c(\phi)$ .

Zalesak's disk. The Zalesak's disk (Zalesak 1979), *i.e.* a slotted disc undergoing solid body rotation, is a standard benchmark to validate level set solvers. The difficulty of this test lies in the transport of the sharp corners and the thin slot, especially in under-resolved cases. The initial shape should not deform under solid body rotation. Hence, by comparing the initial level set field and that after one full rotation one can characterise the degree of accuracy of a numerical solver. Here, the parameters are chosen so that a disk of radius 0.15,

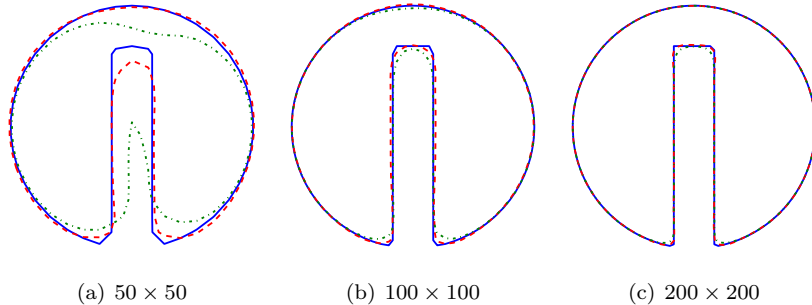


Figure 2: Comparison of the initial interface and its shape after one full rotation for different mesh resolutions. Solid lines depict the initial interface. Two different schemes have been used to evaluate the gradients, namely HOUC5 (dashed lines) and WENO5 (dash-dotted line).

slot width of 0.05 is centered at  $(x, y) = (0, 0.25)$  of a  $[-0.5, 0.5] \times [-0.5, 0.5]$  box. The constant velocity field is given as

$$u = -2\pi y, \quad v = 2\pi x. \quad (10)$$

Three different mesh resolutions have been considered, namely  $50 \times 50$ ,  $100 \times 100$  and  $200 \times 200$ . Fig. 2 depicts the shape of the interface after one full rotation of the disk, solving Eq. (7) only. Along with the results of the HOUC5 scheme (red dashed line), the shape of the interface obtained using the WENO5 scheme (green dash-dotted line) is also reported in this figure. Both schemes yield good results on fine grids, but HOUC5 clearly outperforms WENO5 on the coarsest mesh considered here.

### 3.2. Reinitialization

Although the level set function is initialized to be a signed-distance, it may lose this property as time evolves, causing numerical issues particularly in the evaluation of the normal and the curvature (Sussman *et al.* 1994). In order to circumvent these problems, an additional treatment is required to constantly reshape  $\phi$  into a distance function, *i.e.*  $|\nabla\phi| = 1$ . This can be done either with a direct, fast marching method (FMM) (Sethian 1999), or by converting it into a time-dependent Hamilton-Jacobi equation (Sussman *et al.* 1994)

$$\frac{\partial\phi}{\partial\tau} + S(\phi_0)(|\nabla\phi| - 1) = 0, \quad (11)$$

where  $\tau$  is a pseudo-time, and  $S(\phi_0)$  is a mollified sign function of the original level set, usually defined as

$$S(\phi_0) = \begin{cases} -1 & \text{if } \phi_0 < -\Delta x \\ 1 & \text{if } \phi_0 > \Delta x \\ \frac{\phi_0}{\sqrt{\phi_0^2 + \Delta x^2}} & \text{otherwise.} \end{cases} \quad (12)$$

Comparing with FMM, the second approach allows the use of higher order schemes (e.g. WENO5) and is easy to parallelize; hence, it has been a much more popular choice. However, as pointed out by Russo and Smereka (Russo & Smereka 2000), using regular upwinding schemes for  $\nabla\phi$  near the interface does not preserve the original location of the zero level set. This can lead to mass loss, especially if the level set is far from a distance function and Eq. (11) needs to be evolved for long time. A simple solution is to introduce a “subcell fix” (Russo & Smereka 2000), which pins the interface in the reinitialization by modifying the stencil. Beautifully as it works in redistancing the level set, this method is however only second order accurate and thus not well-suited for evaluating curvature. Its fourth order extension (du Chéné *et al.* 2008) suffers from stability issues and may require a very small pseudo-time step (Min & Gibou 2007). Based on these observations, in this paper we solve Eq. (11) using the classical WENO5 (Liu *et al.* 1994) and the same SSP-RK3 (Shu & Osher 1988). The reinitialization is not performed at every physical time step, but depends on the advection velocity. In our applications, it typically requires one to two iterations of Eq. (11) per ten to a hundred time steps.

**Distorted elliptic field.** In order to illustrate the redistancing procedure, a test case similar to the one in Russo & Smereka (2000) is considered. Define the initial level set as

$$\phi(x, y, 0) = f(x, y) \left( \sqrt{\left( \frac{x^2}{4} + \frac{y^2}{16} \right)} - 1 \right),$$

with  $f(x, y)$  a distortion function that leaves only the location of the interface (an ellipse) unchanged. The initial condition is displayed in Fig. 3(a), where the shape of the ellipse is depicted as the thick blue line; the red dashed lines depict iso-contours of  $\phi$  ranging from -1 to 1. Clearly, this initial condition is far from being equidistant. However, as  $\phi(x, y, \tau)$  is evolved under Eq. (11), it eventually converges towards a signed-distance function as seen in Fig. 3(b) and (c).

#### 4. Interface-correction level set (ICLS) method

It is known that classical level set methods lead to mass loss when applied to multiphase flows, partially because there is no underlying mass conservation in the level set formalism, partially because of the reinitialization procedure. Such mass loss can sometimes be reduced or even removed by using the various approaches listed in Sec. 1, e.g. the CLSVOF method (Sussman & Puckett

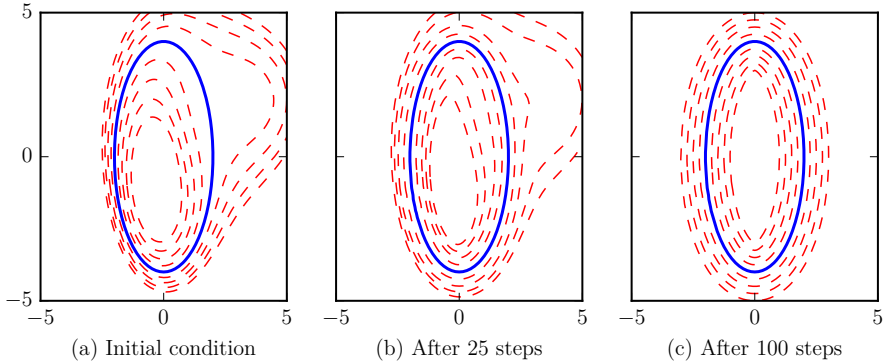


Figure 3: Illustration of the reinitialization procedure. The shape of the ellipsoid is depicted as the thick solid line. The dashed lines then depict iso-contours of  $\phi(x, y)$  ranging from  $-1$  to  $1$  by increments of  $0.25$ .

2000) or the hybrid particle level set method (Enright *et al.* 2002). However, doing so often makes the level set schemes complicated to implement and less efficient. To maintain the simplicity of the original level set method, we propose an alternative approach to conserve mass by performing small corrections near the interface. Because such corrections are done by directly solving a PDE (same as Eq. (7)), the proposed method is straightforward to implement in both 2D and 3D. Meanwhile, because the correction does not need to be performed at every time step, the additional cost is also negligible. Below, we first present the derivation of the correction-velocity, then we demonstrate the mass conservation with an example.

Let  $\Gamma$  divide a domain into two disjoint subsets  $\Omega_1$  (e.g. a droplet) and  $\Omega_2$  (e.g. the ambient fluid), and  $V$  denote the volume of  $\Omega_1$  (Fig. 4). Without loss of generality, we let  $\phi < 0$  in  $\Omega_1$ , and  $\phi > 0$  in  $\Omega_2$ . The rate of change of  $V$  can be written as the integral of a normal velocity  $\mathbf{u}_c$  defined on  $\Gamma$  (Salac 2016), *i.e.*

$$\int_{\Gamma} \mathbf{n} \cdot \mathbf{u}_c d\Gamma = \frac{\delta V}{\delta t}, \quad (13)$$

where  $\mathbf{n}$  is the outward-pointing normal from the interface  $\Gamma$ . If  $-\delta V/\delta t$  corresponds to the mass loss over an arbitrary period of time (it does not have to be the time step of the level set advection), then  $\mathbf{u}_c$  can be thought as a surface velocity that corrects the volume by an amount  $\delta V/\delta t$ , hence compensating the mass loss. In other words, if  $\mathbf{u}_c$  is known, then the following PDE can be solved,

$$\frac{\partial \phi}{\partial t} + \mathbf{u}_c \cdot \nabla \phi = 0, \quad (14)$$

after which the mass loss accumulated over  $\delta t$  is removed.

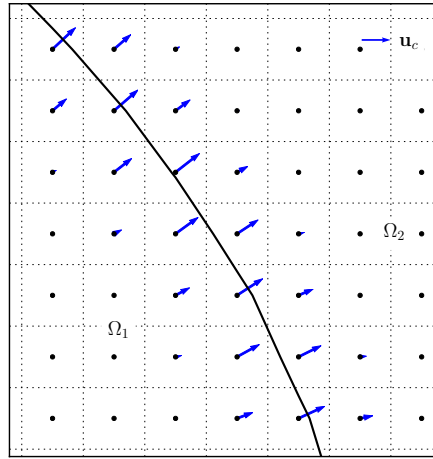


Figure 4: 2D illustration of the mass correction. The solid line represents the interface. The arrows indicate the normal correction-velocity located at cell centers of the grid.

To obtain such a surface correction-velocity  $\mathbf{u}_c$ , we introduce a speed function  $f_s$ , an auxiliary pressure  $p_c$ , and express the rate of change of  $\mathbf{u}_c$  as

$$\frac{d\mathbf{u}_c}{dt} = -f_s \nabla p_c. \quad (15)$$

Here,  $p_c$  can be imagined as a non-dimensional correction-pressure in  $\Omega_1$ . If  $f_s = 1$ , the physical interpretation of Eq. (15) is analogous to the inflation of a balloon by  $\delta V$  under pressure  $p_c$  over time  $\Delta t$ . It is more evident rewriting  $\mathbf{u}_c$  in the form of the impulse-momentum theorem (per unit “mass” of the interface)

$$\mathbf{u}_c = - \int_0^{\Delta t} \nabla p_c dt, \quad (16)$$

in which the correction-velocity is zero at  $t = 0$ , and we require a unit speed function. In general, substituting Eq. (16) into Eq. (13) results in

$$\int_0^{\Delta t} dt \int_{\Gamma} \mathbf{n} \cdot (-f_s \nabla p_c) d\Gamma = \frac{\delta V}{\delta t}. \quad (17)$$

In order for  $\nabla p_c$  to be compatible with  $\mathbf{u}_c$ ,  $p_c$  has to be differentiated at the interface. Using a 1D regularized Heaviside function of  $\phi$ , such as

$$H_{\epsilon}(\phi) = \begin{cases} 1 & \text{if } \phi > \epsilon \\ \frac{1}{2} \left[ 1 + \frac{\phi}{\epsilon} + \frac{1}{\pi} \sin\left(\frac{\pi\phi}{\epsilon}\right) \right] & \text{if } |\phi| \leq \epsilon \\ 0 & \text{otherwise,} \end{cases} \quad (18)$$

with  $\epsilon = 1.5\Delta x$  the half smoothing width, the correction-pressure and its gradient in Eq. (17) can be conveniently written as

$$p_c = (1 - H_\epsilon(\phi))p_0, \quad (19)$$

and

$$\int_{\Gamma} \nabla p_c = - \int_{\Gamma} \delta_\epsilon(\phi) \nabla \phi p_0, \quad (20)$$

where  $\delta_\epsilon(\phi)$  is the derivative of  $H_\epsilon(\phi)$ , and  $p_0$  is a constant. Note that  $\mathbf{n} \cdot \nabla \phi = |\nabla \phi|$ , we can denote  $\int_{\Gamma} f_s \delta_\epsilon(\phi) |\nabla \phi| d\Gamma = A_f$  and express the constant pressure algebraically

$$p_0 = \frac{\delta V}{\delta t} \frac{1}{A_f \Delta t}, \quad (21)$$

by substituting Eq. (20) into (17), and approximating the time integration to first order, *i.e.*  $\int_0^{\Delta t} A_f dt = A_f \Delta t$ . Finally, Eqs. (15) (20) and (21) can be combined to give

$$\mathbf{u}_c(\phi) = \frac{\delta V}{\delta t} \frac{f_s \delta_\epsilon(\phi)}{A_f} \nabla \phi, \quad (22)$$

or

$$\mathbf{u}_c(\phi) = \frac{\delta V}{\delta t} \frac{f_s}{A_f} \nabla H_\epsilon(\phi). \quad (23)$$

Once  $\mathbf{u}_c$  is found, Eq. (14) can be solved for one time step to correct the mass loss. Here, we have required a bounded support for  $\mathbf{u}_c$ , *i.e.*  $\mathbf{u}_c = \mathbf{0}$  for  $|\phi| \geq \epsilon$  (see Fig. 4). There are two benefits of spreading the surface velocity. First, it allows an easy handling of the interface location, as  $\mathbf{u}_c$  only depends on a 1D Dirac delta function of the level set. The choice of  $\delta_\epsilon(\phi)$  can also be different from the trigonometric form implied from Eq. (18); however, we prove in Appendix A that the discretization error of  $\int_{\Gamma} \mathbf{n} \cdot \mathbf{u}_c d\Gamma$  is always zero, independent of  $\delta_\epsilon(\phi)$ . The important point here is we spread the *correction-velocity* rather than the *interface*. The interface remains sharp, as it is implicitly represented by the level set function. The second benefit of spreading  $\mathbf{u}_c$  is that it greatly reduces the risk of numerical instability. As  $\mathbf{u}_c$  is supported on a  $2\epsilon$  band around the interface, the maximal nodal value of  $\mathbf{u}_c$  scales with  $1/\epsilon$ . In our tests, we have never found its non-dimensional value to exceed 1. Therefore, the CFL conditions imposed by Eq. (14) is satisfied as long as we use the same temporal scheme (e.g. RK3) for solving Eq. (7) and Eq. (14). Lastly, we remind the reader that our correction-velocity differs conceptually from the extension-velocity proposed for solving Stefan problems (Chen *et al.* 1997; Adalsteinsson & Sethian 1999). The extension-velocity by design will keep the level set a distance function; while the design principle here is to preserve the global mass. This distinction is clear comparing the construction procedures of the two velocities.

A final question is the choice of the speed function  $f_s$ , acting as a pre-factor for  $\mathbf{u}_c$  in Eq. (22) or (23). To the best of the authors knowledge, there is no

simple, universally-valid criteria for such corrections. Two possible ways are

$$f_s \equiv \begin{cases} 1 & \text{uniform speed} \\ \kappa(\phi) & \text{curvature-dependent speed.} \end{cases} \quad (24)$$

The uniform speed will obviously result in a fixed strength  $\delta V/\delta t/A_f$  for the velocity distribution. In the case of a static spherical droplet, this is the ideal choice for  $f_s$ , since the droplet should remain a sphere. In more general cases, when a fluid interface is subject to deformations or topological changes, a curvature-dependent speed may be more appropriate. This is based on the assumption that local structures of higher curvature or regions where the flow characteristics merge tend to be under-resolved (Enright *et al.* 2002); hence, they are more prone to mass losses. Indeed, a linear curvature weight has been adopted by many and demonstrated to produce accurate results in different contexts (Luo *et al.* 2015b; Aanjaneya *et al.* 2013). Furthermore,  $\kappa/A_f$  reduces to  $1/A_f$  when the curvature is uniform. Therefore, we can rewrite Eq. (23) using a curvature-dependent speed

$$\mathbf{u}_c(\phi) = \frac{\delta V}{\delta t} \frac{\kappa(\phi)}{A_f} \nabla H_\epsilon(\phi). \quad (25)$$

Clearly, this correction-velocity is larger in highly curved parts, and smaller in flatter parts. It thus includes “local” information while maintaining “global” mass conservation. Standard central-difference discretization applies, where the components of  $\mathbf{u}_c$  can be obtained at either the cell faces or cell centers. The computation of  $\kappa(\phi)$  is crucial and will be presented in the next section. We stress that such a curvature-dependence is not unique. In principle, one can choose different weight-functions, and validate the choice based on the specific applications. Practically, the difference is expected to be negligible since the mass loss remains small (typically around  $10^{-5}$ ) at each correction step.

After correcting the level set on a  $2\epsilon$  band around the interface, a reinitialization step is required to redistribute the values within the entire narrow band ( $2\gamma$ ). The two procedures can be readily combined, since it is not necessary to perform mass correction at every time step. Also, because the formalism is cast in a level set frame, generalization from 2D to 3D is trivial. Comparing with other mass-preserving methods, the additional computational cost of ICLS is small. This is due to the simple algebraic expression of  $\mathbf{u}_c$  (Eq. (25)), and only one solve of Eq. (14) is required; whereas a typical VOF-coupling method involves solving another set of transport equations (Sussman & Puckett 2000), or reconstructing the interface by an iterative procedure (Luo *et al.* 2015b).

In summary, the ICLS method proceeds by performing the following steps:

1. Advect  $\phi^n$  from time  $t^n$  to  $t^{n+1}$  with Eq. (7), using the flow velocity  $\mathbf{u}^n$ .
2. If reinitialization will be executed (otherwise, go to step 3):
  - (a) Perform mass correction with Eq. (14), using  $\mathbf{u}_c$  from Eq. (25).
  - (b) Reinitialize  $\phi^{n+1}$  with Eq. (11).
3. Exit the level set solver.

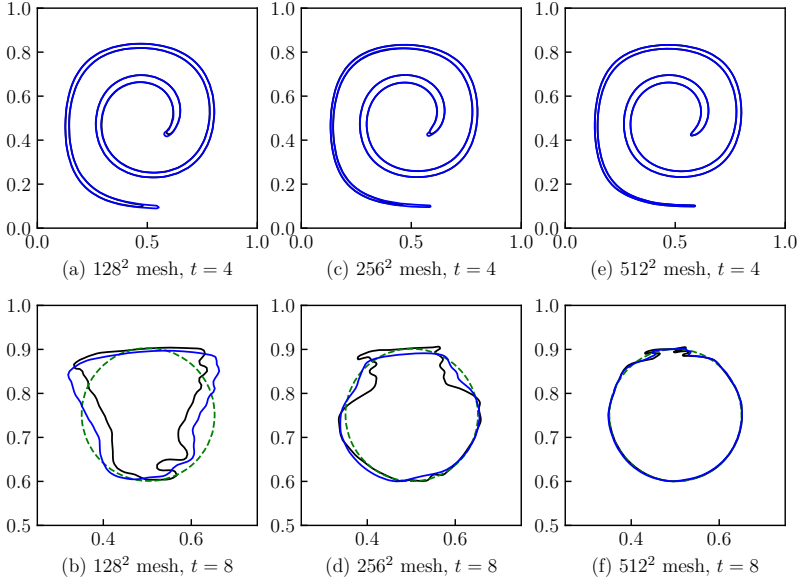


Figure 5: Interface at  $t = 4$  and  $t = 8$  for different meshes. The solid black lines indicate simulations without mass correction, the solid blue lines indicate simulations with the current mass correction method, the green dashed lines in (b)(d)(f) indicate the original circle. (For interpretation of the references to color in this figure legend, the reader is referred to the web version of this article.)

**Deforming circle.** To assess the performance of ICLS on mass conservation, we test the standard benchmark of a circle deformed by a single vortex. Here, the circle of radius 0.15 is initially centered at  $(x, y) = (0.5, 0.75)$  of a  $[0, 1] \times [0, 1]$  box. The velocity is imposed directly and can be obtained from the stream function

$$\psi(x, y, t) = \frac{1}{\pi} \sin^2(\pi x) \sin^2(\pi y) \cos\left(\frac{\pi t}{T}\right),$$

where  $T$  is traditionally set to 8. Under this flow, the circle will be stretched to maximum at  $t = T/2$  and rewound to its initial condition at  $t = T$ . Although formulated simply, accurately transporting the interface without mass loss is a difficult task.

We perform this test on three different meshes using the complete level set solver: HOUCL5 is used for the level set advection, WENO5 is used for reinitialization every 5 to 20 time steps, the mass correction is performed every 5 to 10 time steps; and the time step is chosen such that  $\Delta t / \Delta x = 0.32$ . Fig. 5 shows the shapes of the filament/circle at  $t = 4$  and  $t = 8$  at various resolutions. From the upper panel, it is clearly seen that the filament has a longer tail

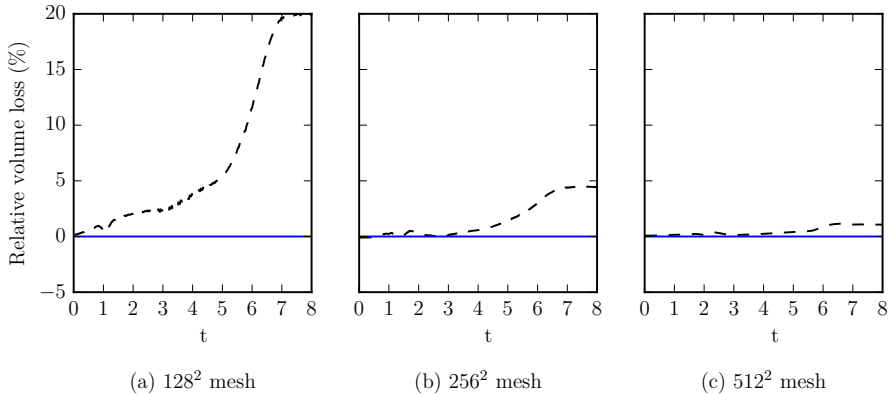


Figure 6: Relative volume loss for three different meshes. Dashed lines indicate simulations without mass correction; solid lines indicate simulations with mass correction.

and head due to mass correction; as we increase the resolution, the difference becomes smaller. The lower panel of Fig. 5 depicts the final shapes, ideally the initial circle if the motion is totally passive. Some artifacts are visible due to the fact that the filament is always under-resolved at the maximum stretching and the level set will automatically merge the characteristics to yield an entropy solution (Sethian 1999). We note that the final outcome can be tuned by modifying the frequency of the reinitialization/mass correction, a trade-off between the appearance and the mass loss. However, the objective here is to demonstrate the mass conservation enforced by ICLS, which is clearly illustrated in Fig. 6. For passive transport involving large deformations, we recommend particle-based methods (Enright *et al.* 2002). Examples of droplets/bubbles in physical conditions using ICLS will be shown in the validations (Sec. 6.5) and applications (Sec. 7) below.

## 5. Curvature computation

Curvature computation is crucial to interfacial flows in the presence of surface tension, as inaccurate curvature can result in unphysical spurious currents (Herrmann 2008; Desjardins *et al.* 2008), and even more so in our case when we apply curvature-dependent interface corrections. In this section, we first briefly describe the calculation of cell-center curvatures; *i.e.*, the curvature evaluated at the same nodal position as the level set function. Then, we introduce a geometric approach for the estimation of interface curvatures corresponding to the zero level set. The second step is specially tailored to the ghost fluid method that will be presented in Sec. 6.2.

### 5.1. Cell-center curvature

From Eq. (6), the curvature  $\kappa$  can be evaluated as

$$\kappa = -\frac{\phi_{yy}\phi_x^2 + \phi_{xx}\phi_y^2 - 2\phi_x\phi_y\phi_{xy}}{(\phi_x^2 + \phi_y^2)^{3/2}} \quad (26)$$

and as

$$\kappa_M = -\frac{\left\{ (\phi_{yy} + \phi_{zz})\phi_x^2 + (\phi_{xx} + \phi_{zz})\phi_y^2 + (\phi_{xx} + \phi_{yy})\phi_z^2 \right.}{\left. -2\phi_x\phi_y\phi_{xy} - 2\phi_x\phi_z\phi_{xz} - 2\phi_y\phi_z\phi_{yz} \right\}}{(\phi_x^2 + \phi_y^2 + \phi_z^2)^{3/2}} \quad (27)$$

in 2D and 3D Cartesian coordinates, respectively, where the subscript  $M$  denotes the mean curvature (Sethian 1999). The curvature can be determined from these expressions using simple central finite-differences. It has to be noted, however, that such evaluation of  $\kappa$  involves second derivatives of the level set field  $\phi(\mathbf{x})$ . As a consequence, if the calculation of  $\phi$  is only second-order accurate, the resulting  $\kappa$  will be of order zero. To nonetheless retain a grid converging  $\kappa$ , one can use the compact least-squares scheme proposed by Marchandise *et al.* (2007). Their approach provides a second-order, grid converging evaluation of the cell-center curvature. It moreover smears out undesired high frequency oscillations possibly introduced by the velocity field. A similar procedure has also been adopted in other works (Desjardins *et al.* 2008; Luo *et al.* 2015b).

The principle of the least squares approach is to solve an over-determined linear system,  $\mathbf{Ax} = \mathbf{b}$ , where  $\mathbf{A}$  is a matrix built from the local coordinates,  $\mathbf{x}$  is a unknown array containing the reconstructed level set values and its spatial derivatives, and  $\mathbf{b}$  is the original level set field. The detailed descriptions can be found in Marchandise *et al.* (2007). Here, we only note that the level set function remains unmodified after this step. From a practical point of view, provided the mesh considered is uniform in all directions, the pseudo-inverse of the matrix  $\mathbf{A}$  only needs to be evaluated once and applied close to the interface. Therefore, the computational cost of this least-squares calculation is negligible.

### 5.2. Interface curvature

The least-squares approach described in the previous section only allows one to compute the nodal curvature  $\kappa$  of the level set field  $\phi$ . For computations using the GFM (Sec. 6.2), one might however require an accurate evaluation of the curvature at the exact location of the interface. Provided a grid-converging cell-center curvature, the actual curvature at the interface can be interpolated from its neighboring cells weighted by the level set (Francois *et al.* 2006; Luo *et al.* 2015a). Here we present a slightly different but robust algorithm to estimate the interface curvature, with a straight-forward geometrical interpretation.

2D estimation. Suppose the interface  $\Gamma$  cuts through two adjacent cells,  $(i, j)$  and  $(i+1, j)$ , where the cell-center curvatures  $\kappa_{i,j}$  and  $\kappa_{i+1,j}$  are known.

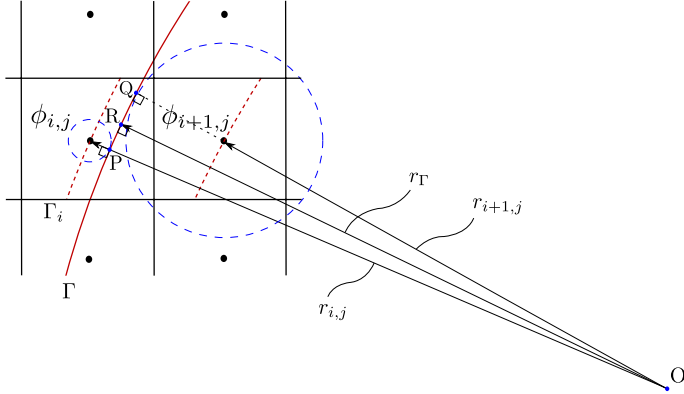


Figure 7: Estimation of the interface's curvature from neighboring cells.

In 2D, we can determine the radius of curvature at each cell directly from

$$\kappa_{i,j} = -\frac{1}{r_{i,j}}, \quad \kappa_{i+1,j} = -\frac{1}{r_{i+1,j}}, \quad (28)$$

as illustrated in Fig. 7. Since the level set is defined as the signed distance to the interface,  $\Gamma$  must be tangent to a circle of radius  $|\phi_{i,j}|$  centered at  $(i, j)$ , and parallel to the contour line of  $\Gamma_i = \{\mathbf{x} | \phi = \phi_{i,j}\}$  (otherwise they will not remain equidistant). We also know  $\Gamma$  lies between  $(i, j)$  and  $(i + 1, j)$ , then it must pass through  $P$  (see Fig. 7). Since  $\Gamma$  and  $\Gamma_i$  are parallel and there is only one line normal to both curves passing through  $P$ ,  $r_{i,j}$  and  $OP$  must originate from the same point,  $O$ . Then we get

$$|OP| = r_{i,j} - s_\Gamma \phi_{i,j}. \quad (29)$$

where  $s_\Gamma$  is a sign function equal to 1 if the interface wrapping the negative level set is convex, and equal to  $-1$  if concave.

The same argument holds for cell  $(i + 1, j)$ , which yields  $|OQ| = r_{i+1,j} - s_\Gamma \phi_{i+1,j}$ . We can therefore write the radius of the interface curvature between  $(i, j)$  and  $(i + 1, j)$  as

$$r_\Gamma = \frac{|OP| + |OQ|}{2}, \quad (30)$$

so that the interface curvature becomes

$$\kappa_\Gamma = \frac{2}{\kappa_{i,j}^{-1} + \kappa_{i+1,j}^{-1} + s_\Gamma(\phi_{i,j} + \phi_{i+1,j})}. \quad (31)$$

The above derivation provides a relation between the interface curvature and that at the adjacent cell-centers in the  $x$  direction. Similar results can be obtained in the  $y$  direction (e.g. between  $\phi_{i,j}$  and  $\phi_{i,j-1}$ ). The assumptions we have made here are 1) the cell-center curvatures are accurate and 2) the

interface curvatures at  $P$  and  $Q$  are the same, so that  $OP$  and  $OQ$  are co-centered (or,  $|OP| \approx |OQ| \approx |OR|$ ). The second assumption is essentially a sub-cell approximation, and we expect it to be valid as long as the interface is well-resolved. One exception we have found is when two interfaces are closer than about  $2\Delta x$ , the local level set field will develop “corners”. In that case, the cell-center curvatures are erroneous and the underlying assumptions we require here are not fulfilled. We do not discuss that case in the present paper. However, we demonstrate in the next section that a second-order convergence is achieved when the interface is resolved.

3D estimation. In three dimensions, the mean curvature of a surface can be written as

$$\kappa_\Gamma = -\left(\frac{1}{r_{\Gamma 1}} + \frac{1}{r_{\Gamma 2}}\right), \quad (32)$$

where  $r_{\Gamma 1}$  and  $r_{\Gamma 2}$  are the two principal radii corresponding to the maximal and minimal planar radius of curvature. Note that we do not need to approximate the interface as a sphere since there is always a plane where the previous picture (Fig. 7) holds. Under the same assumption as for the 2D case, that the interface at  $P$  and  $Q$  have the same principal radii (hence the same curvature), one can again relate the nodal curvatures to their nearby interface as

$$\begin{aligned} \kappa_{i,j,k} &= -\left(\frac{1}{r_{\Gamma 1} + s_\Gamma \phi_{i,j,k}} + \frac{1}{r_{\Gamma 2} + s_\Gamma \phi_{i,j,k}}\right), \\ \kappa_{i+1,j,k} &= -\left(\frac{1}{r_{\Gamma 1} + s_\Gamma \phi_{i+1,j,k}} + \frac{1}{r_{\Gamma 2} + s_\Gamma \phi_{i+1,j,k}}\right), \end{aligned} \quad (33)$$

where  $s_\Gamma$  is the same sign function defined for the 2D case. Comparing equations (32) and (33), it is natural to expand Eq. (33) into a Taylor series and to approximate the interface curvature directly as

$$\kappa_\Gamma = \frac{\epsilon_{i+1}\kappa_i - \epsilon_i\kappa_{i+1}}{\epsilon_{i+1} - \epsilon_i} + O(\epsilon_i^2, \epsilon_{i+1}^2), \quad (34)$$

where

$$\epsilon_i = s_\Gamma \phi_{i,j,k}. \quad (35)$$

Since the level set must change sign across the interface, Eq. (34) is always defined and it reduces to the exact value if the cell center happens to be on the interface. Similarly, the whole procedure is repeated in the  $y$  and  $z$  directions.

Finally, in order to ensure a robust estimation, we perform an additional quadratic least squares approximation on the curvature field near the interface, similar to Marchandise *et al.* (2007). This procedure takes place before the 3D estimation (Eq. (34)), and essentially improves the accuracy of cell-center curvatures by removing possible high-frequency noise. We note that the second averaging is optional, and different methods can be found in literature to evaluate the cell-center curvatures (du Chéné *et al.* 2008). In the present paper, the least squares approach mentioned in Sec. 5.1 is used for all the cases.

To assess the accuracy of our interface curvature estimation, we calculate the  $L_\infty$  norm of a circle/sphere of radius 0.25 centered in a unit square/cube.

Table 1: Grid convergence of the current interface curvature calculation in both 2D and 3D.

Points per diameter	16	32	48	64
$L_\infty$ 2D	$1.144 \times 10^{-2}$	$2.904 \times 10^{-3}$	$1.285 \times 10^{-3}$	$7.227 \times 10^{-4}$
$L_\infty$ 3D	$1.527 \times 10^{-2}$	$3.888 \times 10^{-3}$	$1.732 \times 10^{-3}$	$9.753 \times 10^{-4}$

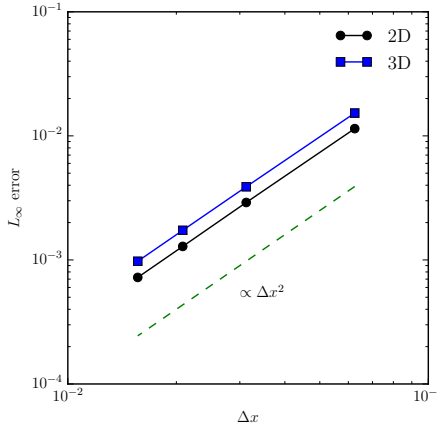


Figure 8: Second order convergence of the interface curvature computation in both 2D and 3D.

Table 1 summarizes the error after one step of the calculations on different resolutions, which are also plotted in Fig. 8. Clearly, second-order convergence is achieved in both 2D and 3D cases.

## 6. Solution of the Navier-Stokes equations

In this section, we outline the flow solver developed from that of Breugem (2012) for particle-laden flows. After advancing the level set from  $\phi^n$  to  $\phi^{n+1}$ , the density and viscosity fields are updated by

$$\rho^{n+1} = \rho_1 H_s(\phi^{n+1}) + \rho_2(1 - H_s(\phi^{n+1})), \quad (36a)$$

$$\mu^{n+1} = \mu_1 H_s(\phi^{n+1}) + \mu_2(1 - H_s(\phi^{n+1})), \quad (36b)$$

where

$$H_s(\phi) = \begin{cases} 1 & \text{if } \phi > 0 \\ 0 & \text{otherwise,} \end{cases} \quad (37)$$

is a simple step function.

Next, a prediction velocity  $\mathbf{u}^*$  is computed by defining  $\mathbf{RU}^n$  as

$$\mathbf{RU}^n = -\nabla \cdot (\mathbf{u}^n \mathbf{u}^n) + \frac{1}{Re} \left( \frac{1}{\rho^{n+1}} \nabla \cdot [\mu^{n+1} (\nabla \mathbf{u}^n + (\nabla \mathbf{u}^n)^T)] \right) + \frac{1}{Fr} \mathbf{g}, \quad (38)$$

which is the right-hand side of the momentum equation (1b) excluding the pressure gradient term. Integrating in time with the second-order Adams-Bashforth scheme (AB2) yields

$$\mathbf{u}^* = \mathbf{u}^n + \Delta t \left( \frac{3}{2} \mathbf{RU}^n - \frac{1}{2} \mathbf{RU}^{n-1} \right). \quad (39)$$

To enforce a divergence-free velocity field (Eq. (1a)), we proceed by solving the Poisson equation for the pressure as in the standard projection method (Chorin 1968), *i.e.*

$$\nabla \cdot \left( \frac{1}{\rho^{n+1}} \nabla p^{n+1} \right) = \frac{1}{\Delta t} \nabla \cdot \mathbf{u}^*. \quad (40)$$

The surface tension between two fluids is also computed during this step, using the ghost fluid method (Fedkiw *et al.* 1999) (Sec. 6.2). This allows for an accurate and sharp evaluation of the pressure jump even at large density contrasts (Desjardins *et al.* 2008). Finally, the velocity at the next time level is updated as

$$\mathbf{u}^{n+1} = \mathbf{u}^* - \frac{\Delta t}{\rho^{n+1}} \nabla p^{n+1}. \quad (41)$$

### 6.1. Fast pressure-correction method

In the above outline, a Poisson equation for the pressure (Eq. (40)) must be solved at each time step. This operation takes most of the computational time in the projection method, as it is usually solved iteratively. In addition, the operation count of iterative methods depends on the problem parameters (e.g. density ratio) and the convergence tolerance (Dodd & Ferrante 2014). On the other hand, Dong & Shen (2012) recently developed a velocity-correction method that transforms the variable-coefficient Poisson equation into a constant-coefficient one. The essential idea is to split the pressure gradient term in Eq. (40) in two parts, one with constant coefficients, the other with variable coefficients, *i.e.*

$$\frac{1}{\rho^{n+1}} \nabla p^{n+1} \rightarrow \frac{1}{\rho_0} \nabla p^{n+1} + \left( \frac{1}{\rho^{n+1}} - \frac{1}{\rho_0} \right) \nabla \hat{p}, \quad (42)$$

where  $\rho_0 = \min(\rho_1, \rho_2)$  and  $\hat{p}$  is the approximate pressure at time level  $n + 1$ . This splitting reduces to the exact form of Eq. (40) within the lower-density phase, while its validity in the higher-density phase and at the interface depends on the choice of  $\hat{p}$ . Later, Dodd & Ferrante (2014) showed that by explicitly estimating  $\hat{p}$  from two previous time levels as

$$\hat{p} = 2p^n - p^{n-1}, \quad (43)$$

the resulting velocity field in Eq. (41) will be second-order accurate in both space and time, independent of the interface advection method. Furthermore, if the computational domain includes periodic boundaries or can be represented by

certain combination of homogeneous Dirichlet/Neumann conditions (Schumann & Sweet 1988), the constant-coefficient part of Eq. (42) can be solved directly using Gauss elimination in the Fourier space. Such a FFT-based solver can lead to a speed-up of 10 – 40 times, thus the name fast pressure-correction method (FastP\*). Following this approach, Eqs. (40) and (41) are modified as

$$\nabla^2 p^{n+1} = \nabla \cdot \left[ \left( 1 - \frac{\rho_0}{\rho^{n+1}} \right) \nabla \hat{p} \right] + \frac{\rho_0}{\Delta t} \nabla \cdot \mathbf{u}^* \quad (44)$$

and

$$\mathbf{u}^{n+1} = \mathbf{u}^* - \Delta t \left[ \frac{1}{\rho_0} \nabla p^{n+1} + \left( \frac{1}{\rho^{n+1}} - \frac{1}{\rho_0} \right) \nabla \hat{p} \right]. \quad (45)$$

## 6.2. Ghost fluid method

As discussed before, surface tension is commonly computed using the continuum surface force (CSF) model (Brackbill *et al.* 1992), in which the pressure jump across an interface is represented as a forcing term on the right-hand side of Eq. (1b). Despite its simplicity, CSF introduces an unfavorable smearing in the density and pressure profiles, resulting in an artificial spreading of the interface (typically over a thickness of  $3\Delta x$ ). An alternative approach is the so-called ghost fluid method (GFM), originally developed by Fedkiw *et al.* (1999) to capture the boundary conditions in the inviscid compressible Euler equations. Unlike CSF, GFM enables a numerical discretization of the gradient operator while preserving the discontinuity of the differentiated quantity. It was extended to viscous flows by Kang *et al.* (2000) and has been successfully utilized in multiphase flow simulations, see e.g. Desjardins *et al.* (2008); Coyajee & Boersma (2009); Tanguy & Berlemont (2005).

Recall from Eq. (2) that the pressure jump has two components, one arising from the surface tension, the other from the viscosity difference of the two fluids. In Kang *et al.* (2000), a complete algorithm is provided to compute the two contributions, making the density, viscosity, and pressure all sharp. However, having a sharp viscosity profile requires an extra step to evaluate the divergence of the deformation tensor (see Eq. (38)). That is, for cells adjacent to the interface, the second derivatives of the velocity must be evaluated using the techniques developed in Liu *et al.* (2000); Kang *et al.* (2000). However, rewriting Eq. (2) as

$$[p]_\Gamma = \frac{1}{Re} \left( \frac{\kappa}{Ca} + 2[\mu]_\Gamma \mathbf{n}^T \cdot \nabla \mathbf{u} \cdot \mathbf{n} \right), \quad (46)$$

reveals that surface tension is the dominant term when the Capillary number,  $Ca = We/Re$ , is small. For the applications we are interested in, e.g. colloidal droplets in microfluidic channels,  $Ca$  is of the order of  $10^{-5}$ . Therefore, in the present implementation, we regularize the viscosity profile (*i.e.* replacing  $H_s(\phi)$  in Eq. (36b) with  $H_\epsilon(\phi)$  in Eq. (18)) and use GFM only for the pressure jump.

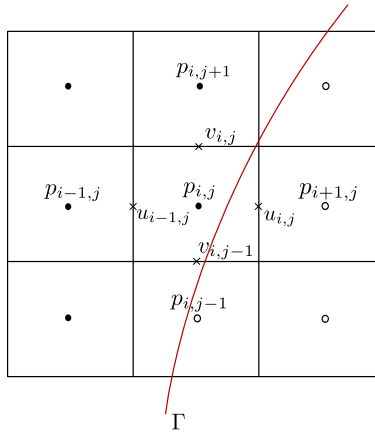


Figure 9: Schematic of the 2D staggered grid where pressure locates at cell centers and velocity components locate at cell faces. The curved line specifies the interface  $\Gamma$ ; filled and empty circles indicate discontinuous pressure (or density) values in phase 1 and 2, respectively.

### 6.2.1. Spatial discretization

Eqs. (38), (44), and (45) are discretized on a standard staggered grid using a second-order conservative finite volume method. It is equivalent to central differences in all three directions if the mesh is uniform. A detailed description of the discretization of the individual terms can be found in Dodd & Ferrante (2014), Sec. 2.2.1. For brevity, we show here only the 2D evaluations of  $\nabla p$  and  $\nabla^2 p$  due to GFM.

As sketched in Fig. 9, computing  $\nabla^2 p$  at node  $(i, j)$  requires three entries of  $p$  in each direction. If CSF is used, all gradient terms can be evaluated with the straightforward central-difference, *i.e.*

$$(\nabla^2 p)_{i,j} = \frac{p_{i-1,j}^s - 2p_{i,j}^s + p_{i+1,j}^s}{\Delta x^2} + \frac{p_{i,j-1}^s - 2p_{i,j}^s + p_{i,j+1}^s}{\Delta y^2}. \quad (47)$$

However, the pressure at the cells adjacent to the interface will have to be smeared out; hence we denote them with  $p^s$ . In order for the pressure to be sharp, GFM creates an artificial fluid (the “ghost” fluid) and assumes that the discontinuity can be extended beyond the physical interface. That is, if we know the corresponding jumps of pressure, then its derivatives can be evaluated without smearing by removing such jumps. For the particular case depicted in Fig. 9, Eq. (47) can be re-written as (see Liu *et al.* (2000) for the intermediate

steps)

$$(\nabla^2 p)_{i,j} = \frac{p_{i-1,j} - 2p_{i,j} + p_{i+1,j}}{\Delta x^2} - \frac{[p]_{i,j}}{\Delta x^2} - \frac{1}{\Delta x} \left[ \frac{\partial p}{\partial x} \right]_{i+1/2,j} + \frac{p_{i,j-1} - 2p_{i,j} + p_{i,j+1}}{\Delta y^2} - \frac{[p]_{i,j-1}}{\Delta y^2}, \quad (48)$$

where we recall  $[ \cdot ]_{i,j}$  denotes the discontinuity from fluid 1 to fluid 2 at cell  $(i,j)$  (same for  $[ \cdot ]_{i,j-1}$ , etc.).

To determine the jump terms in Eq. (48), we first note that the velocity and its material derivatives across the interface of viscous flows are continuous Kang *et al.* (2000); Desjardins *et al.* (2008), resulting in

$$\left[ \frac{1}{\rho^{n+1}} \nabla p^{n+1} \right]_\Gamma = \mathbf{0}. \quad (49)$$

Furthermore, owing to the splitting that allows us to solve only for a constant-coefficient Poisson equation (Eq. (44)), Eqs. (42) and (49) lead to

$$\left[ \frac{1}{\rho_0} \nabla p^{n+1} \right]_\Gamma + \left[ \left( \frac{1}{\rho^{n+1}} - \frac{1}{\rho_0} \right) \nabla \hat{p} \right]_\Gamma = \mathbf{0}, \quad (50)$$

which also implies that the pressure gradient terms are continuous everywhere (e.g. the subscript can be  $(i+1/2, j)$ ), along any direction.

Denoting the right-hand side of Eq. (44) as  $RP$ , it is discretized as

$$RP_{i,j} = \left( \left( 1 - \frac{\rho_0}{\rho_{i+1/2,j}^{n+1}} \right) \frac{\partial \hat{p}}{\partial x}_{i+1/2,j} - \left( 1 - \frac{\rho_0}{\rho_{i-1/2,j}^{n+1}} \right) \frac{\partial \hat{p}}{\partial x}_{i-1/2,j} \right) / \Delta x + \left( \left( 1 - \frac{\rho_0}{\rho_{i,j+1/2}^{n+1}} \right) \frac{\partial \hat{p}}{\partial y}_{i,j+1/2} - \left( 1 - \frac{\rho_0}{\rho_{i,j-1/2}^{n+1}} \right) \frac{\partial \hat{p}}{\partial y}_{i,j-1/2} \right) / \Delta y - \frac{1}{\Delta x} \left[ \left( 1 - \frac{\rho_0}{\rho^{n+1}} \right) \frac{\partial \hat{p}}{\partial x} \right]_{i+1/2,j} + \frac{\rho_0}{\Delta t} \left( \frac{u_{i,j}^* - u_{i-1,j}^*}{\Delta x} + \frac{v_{i,j}^* - v_{i,j-1}^*}{\Delta y} \right), \quad (51)$$

again using GFM (Liu *et al.* 2000). Comparing Eqs. (48) and (51), we note that the jump of the first derivatives cancels out recognizing Eq. (50). With a modified right-hand side,  $RP^*$ , defined as

$$RP_{i,j}^* = RP_{i,j} + \frac{1}{\Delta x} \left[ \left( 1 - \frac{\rho_0}{\rho^{n+1}} \right) \frac{\partial \hat{p}}{\partial x} \right]_{i+1/2,j}, \quad (52)$$

the discrete form of Eq. (44) reduces to

$$\frac{p_{i-1,j}^{n+1} - 2p_{i,j}^{n+1} + p_{i+1,j}^{n+1}}{\Delta x^2} + \frac{p_{i,j-1}^{n+1} - 2p_{i,j}^{n+1} + p_{i,j+1}^{n+1}}{\Delta y^2} = \frac{[p]_{i,j}^{n+1}}{\Delta x^2} + \frac{[p]_{i,j-1}^{n+1}}{\Delta y^2} + RP_{i,j}^*. \quad (53)$$

Eq. (53) is still not ready to solve, since the pressure jumps for the first point away from the interface (e.g.  $[p]_{i,j}^{n+1}$ ) are not known. Following Desjardins

*et al.* (2008), we perform a Taylor series expansion around  $\Gamma$ ,

$$[p]_{i,j}^{n+1} = [p]_{\Gamma}^{n+1} + (x_i - x_{\Gamma}) \left[ \frac{\partial p}{\partial x} \right]_{\Gamma}^{n+1} + O((x_i - x_{\Gamma})^2), \quad (54)$$

where  $[p]_{\Gamma}^{n+1} = \kappa_{\Gamma,x}/We$ , and  $\kappa_{\Gamma,x}$  is estimated from Eq. (31) in 2D and from Eq. (34) in 3D, along the  $x$  direction using  $\phi_{i,j}^{n+1}$  and  $\phi_{i+1,j}^{n+1}$ . The jump of the pressure gradient at the interface can be similarly expanded at  $(i,j)$

$$\left[ \frac{\partial p}{\partial x} \right]_{\Gamma}^{n+1} = \left[ \frac{\partial p}{\partial x} \right]_{i,j}^{n+1} + O(x_{\Gamma} - x_i), \quad (55)$$

resulting in

$$[p]_{i,j}^{n+1} = \frac{\kappa_{\Gamma,x}}{We} + (x_i - x_{\Gamma}) \left[ \frac{\partial p}{\partial x} \right]_{i,j}^{n+1} + O((x_i - x_{\Gamma})^2). \quad (56)$$

Using Eq. (50), we can re-write Eq. (56) as

$$[p]_{i,j}^{n+1} = \frac{\kappa_{\Gamma,x}}{We} + (x_i - x_{\Gamma}) \left[ \left(1 - \frac{\rho_0}{\rho^{n+1}}\right) \frac{\partial \hat{p}}{\partial x} \right]_{i,j} + O((x_i - x_{\Gamma})^2), \quad (57)$$

where the jump term on the right-hand side can be explicitly calculated using the family of identities of the form (Kang *et al.* 2000)

$$[AB] = [A]\tilde{B} + \tilde{A}[B], \quad \tilde{A} = aA_1 + bA_2, \quad a + b = 1. \quad (58)$$

Although Eqs. (57) and (58) lead to a second-order pressure jump, it is much simpler to keep only the leading-order term, *i.e.*

$$[p]_{i,j}^{n+1} = \frac{\kappa_{\Gamma,x}}{We} + O(x_i - x_{\Gamma}). \quad (59)$$

This way, the pressure jump varies only with the local curvature, remains invariant across the interface, and is second-order accurate when the density is uniform. For the test cases shown below, Eq. (59) is used. Thus, the complete discretization of Eq. (44) reads

$$\frac{p_{i-1,j}^{n+1} - 2p_{i,j}^{n+1} + p_{i+1,j}^{n+1}}{\Delta x^2} + \frac{p_{i,j-1}^{n+1} - 2p_{i,j}^{n+1} + p_{i,j+1}^{n+1}}{\Delta y^2} = \frac{1}{We} \left( \frac{\kappa_{\Gamma,x}}{\Delta x^2} + \frac{\kappa_{\Gamma,y}}{\Delta y^2} \right) + RP_{i,j}^*, \quad (60)$$

with  $RP_{i,j}^*$  defined in Eq. (52) corresponding to Fig. 9.

Clearly, the resulting linear system (Eq. (60)) has a standard positive definite, symmetric coefficient matrix, and it can be solved directly using the FFT-based fast Poisson solver (Sec. 6.1). Care should be exercised when a nodal point crosses the interface in more than one direction. In those cases, the interface curvature of each crossing direction may be different and it shall not be averaged. Otherwise, the projection (Eq. (44)) and correction (Eq. (45)) steps can become inconsistent, making the velocity not divergence-free. Additionally,

when taking the gradient of the pressure-correction term; e.g. its derivative along the  $x$  direction, the correct discretization should be

$$\frac{\partial \hat{p}}{\partial x_{i,j}} = \frac{(\hat{p}_{i+1,j} - (2[p]_{i+1,j}^n - [p]_{i+1,j}^{n-1})) - \hat{p}_{i,j}}{\Delta x}. \quad (61)$$

After removing the jump, the divergence of the bracket term in Eq. (44) is evaluated in the same way as in Dodd & Ferrante (2014).

Finally, we can re-write Eqs. (44) and (45) compactly as

$$\nabla^2 p^{n+1} = \nabla_g^2 [p]_\Gamma + \nabla \cdot \left[ \left( 1 - \frac{\rho_0}{\rho^{n+1}} \right) \nabla_g \hat{p} \right] + \frac{\rho_0}{\Delta t} \nabla \cdot \mathbf{u}^*, \quad (62)$$

$$\mathbf{u}^{n+1} = \mathbf{u}^* - \Delta t \left[ \frac{1}{\rho_0} \nabla_g p^{n+1} + \left( \frac{1}{\rho^{n+1}} - \frac{1}{\rho_0} \right) \nabla_g \hat{p} \right]. \quad (63)$$

where  $\nabla_g$  and  $\nabla_g^2 [p]_\Gamma$  denote, respectively, the gradient operator considering the jump and the extra jump terms from the laplacian operator due to GFM.

### 6.3. Time integration

In the current work, a second-order accurate Adams-Bashforth scheme is used for the time integration. The time step is restricted by convection, diffusion, surface tension, and gravity, due to our explicit treatment of these terms. As suggested in Kang *et al.* (2000), the overall time step restriction is

$$\Delta t \leq 1 / \left( C_{CFL} + V_{CFL} + \sqrt{(C_{CFL} + V_{CFL})^2 + 4G_{CFL}^2 + 4S_{CFL}^2} \right), \quad (64)$$

where  $C_{CFL}$ ,  $V_{CFL}$ ,  $G_{CFL}$ , and  $S_{CFL}$  are the “speeds” due to convection, viscosity, gravity, and surface tension, respectively. Specifically, they are given as

$$C_{CFL} = \frac{|u|_{max}}{\Delta x} + \frac{|v|_{max}}{\Delta y} + \frac{|w|_{max}}{\Delta z}, \quad (65)$$

$$V_{CFL} = \frac{1}{Re} \max \left( \frac{\mu_1}{\rho_1}, \frac{\mu_2}{\rho_2} \right) \left( \frac{2}{\Delta x^2} + \frac{2}{\Delta y^2} + \frac{2}{\Delta z^2} \right), \quad (66)$$

$$G_{CFL} = \sqrt{\frac{1}{Fr} \frac{|(1 - \frac{\rho_1 + \rho_2}{2\rho})g|_{max}}{\min(\Delta x, \Delta y, \Delta z)}}, \quad (67)$$

$$S_{CFL} = \sqrt{\frac{1}{We} \frac{|\kappa|_{max}}{\min(\rho_1, \rho_2) [\min(\Delta x, \Delta y, \Delta z)]^2}}. \quad (68)$$

where  $|\kappa|_{max}$  in (68) can be approximated by  $1/\Delta x$  in 2D and  $2/\Delta x$  in 3D, assuming  $\Delta x$  is the smallest grid spacing.

The reasons we choose an explicit temporal scheme rather than an implicit one are twofold. First, for applications involving a large density and viscosity

contrast, the stability restriction imposed by surface tension is usually greater than that imposed by diffusion. Second, an implicit formulation of GFM has been admitted to be challenging to develop (Desjardins *et al.* 2008), and it was shown in a recent study (Denner & Wachem 2015) that a capillary time-step constraint exists, irrespective of the type of implementation, due to the temporal sampling of surface capillary waves. Fortunately, the fast pressure-correction method enables the use of FFT for the constant-coefficient Poisson equation and hence an accurate and fast solution of the two-fluid Navier-Stokes equation can be obtained.

#### 6.4. Full solution procedure

We summarize the full solution procedure as follows:

1. Advance the interface explicitly from  $\phi^n$  to  $\phi^{n+1}$  using the ICLS, and update the density  $\rho^{n+1}$  and the viscosity  $\mu^{n+1}$ .
2. Advance the velocity field explicitly from  $\mathbf{u}^n$  to  $\mathbf{u}^*$  with Eqs. (38) and (39).
3. Project the velocity field by solving the constant-coefficient Poisson Eq. (62) making use of the FastP\* and the GFM.
4. Update the velocity from  $\mathbf{u}^*$  to  $\mathbf{u}^{n+1}$  explicitly with Eq. (63), again using the FastP\* and the GFM.

#### 6.5. Validations

In this section, we validate the coupled ICLS/NS solver using three benchmark examples with increasing complexities. Specifically, the first example verifies the discrete momentum balance for fluids of the same density and viscosity. This concerns the surface tension computed by the GFM using interface curvatures. Then, the density and viscosity ratios are significantly increased (up to  $10^4$ ) to test the combined FastP\* and GFM. Using the same test, we also provide a convergence check of the complete flow solver. Finally, the overall accuracy is assessed by simulating a 3D bubble in comparison with experiments.

##### 6.5.1. Spurious currents

A common problem in multiphase-flow simulations is the artificial velocity generated at the fluid interface due to errors in the curvature computation. To access the significance of such spurious currents, we test a stationary droplet of diameter  $D = 0.4$  placed at the center of a unit box. The surface tension between the inner and outer fluid is  $\sigma = 1$ , the viscosity is uniformly  $\mu = 0.1$ , and the density ratio is 1. By changing the density  $\rho$  of both fluids, the Laplace number  $La = \sigma\rho D/\mu^2$  can be varied. The spurious currents are thus determined from the resulting capillary number  $Ca = |U_{max}|\mu/\sigma$  at a non-dimensional time  $t\sigma/(\mu D) = 250$ . Here, we compare the results on a  $32 \times 32$  mesh with the GFM implementation by Desjardins *et al.* (2008). As listed in Table 2, the capillary numbers from both tests remain very small for all the Laplace numbers, with the present results being one-order smaller.

Table 2: Dependence of spurious current capillary number  $Ca$  on the Laplace number for a static droplet with surface tension on a  $32 \times 32$  mesh in comparison with Desjardins *et al.* (2008).

La	12	120	1,200	12,000	120,000	1,200,000
Ca	$2.85 \times 10^{-6}$	$3.14 \times 10^{-6}$	$3.63 \times 10^{-6}$	$3.87 \times 10^{-6}$	$3.41 \times 10^{-6}$	$5.79 \times 10^{-7}$
Ca (ref)	$4.54 \times 10^{-5}$	$3.67 \times 10^{-5}$	$3.62 \times 10^{-5}$	$4.15 \times 10^{-5}$	$3.75 \times 10^{-5}$	$8.19 \times 10^{-6}$

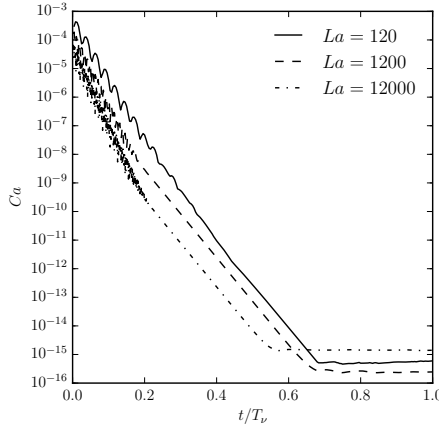


Figure 10: Temporal evolution of the spurious currents without performing level set reinitialization at three Laplace numbers as in Popinet (2009).

We also note that the spurious currents reported in Table 2 are obtained by performing the level set reinitialization at about every 100 time steps. However, if we turn off the reinitialization, such spurious velocity will eventually go to machine zero, as shown in Fig. 10, where time is non-dimensionalized with the viscous time scale,  $T_\nu = \rho D^2 / \mu$ . The nearly exponential decay of  $Ca$  and the collapsing of the three curves are the result of the viscous damping of the spurious velocity, as the shape of droplet relaxes to its numerical equilibrium. Similar results are obtained and explained in greater detail in Popinet (2009) using a balanced-force continuum-surface-force surface-tension formulation and the VOF. The result in Fig. 10 therefore validates the computation of the surface tension with the GFM.

### 6.5.2. Capillary wave

To verify the solver at large density and (dynamic) viscosity contrasts, we simulate a small-amplitude capillary wave for which there exists an analytical solution derived by Prosperetti (1981). Specifically, an initially sinusoidal

Table 3: Temporal and spatial convergence rates for the velocity component  $u$  and the pressure  $p$ .

	$L_2^{4\Delta t, 2\Delta t}$	$L_2^{2\Delta t, \Delta t}$	Rate	$L_2^{4\Delta x, 2\Delta x}$	$L_2^{2\Delta x, \Delta x}$	Rate
$u$	$2.46 \times 10^{-8}$	$1.03 \times 10^{-8}$	1.19	$2.16 \times 10^{-7}$	$5.95 \times 10^{-8}$	1.82
$p$	$1.13 \times 10^{-6}$	$3.85 \times 10^{-7}$	1.46	$3.25 \times 10^{-3}$	$6.11 \times 10^{-4}$	2.67

interface is imposed between two immiscible, viscous fluids of infinite depth and lateral extent. When the lower fluid is heavier, the balance between inertia, viscosity, and surface tension results in a decaying free-surface wave. By requiring matching kinematic viscosity  $\nu_u = \nu_l$  ( $u$  for upper,  $l$  for lower), the solution of the wave amplitude in terms of Laplace transforms can be inverted analytically and compared with the simulation results.

We set up our simulation in the same way as suggested in Dodd & Ferrante (2014). Here, two fluids of equal depth are placed in a  $1 \times 3$  ( $64 \times 192$  grid points) domain, where the streamwise direction ( $L = 1$ ) is periodic and the vertical direction ( $H = 3$ ) wall-bounded. The interface has an initial wavelength of  $\lambda = 1$  and an amplitude of  $a_0 = 0.01$ . With varying density ratios  $\rho_l/\rho_u$ , the non-dimensional parameters for the test are

$$Re = 100, \quad We = 1, \quad Fr = \infty, \quad \rho_l/\rho_u = 10 - 10,000, \quad \nu_l = \nu_u. \quad (69)$$

The CFL number  $\Delta t/\Delta x$  is  $2.5 \times 10^{-2}$  for  $\rho_l/\rho_u = 10$  and  $10^2$ , and it is reduced to  $2.5 \times 10^{-3}$  for  $\rho_l/\rho_u = 10^3$  and  $2.5 \times 10^{-4}$  for  $\rho_l/\rho_u = 10^4$ .

Fig. 11 shows the temporal evolution of the wave amplitude up to  $t = 10$ . The excellent agreement with Prosperetti's analytical solution (Prosperetti 1981) confirms the normal stress balance computed using the GFM. And accurate results at very large density contrasts are realized by combining the FastP\* with GFM. Note that the dynamic viscosity ratio  $\mu_l/\mu_u$  also varies from 10 to  $10^4$ . However, neglecting its contribution to the pressure jump by regularizing the viscosity profile yields accurate results since the Capillary number is small ( $Ca = We/Re = 0.01$ ), as discussed in conjunction with Eq. (46).

### 6.5.3. Convergence

We continue to check the temporal and spatial convergence rates of the coupled ICLS/NS solver. Here, the same test problem as in Sec. 6.5.2 is used, with the non-dimensional parameters given as

$$Re = 500, \quad We = 1, \quad Fr = \infty, \quad H_0 = 0.05, \quad \rho_l/\rho_u = 20, \quad \mu_l/\mu_u = 20, \quad (70)$$

again following Dodd & Ferrante (2014). Placing the fluids in a  $1 \times 1$  box, the flow is simulated under different time steps or on different meshes so that the errors can be computed between successive solutions.

Table 3 shows the convergence rates for the velocity component  $u$  and the pressure  $p$  in the  $L_2$  norm. Here, the temporal convergence is evaluated at

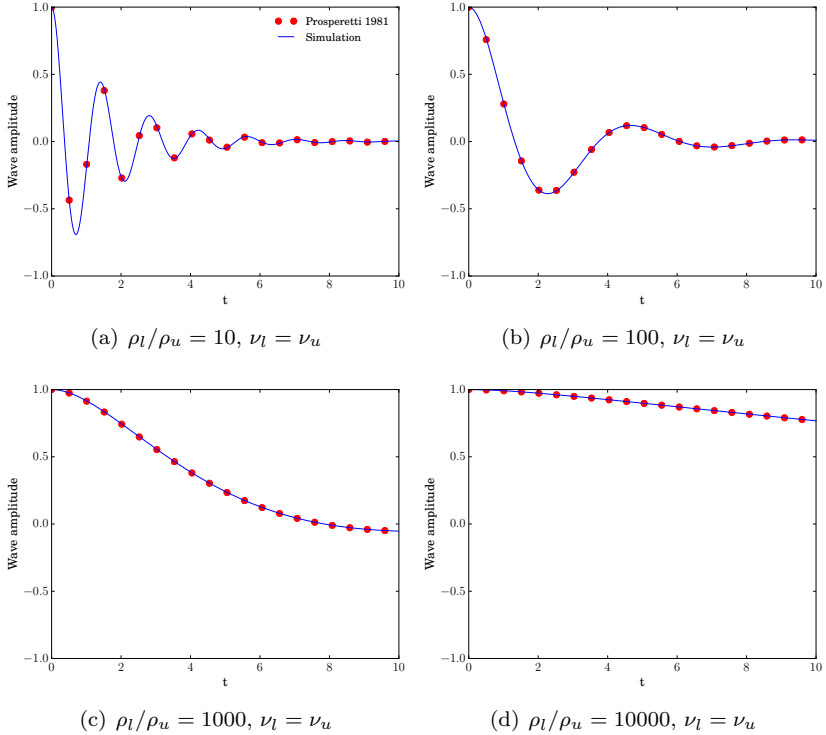


Figure 11: Time development of the capillary wave amplitude (normalized to  $a_0$ ) for increasing density ratios and matching kinematic viscosity in comparison with Prosperetti's analytical solution (Prosperetti 1981).

$t = 6.25 \times 10^{-2}$  on a  $256^2$  grid, by increasing the time step from  $\Delta t = 4.88 \times 10^{-5}$  to  $2\Delta t$  and  $4\Delta t$ . Two iterations of reinitialization are performed every 25 – 100 time steps. The observed convergence rates for both velocity and pressure is between first and second order. Considering that we use RK3 for LS and AB2 for NS, the reduced convergence is probably due to the reinitialization that perturbs the interface. Changing the frequency of the reinitialization, we indeed observe different convergence rates (they can also exceed second order if the density ratio is 1, not shown). Next, the spatial convergence is obtained by successively refining the grid from  $32^2$  to  $64^2$  to  $128^2$ . Using the same time step  $\Delta t = 4.88 \times 10^{-5}$  and interpolating the solution to the coarse grid after one solve, the results display nearly second order convergence for the velocity and a super-convergence for the pressure. We note that the GFM has been proven convergent (but without a rate) for variable-coefficient Poisson equations (Liu & Sideris 2003). Our results thus show improved accuracy in two fluid problems,

when a constant-coefficient Poisson equation is obtained by combining the GFM with the FastP\*.

#### 6.5.4. Rising bubble

Finally, we compute four cases of a rising bubble to access the overall accuracy of the current ICLS/NS solver in 3D in the presence of moderate deformations. Originally documented by Grace (1973), it was observed that a single gas bubble rising in quiescent liquid has four characteristic shapes: spherical, ellipsoidal, skirted, or dimpled. The governing non-dimensional numbers are the Morton number  $M$ , Eotvos number  $Eo$  (sometimes referred to as the Bond number), and the terminal Reynolds number  $Re_t$ , defined as

$$M = \frac{g\mu_l^4}{\rho_l\sigma^3}, \quad Eo = \frac{\Delta\rho gd^2}{\sigma}, \quad Re_t = \frac{\rho_l U_\infty d}{\mu_l}, \quad (71)$$

where  $d$  is the bubble diameter,  $\Delta\rho$  is the density difference,  $U_\infty$  is the terminal velocity of the bubble, and the subscripts  $l$  and  $g$  denote, in order, the liquid and gas phase. The Morton and Eotvos number are defined purely by the material properties of the chosen fluids, while the terminal Reynolds number provides a measure of the steady-state bubble velocity.

Table 4 lists the four representative cases we select for the simulations. A spherical bubble of diameter  $d = 1$  is centered in a domain of size  $(L_x \times L_y \times L_z) = (3d \times 6d \times 3d)$ . A grid of  $96 \times 192 \times 96$  points is used, giving the bubble an initial resolution of 32 points per diameter. Periodic boundary conditions are imposed in the  $x$  (spanwise) and  $y$  (rising) directions whereas no friction, no penetration is enforced in the  $z$  direction. As suggested by Annaland *et al.* (2005), a ratio of 100 between the density and viscosity of liquid and gas is sufficiently high to approximate such gas-liquid systems, leading to  $\Delta\rho \approx \rho_l$ .  $Re$  and  $We$  in Eq. (3) can thus be obtained from  $M$  and  $Eo$  as

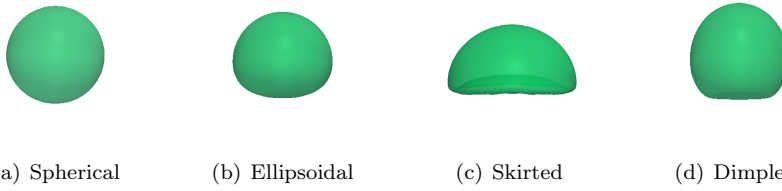
$$Re = \left( \frac{Eo^3}{M} \right)^{1/4}, \quad We = Eo. \quad (72)$$

The CFL number,  $\Delta t / \Delta x$ , is  $1.6 \times 10^{-4}$  for cases (a), (b), and (d), and  $1.6 \times 10^{-3}$  for case (c). The simulation is integrated in time up to  $t = 10$  to ensure the bubble reaches nearly steady state.

The results of the bubble terminal velocities are presented in Table 4. The difference between the computed Reynolds,  $Re_C$ , and the terminal Reynolds,  $Re_G$ , measured by Grace (1973) remains small for all four cases. The bubble mass is conserved, with a maximal mass loss of about 0.02% found in the skirted case, where the bubble undergoes a large and rapid deformation. The corresponding bubble shapes are illustrated in Fig. 12, which clearly displays spherical, ellipsoidal, skirted, and dimpled shapes. We can therefore conclude that the dynamics of a single rising bubble is well-captured.

Table 4: Comparison of computed terminal Reynolds number ( $Re_C$ ) and experimental terminal Reynolds number ( $Re_G$ ) obtained from the Grace diagram (Grace 1973) under four different Morton (M) and Eotvos (Eo) numbers.

Case	Bubble regime	$M$	$Eo$	$Re_G$	$Re_C$	Mass loss (%)
(a)	Spherical	$1 \times 10^{-3}$	1	1.7	1.73	$9.86 \times 10^{-5}$
(b)	Ellipsoidal	0.1	10	4.6	4.57	$3.32 \times 10^{-4}$
(c)	Skirted	1	100	20.0	19.21	$1.64 \times 10^{-2}$
(d)	Dimpled	1000	100	1.5	1.71	$3.28 \times 10^{-3}$



(a) Spherical              (b) Ellipsoidal              (c) Skirted              (d) Dimpled

Figure 12: Bubble shapes resulting from different Morton (M) and Eotvos (Eo) numbers, as indicated in Table 4.

## 7. Droplet interactions

A unique feature of colloidal suspensions is the interaction between neighboring droplets, displaying fascinating behaviors such as self-assembly, self-replication, etc. . The reason for such interactions is rather complex; it often arises from a combination of fluid mechanical effects and physicochemical properties of the substance. To study the droplet interactions in the present ICLS/NS framework, we provide in this section a hydrodynamic model for the depletion forces. The method is a natural extension of the LS and GFM, and we demonstrate the clustering of droplets in various structures from a dumbbell to a face-centered cubic crystal.

### 7.1. Extension to multiple level set

The level set method discussed so far involves one marker function; we call it single level set (SLS) method. Thanks to its Eulerian nature, SLS can describe many droplets at the same time, provided that they do not need to be distinguished from each other. On the other hand, SLS can also be extended to multiple level set (MLS), so that each droplet has its own color function. This has several benefits including distinction and tracking of each droplet, independent curvature computation, and ability to prevent numerical

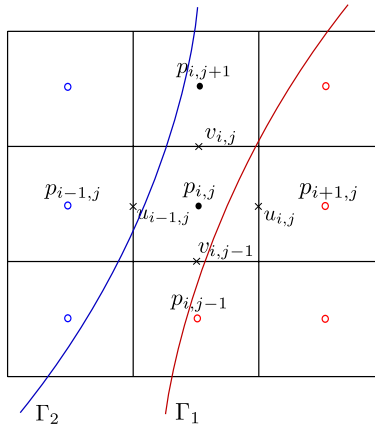


Figure 13: Pressure jump in the presence of multiple interfaces within two grid cells. Red and blue circles indicate nodal pressure in droplet 1 and 2, respectively. (For interpretation of the references to color in this figure legend, the reader is referred to the web version of this article.)

coalescence, etc. . Furthermore, with the narrow band approach (Adalsteinsson & Sethian 1995; Peng *et al.* 1999) and the various other techniques introduced in Sec. 1 (Nielsen & Museth 2006; Brun *et al.* 2012), the additional computational and memory cost as the number of the level set functions increases is limited.

The extension from SLS to MLS is straightforward. Assuming no droplets will overlap, each level set function is simply advected successively. When two droplets get close (typically within two grid cells, see Fig. 13), the pressure jump across each interface needs to be considered and superimposed. That is, Eq. (48) (corresponding to Fig. 9) should be modified as

$$\begin{aligned} (\nabla^2 p)_{i,j} = & \frac{p_{i-1,j} - 2p_{i,j} + p_{i+1,j}}{\Delta x^2} - 2\frac{[p]_{i,j}}{\Delta x^2} - \frac{1}{\Delta x}\left[\frac{\partial p}{\partial x}\right]_{i+1/2,j} + \frac{1}{\Delta x}\left[\frac{\partial p}{\partial x}\right]_{i-1/2,j} \\ & + \frac{p_{i,j-1} - 2p_{i,j} + p_{i,j+1}}{\Delta y^2} - \frac{[p]_{i,j-1}}{\Delta y^2}, \end{aligned} \quad (73)$$

Similarly, all the jumps should be removed consistently when computing the pressure gradient in the subsequent step. The above modification applies to both SLS and MLS, as the compact formulas (Eqs. (62) and (63)) remain the same; although MLS is clearly more accurate in resolving the near field structure.

## 7.2. Near-field interactions

As introduced earlier, colloidal droplets transported in microfluidic devices are subject to various forces, a typical of which is the depletion force. The depletion force arises from the exclusion of the surfactant micelles in the

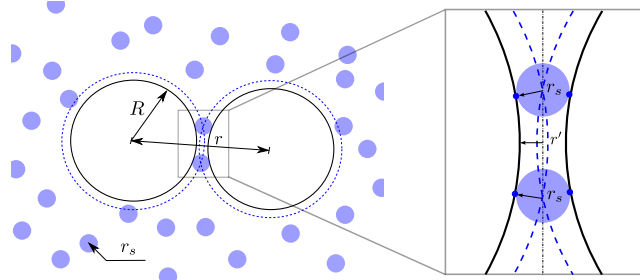


Figure 14: Depletion of surfactant micelles of radius  $r_s$  between larger colloidal droplets of radius  $R$ , separated by distance  $r$ . The dashed lines around larger spheres represent the region from which the centers of small spheres are excluded. They overlap when  $r \leq 2R + 2r_s$ . Inset: a zoom-in sketch of two droplets near contact.

colloidal suspension. It is often characterized as a near-field attracting potential (Asakura & Oosawa 1958; Mewis & Wagner 2012), and plays a key role in the droplet dynamics (Shen *et al.* 2016; Shen 2014). Below, we first provide a brief background on the colloidal theory of the depletion potential, then present a numerical model to enforce the depletion force using MLS and GFM.

### 7.2.1. The colloidal theory of the depletion potential

The original depletion potential model proposed by Asakura & Oosawa (1958) assumes the surfactant micelles as non-interacting hard-spheres. As sketched in Fig. 14, a suspension of such small spheres around the large colloidal droplets creates an osmotic pressure on the droplet surface. When the distance between two droplets is less than the diameter of the surfactant micelles, there will be a pressure defect due to the exclusion of the micelles, thus creating an attracting force. Integrating this force with respect to the inter-droplet distance  $r$  leads to a potential energy

$$U(r) = \begin{cases} \infty & \text{if } r \leq 2R \\ -p_{os}V_{ex} & \text{if } 2R < r \leq 2R + 2r_s \\ 0 & \text{otherwise,} \end{cases} \quad (74)$$

where  $V_{ex}$  is the excluded volume and  $p_{os}$  is the osmotic pressure. For spherical droplets,  $V_{ex}$  can be calculated analytically

$$V_{ex}(r) = \frac{4\pi(R + r_s)^3}{3} \left[ 1 - \frac{3r}{4(R + r_s)} + \frac{r^3}{16(R + r_s)^3} \right], \quad (75)$$

where  $R$  and  $r_s$  are, respectively, the radii of the big and small spheres. The osmotic pressure is given as

$$p_{os} = nkT, \quad (76)$$

where  $n$  is the number density of the small spheres,  $k$  is the Boltzmann constant, and  $T$  is the temperature. The negative sign in Eq. (74) corresponds to the tendency of the system to reduce its potential energy as the overlap increases. This is equivalent to increasing the total entropy of the small spheres (Melby *et al.* 2007), and it provides a physical description of the depletion force even when the droplets are deformable, or when  $p_{os}$  cannot be expressed by the van't Hoff's formula (Eq. (76)) (Asakura & Oosawa 1958).

### 7.2.2. A hydrodynamic model for the depletion force

Based on the above theory, the depletion force acting on a droplet is simply the derivative of the depletion potential, *i.e.*  $F(r) = dU/dr = -p_{os}dV_{ex}/dr$ . However,  $dV_{ex}/dr$  is not always straightforward to evaluate for non-spherical droplets; and unlike rigid-body dynamics,  $F(r)$  cannot be applied directly to the motion of a liquid drop. In order to induce locally an aggregation, we take a closer look at the overlap region. As illustrated in Fig. 14, when the surface distance between two colloidal droplets is less than  $2r_s$ , there is a small area in which the osmotic pressure is subject to a jump. Assuming the concentration of the surfactant micelles changes abruptly, it resembles the jump of the Laplace pressure; however, it will not generate any flow if the pressure is uniform in the depleted region. On the contrary, if the osmotic pressure varies continuously within the overlap, *i.e.*  $p' = p'(r')$ , then we can write it as a Taylor-series expansion from  $r' = r_s$

$$p'(r'/r_s) = p'(1) + \left( \frac{r'}{r_s} - 1 \right) \frac{\partial p'}{\partial r'/r_s}, \quad (77)$$

where the distance to the droplet surface  $r'$  is normalized by the surfactant micelle radius. An expansion of the osmotic pressure with the distance corresponds to a gradient of the micelle concentration near the gap. And if the micelle is much smaller than the droplet, as it is in many microfluidic devices (Shen *et al.* 2016), the gradient will be very sharp. Conversely, when the distance to the surface varies slowly, such as in the gap of a droplet and a flat wall, a uniform pressure will be recovered. Furthermore, a favorable pressure gradient from the overlap center will generate an outflow, pulling the droplets towards each other. Hence, Eq. (77) provides a hydrodynamic model for the depletion force.

In Eq. (77), the gradient of the osmotic pressure  $\partial p'/\partial(r'/r_s)$  is not known *a priori*. It can be obtained by equating the depletion force acting on one droplet, *i.e.*

$$-p_{os}A_{ex} = \int_{\Omega} (p'(1) - p'(r'/r_s)) dS, \quad (78)$$

where  $A_{ex}$  is the effective area of the overlap  $\Omega$ . Assuming a constant  $\partial p'/\partial(r'/r_s)$ , the above yields a linear dependence of the osmotic pressure on  $r'$ . Note that this is not the same as  $p'$  varying linearly with the distance to the overlap center (see Fig. 14). A description of the implementation and verification will be shown in the next section.

---

**Algorithm 1:** A pseudo code for computing the depletion force.

---

Enter the pressure solver. Compute the right-hand side of Eq. (62).

**for**  $m = 1 : (N - 1)$  **do**

    Get the level set for droplet  $m$ ,  $\phi_m$ .

**for**  $n = (m + 1) : N$  **do**

    Get the level set for droplet  $n$ ,  $\phi_n$ .

**where**  $\phi_m < r_s$  and  $\phi_n < r_s$  **do**  $r' = (\phi_m + \phi_n)/2$ , tag as  
        *overlap*.

    Compute  $[p']_\Omega$  from Eqs. (78) and (79) within *overlap*.

**forall**  $i, j, k$  **do**

**if** *entering overlap* **then**

            | Add the osmotic pressure jump  $[p']_{i,j,k}$ .

**else**

            | Remove the osmotic pressure jump  $[p']_{i,j,k}$ .

**end**

**end**

**end**

**end**

Solve for  $p^{n+1}$  regularly using the FastP\* and GFM. Exit the pressure solver.

---

### 7.2.3. A MLS/GFM-based method for computing the depletion force

Provided a hydrodynamic model for the depletion force between two droplets, we can easily generalize it to multiple droplets using the MLS. Thanks to the distance information embedded in the level set functions, it is straightforward to identify the overlap region of arbitrary geometries. Furthermore, as the jump of the osmotic pressure occurs only across the overlap shell, we can define

$$[p']_\Omega = p'(r'/r_s) - p'(1), \quad (79)$$

similar to the Laplace pressure jump  $[p]_\Gamma$  implemented by the GFM. Based on these observations, we propose a numerical method to compute the depletion force as laid out in Algorithm 1.

The overall idea of Algorithm 1 is to enforce the depletion attraction in the projection step through the use of MLS and GFM. Specifically, we first locate the overlap region of a pair of droplets with its own level set function, and define  $r'$  as the average of the two distances. Then, Eq. (78) can be integrated numerically to obtain  $\partial p'/\partial(r'/r_s)$ , which together with Eqs. (77) and (79) gives  $[p']_\Omega$ . This variable pressure jump manifests itself as a modification term on the right-hand side of Eq. (62), allowing us to use GFM to impose it across a sharp overlap shell. The resulting flow is divergence-free provided that all the jump terms are removed consistently in the correction step. Therefore, Eqs. (62) and

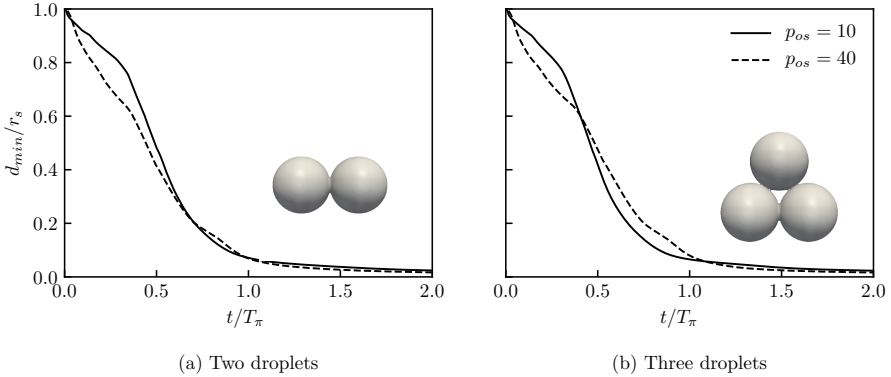


Figure 15: Minimal distance between the droplet surfaces as function of time in the presence of depletion forces proportional to  $p_{os} = 10$  (solid line) and  $p_{os} = 40$  (dashed line). Simulation of (a) two droplets and (b) three droplets suspended in an initially quiescent fluid. Due to symmetry, only the minimal distance is plotted.

(63) are re-formulated as <sup>1</sup>

$$\nabla^2 p^{n+1} = \nabla_g^2 ([p]_\Gamma + [p']_\Omega) + \nabla \cdot \left[ \left( 1 - \frac{\rho_0}{\rho^{n+1}} \right) \nabla_g \hat{p} \right] + \frac{\rho_0}{\Delta t} \nabla \cdot \mathbf{u}^*, \quad (80)$$

and

$$\mathbf{u}^{n+1} = \mathbf{u}^* - \Delta t \left[ \frac{1}{\rho_0} \nabla_g p^{n+1} + \left( \frac{1}{\rho^{n+1}} - \frac{1}{\rho_0} \right) \nabla_g \hat{p} \right]. \quad (81)$$

**Approaching drops.** We verify the depletion force model and its numerical implementation by simulating 2 to 14 approaching droplets in a quiescent fluid environment. Specifically, we set the droplet radius  $R = 0.5$ , the computational domain  $3 \times 3 \times 3$ , and the resolution  $\Delta x = 1/32$ . The radius of the surfactant micelle is set to be  $r_s = 1/16$ , corresponding to  $2\Delta x$ . The viscosity and density ratios of the droplet to the ambient fluid are both 1. The non-dimensional parameters are  $La = 2000$  and  $Fr = \infty$ , leading to a reference Laplace pressure jump  $p_\sigma = 80$  and neglected gravity. The uniform osmotic pressure is either 10 or 40.

The temporal evolutions of the minimal surface distances in the case of two and three droplets are shown in Fig. 15. Here, time is scaled by a factor  $T_\pi = (r_s/R)(p_\sigma/p_{os})$ . The droplets, originally separated by a distance of  $r_s$ , get closer to the limit of the grid spacing at  $t \approx T_\pi$ . For the present study, we let the droplets aggregate without applying any repulsion models, except that

<sup>1</sup>Eqs. (63) and (81) are identical in form; however,  $[p']_\Omega$  has to be removed when evaluating  $\nabla_g p^{n+1}$  and  $\nabla_g \hat{p}$  in Eq. (81), as it is done in Eq. (61)

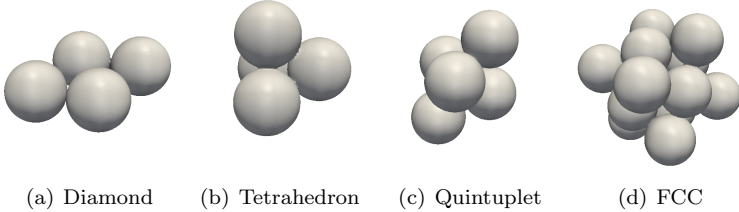


Figure 16: Examples of droplet clusters of different structures.

the magnitude of the osmotic pressure is reduced when  $d_{min}/r_s < 0.1$ . The smooth approaching in all cases and the collapse of the distance curve clearly evidence an attracting depletion force. To assess the robustness of the method, we further tested clustering of droplets into shapes from a 2D diamond to a face-centered cubic (FCC) composed of 14 drops, illustrated here in Fig. 16. FCC represents the unit structure of one of the most compact sphere packings. Therefore, we can conclude that the hydrodynamic model implemented by the MLS/GFM-based method is accurate and robust in computing the depletion forces.

## 8. Conclusion

A numerical method mainly intended for the hydrodynamic simulations of colloidal droplets in microfluidic devices has been developed and validated. The code is based on an efficient and sharp solver of the incompressible, two-fluid Navier-Stokes equations, and uses a mass-conserving level set method to capture the fluid interface. This combination provides a general framework for any multiphase flow problems (see e.g. our recent study on jet instabilities (Tammisola *et al.* 2017)), and allows us to develop specific methods for the simulations of droplets in saturated surfactant suspensions with depletion forces as in the recent experiment in Shen *et al.* (2016). Particularly, we have developed or extended four numerical techniques to improve the general accuracy:

1. A mass-conserving, interface-correction level set method (ICLS) is proposed. As a standalone level set module, it is efficient, accurate, guarantees global mass conservation, and is simple to implement. It also enables corrections that can depend on the local curvature or any other parameter of interest.
2. A geometric estimation of the interface curvature based on nodal curvatures is introduced. As an important ingredient both for the mass correction (ICLS) and the surface tension computation, we show that the calculation converges in second-order both in 2D and 3D, and can lead to machine-zero spurious currents for a stationary 2D droplet.

3. The ghost fluid method (GFM) for the computation of surface tension is combined with the FastP\* method (Dodd & Ferrante 2014). This enables the use of FFT-based solvers for a direct pressure solve, and can accurately account for surface tension at large density ratios.
4. A ghost fluid/multiple level set (GFM/MLS-based) method is also proposed to compute the interaction force caused by depletion potentials between multiple droplets or between droplets and a nearby wall. The approach can possibly be extended to account for surfactant diffusion at the interface and in the liquid.

The last technique applies specifically to the simulation of colloidal droplets in microfluidic devices. This will enable us to further explore the effects of the near-field interactions as those observed experimentally in Shen *et al.* (2016), and potentially improve the design of microfluidic devices. In addition, the combination of the GFM for sharp interfaces and the FastP\* method (Dodd & Ferrante 2014) can be exploited for the simulations of droplet in turbulent flows as in Dodd & Ferrante (2016), adding an accurate representation of evaporation thanks to the ICLS approach proposed here.

## Acknowledgments

The work is supported by the Microflusa project. This effort receives funding from the European Union Horizon 2020 research and innovation programme under Grant Agreement No. 664823. O.T. acknowledges support from Swedish Research Council (VR) through the Grant Nr. 2013-5789. L.B. and J.-C.L. also acknowledge financial support by the European Research Council grant, no. ERC-2013-CoG-616186, TRITOS. The computer time was provided by SNIC (Swedish National Infrastructure for Computing). Last but not least, Z.G. thanks Mehdi Niazi, Michael Dodd, Walter Fornari, Dr. Olivier Desjardins, Dr. Sébastien Tanguy, Dr. Marcus Herrmann, and Dr. David Salac for interesting and helpful discussions.

## Appendix A. Discretization error of $\int_{\Gamma} \mathbf{n} \cdot \mathbf{u}_c d\Gamma$

Similar to Engquist *et al.* (2005), we define the discretization error

$$E = \left| \left( \prod_{k=1}^d \Delta x_k \right) \sum_{j \in Z^d} \hat{\delta}_{\epsilon}(\Gamma, g, \mathbf{x}_j) - \int_{\Gamma} \mathbf{n} \cdot \mathbf{u}_c d\Gamma \right|, \quad (82)$$

where  $\hat{\delta}_{\epsilon}$  is a Dirac delta function of variable strength  $g$  supported on the surface  $\Gamma$ , and  $\mathbf{x} \in \mathbb{R}^d$ . Following the derivations in Sec. 4, the extension of  $g$  to  $\mathbb{R}^d$  is provided by Eq. (22), allowing one to write

$$E = \left| \left( \prod_{k=1}^d \Delta x_k \right) \sum_{j \in Z^d} \frac{\delta V}{\delta t} \frac{f_s \delta_{\epsilon}(\phi(\mathbf{x}_j)) |\nabla \phi(\mathbf{x}_j)|}{A_f} - \int_{\Gamma} \mathbf{n} \cdot \mathbf{u}_c d\Gamma \right|. \quad (83)$$

Here,  $\delta_{\epsilon}(\phi)$  is a one dimensional regularized delta function depending on the level set  $\phi$ , and the expression is simplified noting that  $\mathbf{n} \cdot \nabla \phi = |\nabla \phi|$  (it does

not have to be a distance function). By definition,  $A_f = \int_{\Gamma} f_s \delta_{\epsilon}(\phi) |\nabla \phi| d\Gamma$ , discretely reducing Eq. (83) to

$$E = \left| \frac{\delta V}{\delta t} - \int_{\Gamma} \mathbf{n} \cdot \mathbf{u}_c d\Gamma \right|. \quad (84)$$

Comparing with Eq. (13), it is obvious that  $E = 0$ . That is, the discretization error of  $\int_{\Gamma} \mathbf{n} \cdot \mathbf{u}_c d\Gamma$  used in the mass correction is identically zero, independent of the choice of the regularized delta function.

## REFERENCES

- AANJANEYA, M., PATKAR, S. & FEDKIW, R. 2013 A monolithic mass tracking formulation for bubbles in incompressible flow. *J. Comput. Phys.* **247**, 17–61.
- ADALSTEINSSON, D. & SETHIAN, J. 1995 A fast level set method for propagating interfaces. *J. Comput. Phys.* **111**(2), 269–277.
- ADALSTEINSSON, D. & SETHIAN, J. 1999 The fastconstruction of extension velocities in level set methods. *J. Comput. Phys.* **148**, 2–22.
- ANNALAND, M. v. S., DEEN, N. & KUIPERS, J. 2005 Numerical simulation of gas bubbles behaviour using a three-dimensional volume of fluid method. *Chemical Engineering Science* **60**, 2999–3011.
- ASAKURA, S. & OOSAWA, F. 1958 Interaction between particles suspended in solutions of macromolecules. *Journal of Polymer Science* **XXXIII**, 183–192.
- BRACKBILL, J., KOTHE, D. & ZEMACH, C. 1992 A continuum method for modeling surface tension. *J. Comput. Phys.* **100**, 335–354.
- BREUGEM, W.-P. 2012 A second-order accurate immersed boundary method for fully resolved simulations of particle-laden flows. *Journal of Computational Physics* **231** (13), 4469 – 4498.
- BRUN, E., GUILLETET, A. & GIBOU, F. 2012 A local level-set method using a hash table data structure. *J. Comput. Phys.* **231**, 2528–2536.
- CHEN, S., MERRIMAN, B., OSHER, S. & SMEREKA, P. 1997 A simple level set method for solving stefan problems. *J. Comput. Phys.* **135**, 8–29.
- DU CHÉNÉ, A., MIN, C. & GIBOU, F. 2008 Second-order accurate computation of curvatures in a level set framework using novel high-order reinitialization schemes. *J. Sci. Comput.* **35**, 114–131.
- CHORIN, A. 1968 Numerical solution of the navier-stokes equations. *Math. Comput.* **22**, 745–762.
- COSTA, P. S. 2017 Cans (canonical navier-stokes). <https://github.com/p-costa/CaNS>, accessed: 2017-10-11.
- COYAJEE, E. & BOERSMA, B. 2009 A second-order accurate immersed boundary method for fully resolved simulations of particle-laden flows. *J. Comput. Phys.* **231**, 4469–4498.
- DENNER, F. & WACHEM, B. v. 2015 Numerical time-step restrictions as a result of capillary waves. *J. Comput. Phys.* **285**, 24–40.
- DESJARDINS, O., MOUREAU, V. & PITSCHE, H. 2008 An accurate conservative level set/ghost fluid method for simulating turbulent atomization. *J. Comput. Phys.* **227**, 8395–8416.
- DODD, M. & FERRANTE, A. 2014 A fast pressure-correction method for incompressible two-fluid flows. *J. Comput. Phys.* **273**, 416–434.

- DODD, M. & FERRANTE, A. 2016 On the interaction of taylor length scale size droplets and isotropic turbulence. *J. Fluid Mech.* **806**, 356–412.
- DONG, S. & SHEN, J. 2012 A time-stepping scheme involving constant coefficient matrices for phase-field incompressible flows with large density ratios. *J. Comput. Phys.* **231**, 5788–5804.
- ENGQUIST, B., TORNBERG, A.-K. & TSAI, R. 2005 Discretization of dirac delta functions in level set methods. *J. Comput. Phys.* **207**, 28–51.
- ENRIGHT, D., FEDKIW, R., FERZIGER, J. & MITCHELL, I. 2002 A hybrid particle level set method for improved interface capturing. *J. Comput. Phys.* **183**, 83–116.
- FEDKIW, R., ASLAM, T., MERRIMAN, B. & OSHER, S. 1999 A non-oscillatory eulerian approach to interfaces in multimaterial flows (the ghost fluid method). *J. Comput. Phys.* **152**, 457–492.
- FRANCOIS, M., CUMMINS, S., DENDY, E., KOTHE, D., SICILIAN, J. & WILLIAMS, M. 2006 A balanced force algorithm for continuous and sharp interfacial surface tension models within a volume tracking framework. *J. Comput. Phys.* **213**, 141–173.
- GALUSINSKI, C. & VIGNEAUS, P. 2008 On stability condition for bifluid flows with surface tension: Application to microfluidics. *J. Comput. Phys.* **227**, 6140–6164.
- GRACE, J. R. 1973 Shapes and velocities of bubbles rising in infinite liquids. *Transactions of the Institution of Chemical Engineering* **51**, 116–120.
- HERRMANN, M. 2008 A balanced force refined level set grid method for two-phase flows on unstructured flow solver grids. *J. Comput. Phys.* **227**, 2674–2706.
- KANG, M., FEDKIW, R. & LIU, X.-D. 2000 A boundary condition capturing method for multiphase incompressible flow. *J. Sci. Comput.* **15**, 323–360.
- KUMAR, A. & GRAHAM, M. 2012 Accelerated boundary integral method for multiphase flow in non-periodic geometries. *J. Comput. Phys.* **231**, 6682–6713.
- LALANNE, B., VILLEGRAS, L. R., TANGUY, S. & RISSO, F. 2015 On the computation of viscous terms for incompressible two-phase flows with level set/ghost fluid method. *J. Comput. Phys.* **301**, 289–307.
- LI, F., JOSEPHSON, D. & STEIN, A. 2011 Colloidal assembly: the road from particles to colloidal molecules and crystals. *Angew. Chem. Int. Ed.* **50**, 360–388.
- LIU, X.-D., FEDKIW, R. & KANG, M. 2000 A boundary condition capturing method for poisson's equation on irregular domains. *J. Comput. Phys.* **160**, 151–178.
- LIU, X.-D., OSHER, S. & CHAN, T. 1994 Weighted essentially non-oscillatory schemes. *J. Comput. Phys.* **115**, 200–213.
- LIU, X.-D. & SIDERIS, T. C. 2003 Convergence of the ghost fluid method for elliptic equations with interfaces. *Math. Comput.* **72**, 1731–1746.
- LUO, J., HU, X. & ADAMS, N. 2015a A conservative sharp interface method for incompressible multiphase flows. *J. Comput. Phys.* **284**, 547–565.
- LUO, K., SHAO, C., YANG, Y. & FAN, J. 2015b An mass conserving level set method for detailed numerical simulation of liquid atomization. *J. Comput. Phys.* **298**, 495–519.
- MARCHANDISE, E., GEUZAIN, P., CHEVAUGEON, N. & REMACLE, J.-F. 2007 A stabilized finite element method using a discontinuous level set approach for the computation of bubble dynamics. *J. Comput. Phys.* **225**, 949–974.
- MELBY, P., PREVOST, A., EGOLF, D. & URBACH, J. 2007 Depletion force in a bidisperse granular layer. *Phys. Rev. E* **76**, 051307, 1–5.

- MEWIS, J. & WAGNER, N. 2012 *Colloidal suspension rheology*. New York, USA: Cambridge University Press.
- MIN, C. & GIBOU, F. 2007 A second order accurate level set method on non-graded adaptive cartesian grids. *J. Comput. Phys.* **225**, 300–321.
- MULDER, W., OSHER, S. & SETHIAN, J. 1992 Computing interface motion in compressible gas dynamcis. *J. Comput. Phys.* **100**, 209–228.
- NIELSEN, M. & MUSETH, K. 2006 Dynamic tubular grid: an efficient data structure and algorithms for high resolution level sets. *J. Sci. Comput.* **26**, 261–299.
- NOURGALIEV, R. & THEOFANOUS, T. 2007 High-fidelity interface tracking in compressible flows: unlimited anchored adaptive level set. *J. Comput. Phys.* **227**, 836–866.
- OLSSON, E. & KREISS, G. 2005 A conservative level set method for two phase flow. *J. Comput. Phys.* **210**, 225–246.
- PENG, D., MERRIMAN, B., OSHER, S., ZHAO, H. & KANG, M. 1999 A pde-based fast local level set method. *J. Comput. Phys.* **155**, 410–438.
- PESKIN, C. S. 1972 Flow patterns around heart valves: a numerical method. *J. Comput. Phys.* **10**, 252–271.
- PIJL, S. v. d., SEGAL, A., VUIK, C. & WESSELING, P. 2008 Computing three-dimensional two-phase flows with a mass-conserving level set method. *Comput. Vis. Sci.* **11**, 221–235.
- POPINET, S. 2009 An accurate adaptive solver for surface-tension-driven interfacial flows. *J. Comput. Phys.* **228**, 5838–5866.
- POPINET, S. 2018 Numerical models of surface tension. *Ann. Rev. Fluid Mech.* **50**, 49–75.
- POZRIKIDIS, C. 1992 *Boundary integral and singularity methods for linearized viscous flow*. New York, USA: Cambridge University Press.
- PROSPERETTI, A. 1981 Motion of two superposed viscous fluids. *Phys. Fluids* **24**, 1217.
- RUSSO, G. & SMEREKA, P. 2000 A remark on computing distance functions. *J. Comput. Phys.* **163**, 51–67.
- SACANNA, S. & PINE, D. 2011 Shape-anisotropic colloids: building blocks for complex assemblies. *Curr. Opin. Colloid Interface Sci.* **16**, 96–105.
- SALAC, D. 2016 A general, mass-preserving navier-stokes projection method. *Comput. Phys. Comm.* **204**, 97–106.
- SCARDOVELLI, R. & ZALESKI, S. 1999 Direct numerical simulation of free-surface and interfacial flow. *Ann. Rev. Fluid Mech.* **31**, 567–603.
- SCHUMANN, U. & SWEET, R. A. 1988 Fast fourier transforms for direct solution of poisson's equation with staggered boundary conditions. *J. Comput. Phys.* **75**, 123–137.
- SETHIAN, J. 1999 *Level set method and fast marching method*. New York, USA: Cambridge University Press.
- SHEN, B. 2014 Transport and self-assembly of droplets in microfluidic devices. PhD thesis, Physics. Université Pierre et Marie Curie - Paris VI, english. MNT: 2014PA066499. Tel-01127629.
- SHEN, B., RICOURVIER, J., MALLOGGI, F. & TABELING, P. 2016 Designing colloidal molecules with microfluidics. *Adv. Sci.* **1600012**, 1–7.

- SHU, C.-W. & OSHER, S. 1988 Efficient implementation of essentially non-oscillatory shock-capturing schemes. *J. Comput. Phys.* **77**, 439–471.
- STRAIN, J. 1999a Semi-lagrangian methods for level set equations. *J. Comput. Phys.* **151**(2), 498–533.
- STRAIN, J. 1999b Tree methods for moving interfaces. *J. Comput. Phys.* **151**, 616–648.
- SUSSMAN, M. & FATEMI, E. 1997 An efficient, interface-preserving level set redistancing algorithm and its application to interfacial incompressible fluid flow. *J. Sci. Comput.* **20**, 1165–1191.
- SUSSMAN, M. & PUCKETT, E. 2000 A coupled level set and volume-of-fluid method for computing 3d and axisymmetric incompressible two-phase flows. *J. Comput. Phys.* **162**, 301–337.
- SUSSMAN, M., SMEREKA, P. & OSHER, S. 1994 A level set approach for computing solutions to incompressible two-phase flow. *J. Comput. Phys.* **114**, 146–159.
- TAMMISOLA, O., LOISEAU, J.-C. & BRANDT, L. 2017 Effect of viscosity ratio on the self-sustained instabilities in planar immiscible jets. *Phys. Rev. Fluids* **2**(3) 033903.
- TANGUY, S. & BERLEMONT, A. 2005 Application of a level set method for simulations of droplet collisions. *Int. J. Multiph. Flow* **31**, 1015–1035.
- UHLMANN, M. 2005 A immersed boundary method with direct forcing for simulation of particulate flows. *J. Comput. Phys.* **209**, 448–476.
- VELEV, O. & GUPTA, S. 2009 Materials fabricated by micro- and nanoparticle assembly - the challenging path from science to engineering. *Adv. Mater.* **21**, 1897–1905.
- VELMURUGANA, G., E.M., K. & SALAC, D. 2016 Level set jet schemes for stiff advection equations: The semijet method. *ArXiv* **1509.0283**.
- WÖRNER, M. 2012 Numerical modeling of multiphase flows in microfluidics and micro process engineering: a review of methods and applications. *Microfluid Nanofluid* **12**, 841–886.
- XIA, Y., GATES, B., YIN, Y. & LU, Y. 2000 Monodispersed colloidal spheres: old materials with new applications. *Adv. Mater.* **12**, 693–713.
- YI, G.-R., PINE, D. & SACANNA, S. 2013 Recent progress on patchy colloids and their self-assembly. *J. Phys.: Condens. Matter* **25**, 193101.
- ZALESAK, S. 1979 Fully multidimensional flux-corrected transport algorithms for fluids. *J. Comput. Phys.* **31**, 335–362.
- ZHU, L., RORAI, C., DHRUBADITYA, M. & BRANDT, L. 2014 A microfluidic device to sort capsules by deformability: a numerical study. *Soft Matter* **10**, 7705–7711.

**2**

**Paper 2**



# Integral representation of channel flow with interacting particles

**Itzhak Fouzon<sup>1,2</sup>, Zhouyang Ge<sup>3</sup>, Luca Brandt<sup>3</sup>,  
Alexander Leshansky<sup>1</sup>**

<sup>1</sup> Department of Chemical Engineering, Technion, Haifa 32000, Israel

<sup>2</sup> Department of Computational Science and Engineering, Yonsei University,  
Seoul 120-749, South Korea

<sup>3</sup> Linné FLOW Centre and SeRC, KTH Mechanics, S-100 44 Stockholm, Sweden

*Physical Review E* (2017), vol. **96** (063110)

We construct a boundary integral representation for the low-Reynolds-number flow in a channel in the presence of freely-suspended particles (or droplets) of arbitrary size and shape. We demonstrate that lubrication theory holds away from the particles at horizontal distances exceeding the channel height and derive a multipole expansion of the flow which is dipolar to the leading approximation. We show that the dipole moment of an arbitrary particle is a weighted integral of the stress and the flow at the particle surface, which can be determined numerically. We introduce the equation of motion that describes hydrodynamic interactions between arbitrary, possibly different, distant particles, with interactions determined by the product of the mobility matrix and the dipole moment. Further, the problem of three identical interacting spheres initially aligned in the streamwise direction is considered and the experimentally observed “pair exchange” phenomenon is derived analytically and confirmed numerically. For non-aligned particles, we demonstrate the formation of a configuration with one particle separating from a stable pair. Our results suggest that in a dilute initially homogenous particulate suspension flowing in a channel the particles will eventually separate into singlets and pairs.

---

## 1. Introduction

Hydrodynamic interactions among particles flowing in the fluid confined between two parallel walls at low Reynolds number have recently attracted a considerable attention (Carbajal-Tinoco *et al.* 1997; Acuña Campa *et al.* 1998; Pesché & Nägele 2000*a,b*; Lançon *et al.* 2001; Marcus *et al.* 1999; Santana-Solano & Arauz-Lara 2001, 2002; Cui *et al.* 2004; Cohen *et al.* 2004; Tlusty 2006; Beatus *et al.* 2006, 2012; Sarig *et al.* 2016; Swan & Brady 2010; Durlofsky & Brady 1989; Nott & Brady 1994; Morris & Brady 1998; SINGH & NOTT 2000; Morris 2001; Bhattacharya *et al.* 2006; Shani *et al.* 2014; Shen *et al.* 2016*a, 2014*). The case of particles driven by thermal noise in the absence of a macroscopic flow

was studied in Carbajal-Tinoco *et al.* (1997); Acuña Campa *et al.* (1998); Pesché & Nägele (2000a,b); Lançon *et al.* (2001); Marcus *et al.* (1999); Santana-Solano & Arauz-Lara (2001, 2002); Cui *et al.* (2004); Cohen *et al.* (2004); Tlusty (2006). The hydrodynamic interactions cause long-range correlations in their diffusive motions that are measurable even at distances ten times larger than the particle size (Carbajal-Tinoco *et al.* 1997; Cui *et al.* 2004). In the case of pressure-driven Poiseuille or shear flow the particles are, in addition, dragged by the flow (Durlofsky & Brady 1989; Nott & Brady 1994; Morris & Brady 1998; SINGH & NOTT 2000; Morris 2001; Bhattacharya *et al.* 2006; Beatus *et al.* 2006, 2012; Shani *et al.* 2014; Shen *et al.* 2016a, 2014; Sarig *et al.* 2016).

Identical particles at similar positions inside the channel move at the same velocity if not for hydrodynamic interactions. These interactions induce particle relative motions, which can result in considerable changes of their configuration inside the channel. In the case of a large number of particles the interactions cause also chaotic collisions among the particles (Shani *et al.* 2014).

Theoretical progress has mainly relied on the observation that the far flow caused by a particle confined in a channel is a dipolar flow decaying quadratically with the distance (Cui *et al.* 2004). For disk-like particles with thickness close to the channel width  $h$ , the dipolar flow and its moments were derived from lubrication theory in Tlusty (2006). The dipolar flow holds at distances much larger than the disk radius, where it gives also the leading order hydrodynamic interactions among particles (Tlusty 2006; Beatus *et al.* 2006, 2012; Shani *et al.* 2014).

It was observed in Beatus *et al.* (2012), however, that hydrodynamic interactions of pancake-like disks can also be described at much smaller distances between the disks where dipolar approximation breaks down, yet lubrication theory still holds (Batchelor 1967; Tavakol *et al.* 2017; Szeri 2005; Bruce 2012). This theory predicts that at distances from the particle boundary much larger than  $h$  the depth-averaged flow is an ideal two dimensional flow with potential obeying the Laplace equation. The boundary condition (b. c.), derived somewhat heuristically, is the usual ideal flow b. c. prescribing the velocity component normal to the particle surfaces (Landau & Lifshitz 1987), which allowed to find the hydrodynamic interactions of two close disks, see Beatus *et al.* (2012). Moreover, it was observed that the non-rigidity of the particles makes the lubrication theory valid up to distances from the particles smaller than  $h$ . The calculation of the hydrodynamic interactions for disks of different radii requires solving the Laplace equation with the help of bipolar coordinates, see Sarig *et al.* (2016).

Recently, a practical applications of hydrodynamic interactions among particles in a channel has been proposed. In particular, it is suggested that the combined action of adhesive (non-hydrodynamic) forces and hydrodynamic interactions between microdroplets can result in the formation of regular particle clusters and can thus be potentially used for the production of new materials (Shen *et al.* 2014, 2016a). The hydrodynamic forces are believed to be a

significant factor in these structure formation. Though the particles forming the structure are in a close proximity in the experiments mentioned above, the hydrodynamic interactions are described phenomenologically by a dipolar flow, formally only valid at larger distances. Despite the use of the far-field dipolar flow beyond its domain of validity, the numerical simulations in Shen *et al.* (2014) showed very good agreement with the experimental results (Shen *et al.* 2016a). The above motivates the need for the detailed theoretical study of hydrodynamic interactions among particles in narrow channels.

In this work, we introduce a boundary integral representation of the channel flow in the presence of freely suspended particles. The particles can be rigid or soft (droplets). The representation does not depend on the particle equation of motion, defined by inertia. Boundary integral representations are known to be useful in unconfined flows and can also be applied to confined geometries (Happel & Brenner 1983; Pozrikidis 1992). The flow is here expressed as the sum of the undisturbed Poiseuille flow and an integral over the surfaces of all particles, where the particles can have arbitrary shapes. The derivation is performed for a pressure-driven flow, but identical considerations can be applied to shear flows.

Our representation results in a formula for calculation of the dipole moment, which was previously available only for the case of disk-like particles. The moment is given in terms of a weighted integral of the stress tensor and the flow over the surface(s) of the particle(s). Once this integral is numerically tabulated, the result can be used to approximate the flow in different configurations. Here, we perform simulations for the case of neutrally buoyant rigid spherical particles and compute the integral for different positions of the particle center and different ratios of the particle radius to the channel height, i.e. different confinements.

We use this new integral representation to show that the lubrication theory holds at the particle near proximity, closer than what typically expected. As an example, we solve the problem of three aligned particles moving along the line defined by their centers and the case of three nonaligned particles. We conjecture that this solution is the attractor to which the long-time evolution of arbitrary initial condition converges. We conclude by proposing a mean field description of strong hydrodynamic interactions of close particles in a dense suspension.

## 2. Integral representation for channel flow with particles

In this Section we derive the boundary integral representation for channel flow in the presence of an arbitrary number of particles of arbitrary shape (see Fig. 1 where spherical particles are shown for illustration). It is assumed that the Reynolds number is low and the Stokes equations hold. The derivation uses the reciprocal theorem with the reciprocal flow given by the Stokeslet in a channel (Liron & Mochon 1976), similarly to the derivations in infinite space, see e. g. Pozrikidis (1992). In this Section we make no assumptions on the form of the

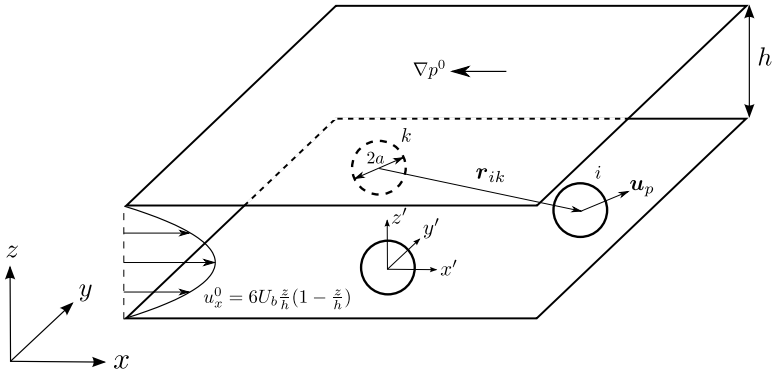


Figure 1: Schematic configuration of spherical particles flowing in the pressure-driven (Poiseuille) flow in a channel.

equation of motion of the particles which may change according to the relevance of inertia. The particles can be rigid, droplets or, e.g. viscoelastic.

The undisturbed flow  $\mathbf{u}^0$ , in the absence of particles, is the Poiseuille flow driven by the constant pressure gradient  $\nabla p^0$ ,

$$u_x^0 = \frac{z(z-h)\nabla_x p^0}{2\eta}, \quad \nabla p^0 = \eta \nabla^2 \mathbf{u}^0. \quad (1)$$

where  $\eta$  is the fluid viscosity,  $z$  is the vertical coordinate and  $h$  is the channel width. The flow is in  $x$ -direction,  $\nabla_x p^0 = -|\nabla_x p^0| \hat{\mathbf{x}}$ . In the presence of a freely suspended particle we look for the solution of,

$$\begin{aligned} \nabla p &= \eta \nabla^2 \mathbf{u}, \quad \nabla \cdot \mathbf{u} = 0, \quad \mathbf{u}(z=0) = \mathbf{u}(z=h) = 0, \\ u_x(\infty) &= \frac{z(z-h)\nabla_x p^0}{2\eta}, \end{aligned} \quad (2)$$

which holds outside the particle. The flow is completely determined when solving for the particle motion, i.e. knowing the instantaneous particle position as it determines the boundary condition  $\mathbf{u}_S(\mathbf{x})$  on the particle surface  $S$ . In the case of a rigid particle,  $\mathbf{u}_S(\mathbf{x}) = \mathbf{v} + \boldsymbol{\omega} \times (\mathbf{x} - \mathbf{y})$  where  $\mathbf{v}$  and  $\boldsymbol{\omega}$  are the particle translational and angular velocities and  $\mathbf{y} = (x_p, y_p, z_p)$  is the coordinate of the particle center of mass. The velocities  $\mathbf{v}$  and  $\boldsymbol{\omega}$  are determined by the solution of the equation for the particle motion coupled with the flow. These velocities could be time-independent as in the case of the steady motion of a neutrally buoyant rigid particle or the case of a non-neutrally buoyant particle after sedimentation when reaching the bottom wall (the theoretical determination of these velocities is impossible generally because of the interaction with the walls). These velocities can also be time-dependent as in the case of a transient flow or the gravitational settling of a non-neutrally buoyant particle. If several

particles are considered, a time-dependent configuration can be induced by their interactions. We assume here that the time variations are not fast so that the unsteady time-derivative term of the Navier-Stokes equations is negligible (for the steady motion of one particle the time-derivative is the spatial derivative of the flow along the streamline which is small because of the smallness of the Reynolds number). In the case of droplets the boundary condition on the surface is determined by matching with the inner flow. However there is no need for solving for this inner flow since the detailed form of  $\mathbf{u}_S(\mathbf{x})$  is irrelevant for the derivation of the present representation. The generalization of the problem to the case of many particles is obvious.

*Implications of lubrication theory.*—Some conclusions on the flow at distances from the particle much larger than the channel width  $h$  can be obtained from lubrication theory (Batchelor 1967; Tavakol *et al.* 2017; Szeri 2005; Bruce 2012). The lubrication theory predicts that at these distances,

$$\mathbf{u} = \frac{z(z-h)\nabla p}{2\eta}, \quad (3)$$

with a certain  $z$ -independent  $p$ . Clearly, at large distances,  $p \approx p^0$  at the leading order. The depth-averaged velocity  $\mathbf{u}_d$  is the ideal potential two-dimensional flow,

$$\mathbf{u}_d = \nabla\phi, \quad \phi = -\frac{h^2 p}{12\eta}, \quad \nabla^2\phi = 0. \quad (4)$$

In some cases this helps determining the flow completely.

*Large disks.*—Large non-wetting droplets squeezed between the walls of a Hele-Shaw cell have pancake-like shapes. These can be modeled as disks with radius  $a \gg h$  and height close to  $h$ , i.e., they almost fill the entire channel height (Thulst 2006; Beatus *et al.* 2006, 2012; Shani *et al.* 2014). In this case, one can use Eqs. (3)-(4) at distances from the body that are much larger than  $h$  but much smaller than  $a$ . Thus the ideal flow holds outside the narrow boundary layer near the particle surface whose characteristic size  $l_0$  is of the order  $h$ , much smaller than the particle horizontal size  $a$ . We call the layer containing the flow vorticity the viscous layer and assume that there is no flux of mass through the surface of the droplet, which keeps its shape and volume. Thus, in the frame of reference moving with the disk, the normal velocity component is zero at the outer boundary of the layer and the ideal flow outside the layer is determined uniquely by this boundary condition. However the geometry of the layer is not always known and the complete determination of the flow not possible. If we are only interested in the flow outside the immediate  $l_0$ -vicinity of the viscous layer, we can set the boundary condition for the ideal flow on the disk itself, exploiting the fact that  $l_0 \ll a$ . The flow is then found as the dipole potential (Thulst 2006),

$$\phi = -\frac{h^2 p^0}{12\eta} - \frac{\mathbf{d} \cdot \hat{\mathbf{r}}}{r}, \quad \nabla^2\phi = 0, \quad \mathbf{d} = a^2 \mathbf{v}, \quad (5)$$

where  $\mathbf{d}$  is the dipole moment,  $\mathbf{v} = -v\hat{\mathbf{x}}$  is the difference between the disk velocity and  $-h^2\nabla p_0/(12\eta)$ . It is readily seen that the normal, radial component of the velocity  $\nabla\phi$  on the surface of the disk is  $[\mathbf{v} - h^2\nabla p^0/(12\eta)] \cdot \hat{r}$ . Note that the velocity  $v > 0$  since the particle moves slower than the fluid.

The tangential velocity component on the outer boundary of the viscous layer obtained from Eq. (5) does not match the tangential velocity of the droplet surface. In contrast with the normal component, which can be considered almost constant through the viscous layer, the tangential component changes quickly through this layer to match the inner flow at the droplet surface. As example, in the limit of high droplet viscosity, the condition on the disk surface is that the flow is the appropriate superposition of translation and solid body rotation. Similar viscous layers occur for rigid bodies oscillating in the fluid (Landau & Lifshitz 1987). The ideal flow was obtained in Thusty (2006) and here we describe how this ideal flow fits the complete equations for the viscous flow.

*Boxes.*—Another case where the flow can be fixed without detailed calculations is the case of a box whose smallest dimension is close to  $h$  and the longer dimensions are much larger than  $h$ . If the box is located in the channel so that the flow is perpendicular to its longer axis with length  $l \gg h$  then far from the ends of the box we find the ideal two-dimensional flow with constant velocity on the line. The solution for the ideal flow with constant velocity on an infinite linear boundary is the uniform flow. We thus conclude that in the frame moving with the box there is a region of stagnant flow behind the box, whose size is of order  $l$ .

Generally, the flow can be inferred from the lubrication theory in quite a detail for particles whose horizontal dimensions are much larger than  $h$  and whose vertical dimension is close to  $h$ . The flow outside the narrow viscous layer near the particle surface is  $z(z-h)$  times the two-dimensional ideal flow determined by the boundary condition of zero normal velocity on the particle surface. The tangential velocity changes fast across the viscous layer. However, if the particle horizontal dimensions are not large or the dimensions are large but the vertical dimension is not close to  $h$ , a different approach is needed.

*Boundary integral representation from the reciprocal theorem.*—We use the reciprocal theorem (Happel & Brenner 1983; Pozrikidis 1992) using as the reciprocal flow the solution of Liron & Mochon (1976) for the point-force or Stokeslet between two parallel plates, i.e.

$$\begin{aligned} -\nabla p^S + \eta \nabla^2 \mathbf{u}^S + \mathbf{g}\delta(\mathbf{x} - \mathbf{x}_0) &= 0, \quad \nabla \cdot \mathbf{u}^S = 0, \\ \mathbf{u}^S(z=0) &= \mathbf{u}^S(z=h) = 0, \quad \mathbf{u}^S(x^2 + y^2 \rightarrow \infty) = 0. \end{aligned} \quad (6)$$

Analogously to the flow due to a point-force acting on a viscous fluid in infinite space (e.g. Pozrikidis (1992)), the solution depends linearly on the source forcing  $\mathbf{g}$ ,

$$\mathbf{u}^S(\mathbf{x}) = \frac{1}{8\pi\eta} S_{ik}(\mathbf{x}, \mathbf{x}_0) g_k, \quad (7)$$

where we introduced the tensor  $S_{ik}$  independent of  $\mathbf{g}$ . Similarly for the stress tensor of the Stokeslet solution we can write,

$$\begin{aligned}\sigma_{ik}^S(\mathbf{x}) &= -p^S \delta_{ik} + \eta (\nabla_k u_i^S + \nabla_i u_k^S) = \frac{T_{ilk}(\mathbf{x}, \mathbf{x}_0) g_l}{8\pi}, \\ \nabla_k T_{ilk} &= -8\pi \delta_{il} \delta(\mathbf{x} - \mathbf{x}_0), \quad T_{ilk} = -p_l \delta_{ik} + \nabla_k S_{il} + \nabla_i S_{kl},\end{aligned}\quad (8)$$

where  $T_{ilk}$  is a third-rank tensor independent of  $\mathbf{g}$  and we defined the  $\mathbf{g}$ -independent  $p_l$  by  $p^S = \mathbf{p} \cdot \mathbf{g}/(8\pi)$ . We use the Lorentz identity,

$$\nabla_k [u_i \sigma_{ik}^S - u_i^S \sigma_{ik}] + \mathbf{u} \cdot \mathbf{g} \delta(\mathbf{x} - \mathbf{x}_0) = 0, \quad (9)$$

readily inferred from the Stokes equations with  $\sigma_{ik}$  the stress tensor of the flow defined by Eqs. (2),

$$\sigma_{ik} = -p \delta_{ik} + \eta (\nabla_i u_k + \nabla_k u_i). \quad (10)$$

Substituting  $\mathbf{u}^S$  and  $\boldsymbol{\sigma}^S$  from Eqs. (7)-(8) in Eq. (9) and using the above identity we find that,

$$\begin{aligned}8\pi \eta u_l(\mathbf{x}') \delta(\mathbf{x}' - \mathbf{x}) &= \frac{\partial}{\partial x'_k} [S_{il}(\mathbf{x}', \mathbf{x}) \sigma_{ik}(\mathbf{x}')] \\ &\quad - \eta u_i(\mathbf{x}') T_{ilk}(\mathbf{x}', \mathbf{x}).\end{aligned}\quad (11)$$

Integrating this equation over  $\mathbf{x}'$  outside the particles,

$$\begin{aligned}u_l &= f_l - \sum_n \int_{S_n} \frac{S_{il}(\mathbf{x}', \mathbf{x}) \sigma'_{ik} dS'_k}{8\pi \eta} \\ &\quad + \sum_n \int_{S_n} \frac{u_i(\mathbf{x}') T_{ilk}(\mathbf{x}', \mathbf{x}) dS'_k}{8\pi},\end{aligned}\quad (12)$$

where  $f$  is the integral over the far surface at infinity,  $S_n$  is the surface of the  $n$ -th particle and  $dS_k$  is aligned with the outward normal to the particle surface. There is no contribution from the channel boundaries  $z = 0$  and  $z = h$  since both flows vanish there.

We assume that the particles are confined in a finite region so that the flow far from the particles is the Poiseuille flow given by Eq. (1), see Eq. (2). Since the Stokeslet decays far from the source, the second and the third terms on the RHS of Eq. (12) decay to zero at large distances from the particles. Thus, the asymptotic approach of  $\mathbf{u}$  to the Poiseuille flow at large distances implies the asymptotic equality of  $f$  to the Poiseuille flow. It is readily seen using the asymptotic form of the Stokeslet at large horizontal distances, provided in the next Section, and the asymptotic, Poiseuille, form of the flow, that  $f$  is determined by terms independent of the particles, that is terms that would be the same for the case of no particles. Thus necessarily  $f$  is the Poiseuille flow given by Eq. (1). This is confirmed by the direct calculation in Appendix

Appendix A. We therefore conclude that,

$$\begin{aligned} u_l = & \frac{\delta_{lx} z(z-h) \nabla_x p^0}{2\eta} - \sum_n \int_{S_n} \frac{S_{il}(\mathbf{x}', \mathbf{x}) \sigma'_{ik} dS'_k}{8\pi\eta} \\ & + \sum_n \int_{S_n} \frac{u_i(\mathbf{x}') T_{ilk}(\mathbf{x}', \mathbf{x}) dS'_k}{8\pi}. \end{aligned} \quad (13)$$

This integral representation of the flow involves no approximations and holds for particles of arbitrary shape. The flow is determined by the values of  $\mathbf{u}$  and  $\sigma_{ik}$  at the particle surface. When the distance between the particles are much larger than their size the hydrodynamic interactions are negligible and  $\mathbf{u}$  and  $\sigma_{ik}$  are approximately those of an isolated particle. However, the current representation works also when the particles are close to each other so that the hydrodynamic interactions change significantly the values of  $\mathbf{u}$  and  $\sigma_{ik}$  at the particle surface.

*Simplification for rigid surface.*—The integral representation above simplifies in the case of rigid surfaces when the flow on the surface of the particles is the superposition of translation and solid-body rotation. This is not only the case of rigid particles described after Eq. (2), but often also the case of small bubbles where impurities present in the fluid accumulate at the surface making it effectively rigid. In this case, experiments demonstrate that the behavior of these bubbles is similar to that of rigid particles (Happel & Brenner 1983; Levich 1977). In these and similar cases the flow at the particle surface  $u_i(\mathbf{x}')$  has the form  $c_i + \epsilon_{irm} x'_m \tilde{c}_r$  where both  $\mathbf{c}$  and  $\tilde{\mathbf{c}}$  are independent of  $\mathbf{x}'$ . Hence the last term in Eq. (13) drops out because for  $\mathbf{x}$  outside the particle interior  $V_p$ ,

$$\begin{aligned} \int_{S_p} dS'_k T_{ilk}(\mathbf{x}', \mathbf{x}) &= \int_{V_p} dV \nabla'_k T_{ilk} = 0, \\ \epsilon_{irm} \int_S dS'_k x'_m T_{ilk}(\mathbf{x}', \mathbf{x}) &= \epsilon_{irm} \int_{V_p} dV \delta_{mk} T_{ilk} = 0, \end{aligned} \quad (14)$$

cf. Pozrikidis (1992). Note that we made use of the fact that  $\epsilon_{irm}$  is antisymmetric over indices  $i, m$  whereas  $T_{ilm}$  is symmetric with respect to those indices. We conclude that in the case of many particles with rigid surfaces,

$$u_l = \frac{\delta_{lx} z(z-h) \nabla_x p^0}{2\eta} - \sum_n \int_{S_n} \frac{S_{il}(\mathbf{x}', \mathbf{x}) \sigma'_{ik} dS'_k}{8\pi\eta}, \quad (15)$$

The representations derived here are thus useful to describe the flow.

### 3. Derivation of lubrication theory

In this Section we demonstrate that Eqs. (13) and (15) imply that the predictions of the lubrication theory hold at horizontal distances from the particles larger than  $h$ . This is less restrictive than the usual condition of applicability of the lubrication theory for distances much larger than  $h$ , cf. Sarig *et al.* (2016). This

property comes from the Stokeslet flow which obeys the lubrication theory at distances larger than  $h$ . We use the representation

$$S_{il}(\mathbf{x}', \mathbf{x}) = \frac{12z'(h-z')z(z-h)\nabla_i\nabla_l \ln \rho}{h^3} + \tilde{S}_{il}(\mathbf{x}', \mathbf{x}), \quad (16)$$

where  $\rho$  is the length of  $\boldsymbol{\rho} = (x - x', y - y')$  (thus  $\nabla_i\nabla_l \ln \rho = 0$  if one of the indices is  $z$ ). It was observed in Liron & Mochon (1976) that  $\tilde{S}_{il}$  decays exponentially in  $\rho$  with exponent at least  $\pi/h$ , that is the smallness is at least  $\exp(-\pi\rho/h)$ . Thus already at  $\rho \approx h$  we can discard the last, non-potential term in Eq. (16). The resulting approximation to the Stokeslet flow,

$$S_{il}(\mathbf{x}', \mathbf{x}) \approx S_{il}^0(\mathbf{x}', \mathbf{x}) = \frac{12z'(h-z')z(z-h)\nabla_i\nabla_l \ln \rho}{h^3}, \quad (17)$$

is the two-dimensional potential flow times  $z'(h-z')$ , in agreement with the predictions of the lubrication theory, see Eq. (3). Note that  $S_{il}^0(\mathbf{x}', \mathbf{x})$  is a symmetric function of  $\mathbf{x}$  and  $\mathbf{x}'$ , whose dependence on the horizontal coordinates is via the difference  $\boldsymbol{\rho}$  only. We consider the corresponding pressure  $p^0$  that approximately solves the corresponding Stokes equation  $\nabla'_i p_l^0(\mathbf{x}', \mathbf{x}) = \nabla'^2 S_{il}^0(\mathbf{x}', \mathbf{x})$ , see the second of Eqs. (8). Here  $\nabla'_i$  designates the derivative over  $x'_i$  and we do not write the  $\delta(\mathbf{x}' - \mathbf{x})$  term on the RHS. We thus find ( $l \neq z$ ),

$$p_l^0(\mathbf{x}', \mathbf{x}) = \frac{24z(z-h)\rho_l}{h^3\rho^2} = \frac{24z(z-h)}{h^3}\nabla_l \ln \rho. \quad (18)$$

Here,  $p^0$  is the leading order approximation for the pressure of the Stokeslet at large distances (Liron & Mochon 1976), with an exponentially small correction. We can write ( $l \neq z$  but  $i$  or  $k$  can be  $z$ ),

$$T_{ilk}(\mathbf{x}', \mathbf{x}) = -p_l^0 \delta_{ik} + \nabla'_k S_{il}^0 + \nabla'_i S_{kl}^0 + \tilde{T}_{ilk}(\mathbf{x}', \mathbf{x}), \quad (19)$$

where  $\tilde{T}_{ilk}(\mathbf{x}', \mathbf{x})$  decays exponentially in  $\rho$  with exponent at least  $\pi/h$ , cf. Eq. (8). The stress tensor  $T_{ilk}(\mathbf{x}', \mathbf{x})$  is exponentially small when one of the indices is  $z$ . We find using the expressions for  $p_0$  and  $S_{il}^0$ ,

$$\begin{aligned} T_{ilk}(\mathbf{x}', \mathbf{x}) &\approx \frac{24z(h-z)}{h^3} \nabla_l [(\delta_{ik} + z'(h-z')\nabla_i\nabla_k) \ln \rho] \\ &+ \frac{12(h-2z')z(z-h)}{h^3} (\delta_{kz}\nabla_i + \delta_{iz}\nabla_k) \nabla_l \ln \rho, \end{aligned} \quad (20)$$

where we neglected exponentially small correction. We find from Eq. (13) that,

$$\mathbf{u}(\mathbf{x}) = \frac{z(z-h)\nabla p}{2\eta} + O\left(e^{-\pi \min[\rho_n]/h}\right); \quad \nabla^2 p = 0, \quad (21)$$

where  $\mathbf{u} = (u_x, u_y)$  and  $\min[\rho_n]$  is the distance from  $\mathbf{x}$  to the closest boundary of a particle. The pressure  $p$  in this formula is independent of  $z$  as predicted by

the lubrication theory used in Eq. (3) with,

$$\begin{aligned} p = p^0 + \sum_n \delta p_n, \quad \delta p_n = & \frac{3\nabla_i}{\pi h^3} \int_{S_n} z'(z' - h) \ln \rho \sigma'_{ik} dS'_k \\ & - \frac{6\eta}{\pi h^3} \int_{S_n} dS'_k (\delta_{ik} + z'(h - z') \nabla_i \nabla_k) u_i(\mathbf{x}') \ln \rho \\ & + \frac{3\eta}{\pi h^3} \int_{S_n} dS'_k (h - 2z') (\delta_{kz} \nabla_i + \delta_{iz} \nabla_k) u_i(\mathbf{x}') \ln \rho, \end{aligned} \quad (22)$$

where  $\delta p_n$  is the pressure perturbation due to the  $n$ -th particle and the summation over repeated indices is from 1 to 3. Eqs. (21)-(22) are one of the main results of our work. These provide a refinement of the lubrication theory demonstrating that Eq. (3) holds under the condition  $\exp(-\pi \min[\rho_n]/h) \ll 1$ , which is difficult to show using the classic lubrication theory as it demands the strong inequality  $\min[\rho_n] \gg h$ . For instance, at  $\min[\rho_n] = h$  the exponential factor is  $\sim 0.04$ . The result holds both for droplets and rigid particles where for rigid particles the last two lines of Eq. (22) become zero and the equation reduces to

$$p = p^0 + \frac{3\nabla_i}{\pi h^3} \sum_n \int_{S_n} z'(z' - h) \ln \rho \sigma'_{ik} dS'_k. \quad (23)$$

We have good control of the correction terms to Eqs. (21)-(23) from the series representation of  $\tilde{S}_{il}(\mathbf{x}', \mathbf{x})$  provided in Liron & Mochon (1976).

The pressure  $p$  solves the two-dimensional Laplace equation in the domain between the particles since it is formed by integrals of the fundamental solution of the Laplace equation  $\ln \rho$  over the particle boundaries. The formula for  $p$  matches the ideal flow that holds beyond the horizontal distance  $h$  from the particles with the fully viscous flow near the particles. The viscous layer is the neighborhood of the boundary of each particle where Eq. (22) breaks down. Though the solution for  $p$  is given in terms of the unknown velocities and stress tensors on the surfaces of the particles, it seems that this is as much as can be done generally: the matching problem is not solvable for any general particle shape. It does simplify for disk-like particles as described previously.

*Hydrodynamic interactions of pancake-like droplets.*—Eqs. (21)-(22) provide support for the observation that the width of the viscous layer around disk-like droplets is not larger than  $h$ . The formulae tell that, unless the distance between the droplet surfaces is smaller than  $h$ , the (horizontal) flow outside the viscous layers near the particles is an ideal potential flow. This flow can be determined using the boundary condition that the normal velocity at the outer boundary of the viscous layer coincides with the normal component of the translational velocity of the particle. Since the layer width is of the order of  $h$ , and as long as the distance between the droplets is larger than  $h$  (but possibly much smaller than  $a$ ) we can impose the boundary condition on the particle surface, neglecting the finite width of this viscous layer as we did for the case of the single large disk, see Eq. (5). Similarly, in the presence of many particles whose

separation is larger than  $h$ , the flow outside the boundary layer is described by a pressure field  $p$  that obeys (Sarig *et al.* 2016; Beatus *et al.* 2012),

$$\nabla^2 p = 0, \quad \left( \mathbf{v}_n + \frac{h^2 \nabla p}{12\eta} \right) \cdot \hat{n}_n = 0, \quad (24)$$

where  $\mathbf{v}_n$  is the velocity of  $n$ -th particle,  $\hat{n}_n$  is the unit vector normal to the surface of the  $n$ -th particle. The pressure gradient is taken at the outer boundary of the viscous layer of the  $n$ -th particle. However, since the latter is narrow, one can consider  $\nabla p$  on the surface of the  $n$ -th particle without affecting significantly the solution for the pressure outside the viscous layers. To find the pressure inside the layers would require a separate study. For close droplets the pressure determined by Eq. (24) is different from the superposition of the dipole solutions given by Eqs. (4)-(5) due to the near-field interactions.

Finally, we demonstrate that the force exerted on the particles, determined by the viscous stress tensor at the particle surface, can be obtained from the ideal flow description. The force  $\mathbf{F}^n$  on particle  $n$  is determined by the following integral over the particle surface,

$$\mathbf{F}_i^n = \int_{S_n} \sigma_{ik} dS_k = \int_{outer} \sigma_{ik} dS_k, \quad (25)$$

where the last integral is over the outer boundary of the viscous layer of the  $n$ -th particle and we used  $\nabla_k \sigma_{ik} = 0$ . We can neglect the viscous contribution to the stress tensor at the outer boundary and find

$$\mathbf{F}^n \approx - \int_{outer} pdS \approx - \int_{S_n} pdS, \quad (26)$$

where we must use the pressure  $p$  determined from Eq. (24) in the last term and not the true pressure on the surface of the particle. Thus, the force coincides with that in an ideal flow and, effectively, we can assume that the ideal flow holds everywhere disregarding the no-slip boundary condition. This provides a consistent basis for the study of hydrodynamic interactions between large droplets at small distances as performed in Sarig *et al.* (2016); Beatus *et al.* (2012).

#### 4. Multipole expansion

The flow at large distances from the particles can be effectively studied using the multipole expansion. The distances must be larger than  $h$  and much larger than the particle size. We perform here this expansion in terms of  $\delta p_n$  in Eq. (22), solution of the two-dimensional Laplace equation. We write  $\delta p_n$  as,

$$\begin{aligned} \delta p_n = & \frac{3}{\pi h^3} \int_{S_n} dS'_k (z'(z' - h) \sigma'_{ik} \nabla_i - \eta u_i(\mathbf{x}') (2\delta_{ik} \\ & + 2z'(h - z') \nabla_i \nabla_k + (h - 2z') (\delta_{kz} \nabla_i + \delta_{iz} \nabla_k))) \ln \rho. \end{aligned} \quad (27)$$

We provide next the expansion in Cartesian and polar coordinates as in three-dimensional electrostatics (Jackson 1962).

We set the origin of the coordinate system inside the  $n$ -th particle. To determine the multipole expansion in Cartesian coordinates we consider the Taylor series (remind that  $\rho = |\mathbf{r} - \mathbf{r}'|$ ),

$$\ln \rho = \ln r - r'_l \nabla_l \ln r + \frac{r'_l r'_p}{2} \nabla_l \nabla_p \ln r + \dots, \quad (28)$$

where dots stand for higher-order terms. Substituting into Eq. (27) one obtains the Cartesian form of the multipole expansion. The leading-order  $\ln r$  term in the series,

$$\begin{aligned} \delta p_n = & \frac{3}{\pi h^3} \int_{S_n} dS'_k (z'(z' - h) \sigma'_{ik} \nabla_i - \eta u_i(\mathbf{x}') (2\delta_{ik} \\ & + 2z'(h - z') \nabla_i \nabla_k + (h - 2z') (\delta_{kz} \nabla_i + \delta_{iz} \nabla_k))) \ln r, \end{aligned} \quad (29)$$

has a contribution proportional to  $\int \mathbf{u} \cdot d\mathbf{S}$ , i.e. proportional to  $\ln r$ . Further assuming the droplet is incompressible  $\int \mathbf{u} \cdot d\mathbf{S} = 0$ . In this case, the leading order term at larger distances is given by the dipole term,

$$\begin{aligned} \delta p_n = & \frac{3}{\pi h^3} \int_{S_n} dS'_k (z'(z' - h) \sigma'_{ik} \nabla_i - \eta u_i(\mathbf{x}') (h - 2z') \\ & (\delta_{kz} \nabla_i + \delta_{iz} \nabla_k)) \ln r + \frac{6\eta \nabla_l \ln r}{\pi h^3} \int_{S_n} r'_l \mathbf{u} \cdot d\mathbf{S}, \end{aligned} \quad (30)$$

where the last term comes from the next-order term in the expansion of the logarithm. This term can be simplified for droplets that do not change their shape, such as the pancake-like droplets considered previously, since the slip and flow on the surface are irrelevant. For instance, for a spherical droplet whose center moves with velocity  $\mathbf{v}$ , one obtains  $\int_{S_n} r'_l \mathbf{u} \cdot d\mathbf{S} = v_k \int_{S_n} r'_l dS_k = 4\pi a^3 v_l / 3$ . The complete expansion becomes,

$$\begin{aligned} \delta p_n = & \frac{3}{\pi h^3} \int_{S_n} dS'_k (z'(z' - h) \sigma'_{ik} \nabla_i - \eta u_i(\mathbf{x}') (2\delta_{ik} \\ & + 2z'(h - z') \nabla_i \nabla_k + (h - 2z') (\delta_{kz} \nabla_i + \delta_{iz} \nabla_k))) (\ln r \\ & - r'_l \nabla_l \ln r + \frac{r'_l r'_p}{2} \nabla_l \nabla_p \ln r + \dots). \end{aligned} \quad (31)$$

The expansion in polar coordinates is found observing that for  $r' < r$ ,

$$\begin{aligned} \ln |\mathbf{r} - \mathbf{r}'| = & \ln r \\ & - \sum_{n=1}^{\infty} \left( \frac{r'}{r} \right)^n \frac{\cos(n\theta) \cos(n\theta') + \sin(n\theta) \sin(n\theta')}{n}. \end{aligned} \quad (32)$$

This formula represents the fundamental solution  $\ln |\mathbf{r} - \mathbf{r}'|$  in terms of the elementary solutions of Laplace equation,  $r^{-k} \exp(ik\theta)$  and  $r'^p \exp(ip\theta')$  with  $k$  and  $p$  positive integers. This is the counterpart of the expansion of  $|\mathbf{r} - \mathbf{r}'|^{-1}$  in spherical harmonics adopted in three-dimensional multipole expansion in electrostatics (Jackson 1962) and, in fact, it can be derived from that expansion

by confining  $\mathbf{r}$ ,  $\mathbf{r}'$  in a plane. We provide here a simpler derivation. We consider,

$$\ln |\mathbf{r} - \mathbf{r}'| = \ln r + \frac{\ln(1 - 2\epsilon \cos \gamma + \epsilon^2)}{2}, \quad \epsilon = \frac{r'}{r}, \quad (33)$$

where  $\gamma$  is the angle between  $\mathbf{r}$  and  $\mathbf{r}'$  and  $\epsilon < 1$ . We recall the Fourier series,

$$\ln(1 - 2\epsilon \cos \gamma + \epsilon^2) = - \sum_{n=1}^{\infty} \frac{2\epsilon^n \cos(n\gamma)}{n} \quad (34)$$

where the integrals for the Fourier coefficients can be obtained using the residue theorem (Gradshteyn & Ryzhik 2014). Finally, introducing the polar angles  $\theta$  and  $\theta'$  for  $\mathbf{r}$  and  $\mathbf{r}'$ , respectively, and using  $\gamma = \theta' - \theta$  we obtain Eq. (32). The multipolar expansion in polar coordinates is finally

$$\begin{aligned} \delta p_n = & \frac{3}{\pi h^3} \int_{S_n} dS'_k (z'(z' - h) \sigma'_{ik} \nabla_i - \eta u_i(\mathbf{x}') (2\delta_{ik} \\ & + 2z'(h - z') \nabla_i \nabla_k + (h - 2z') (\delta_{kz} \nabla_i + \delta_{iz} \nabla_k))) (\ln r \\ & - \sum_{n=1}^{\infty} \left( \frac{r'}{r} \right)^n \frac{\cos(n\theta) \cos(n\theta') + \sin(n\theta) \sin(n\theta')}{n}) , \end{aligned} \quad (35)$$

which gives the pressure as a superposition of elementary solutions  $r^{-k} \exp(ik\theta)$ . The formulae simplify for rigid particles to

$$\begin{aligned} \delta p_n = & \frac{3}{\pi h^3} \int_{S_n} dS'_k z'(z' - h) \sigma'_{ik} \nabla_i (\ln r \\ & - r'_l \nabla_l \ln r + \frac{r'_l r'_p}{2} \nabla_l \nabla_p \ln r + \dots) \end{aligned} \quad (36)$$

and

$$\begin{aligned} \delta p_n = & \frac{3}{\pi h^3} \int_{S_n} dS'_k z'(z' - h) \sigma'_{ik} \nabla_i (\ln r \\ & - \sum_{n=1}^{\infty} \left( \frac{r'}{r} \right)^n \frac{\cos(n\theta) \cos(n\theta') + \sin(n\theta) \sin(n\theta')}{n}) . \end{aligned} \quad (37)$$

The multipole expansion of the flow is derived by taking the gradient of the pressure using Eq. (21). As an example, the perturbation of the Poiseuille flow due to a rigid particle,  $\delta u_k$ , is up to a cubically decaying term,

$$\begin{aligned} \delta u_k = & - \frac{3z(z-h)s_i}{2\pi h^3 \eta} \nabla_k \nabla_i \ln r - \frac{3z(z-h)}{2\pi h^3 \eta} \\ & \times \nabla_k \nabla_i \frac{1}{r} \int_S dS'_k z'(z' - h) \sigma'_{ik} r' \cos(\theta - \theta'), \end{aligned} \quad (38)$$

where we introduced,

$$s_i = \int_S z'(h - z') \sigma'_{ik} dS'_k . \quad (39)$$

The first term in Eq. (38) is a dipole and the second term a quadrupole. Similarly, we can write the corresponding and higher-order terms for droplets.

## 5. Leading-order behavior at large distances

In this Section we consider the leading order behavior of the flow at large horizontal distances from the particle(s). The distances must be larger than  $h$  (but not much larger) and much larger than the size of the particles. The far-field flow perturbation  $\delta\mathbf{u}_n$  due to the  $n$ -th particle is given by the dipole flow,

$$\delta\mathbf{u}_n = \frac{z(z-h)}{2\eta} \nabla \delta p_n, \quad \delta p_n = -\frac{3}{\pi h^3} (\mathbf{s}_n \cdot \nabla) \ln r, \quad (40)$$

where

$$\begin{aligned} (\mathbf{s}_n)_i &= \int_{S_n} dS'_k z' (h - z') \sigma'_{ik} + \eta \int_{S_n} dS'_z (h - 2z') u_i(\mathbf{x}') \\ &\quad + \eta \int_{S_n} dS'_i (h - 2z') u_z(\mathbf{x}') - 2\eta \int_{S_n} r'_i \mathbf{u} \cdot dS, \end{aligned} \quad (41)$$

see Eqs. (21) and (30). For rigid particles this reduces to Eq. (39) which is why we use the same letter for the coefficient  $s_i$ . We find that the perturbation of the potential of the depth-averaged flow  $\delta\phi_n = -h^2 \delta p_n / (12\eta)$  is,

$$\delta\phi_n = -\frac{\tilde{\mathbf{d}}_n \cdot \hat{r}}{r}, \quad \tilde{\mathbf{d}}_n = -\frac{\mathbf{s}_n}{4\pi\eta h}, \quad (42)$$

see Eq. (4). Thus, the flow perturbation at large distances is the dipolar flow with effective dipole moment  $\tilde{\mathbf{d}}$ . We can describe the far-field impact of a particle of arbitrary shape on the flow introducing the source in the potential equation,  $\nabla^2 \delta\phi_n = -2\pi(\tilde{\mathbf{d}}_n \cdot \nabla)\delta(x)\delta(y)$  so that the full potential  $\phi$  obeys,

$$\nabla^2 \phi = -2\pi \sum_n (\tilde{\mathbf{d}}_n \cdot \nabla) \delta(x - x_n) \delta(y - y_n) \quad (43)$$

where  $(x_n, y_n)$  are the horizontal coordinates of some point inside the  $n$ -th particle (observe that  $p^0$  is a linear function and has zero laplacian).

The resulting correction to the Poiseuille flow is that of a particle that moves in direction of  $\mathbf{s}$ , see Eq. (5),

$$\delta u_k(\mathbf{x}) = \frac{3s_i z(h-z)}{\pi\eta h^3(x^2 + y^2)} \left[ \frac{\delta_{ik}}{2} - \frac{x_i x_k}{x^2 + y^2} \right], \quad \rho \gg h. \quad (44)$$

The lateral,  $y$  and  $z$ , components of  $\mathbf{s}$  vanish for particles that have fore-and-aft symmetry. This can be shown in the same way as for the absence of lateral migration of spheres in a channel (Leal 2007; Bretherton 1962). The reversal of the sign of  $\mathbf{u}$  and  $p$  produces another solution of the system of Eqs. (2). This solution has opposite sign of the stress tensor and velocity and thus of  $\mathbf{s}$ . However, it describes the same physical situation and thus must have the same lateral components of  $\mathbf{s}$ , hence these components must vanish. Thus, for spheres or ellipsoids  $\mathbf{s} = s\hat{\mathbf{x}}$ . In contrast, for particles whose shape is an arc or similar one can have a non-zero  $s_y$  and  $s_z$ .

We consider a spherical particle as an example of a particle with fore-and-aft symmetry. We can introduce  $s_i = s(z_p)\delta_{ix}$  where,

$$\begin{aligned} s(z_p) &= \int_S z'(h-z')\sigma'_{xk}dS'_k + \eta \int_{S_n} dS'_z(h-2z')u_x(\mathbf{x}') \\ &\quad + \eta \int_{S_n} dS'_x(h-2z')u_z(\mathbf{x}') - 2\eta \int_{S_n} r'_x \mathbf{u} \cdot d\mathbf{S}, \end{aligned} \quad (45)$$

with  $z_p$  the vertical position of the particle center. In this case, the flow is

$$\begin{aligned} \delta u_x(\mathbf{x}) &= \frac{3s(z_p)z(h-z)}{2\pi\eta h^3(x^2+y^2)} \frac{y^2-x^2}{x^2+y^2}, \\ \delta u_y(\mathbf{x}) &= -\frac{3s(z_p)z(h-z)}{2\pi\eta h^3(x^2+y^2)} \frac{2xy}{x^2+y^2}. \end{aligned} \quad (46)$$

It is plausible that  $s(z_p) > 0$  because the particle is always lagging behind the local flow. This is confirmed by the direct numerical simulations reported below.

The formulas provided here give the possibility of tabulating the particle dipole moments from numerical simulations for future use. For a spherical particle of fixed radius the dipole moment depends on the vertical coordinate  $z_p$ . The solution of the flow equations in the presence of an isolated sphere would give the stress tensor and the surface velocity with which we can find  $s(z_p)$ . We illustrate this procedure for the case where the particle is a rigid sphere with same density as that of the fluid. The equation of motion is,

$$m \frac{dv_i}{dt} = \int_S \sigma_{ik} dS_k, \quad (47)$$

where  $m$  is the mass of the particle and gravity does not influence the motion since the particle is assumed to be neutrally buoyant. This equation is coupled to the time- dependent Navier-Stokes equations where the unsteady term is not negligible during the transients. The particle eventually reaches a constant velocity and the fluid flow is governed by the steady Stokes equations due to the small Reynolds number. Thus, our derivation of the far flow holds with the dipole coefficient for rigid particles,

$$s(z_p) = \int_S z'(h-z')\sigma'_{xk}dS'_k. \quad (48)$$

We computed here  $s(z_p)$  using the numerically determined  $\sigma_{xk}$  for different  $z_p$  and different radii of the sphere. The results are summarized in Tables 1 - 3 (see Appendix Appendix B for details). Here, the particle relative velocity, defined as  $\delta u_p = u_p - u_x^0$  where  $u_p$  is the particle center velocity, is non-dimensionalized by the bulk velocity of the undisturbed channel flow  $U_b = -h^2\nabla_x p^0/(12\eta)$ . The reduction of the translational velocity as the particle is placed closer to one wall or as the particle size increases is consistent with previous computations using the boundary integral method (Staben *et al.* 2003).

We also report the values of  $\hat{s}(z_p) = 3s(z_p)/(2\pi\eta h^3)$ , the common pre-factor in Eq. (46). We note that, though overall small,  $\hat{s}$  increases as the particle

Table 1: Relative particle velocity  $\delta u_p/U_b$  and magnitude of  $\hat{s}$  as function of the particle centre position  $z_p/h$  for spherical particles of radius  $a = h/6$  obtained from the numerical simulations.

$z_p/h$	0.50	0.55	0.60	0.65	0.70	0.75	0.80
$\delta u_p/U_b$	-0.06	-0.06	-0.06	-0.07	-0.07	-0.09	-0.17
$\hat{s} \times 10^{-3}$	1.8	2.2	3.7	6.3	10.6	17.8	30.0

Table 2: Relative particle velocity  $\delta u_p/U_b$  and magnitude of  $\hat{s}$  as function of the particle centre position  $z_p/h$  for spherical particles of radius  $a = h/3$  obtained from the numerical simulations.

$z_p/h$	0.50	0.55	0.60	0.65
$\delta u_p/U_b$	-0.24	-0.25	-0.30	-0.45
$\hat{s} \times 10^{-2}$	4.1	4.9	7.6	15.8

Table 3: Relative particle velocity  $\delta u_p/U_b$  and magnitude of  $\hat{s}$  as function of the particle centre position  $z_p/h$  for spherical particles of radius  $a = h/2.25$  obtained from the numerical simulations.

$z_p/h$	0.50
$\delta u_p/U_b$	-0.52
$\hat{s} \times 10^{-1}$	2.1

approaches one wall or as the confinement increases, as the relative velocity  $\delta u_p$ . The resulting  $\hat{s}$ , quantifying the local velocity disturbance generated by one particle, along with the spatial dependence in the horizontal plane, allows for predictions of the far-field interactions of spheres. These will be examined in Section 6.

Finally, we return to the lubrication theory by showing some typical depth-average velocity field in Fig. 2 and the velocity decay in Fig. 3. As mentioned earlier, the lubrication theory is valid at horizontal distances larger than the height of the channel. Fig. 2 depicts the flow field due to a sphere of diameter equal to  $2/3$  of the channel height. The non-zero vertical vorticity outside the particle indicates the non-ideal structure of the depth-average flow, in contrast to the simple mass dipole of a disk (see Eq. 5). However, as the confinement increases, the disturbance velocity asymptotes the leading-order quadratic decay, as shown in Fig. 3.

## 6. Interactions

In this Section, we introduce equations that describe interactions of well-separated particles and solve them in some specific cases. We start by observing

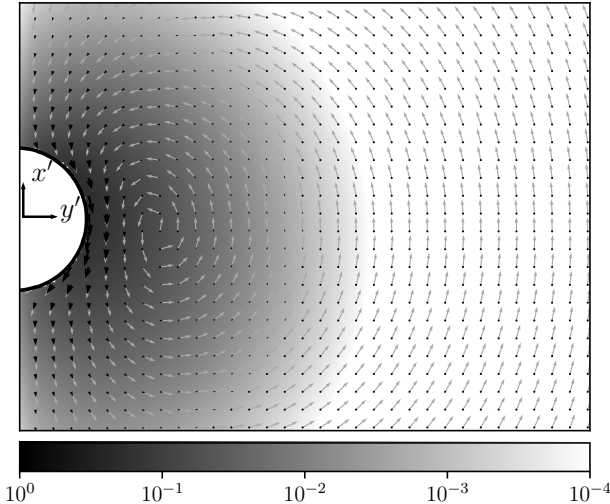


Figure 2: Depth-averaged disturbance flow around a sphere from the numerical simulations. The heavy arrows indicate the magnitude and light arrows the direction. The color in the background depicts the decay of the vorticity outside the sphere. The particle travels in the  $x'$  direction and is located at the mid-channel ( $z_p/h = 0.5$ ), with  $h/(2a) = 1.5$ . Only half of the plane is shown due to symmetry.

that because of the linearity of the problem, the steady state (horizontal) velocity  $\mathbf{v}_0$  of an isolated particle driven by the Poiseuille flow according to Eq. (2) is given by

$$\mathbf{v}_0 = -\hat{M}\nabla p^0, \quad (49)$$

where we assume  $\mathbf{v}_0$  is a function of  $\nabla p^0$  that can be any constant vector in the plane. Indeed,  $\mathbf{v}_0$  is a linear function of  $\nabla p^0$  that is zero when there is no driving flow. Since  $\hat{M}$  connects the velocity  $\mathbf{v}_0$  with the force per unit volume of the fluid, we call  $\hat{M}$  the mobility matrix though it differs from the more commonly used coefficient between the velocity and the force on the particle (Happel & Brenner 1983). The two-by-two mobility matrix  $\hat{M}$  depends on the shape of the particle, whether the particle is rigid or droplet, and the particle position in the channel. The equation neglects gravitational settling, absent for neutrally buoyant particles or particles whose sedimentation is stopped by interactions with the walls, (as the pancake-like droplets) or because settling is negligible at relevant time scales. In cases with sedimentation velocity  $\mathbf{v}_s$  so low that the particle stays in quasi-steady state we have,

$$\mathbf{v}_0 = -\hat{M}(t)\nabla p^0 + \mathbf{v}_s, \quad (50)$$

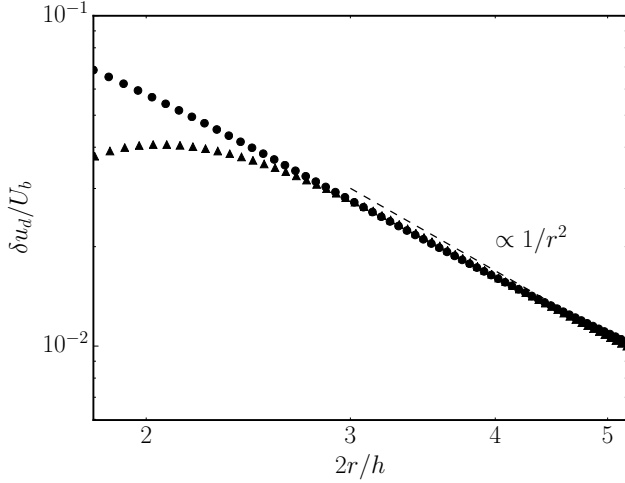


Figure 3: Spatial variation of the normalized streamwise depth-averaged disturbance-velocity,  $\delta u_d/U_b$ , along the streamwise ( $y = 0$ , circle) and spanwise ( $x = 0$ , triangle) directions away from the particle center. The particle is located at the mid-channel ( $z_p/h = 0.5$ ), with  $h/(2a) = 1.125$ . The collapse of the disturbance-velocity away from the particle confirms the leading-order dipolar decay (dashed line).

where the matrix  $\hat{M}(t)$  is determined by the instantaneous configuration in the channel, which may depend on time due to sedimentation.

We next consider interactions of many well-separated particles. The flow induced at the position of the  $i$ -th particle by the other particles is a quasi-Poiseuille flow,

$$\mathbf{u} = \frac{z(z-h)\nabla p}{2\eta}, \quad p = p^0 - \sum_{k \neq i} \frac{3}{\pi h^3} (\mathbf{s}_k \cdot \nabla) \ln |\mathbf{r} - \mathbf{r}_k|, \quad (51)$$

where  $\mathbf{r}_k$  is the horizontal position of the  $k$ -th particle, see Eqs. (21), (40). We observe that we can neglect variations of  $\nabla p$  over the particle since the rest of the particles are well-separated. Thus, at the leading order in large distances between the particles the  $i$ -th particle assumes the horizontal velocity,

$$\frac{d\mathbf{r}_i}{dt} = -\hat{M}_i \nabla \left( p^0 - \sum_{k \neq i} \frac{3}{\pi h^3} (\mathbf{s}_k \cdot \nabla) \ln |\mathbf{r} - \mathbf{r}_k| \right)_{\mathbf{r}=\mathbf{r}_i}, \quad (52)$$

where  $\hat{M}_i$  describes the geometry of the  $i$ -th particle. The sedimentation velocity can be included in a straightforward way. This is the equation that describes the long-range interactions of the particles. The presented derivation avoids the problem with boundary conditions encountered in the derivation of

Shani *et al.* (2014) for the case of droplets. In that case, the derivation started with the flow induced by other particles at the position of the  $i$ -th particle and not the pressure. Since for particles of finite extent it becomes non-obvious where the three-dimensional flow must be considered, our derivation seems to be useful for a proper consideration of particles whose vertical size is smaller than  $h$ .

We consider the case of spherical particles or droplets of radius  $a$  smaller than  $h/2$ . In this case  $\hat{M}_i$  is  $M(z_i)$  times the unit matrix where the scalar coefficient  $M$  depends on the vertical coordinate  $z_i$  of the  $i$ -th particle. Similarly  $s_k = s(z_k)\hat{x}$  where  $s(z)$  was introduced previously. We find,

$$\dot{\mathbf{r}}_i = -M(z_i)\nabla p^0 + \sum_{k \neq i} \frac{3M(z_i)s(z_k)}{\pi h^3 r_{ik}^2} \left[ \hat{\mathbf{x}} - \frac{2(\mathbf{r}_{ik} \cdot \hat{\mathbf{x}}) \mathbf{r}_{ik}}{r_{ik}^2} \right],$$

where  $\mathbf{r}_{ik} = \mathbf{r}_i - \mathbf{r}_k$ . Thus for pair of particles,

$$\dot{\mathbf{r}} = (M(z_1) - M(z_2))\nabla p^0 + \frac{3\delta_{12}}{\pi h^3 r^2} \left[ \hat{\mathbf{x}} - \frac{2x\mathbf{r}}{r^2} \right], \quad (53)$$

where  $\mathbf{r} = \mathbf{r}_2 - \mathbf{r}_1 = (x, y, z)$  and we introduced,

$$\delta_{12} = M(z_2)s(z_1) - M(z_1)s(z_2). \quad (54)$$

Another case when Eqs. (52) simplify significantly is for pancake-like droplets that almost completely fill the channel in the vertical direction. In this case  $M$  and  $s$  are constant since no variation of the vertical position of the particles is possible. We see immediately that the configuration of two droplets is stable in the dipole approximation where  $\dot{\mathbf{r}}$  in Eq. (53) is zero (in a higher-order quadrupole approximation proportional to  $r^{-3}$  the pair would not be stable). For many particles, the equations of motion in the frame that moves with the velocity of the isolated droplet  $-M\nabla p^0$  become,

$$\frac{d\mathbf{r}_i}{dt} = \sum_{k \neq i} \frac{q}{r_{ik}^2} \left[ \hat{\mathbf{x}} - \frac{2(\mathbf{r}_{ik} \cdot \hat{\mathbf{x}}) \mathbf{r}_{ik}}{r_{ik}^2} \right], \quad q = \frac{3Ms}{\pi h^3}. \quad (55)$$

These equations hold also for spherical particles located at the same distance from the mid-plane where we must use for  $M$  and  $s$  the values at the corresponding  $z$ . This is the case where the particles have identical vertical coordinate or their coordinates can be obtained by reflection with respect to the mid plane. Other cases of symmetric particles where Eq. (55) hold can be considered. If gravitational settling is relevant,  $\mathbf{r}_{ik}$  will change via time-dependent  $s = s(z(t))$ . It is assumed below that the change of  $s = s(z(t))$  can be neglected over the time scales of interest.

It is often the case that we have two spherical particles at the same vertical distance from the walls. This can be the case of spherical droplets created at some fixed place in the channel and then transported down the flow Shen *et al.* (2014). In this case, an isolated pair is stable in the dipole approximation: we have  $\dot{\mathbf{r}} = 0$  in Eq. (53) for  $z_1 = z_2$ .

This characterizes the basic property of the interaction given by Eq. (55), that the velocity induced by particle  $i$  at the position of the  $k$ -th particle is equal to the velocity induced by particle  $k$  at the position of the  $i$ -th particle. Thus the interparticle distances can change only if there are three or more particles. We can re-write the equation of motion as

$$\begin{aligned} \frac{d\mathbf{r}_{ik}}{dt} = & \sum_{l \neq i, l \neq k} \left( \frac{q}{r_{il}^2} \left[ \hat{\mathbf{x}} - \frac{2(\mathbf{r}_{il} \cdot \hat{\mathbf{x}}) \mathbf{r}_{il}}{r_{il}^2} \right] \right. \\ & \left. - \frac{q}{r_{kl}^2} \left[ \hat{\mathbf{x}} - \frac{2(\mathbf{r}_{kl} \cdot \hat{\mathbf{x}}) \mathbf{r}_{kl}}{r_{kl}^2} \right] \right). \end{aligned} \quad (56)$$

We start by considering in more detail the simplest case of two particles whose distance is constant in time. If the particles have the same  $y$ -coordinate then the  $x$ -coordinates obey,

$$\frac{dx_1}{dt} = \frac{dx_2}{dt} = -\frac{q}{(x_1 - x_2)^2}. \quad (57)$$

In this case the particles form a simple cluster with fixed distance that moves as a whole slower than the particles separately. We consider now two particles at different spanwise locations,  $y_1 = y$ ,  $y_2 = 0$ ,

$$\begin{aligned} \frac{dx_1}{dt} = \frac{dx_2}{dt} &= q \frac{(y_1 - y_2)^2 - (x_1 - x_2)^2}{[(x_1 - x_2)^2 + (y_1 - y_2)^2]^2}, \\ \frac{dy_1}{dt} = \frac{dy_2}{dt} &= -q \frac{2(x_1 - x_2)(y_1 - y_2)}{[(x_1 - x_2)^2 + (y_1 - y_2)^2]^2}. \end{aligned} \quad (58)$$

The RHSs are constant because inter-particle distances are but the velocity of the cluster of the two particles can change sign unlike the previous case. For two particles with the same  $x$  coordinate, the  $x$ - component of their velocity increases while the  $y$ -component is zero, see Shen *et al.* (2014) for experimental observations.

Next, we consider the simplest case with changing inter-particle distances: three particles at the same height. From the analysis of the two-particle dynamics, a possible solution is that particles form a cluster of two particles with the third farther away. The interactions of the single distant particle with the clustered particles decay quadratically with the distance and can be assumed negligible. Thus, the isolated particle moves with the velocity of one single sphere. The cluster keeps its configuration and moves at a constant velocity  $(q/r^2)[\hat{\mathbf{x}} - 2(\mathbf{r} \cdot \hat{\mathbf{x}}) \mathbf{r}/r^2]$  with respect to the third particle. If this velocity is such to increase the separation between the cluster and the third particle, this solution will continue ad infinitum. It is thus plausible to assume that any arbitrary initial configuration of three particles will separate asymptotically in one cluster and one particle. We will prove this below for the practically important case of three particles aligned in the streamwise,  $x$ -, direction. This case can be observed when the particles are injected in the flow at the same location.

The distances between three particles are determined by two vectors  $\mathbf{r}_{12}$  and  $\mathbf{r}_{13}$  that obey,

$$\begin{aligned}\dot{\mathbf{r}}_{12} &= \frac{q}{r_{13}^2} \left[ \hat{\mathbf{x}} - \frac{2(\mathbf{r}_{13} \cdot \hat{\mathbf{x}}) \mathbf{r}_{13}}{r_{13}^2} \right] - \frac{q}{r_{23}^2} \left[ \hat{\mathbf{x}} - \frac{2(\mathbf{r}_{23} \cdot \hat{\mathbf{x}}) \mathbf{r}_{23}}{r_{23}^2} \right], \\ \dot{\mathbf{r}}_{13} &= \frac{q}{r_{12}^2} \left[ \hat{\mathbf{x}} - \frac{2(\mathbf{r}_{12} \cdot \hat{\mathbf{x}}) \mathbf{r}_{12}}{r_{12}^2} \right] - \frac{q}{r_{23}^2} \left[ \hat{\mathbf{x}} - \frac{2(\mathbf{r}_{23} \cdot \hat{\mathbf{x}}) \mathbf{r}_{23}}{r_{23}^2} \right].\end{aligned}\quad (59)$$

The solution described above pertaining the cluster of two particles (named here 2 and 3) and the faraway particle 1 corresponds to neglecting the first terms in the RHSs,

$$\dot{\mathbf{r}}_{12} \approx \dot{\mathbf{r}}_{13} \approx -\frac{q}{r_{23}^2} \left[ \hat{\mathbf{x}} - \frac{2(\mathbf{r}_{23} \cdot \hat{\mathbf{x}}) \mathbf{r}_{23}}{r_{23}^2} \right] \approx \text{const}, \quad (60)$$

where  $\mathbf{r}_{23}$  is approximately constant. At large times the constant vector  $\mathbf{r}_{23}$  has become much smaller than the linearly growing  $\mathbf{r}_{12}$  and  $\mathbf{r}_{13}$ . We have that  $\mathbf{r}_{23} = \mathbf{r}_{13} - \mathbf{r}_{12}$  obeys the equation,

$$\dot{\mathbf{r}}_{23} = \frac{q}{r_{12}^2} \left[ \hat{\mathbf{x}} - \frac{2(\mathbf{r}_{12} \cdot \hat{\mathbf{x}}) \mathbf{r}_{12}}{r_{12}^2} \right] - \frac{q}{r_{13}^2} \left[ \hat{\mathbf{x}} - \frac{2(\mathbf{r}_{13} \cdot \hat{\mathbf{x}}) \mathbf{r}_{13}}{r_{13}^2} \right],$$

where the RHS decays quadratically with time, in agreement with the assumption of constant  $\mathbf{r}_{23}$ .

We prove that the separation of 3 particles into one binary cluster and one isolated particle holds for arbitrary initial conditions when all three particles lie on the same line in the  $x$ -direction. It is clear that the separation can occur in two ways in this case: either particles 1 and 2 form a cluster or 2 and 3. Here we assume the ordering  $x_1 > x_2 > x_3$ . As the cluster moves slower than the isolated particle, the third particle would catch up with the binary cluster, made of 1 and 2. Hence the only stable configuration is a cluster of particles 2 and 3 whose distance from particle 1 increases linearly with time due to the cluster deceleration. Formally,

$$\begin{aligned}\dot{x}_{12} &= -q \left( \frac{1}{x_{13}^2} - \frac{1}{(x_{13} - x_{12})^2} \right), \\ \dot{x}_{13} &= -q \left( \frac{1}{x_{12}^2} - \frac{1}{(x_{13} - x_{12})^2} \right).\end{aligned}$$

Introducing  $x = x_{12}$  and  $r = x_{13}/x_{12}$  where  $r > 1$ , we can write

$$\begin{aligned}\dot{x} &= -\frac{q}{x^2} \left( \frac{1}{r^2} - \frac{1}{(r-1)^2} \right) = -\frac{q(1-2r)}{x^2 r^2 (r-1)^2}, \\ \dot{x} + \frac{x\dot{r}}{r} &= -\frac{q}{x^2} \left( \frac{1}{r} - \frac{1}{r(r-1)^2} \right).\end{aligned}\quad (61)$$

The distance  $r$  obeys,

$$\begin{aligned} x^3 \dot{r} &= -q \left( 1 - \frac{1}{(r-1)^2} \right) + q \left( \frac{1}{r} - \frac{r}{(r-1)^2} \right) \\ &= -\frac{q(r-1)}{r} - \frac{q}{r-1} = -\frac{q(r^2-r+1)}{r(r-1)}. \end{aligned} \quad (62)$$

Hence  $r(t)$  decreases in time monotonously and we can write

$$\begin{aligned} \frac{d \ln x}{ds} &= q \left( \frac{1}{(r-1)^2} - \frac{1}{r^2} \right), \\ \frac{dr}{ds} &= -\frac{q(r^2-r+1)}{r(r-1)}, \quad \frac{ds}{dt} = \frac{1}{x^3(t)}. \end{aligned} \quad (63)$$

We can solve for  $s(r)$ ,

$$\begin{aligned} \frac{ds}{dr} &= -\frac{1}{q} + \frac{1}{q(r^2-r+1)}, \quad s(r) = \frac{r_0 - r}{q} \\ &+ \frac{2}{q\sqrt{3}} \arctan \left( \frac{2r-1}{\sqrt{3}} \right) - \frac{2}{q\sqrt{3}} \arctan \left( \frac{2r_0-1}{\sqrt{3}} \right), \end{aligned} \quad (64)$$

where  $r_0 = r(s=0)$ . The inversion of this formula, to find  $r(s)$ , gives a transcendental equation. However, the asymptotic properties of the solution can be derived without solving the equation. When  $s$  increases,  $r$  decreases reaching  $r = 1$  at a finite value  $s = s_*$  where,

$$s_* = \frac{r_0 - 1}{q} + \frac{\pi}{3q\sqrt{3}} - \frac{2}{q\sqrt{3}} \arctan \left( \frac{2r_0 - 1}{\sqrt{3}} \right). \quad (65)$$

The situation of  $r$  reaching 1 would correspond to coalescence of the second and the third particles. This happens only asymptotically, as  $s = s_*$  corresponds to infinite physical time,  $t(s_*) = \infty$ . We have directly from Eq. (64) that  $s'(r=1) = 0$  and  $s'' = (1-2r)/[q(r^2-r+1)^2]$  which gives,

$$\begin{aligned} s(r) &\approx s_* + (r-1)s'(r=1) + \frac{(r-1)^2 s''(r=1)}{2} \\ &= s_* - \frac{(r-1)^2}{2q}, \quad (r-1)^2 = 2q(s_* - s). \end{aligned} \quad (66)$$

We can find  $x$  as a function of  $r$  observing that,

$$\frac{d \ln x}{dr} = \frac{d \ln x}{ds} \frac{ds}{dr} = - \left( \frac{1}{r-1} + \frac{1}{r} \right) \frac{1}{r^2-r+1}. \quad (67)$$

Integration of the above gives (with  $x_0 = x(t=0)$ ),

$$\ln \left( \frac{x}{x_0} \right) = \ln \frac{r_0(r_0-1)}{r_0^2-r_0+1} - \ln \frac{r(r-1)}{r^2-r+1}, \quad (68)$$

where we used,

$$\int \left( \frac{1}{r-1} + \frac{1}{r} \right) \frac{1}{r^2-r+1} dr = \ln \frac{r(r-1)}{r^2-r+1}. \quad (69)$$

We find from Eq. (68) that,

$$x = x_0 \frac{r_0(r_0 - 1)(r^2 - r + 1)}{r(r - 1)(r_0^2 - r_0 + 1)}. \quad (70)$$

In the limit of large times where  $r$  approaches 1 from above we have,

$$x \approx \frac{r_0(r_0 - 1)x_0}{(r - 1)(r_0^2 - r_0 + 1)} \approx \frac{r_0(r_0 - 1)x_0}{(r_0^2 - r_0 + 1)\sqrt{2q(s_* - s)}}, \quad (71)$$

where we used Eq. (66). Finally we restore the physical time using,

$$\frac{dt}{ds} = x^3(s) \approx \frac{r_0^3(r_0 - 1)^3 x_0^3}{(r_0^2 - r_0 + 1)^3 (2q)^{3/2} (s_* - s)^{3/2}}, \quad (72)$$

and obtain,

$$t(s) \approx \frac{r_0^3(r_0 - 1)^3 x_0^3}{q(r_0^2 - r_0 + 1)^3 \sqrt{2q(s_* - s)}}. \quad (73)$$

We conclude from Eqs. (66), (71) that the long-time asymptotic form of the solution is,

$$x(t) = \frac{qt(r_0^2 - r_0 + 1)^2}{r_0^2(r_0 - 1)^2 x_0^2}, \quad r(t) = 1 + \frac{x_0^3 r_0^3 (r_0 - 1)^3}{qt(r_0^2 - r_0 + 1)^3}. \quad (74)$$

This implies that the distance between the second and the third particles reaches a constant value at large times,

$$\begin{aligned} x_{23}(t) &= x(t)(r(t) - 1) \approx \frac{x_0 r_0 (r_0 - 1)}{r_0^2 - r_0 + 1} \\ &= \frac{x_{13}(0)x_{23}(0)x_{12}(0)}{x_{13}(0)x_{23}(0) + x_{12}^2(0)}. \end{aligned} \quad (75)$$

To conclude, we can write,

$$x(t) = \frac{qt}{x_{23}^2}, \quad (76)$$

in agreement with the form given by Eq. (60). This relation proves the separation in cluster and faraway particle and provides the distance between the particles in the cluster as function of the initial conditions.

The obtained formulas provide a theoretical explanation for the pair exchange observed in the experiments by Shen *et al.* (2014), and confirmed by numerical simulations as illustrated in Fig. 4. We consider initial conditions for which particles 1 and 2 are close and the third particle is trailing behind. In this case  $x_{12}^2(0) \ll x_{13}(0), x_{23}(0)$  and Eq. (75) becomes,

$$x_{23}(t) = x_{12}(0). \quad (77)$$

Thus, for long times the distance between the third and the second particle becomes equal to the initial distance between the first and the second particle, that is an exchange takes place.

We can also prove the separation in one cluster and one faraway particle for initial conditions where the particles are "almost" aligned, i.e.  $y_{12}$  and  $y_{13}$

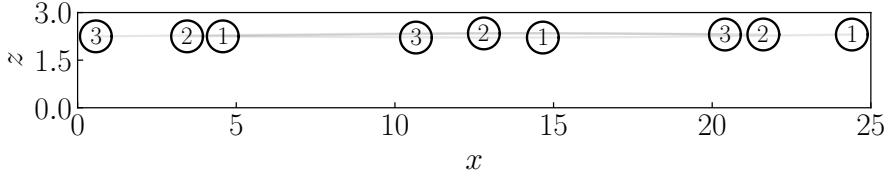


Figure 4: Pair exchange phenomenon as obtained from numerical simulations. Initially particles 1 are 2 are close and particle 3 is trailing behind the pair. As a result of hydrodynamic interactions the trailing particle is catching up with the pair, while the leading particle breaks away from the newly formed pair, whereas the trailing particles 2 and 3 are separated by the same distance as 1 and 2 were initially.

are much smaller than the smallest of  $x_{12}$  and  $x_{13}$ . If the  $y$ -components of the particle positions are linearly ordered, the equations for  $x_{ik}$  do not change and the evolution of  $x_{ik}$  is as above. The  $y$ -components obey,

$$\begin{aligned}\dot{y}_{12} &= -\frac{2qy_{13}}{x_{13}^3} + \frac{2qy_{23}}{(x_{13} - x_{12})^3}, \quad \dot{y}_{23} = \frac{2qy_{13}}{x_{13}^3} - \frac{2qy_{12}}{x_{12}^3} \\ \dot{y}_{13} &= -\frac{2qy_{12}}{x_{12}^3} + \frac{2qy_{23}}{(x_{13} - x_{12})^3},\end{aligned}\tag{78}$$

where  $x_{ik}(t)$  are determined from the previous solution. Since  $x_{12}$ ,  $x_{13}$  grow linearly with time at large times then the asymptotic form of the solution is,

$$y_{12} = y_{13} = \frac{2qct}{x_0^3}, \quad y_{23} = c = \text{const.}$$

This solution indicates that the first particle separates from the binary cluster at constant small but finite angle  $\phi$  with respect to the  $x$ -direction given by,

$$\phi = \frac{y_{12}}{x_{12}} \approx \frac{y_{13}}{x_{13}} \approx \frac{c}{x_0 \sqrt{2}},\tag{79}$$

Self-consistency with the assumption of smallness of  $y_{ik}$  demands that  $c \ll x_0$ . This assumption can be guaranteed by the smallness of the initial conditions on  $y_{ik}$  because of the linearity of the equations in  $y_{ik}$ .

Thus we demonstrated the for initial conditions where the particles are aligned in the  $x$ -direction, or almost aligned, the solution at large times takes the form of a cluster of particles 2 and 3, those two initially upstream, with constant distance  $r_{23}$  and the first particle separating from the cluster according to Eq. (60).

We formulate the hypothesis that any arbitrary initial configuration of three particles will lead at large times to a binary cluster and the third particle linearly separating from it. It seems that the evolution from any arbitrary initial conditions cannot be solved analytically, but only numerically: a reduction from

four to three degrees of freedom can be obtained, but the resulting equations could not be solved.

To conclude, we describe the properties of cluster solutions assuming constant  $\mathbf{r}_{23}$ , of magnitude  $r_{23}$ , and angle  $\phi$  with respect to the  $x$ -axis. Using Eq. (60), we write

$$\dot{x}_{12} \approx \dot{x}_{13} \approx \frac{q \cos(2\phi)}{r_{23}^2}, \quad \dot{y}_{12} \approx \dot{y}_{13} \approx \frac{q \sin(2\phi)}{r_{23}^2}.$$

We can assume with no loss of generality that  $x_2 \geq x_3$  so that  $\phi$  is in the range  $-\pi/2 \leq \phi \leq \pi/2$ . Four different solutions can therefore be identified, assuming the cluster at large time can be denoted as a point at the origin. In the range  $0 \leq \phi \leq \pi/4$  the first particle leaves the cluster behind when going to infinity inside the first quadrant. In the range  $-\pi/4 \leq \phi \leq 0$ , the first particle leaves the cluster behind when going to infinity inside the second quadrant. In the case of  $\pi/4 \leq \phi \leq \pi/2$  the cluster leaves the first particle behind and to the right. Finally in the case of  $-\pi/2 \leq \phi \leq -\pi/4$  the cluster leaves the first particle behind and to the left.

It is clear from the above that the configuration with distant pairs or singlets of particles is stable: the singlets separate ballistically from the stable pairs which maintain the pair distance constant. In contrast, clusters of three and probably more particles are unstable. Thus, we conjecture that under arbitrary initial conditions an arbitrary number of distant particles will separate at large times into a collection of singlets and pairs if the solution is dilute. For suspensions of many particles this implies that hydrodynamic interactions increase the probability of particles to be isolated or in pairs, rather than forming clusters composed of many particles. In dense suspensions, the interactions discussed above do not have time to occur and we rather expect chaotic collisions of particles (Shani *et al.* 2014).

## 7. Concluding remarks

In the present paper, we provided a boundary integral representation for the flow due to particles (rigid ones or droplets) freely-suspended in a channel flow. The particle number, size and shape and the inter-particle distances are arbitrary. We have thus demonstrated the utility of this representation.

For an isolated particle, the proposed representation is useful for the study of the far-field flow. At the leading order, the far flow is dipolar flow with the dipole moment given by a weighted integral of the stress tensor and the flow over the particle surface. This defines the far flow completely. The flow was previously available only for strongly confined pancake-like droplets that almost block the channel in the vertical direction. We also determine the dipole moment integral numerically for neutrally buoyant rigid sphere. Further, we provide the multipole expansion from which the far flow can be found with any desired accuracy.

For close particles, the representation is helpful for the study of hydrodynamic interactions. It demonstrates clearly that the range of validity of the lubrication theory is larger than expected from the usual approach (Batchelor 1967; Tavakol *et al.* 2017; Szeri 2005; Bruce 2012). Our representation also solves the problem of matching the ideal flow holding far from the particles with the fully viscous flow near the particle surface. The solution is expressed in terms of the unknown surface velocity and stress tensor. This sheds light on the use of the ideal flow approximation in previous works on disk-like particles (Shani *et al.* 2014; Sarig *et al.* 2016) and helps to consider particles of other shapes.

We introduced the equation of motion of particles interacting at long distances, refining previous derivation for droplets (Shani *et al.* 2014) and extending it to the case of arbitrary, possibly different, interacting particles. We solved the three-body problem of hydrodynamic interactions for the case of identical symmetric particles aligned in the stream-wise direction. This solution provides theoretical support for the pair exchange phenomenon observed previously in experiments (Shen *et al.* 2014). We provide special solutions for the three-body problem and demonstrate that it is plausible that these solutions describe the long-time asymptotic evolution for arbitrary initial conditions. We further demonstrate the application of the theory to the many body problem.

We did not consider potential lateral migration induced by hydrodynamic interactions. It can be readily seen that a pair of distant spherical particles with different vertical coordinates will separate laterally because the coordinate-dependent mobility matrices and dipole moments will differ for these particles. The study of this instability will be the object of future work.

The representation proposed here is a good starting point for a mean-field description of strong hydrodynamic interactions of close particles. We notice after Eq. (15) that the effect of the interactions can be described by a change of the stress-tensors and velocities at the particle surfaces. Thus the model description of the interaction boils down to the model description of surface stress tensors and velocity. This can be done by introducing the mean field  $\nabla p$  whose direction can differ from the direction of the undisturbed flow. We assume that the stress tensor and flow on the surface of each particle is that for an isolated particle in the Poiseuille flow with pressure gradient  $\nabla p$  (e.g., the particle velocity is equal to minus the mobility matrix times  $\nabla p$ ). Using this in Eq. (15) one can find the flow in terms of  $\nabla p$ . A closed integral equation for  $\nabla p$  can then be obtained from the Stokes flow equations. The study of this equation is planned as future work.

This study was majorly motivated by recent experiments on the formation of droplet clusters in a microfluidic channel (Shen *et al.* 2014, 2016a). The theoretical modeling in Shen *et al.* (2016a) assumed that flow-assisted clustering of weakly confined spherical droplets in close proximity is driven by the combination of non-hydrodynamic (adhesive, e.g., depletion forces) and hydrodynamic interactions of dipolar nature similar to interactions of strongly confined

(pancake-like) droplets in Hele-Shaw cells. The qualitative agreement between the results of the numerical simulations and experimental results in Shen *et al.* (2016a) suggested that *ad hoc* modeling of hydrodynamic interactions by dipolar flow is admissible. The present study shows that far-field interactions of weakly confined droplets are indeed of dipolar nature, however their magnitude is too weak to lead to relative motion between freely suspended particles on the time scale of the experiment. Moreover, the present study, as well as the calculations of the interactions at small distances in Beatus *et al.* (2012); Sarig *et al.* (2016), suggest that hydrodynamic interactions at close proximity cannot be described by dipolar flows. We thus believe that the reason for the qualitative agreement between the numerical results and the experiment (using unknown magnitude of the adhesive forces as an adjustable parameter) is that the adhesive force diverges at contact dominating the particle dynamics. The dipolar hydrodynamic interactions provided the source of sliding (tangential) motions of the particles necessary for the particle rearrangement and not provided by the adhesive (radial) forces. However, the particular functional form (e.g., dipolar or other) of these interactions seems to be of minor importance as long as these provide some tangential mobility. An accurate *quantitative* predictive theory of flow-assisted clustering requires the knowledge of the near-field hydrodynamic interactions, including an accurate treatment of the non-uniform flow near the inlet. This will be the object of a future work.

## Acknowledgement

The work is supported by the Microflusa project. The Microflusa project receives funding from the European Union Horizon 2020 research and innovation programme under Grant Agreement No. 664823.

## Appendix A. Calculation of the far-field term $f_l(\mathbf{x}_0)$

In this appendix, we present a direct calculation of the far-field term  $f_l(\mathbf{x}_0)$  in Eq. (12). We find from volume integration of Eq. (11) the boundary term,

$$\begin{aligned}
f_l(\mathbf{x}_0) = & \frac{1}{8\pi\eta} \int_{-L}^L dy \int_0^h dz [S_{il}(L - x_0, y - y_0, z, z_0) \\
& \sigma_{ix}(L, y, z) - S_{il}(-L - x_0, y - y_0, z, z_0)\sigma_{ix}(-L, y, z)] \\
& + \frac{1}{8\pi\eta} \int_{-L}^L dx \int_0^h dz [S_{il}(x - x_0, L - y_0, z, z_0) \\
& \sigma_{iy}(x, L, z) - S_{il}(x - x_0, -L - y_0, z, z_0)\sigma_{iy}(x, -L, z)] \\
& - \frac{1}{8\pi} \int_{-L}^L dy \int_0^h dz [T_{ilx}(L - x_0, y - y_0, z, z_0)u_i(L, y, z) \\
& - T_{ilx}(-L - x_0, y - y_0, z, z_0)u_i(-L, y, z)] - \frac{1}{8\pi} \\
& \times \int_{-L}^L dx \int_0^h dz [T_{ily}(x - x_0, L - y_0, z, z_0)u_i(x, L, z) \\
& - T_{ily}(x - x_0, -L - y_0, z, z_0)u_i(x, -L, z)]; \quad L \rightarrow \infty.
\end{aligned}$$

The Stokeslet decays exponentially in the  $z$ -direction so  $f_z = 0$ . To find the remaining components we use

$$\sigma_{ix}(L, y, z) = -L\nabla_x p^0 \delta_{ix} + \frac{(2z - h)\nabla_x p^0 \delta_{iz}}{2}. \quad (80)$$

We find that  $f_x$  is determined by the asymptotic solution for channel flow and is not affected by the presence of the spherical particle,

$$\begin{aligned}
f_x(\mathbf{x}_0) = & -\frac{L\nabla_x p^0}{8\pi\eta} \int_{-L}^L dy \int_0^h dz [S_{xx}(L, y - y_0, z, z_0) \\
& + S_{xx}(-L, y - y_0, z, z_0)] \\
& - \frac{\nabla_x p^0}{8\pi\eta} \int_{-L}^L dx \int_0^h dz [S_{yx}(x - x_0, L, z, z_0) \\
& - S_{yx}(x - x_0, -L, z, z_0)] \\
& - \frac{1}{8\pi} \int_{-L}^L dy \int_0^h dz \frac{z(z - h)\nabla_x p^0}{2\eta} [T_{xxx}(L, y - y_0, z, z_0) \\
& - T_{xxx}(-L, y - y_0, z - z_0)] \\
& - \frac{1}{8\pi} \int_{-L}^L dx \int_0^h dz \frac{z(z - h)\nabla_x p^0}{2\eta} [T_{xxy}(x - x_0, L, z, z_0) \\
& - T_{xxy}(x - x_0, -L, z - z_0)]; \quad L \rightarrow \infty. \quad (81)
\end{aligned}$$

Thus, this must be the unperturbed channel flow as readily verified. Rescaling the integration variable by  $L$  and keeping leading order terms we have,

$$\begin{aligned}
 f_x(\mathbf{x}_0) = & -\frac{L^2 \nabla_x p^0}{8\pi\eta} \int_{-1}^1 dy \int_0^h dz [S_{xx}(L, Ly, z, z_0) \\
 & + S_{xx}(-L, Ly, z, z_0)] \\
 & -\frac{L^2 \nabla_x p^0}{8\pi\eta} \int_{-1}^1 dx \int_0^h dzx [S_{yx}(Lx, L, z, z_0) \\
 & - S_{yx}(Lx, -L, z, z_0)] \\
 & -\frac{L}{8\pi} \int_{-1}^1 dy \int_0^h dz \frac{z(z-h)\nabla_x p}{2\eta} [T_{xxx}(L, Ly, z, z_0) \\
 & - T_{xxx}(-L, Ly, z - z_0)] \\
 & -\frac{L}{8\pi} \int_{-1}^1 dx \int_0^h dz \frac{z(z-h)\nabla_x p}{2\eta} [T_{xxy}(Lx, L, z, z_0) \\
 & - T_{xxy}(Lx, -L, z - z_0)]. \tag{82}
 \end{aligned}$$

So far the calculation involved the complete Stokeslet solution. To determine  $f_l$  we can use the asymptotic form of the Stokeslet at large distances, which is for the stress tensor,

$$T_{ilk} = -24 \frac{r_l}{\rho^2} (z_0/h^2) (1 - z_0/h) \delta_{ik} + O\left(\frac{1}{\rho^2}\right). \tag{83}$$

Using these formulas for  $S_{ik}$  and  $T_{ilk}$ , one can write

$$\begin{aligned}
 f_x = & \frac{\nabla_x p^0}{8\pi\eta} \int_{-1}^1 dy \int_0^h dz \frac{24z(z-h)z_0(z_0-h)(y^2-1)}{(1+y^2)^2 h^3} \\
 & -\frac{\nabla_x p}{4\pi\eta} \int_{-1}^1 dx \int_0^h dzx^2 \left[ \frac{24z(z-h)z_0(z_0-h)}{(1+x^2)^2 h^3} \right] \\
 & -\frac{1}{4\pi} \int_{-1}^1 dy \int_0^h dz \frac{z(z-h)\nabla_x p}{2\eta} \left[ 24 \frac{z_0(z_0-h)}{(1+y^2)h^3} \right].
 \end{aligned}$$

Integrating over  $z$ , this can be written as,

$$\begin{aligned}
 f_x = & \frac{\nabla_x p z_0(z_0-h)}{2\eta} \left( \int_{-1}^1 \frac{dy}{\pi(1+y^2)} \left[ \frac{2}{1+y^2} - 1 \right] \right. \\
 & \left. + \frac{1}{\pi} \int_{-1}^1 dx \frac{2x^2}{(1+x^2)^2} + \frac{1}{\pi} \int_{-1}^1 dy \left[ \frac{1}{(1+y^2)} \right] \right). \tag{84}
 \end{aligned}$$

Performing the integrals we confirm that indeed  $f_x$  is the flow given by Eq. (1).

## Appendix B. Numerical integration of $s$

We compute the weighted dipole moment  $\mathbf{s}$  in Eq. (39) by directly simulating a rigid spherical particle of radius  $a$  transported in a doubly-periodic channel using the immersed boundary method (IBM), see Breugem (2012); Lambert *et al.* (2013); Picano *et al.* (2015) for more details and validations.

In the IBM, there are two meshes; one Eulerian mesh for the flow and one Lagrangian mesh for the moving particle. The two meshes are coupled through a multidirect forcing scheme that ensures the approximate no-slip/no-penetration condition on the particle surface.

The motion of the particle is described by the Newton-Euler equations, given for the translational velocity by Eq. (47)). The equation does not contain the gravitational force which is assumed to be balanced either by the particle interactions with the bottom wall (the case of particle near the wall) or by buoyancy (the case of density-matched particle). We also assume that particle-wall collisions are absent (*cf.* Eq. (3a) in Breugem (2012)).

The flow outside the particle is governed by the incompressible Navier-Stokes (NS) equations with the no-slip boundary conditions on the surface of the rigid particle described in connection with Eq. (2). Although the steady state flow obeys the Stokes equations, computation of the transients demands inclusion of the time derivative in the NS equations. In our simulations, the full NS equations are computed at a small Reynolds number ( $\sim 10^{-1}$ ), *viz.*

$$Re \left( \frac{\partial \mathbf{u}}{\partial t} + \nabla \cdot (\mathbf{u} \mathbf{u}) \right) = \nabla \cdot \boldsymbol{\sigma} + \mathbf{f}, \quad (85)$$

where  $Re = \rho_f U_b (2a)/\eta$  is the Reynolds number,  $U_b$  the channel bulk velocity,  $\rho_f$  ( $= \rho_p$ ) the fluid density and  $\mathbf{f}$  the IBM force enforcing that the no-slip boundary condition (in this formulation pressure is rescaled by  $Re$ .) We discretize these equations using a second-order finite volume scheme. Finding the flow at given translational and rotational particle velocities we obtain the viscous stress which is used for updating these velocities as in Eq. (47). Numerically, the LHS of Eq. (47) is computed at each time step by summing the forces exerted on all the Lagrangian points, in addition to the volumetric forces inside the particle (see Eq. (8a) in Breugem (2012) for the full expression). In our case, this is simply

$$m \frac{d\mathbf{v}}{dt} \approx - \sum_{l=1}^{N_l} \mathbf{F}_l \Delta V_l + \rho_f \frac{d}{dt} \left( \int_{V_p} \mathbf{u} dV \right), \quad (86)$$

where  $-\mathbf{F}_l$  the force acting on the  $l$  Lagrangian point centred at a shell element of volume  $\Delta V_l$ , and  $N_l$  the total number of Lagrangian points.

At the steady state,

$$\int_S \boldsymbol{\sigma} \cdot d\mathbf{S} \approx - \sum_{l=1}^{N_l} \mathbf{F}_l \Delta V_l, \quad (87)$$

corresponding to the solution of the steady state the Stokes equations, Eq. (2).

Provided that the interpolation and spreading between  $\mathbf{f}_{i,j,k}$  and  $-\mathbf{F}_l$  preserves the local stress, we obtain the dimensionless weighted dipole moment  $\tilde{\mathbf{s}}$  needed to compute particle interactions as

$$\tilde{\mathbf{s}} = - \sum_{l=1}^{N_l} z_l (h - z_l) \mathbf{F}_l \Delta V_l. \quad (88)$$

The dimensional  $s$  is thus  $\eta U_b(2a)^3 \tilde{s}$ .

## REFERENCES

- BATCHELOR, G. 1967 *An introduction to fluid dynamics*. Cambridge University Press.
- BEATUS, T., BAR-ZIV, R. H. & TLUSTY, T. 2012 The physics of 2d microfluidic droplet ensembles. *Physics Reports* **516** (3), 103 – 145, the physics of 2D microfluidic droplet ensembles.
- BEATUS, T., TLUSTY, T. & BAR-ZIV, R. H. 2006 Phonons in a one-dimensional microfluidic crystal. *Nat. Phys.* **2**, 743.
- BHATTACHARYA, S., BLAWZDZIEWICZ, J. & WAJNRYB, E. 2006 Hydrodynamic interactions of spherical particles in poiseuille flow between two parallel walls. *Physics of Fluids* **18** (5), 053301.
- BRETHERTON, F. P. 1962 The motion of rigid particles in a shear flow at low reynolds number. *Journal of Fluid Mechanics* **14** (2), 284–304.
- BREUGEM, W.-P. 2012 A second-order accurate immersed boundary method for fully resolved simulations of particle-laden flows. *Journal of Computational Physics* **231** (13), 4469 – 4498.
- BRUCE, R. W. E. 2012 *Handbook of Lubrication and Tribology*. Cambridge University Press.
- ACUÑA CAMPA, H., CARBAJAL-TINOCO, M. D., ARAUZ-LARA, J. L. & MEDINA-NOYOLA, M. 1998 Collective dynamics in quasibidimensional colloidal suspensions. *Phys. Rev. Lett.* **80**, 5802–5805.
- CARBAJAL-TINOCO, M. D., CRUZ DE LEÓN, G. & ARAUZ-LARA, J. L. 1997 Brownian motion in quasibidimensional colloidal suspensions. *Phys. Rev. E* **56**, 6962–6969.
- COHEN, I., MASON, T. G. & WEITZ, D. A. 2004 Shear-induced configurations of confined colloidal suspensions. *Phys. Rev. Lett.* **93**, 046001.
- CUI, B., DIAMANT, H., LIN, B. & RICE, S. A. 2004 Anomalous hydrodynamic interaction in a quasi-two-dimensional suspension. *Phys. Rev. Lett.* **92**, 258301.
- DURLOFSKY, L. J. & BRADY, J. F. 1989 Dynamic simulation of bounded suspensions of hydrodynamically interacting particles. *Journal of Fluid Mechanics* **200**, 39–67.
- GRADSHTEYN, I. S. & RYZHIK, I. M. 2014 *Table of integrals, series, and products*. Academic press.
- HAPPEL, J. & BRENNER, H. 1983 *Low Reynolds number hydrodynamics: with special applications to particulate media*. The Hague: Martinus Nijhoff Publishers.
- JACKSON, J. D. 1962 *Classical electrodynamics*. John Wiley and Sons.
- LAMBERT, R. A., PICANO, F., BREUGEM, W.-P. & BRANDT, L. 2013 Active suspensions in thin films: nutrient uptake and swimmer motion. *Journal of Fluid Mechanics* **733**, 528–557.
- LANÇON, P., BATROUNI, G., LOBRY, L. & OSTROWSKY, N. 2001 Drift without flux: Brownian walker with a space-dependent diffusion coefficient. *Europhysics Letters (EPL)* **54** (1), 28–34.
- LANDAU, L. D. & LIFSHITZ, E. M. 1987 *Fluid mechanics*.
- LEAL, L. 2007 *Advanced transport phenomena: fluid mechanics and convective transport processes*. Cambridge University Press.
- LEVICH, V. 1977 *Physicochemical hydrodynamics*. Advance Publications.

- LIRON, N. & MOCHON, S. 1976 Stokes flow for a stokeslet between two parallel flat plates. *Journal of Engineering Mathematics* **10** (4), 287–303.
- MARCUS, A. H., SCHOFIELD, J. & RICE, S. A. 1999 Experimental observations of non-gaussian behavior and stringlike cooperative dynamics in concentrated quasi-two-dimensional colloidal liquids. *Phys. Rev. E* **60**, 5725–5736.
- MORRIS, J. & BRADY, J. 1998 Pressure-driven flow of a suspension: Buoyancy effects. *International Journal of Multiphase Flow* **24** (1), 105 – 130.
- MORRIS, J. F. 2001 Anomalous migration in simulated oscillatory pressure-driven flow of a concentrated suspension. *Physics of Fluids* **13** (9), 2457–2462.
- NOTT, P. R. & BRADY, J. F. 1994 Pressure-driven flow of suspensions: simulation and theory. *Journal of Fluid Mechanics* **275**, 157–199.
- PESCHÉ, R. & NÄGELE, G. 2000a Stokesian dynamics study of quasi-two-dimensional suspensions confined between two parallel walls. *Phys. Rev. E* **62**, 5432–5443.
- PESCHÉ, R. & NÄGELE, G. 2000b Stokesian dynamics study of quasi-two-dimensional suspensions confined between two parallel walls. *Phys. Rev. E* **62**, 5432–5443.
- PICANO, F., BREUGEM, W.-P. & BRANDT, L. 2015 Turbulent channel flow of dense suspensions of neutrally buoyant spheres. *Journal of Fluid Mechanics* **764**, 463–487.
- POZRIKIDIS, C. 1992 *Boundary integral and singularity methods for linearized viscous flow*. Cambridge University Press.
- SANTANA-SOLANO, J. & ARAUZ-LARA, J. L. 2001 Hydrodynamic interactions in quasi-two-dimensional colloidal suspensions. *Phys. Rev. Lett.* **87**, 038302.
- SANTANA-SOLANO, J. & ARAUZ-LARA, J. L. 2002 Short-time dynamics of colloidal particles confined between two walls. *Phys. Rev. E* **65**, 021406.
- SARIG, I., STAROSVETSKY, Y. & GAT, A. D. 2016 Interaction forces between microfluidic droplets in a hele-shaw cell. *Journal of Fluid Mechanics* **800**, 264–277.
- SHANI, I., BEATUS, T., BAR-ZIV, R. H. & TLUSTY, T. 2014 Long-range orientational order in two-dimensional microfluidic dipoles. *Nature Phys.* **10**, 140–144.
- SHEN, B., LEMAN, M., REYSSAT, M. & TABELING, P. 2014 Dynamics of a small number of droplets in microfluidic hele–shaw cells. *Experiments in Fluids* **55** (5), 1728.
- SHEN, B., RICOUVIER, J., MALLOGGI, F. & TABELING, P. 2016 Designing colloidal molecules with microfluidics. *Advanced Science* **3** (6), 1600012.
- SINGH, A. & NOTT, P. R. 2000 Normal stresses and microstructure in bounded sheared suspensions via stokesian dynamics simulations. *Journal of Fluid Mechanics* **412**, 279–301.
- STABEN, M. E., ZINCHENKO, A. Z. & DAVIS, R. H. 2003 Motion of a particle between two parallel plane walls in low-reynolds-number poiseuille flow. *Physics of Fluids* **15** (6), 1711–1733.
- SWAN, J. W. & BRADY, J. F. 2010 Particle motion between parallel walls: Hydrodynamics and simulation. *Physics of Fluids* **22** (10), 103301.
- SZERI, A. Z. 2005 *Fluid film lubrication: theory and design*. Cambridge University Press.
- TAVAKOL, B., HOLMES, D. P., FROEHLICHER, G. & STONE, H. A. 2017 Extended lubrication theory: Improved estimates of flow in channels with variable geometry. *ArXiv* (1403.2343).

- TLUSTY, T. 2006 Screening by symmetry of long-range hydrodynamic interactions of polymers confined in sheets. *Macromolec* **39**, 3927.



# Paper 3

3



# Flow-assisted droplet assembly in a 3D microfluidic channel

Zhouyang Ge, Outi Tammisola, Luca Brandt

Linné FLOW Centre and SeRC, KTH Mechanics, S-100 44 Stockholm, Sweden

*Soft Matter* (2019), vol. **15**, 3451–3460

Self-assembly of soft matter, such as droplets or colloids, has become a promising scheme to engineer novel materials, model living matter, and explore non-equilibrium statistical mechanics. In this article, we present detailed numerical simulations of few non-Brownian droplets in various flow conditions, specifically, focusing on their self-assembly within a short distance in a three-dimensional (*3D*) microfluidic channel, cf. Shen *et al.* (2016a). Contrary to quasi two-dimensional (*q2D*) systems, where dipolar interaction is the key mechanism for droplet rearrangement, droplets in *3D* confinement produce much less disturbance to the underlying flow, thus experiencing weaker dipolar interactions. Using confined simple shear and Poiseuille flows as reference flows, we show that the droplet dynamics is mostly affected by the shear-induced cross-stream migration, which favors chain structures if the droplets are under an attractive depletion force. For more compact clusters, such as three droplets in a triangular shape, our results suggest that an inhomogeneous cross-sectional inflow profile is further required. Overall, the accelerated self-assembly of a small-size droplet cluster results from the combined effects of strong depletion forces, confinement-mediated shear alignments, and fine-tuned inflow conditions. The deterministic nature of the flow-assisted self-assembly implies the possibility of large throughputs, though calibration of all different effects to directly produce large droplet crystals is generally difficult.

---

## 1. Introduction

Recent advances in colloidal science have generated a growing interest in the fabrication of functional materials, especially those possessing photonic band gaps (Ho *et al.* 1990; Subramanian *et al.* 1999; Seelig *et al.* 2003; Wong *et al.* 2003; Shen *et al.* 2016b). Colloids – particles or droplets of (sub-)micron scale – are manipulated with high precision to self-organize into controlled patterns, which then form a library of basic building blocks for more complex structures (Sacanna & Pine 2011). Conceivably, such direct assembly is also the most efficient mechanism for material synthesis. Colloidal self-assembly has thus become a promising scheme to engineer novel materials, mimicking the machinery of nature (van Blaaderen 2003).

Currently, there are many strategies to synthesize colloidal building blocks, e.g. creating a short-range depletion potential in a microwell (Meng *et al.* 2010), exploiting shape/surface anisotropy of the colloids (Sacanna & Pine 2011; Evers *et al.* 2016), using patterned substrates as templates (Yin *et al.* 2001), or even jamming droplets with a micro-mixer (Ricouvier *et al.* 2017). Among these, *flow-assisted* self-assembly seems especially appealing, since the microfluidic droplets are driven by an external flow rather than Brownian motions, reducing the range of assembly time from days down to seconds (c.f. the experiment of (McMullen *et al.* 2018) as an example). With the potential of being optimized and applied in parallel, microfluidics appears to be the fastest pathway towards photonic material generation.

Following this approach, Shen *et al.* (2016b) recently demonstrated the generation and self-assembly of droplet strings into a rich variety of (non-)compact structures, including chains, triangles, diamonds, crosses, etc. . in a simple microfluidic device (see Fig. 1). Unlike most previous studies (Cui *et al.* 2004; Beatus *et al.* 2006; Janssen *et al.* 2012; Uspal *et al.* 2013; Desreumaux *et al.* 2013; Zhu & Gallaire 2016), where droplets under strong confinement interact via dipolar flows (Beatus *et al.* 2017; Diamant 2009), these droplets are smaller than the smallest dimension of the microfluidic channel. Specifically, the droplets are tens to hundreds microns in diameter, while the channel height is about three times larger. As a consequence, typical quasi two-dimensional ( $q2D$ ) arguments do not apply, and the dynamics is fully three-dimensional ( $3D$ ). In the latter case, the complete Navier-Stokes (or Stokes) equations have to be solved to obtain a correct physical understanding of the system,<sup>2</sup> wherein prior simulations mainly focus on the deformation and migration of a single drop, or an evenly spaced array of drops (Couliette & Pozrikidis 1998; Griggs *et al.* 2007; Janssen & Anderson 2007). Interestingly, assuming a tunable far-field dipolar interaction, Shen *et al.* (2016b) could however model the droplet motions up to a “semiquantitative” level, reproducing the sophisticated self-assembly observed in experiments. This apparent contradiction motivates us to pursue a detailed numerical study of the relatively fast droplet self-assembly in order to investigate the interactions in their microfluidic channel.

In the following, we first present a numerical methodology for the dynamics of two viscous fluids, including a hydrodynamic model for the near-field depletion force, a localized attractive force between suspending droplets. Applying this methodology, we then show results of extensive simulations of two to ten droplets in quiescent, shear-, and pressure-driven channel flows, each of which isolating an individual effect contributing to the self-assembly. Here, the focus is on the clustering and droplet interactions within a short distance from their initial release rather than the production of the droplets, which has been studied previously Chakraborty *et al.* (2017). Our aim is to elucidate the physical

---

<sup>2</sup>A notable exception is the dynamics of two droplets in unbounded linear flows solved analytically by Batchelor & Green (1972b).

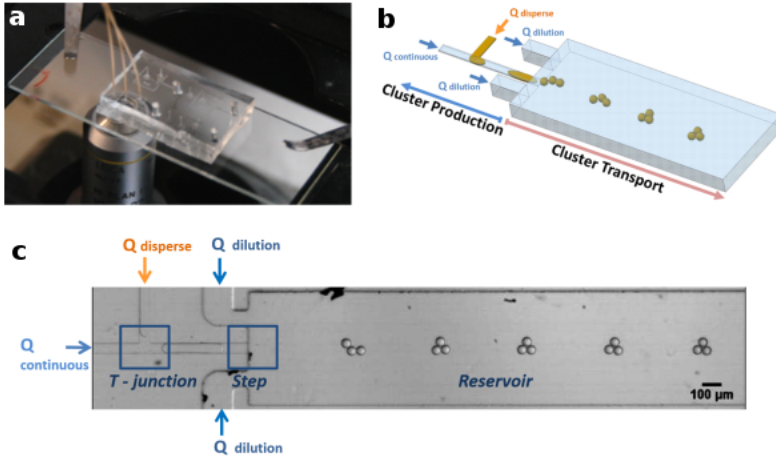


Figure 1: (a) Photo of a microfluidic channel placed above a desktop microscope. (b) Schematic of the channel geometry and generation of the droplet clusters. The main channel has a typical dimension of ( $50 \mu\text{m} \times 600 \mu\text{m} \times 5000 \mu\text{m}$ ) in height, width, and length; hence, it can be considered as a Hele-Shaw cell. (c) Bottom view of the droplet self-assembly observed from the microscope. Pictures courtesy of Dr. Joshua Ricouvier. For more details, see Shen *et al.* (2016b).

picture of the hydrodynamic interactions, potentially improving the design of more efficient microfluidic systems.

## 2. Models and methods

### 2.1. Hydrodynamic model

The dynamics of two immiscible, Newtonian fluids in incompressible flows is governed by the Navier-Stokes equations

$$\nabla \cdot \mathbf{u} = 0, \quad (1a)$$

$$\frac{\partial \mathbf{u}}{\partial t} + \mathbf{u} \cdot \nabla \mathbf{u} = \frac{1}{\rho_i Re} \left( -\nabla p + \nabla \cdot [\mu_i (\nabla \mathbf{u} + \nabla \mathbf{u}^T)] \right) + \frac{\mathbf{g}}{Fr}, \quad (1b)$$

where  $\mathbf{u}$ ,  $p$ ,  $\mathbf{g}$ ,  $\rho_i$  and  $\mu_i$  denote the non-dimensional velocity, pressure, unit gravitational vector, density, and dynamic viscosity, respectively. Eq. (1b) is written for each fluid component,  $i$  ( $= 1$  for the carrier fluid,  $2$  for the droplet), requiring a pressure boundary condition across the fluid interface

$$p_2 - p_1 = \frac{\kappa}{Ca}, \quad (2)$$

with  $\kappa$  being the mean curvature (the contribution due to the viscosity difference is neglected assuming matching viscosity (Batchelor 1967)).

So far, we have introduced three non-dimensional numbers:  $Re$ ,  $Ca$ , and  $Fr$ , denoting the Reynolds, capillary, and Froude numbers, separately. Choosing fluid 1 as the reference phase, they are defined as

$$Re = \frac{\tilde{\rho}_1 \tilde{U} \tilde{L}}{\tilde{\mu}_1}, \quad Ca = \frac{\tilde{\mu}_1 \tilde{U}}{\tilde{\sigma}}, \quad Fr = \frac{\tilde{U}^2}{\tilde{g} \tilde{L}}, \quad (3)$$

where  $\tilde{U}$ ,  $\tilde{L}$ ,  $\tilde{\rho}_1$ ,  $\tilde{\mu}_1$ ,  $\tilde{\sigma}$ , and  $\tilde{g}$  denote the reference *dimensional* velocity, length, density, dynamic viscosity, surface tension, and gravitational acceleration. Following the experiments in Shen *et al.* (2016b), typical values of the reference velocity and length are  $\tilde{U} \sim 100 \text{ } \mu\text{m/s}$  and  $\tilde{L} \sim 100 \text{ } \mu\text{m}$ , leading to  $Re \sim 10^{-2}$ ,  $Ca \sim 10^{-5}$ , and  $Fr \sim 10^{-5}$  for oil-water systems. Therefore, inertial (but not gravitational) effects are negligible and the droplets shall remain mostly spherical. In the simulations that we are going to present, however, these numbers are enlarged within reasonable physical limits also to reduce the computation time. Specifically,  $Re$  has been increased up to 10 in most cases except those in Sec. 3.2 (where  $Re = 1$ ) and those in Sec. 3.3.2 (where  $Re = 0.1$ );  $Ca$  is in the order of  $10^{-3} \sim 10^{-2}$  depending on the  $Re$ ; whereas  $Fr = 0.025$  if gravity is enabled (otherwise  $\infty$ ). In general, the Reynolds number cannot be arbitrarily increased as it is proportional to the fluid inertia. The reason we *can* increase it here is essentially due to the uniformity of the underlying flow. In this case, the mere effect of further reducing the  $Re$  is stretching the time scale, making the computations significantly longer. We have tested all cases at smaller  $Re$ 's to ensure that the differences are negligible in the case of fully developed Couette and Poiseuille flows. This is discussed in more details in Appendix A.

Finally, we note that the surface tension can also vary due to temperature or surfactant concentration gradients, leading to Marangoni stress along the surface. The detailed chemistry is rather complex Eastoe & Dalton (2000); in the present paper, we assume constant and uniform surface tension  $\tilde{\sigma}$  to reduce the number of the governing parameters.

## 2.2. Depletion theory

Droplets suspended in an ambient fluid dissolved by surfactant molecules typically experience an attractive depletion force. The first model to describe such interaction was proposed by Asakura & Oosawa (1958), who assumed the surfactant micelles to be non-interacting hard spheres. As sketched in Fig. 2, a suspension of such small spheres around the large colloidal droplets creates an osmotic pressure on the droplet surface. When the distance between two droplets is less than the diameter of the surfactant micelles, the pressure defect due to the exclusion of the micelles pulls the drops even closer, corresponding to an attractive force. Integrating this force with respect to the inter-droplet distance  $r$  leads to a potential energy

$$U(r) = \begin{cases} \infty & \text{if } r \leqslant 2R \\ -p_{os} V_{ex} & \text{if } 2R < r \leqslant 2R + 2r_s \\ 0 & \text{otherwise,} \end{cases} \quad (4)$$

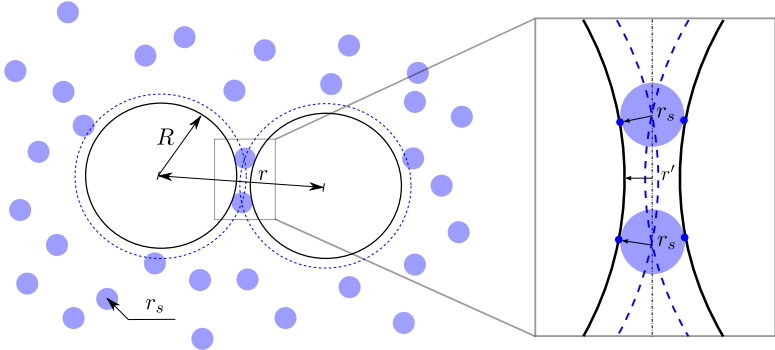


Figure 2: Depletion of surfactant micelles of radius  $r_s$  between larger colloidal droplets of radius  $R$ , separated by distance  $r$ . The dashed lines around larger spheres represent the region from which the centers of small spheres are excluded. They overlap when  $r \leq 2R + 2r_s$ . Inset: a zoom-in sketch of two droplets near contact.

where  $V_{ex}$  is the excluded volume and  $p_{os}$  is the osmotic pressure. For spherical droplets,  $V_{ex}$  can be calculated analytically

$$V_{ex}(r) = \frac{4\pi(R + r_s)^3}{3} \left[ 1 - \frac{3r}{4(R + r_s)} + \frac{r^3}{16(R + r_s)^3} \right], \quad (5)$$

where  $R$  and  $r_s$  are, respectively, the radii of the big and small spheres. The osmotic pressure is given as

$$p_{os} = nkT, \quad (6)$$

where  $n$  is the number density of the small spheres,  $k$  the Boltzmann constant, and  $T$  the temperature. The negative sign in Eq. (4) corresponds to the tendency of the system to reduce its potential energy as the overlap increases. This is equivalent to increasing the total entropy of the small spheres (Melby *et al.* 2007), and it provides a physical description of the depletion force even when the droplets are deformable, or when  $p_{os}$  cannot be expressed by the van't Hoff's formula (Eq. (6)) (Asakura & Oosawa 1958).

Based on the above theory, we consider the depletion potential in the hydrodynamic model by adding an osmotic pressure,  $p'(r')$ , near the overlap region ( $r'$  being the normalized distance to the droplet surface, see Fig. 2). Specifically, we write  $p'$  as a Taylor-series expansion from  $r' = r_s$

$$p'(r'/r_s) = p'(1) + \left( \frac{r'}{r_s} - 1 \right) \frac{\partial p'}{\partial r'/r_s}, \quad (7)$$



Figure 3: (left) Two droplets approaching in a quiescent flow, and (right) close-up of the flows in the gap due to the depletion force.

with a constant  $\partial p'/\partial(r'/r_s)$  satisfying the original depletion force acting on one droplet, i.e.

$$-p_{os}A_{ex} = \int_{\Omega} (p'(1) - p'(r'/r_s))dS, \quad (8)$$

where  $A_{ex}$  is the effective area of the overlap  $\Omega$ . Note that, in this formulation, we do not require  $p_{os}$  to be a thermodynamic pressure; instead, its strength can be defined by a non-dimensional number

$$\Pi = \frac{p_{os}}{\kappa/Ca}, \quad (9)$$

which normalizes  $p_{os}$  by the Laplace pressure due to surface tension. Doing so, the osmotic pressure varies continuously within the overlap and depends linearly on  $r'$ . An expansion of the osmotic pressure with the distance corresponds to a gradient of the micelle concentration near the gap; and if the micelle is much smaller than the droplet, as it is in the microfluidic device of interest (Shen *et al.* 2016*b*), the gradient will be very sharp. Conversely, when the distance to the surface varies slowly, such as in the gap of a squeezed droplet and a flat wall, a uniform pressure will be recovered. In essence, what we propose here is a method to model the osmotic pressure as an equivalent mechanical pressure such that a favorable pressure gradient from the center of the overlap region generates an outflow, pulling the droplets towards each other. This is clearly illustrated in Fig. 3, where two droplets approach each other due to the locally induced depletion flow.

### 2.3. Numerical methods

The above governing equations are solved numerically using the interface-correction level set/ghost fluid method (ICLS/GFM) (Ge *et al.* 2018). The equations are discretized in space by the finite volume method, and integrated in time using the second-order Adam-Bashforth scheme. Combining several computational techniques, including the fast pressure correction method (Dodd & Ferrante 2014), the GFM (Fedkiw *et al.* 1999), and the fast Fourier transform (FFT) (Schumann & Sweet 1988), discontinuous quantities are treated sharply

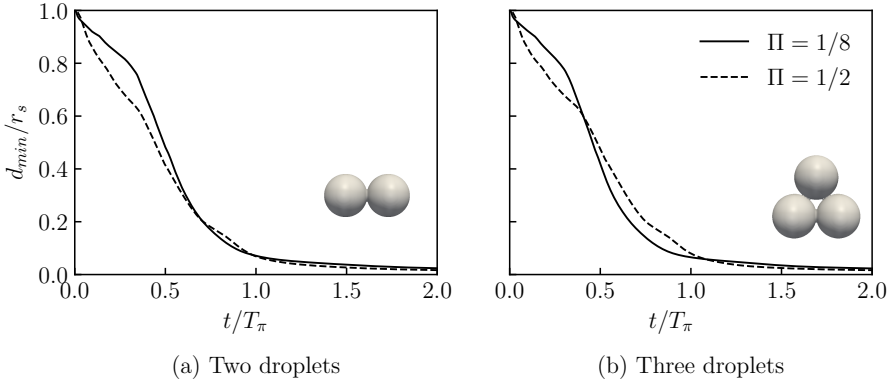


Figure 4: Minimal distance between the droplet surfaces as function of time in the presence of depletion forces proportional to  $\Pi = 1/8$  (solid line) and  $\Pi = 1/2$  (dashed line). Simulation of (a) two droplets and (b) three droplets suspended in an initially quiescent fluid. Due to symmetry, only the minimal distance is plotted.

at high efficiency. For the detailed algorithm and validations, we refer to Ge *et al.* (2018). The source code is also publicly available on GitHub (Ge 2018).

### 3. Results

In the following, we present simulation results of droplet motions in three types of flows: quiescent, shear-, and pressure-driven channel flows. In the last case, both Poiseuille flows and a non-uniform channel flow are considered. The purpose of using different flow types is to disentangle the effects of the depletion force, the droplet-droplet hydrodynamic interaction, and the droplet-flow interaction. The simpler cases can be seen as model problems towards understanding of the more complex motions of droplet ensembles in realistic microfluidic devices.

#### 3.1. Approaching droplets in quiescent flows

##### 3.1.1. 2 and 3 droplets

The simplest case of droplet self-assembly is identical drops approaching in quiescent flows, i.e. no external flow motions. In such a case, the remaining fluid parameters can be grouped into two non-dimensional numbers, i) the Laplace number  $La = \tilde{\sigma} \tilde{\rho}_1 (2\tilde{R}) / \mu_1^2$ , where  $\tilde{R}$  is the droplet radius; and ii) the osmotic-to-Laplace pressure ratio  $\Pi = p_{os}/p$ .<sup>3</sup>  $La$  relates surface tension to

<sup>3</sup>The density and viscosity ratios between the drop and the carrier fluids are assumed to be unity. See Appendix A for the detailed numerical setup.

the viscous stress, which can also be expressed as  $La = Re/Ca$ .  $\Pi$  indicates the magnitude of the uniform osmotic pressure  $p_{os}$  due to depletion of the surfactant micelles, scaled by a reference Laplace pressure  $p$  due to surface tension (cf. Eq. (9)). In the following, we assume  $La = 2000$  and  $\Pi = 1/8$  or  $1/2$ , corresponding to the limit  $Ca \ll Re \ll 1$  and conditions above the critical micelle concentrations (CMC, see dimensional analysis below) as in the experiments (Shen *et al.* 2016*b*).

The approach of two and three droplets is illustrated in Fig. 4, where the minimal distance between the droplet surfaces  $d_{min}$ , normalized by the surfactant micelle radius  $r_s$ , is shown as a function of time. Here, time is re-scaled by the factor  $T_\pi = \tilde{r}_s/(\tilde{R}\Pi)$  to account for the size contrast of the droplet and the surfactant micelle, thus indicating an inverse scaling of the approaching time with the osmotic pressure for inertialess droplets, i.e.  $T \propto \Pi^{-1}$ . Indeed, for both  $\Pi = 1/8$  and  $1/2$ , our results show that  $d_{min}$  approaches the limit of the grid spacing at  $t \approx T_\pi$ . The smooth approach in both cases and the collapse of the distance curves thus verify our modeling of the near field chemical interaction, consistent with an attracting depletion force.

We note that  $T_\pi$  is not a physical time scale (it is dimensionless). One possible definition for the depletion time scale is  $\tilde{\tau}_\pi = \tilde{r}_s \tilde{\mu}_1 / (\tilde{R} \tilde{p}_{os})$ , which can be rewritten as  $T_\pi Ca \tilde{\tau}$ , with a convection time scale  $\tilde{\tau} = 2\tilde{R}/\tilde{U}$  in the range of 0.1 to 1 s typically. By substitution of usual values of colloidal systems, e.g.  $\tilde{r}_s = 1 \text{ nm}$ ,  $\tilde{\mu}_1 = 10^{-3} \text{ kg/m-s}$ ,  $\tilde{R} = 10 \mu\text{m}$ , and  $\tilde{p}_{os} = 100 \text{ Pa}$  (corresponding to surfactant micelles concentration of 5 CMC, see Shen (2014), p112), the estimated time scale is 1 ns. Although  $\tilde{\tau}_\pi$  can be amplified by increasing the viscosity of the suspending fluid or reducing the micelles concentration, its magnitude is so small that the approaching can be considered instantaneous. Therefore, in practical microfluidic devices such as those in Shen *et al.* (2016*b*), one cannot expect to detect the dynamical approaching process due to depletion forces. The droplets will appear either bound or separated, depending on the surfactant concentration and flow conditions.

### 3.1.2. 4 to 10 droplets

To further demonstrate the effect of the depletion force, we “virtually” assemble four to ten droplets under various initial configurations to form stable clusters as illustrated in Fig. 5. These clusters can be either 2D or 3D, exhibiting different levels/kinds of symmetry. In our simulations, the shape of the cluster is solely determined by the initial droplet arrangement, in the absence of any disturbance or other driving forces. Permitting disturbances, such as vibrations or thermal noises, would eventually lead to the formation of “rigid clusters”, i.e. clusters that cannot be reshaped by a small amount of inter-droplet displacement. Analytically, the number of possible rigid clusters grows rapidly with the number of droplets ( $N$ ). For example, there is only one possible rigid cluster for  $N = 4$ , while there are 259 possibilities for  $N = 10$ , for packing of  $3N - 6$  contacts

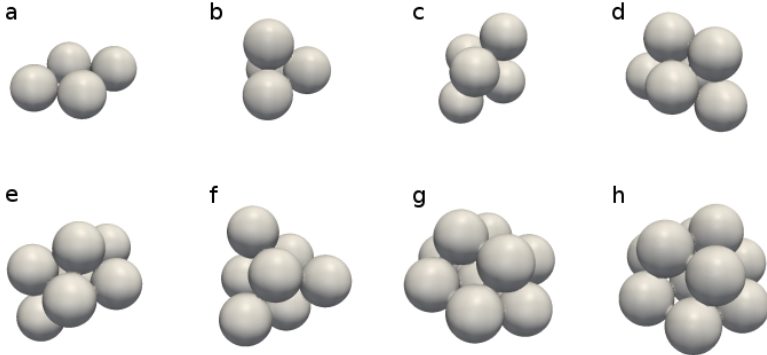


Figure 5: Packing of  $N$  droplets due to the near field depletion force. (a-b)  $N = 4$ , (c)  $N = 5$ , (d)  $N = 6$ , (e)  $N = 7$ , (f)  $N = 8$ , (g)  $N = 9$ , (h)  $N = 10$ .

(Holmes-Cerfon 2016). For brevity, we only illustrate two examples for  $N = 4$  (including one planar cluster) and one example for  $N = 5$  to 10 in Fig. 5.

We remind that the specific coordinates of the sphere packings bear no more significance than other possibilities in our simulations. They are arbitrarily chosen to illustrate the self-assembly due to the near field attraction. This is not the case for trapped equilibrium clusters, where less symmetric geometries are found to be favored by the entropic depletion force (Meng *et al.* 2010; Klein *et al.* 2018). Nor is it similar to colloidal particles interacting via short-range attractive, long-range repulsive potentials, where complex phase transitions emerge depending on the competition of the interactions (Mani *et al.* 2014; Das *et al.* 2018). Here, the self-assembly is microfluidic-based, driven by the hydrodynamics rather than the minimization of free energy over long periods. We examine the effect of the flow next.

### 3.2. Sticky droplets in shear-driven channel flows

When the droplets are carried by an external flow, their interactions are undoubtedly affected by the flow conditions, droplet-flow interactions and flow-induced droplet-droplet interactions (Fouxon *et al.* 2017). To study these additional effects, we consider an elementary flow field, the wall-bounded simple shear flow, defined as  $(u, v, w) = (0, \dot{\gamma}z, 0)$  for  $z \in [-L_z/2, L_z/2]$ . Here,  $v$  is the only non-zero velocity component, its magnitude varies linearly with the  $z$  coordinate, and  $\dot{\gamma}$  is the shear rate (see Fig. 6a). The presence of droplets will locally modify this flow field, which we sustain by enforcing opposite motions of two moving plates at  $z = \pm L_z/2$ .

Dating back to Taylor (1934), the deformation and motion of single or multiple droplet(s)/particle(s) have been studied extensively in simple shear flows (Lin *et al.* 1970; Batchelor & Green 1972*b,a*; Zinchenko 1983, 1984;

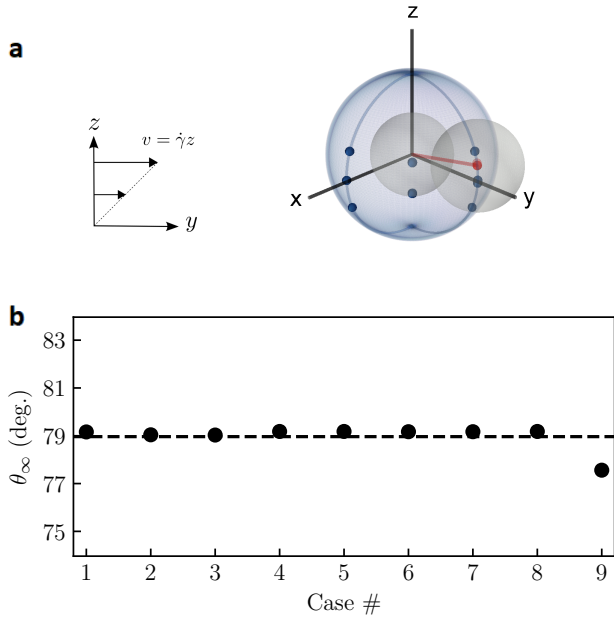


Figure 6: Stable configuration of a droplet pair in the simple shear flow. (a) Spherical diagram of the initial (blue dots) and final (red dots) positions of the second droplet in the reference frame of the first droplet. The blue arcs mark the border of the first quadrant where nine initial positions are considered. The undisturbed flow is a simple shear in the  $yz$  plane. (b) Steady-state polar angle,  $\theta_\infty$ , corresponding to the cases in Table 1. The average value is 79 deg. (dashed line). The stable azimuthal angle is identically 0.

Zurita-Gotor *et al.* 2007). In the case of spherical particles/droplets, previously identified interaction modes include closed trajectories (particles rotate around each other in the vorticity plane), open-and-symmetric trajectories (particles return to their original  $z$  positions after passing each other), and swapping trajectories (particles exchange the  $z$  position after a binary encounter). The first two modes are generic features of a dilute suspension of particles or non-deforming/non-coalescing droplets, while the last mode arises when the particles are under relatively large geometric confinement. Conceivably, adding a near-field depletion force shall not alter these three modes as it is only activated at nearly touching, when the particles are already in a bound pair. What is yet to be explored, however, is when the gap between the two confining plates is smaller than the sum of the particle diameters (i.e.  $L_z/D < 2$ ), thus disabling the occurrence of the Batchelor-Green type of closed orbit.

Table 1: Initial polar ( $\theta$ ) and azimuthal ( $\phi$ ) angles of the second droplet in the reference frame of the first droplet.  $\theta$  and  $\phi$  are measured from the  $z$ - and  $x$ -axes, respectively (see Fig. 6(a)).

Case #	1	2	3	4	5	6	7	8	9
$\theta$ (deg.)	70	70	70	89	89	89	91	110	110
$\phi$ (deg.)	90	45	0	90	45	0	90	90	0

Fig. 6(a) illustrates various initial conditions of two touching droplets, corresponding to the nine cases listed in Table 1, at  $L_z/D = 1.5$ . Specifically, the initial positions of the second droplet is given in the spherical coordinates centered at the first one, where all cases are located in one quadrant-sphere as we do not distinguish between the two droplets (the rest are equivalent due to symmetry). Contrary to the less confined conditions where a bound pair would rotate indefinitely relative to each other under shear (Batchelor & Green 1972b; Zinchenko 1984), Fig. 6 shows that the droplets tend to reside in the vorticity plane (i.e. the  $yz$  plane) with a stable polar angle  $\theta_\infty \approx 79$  deg. This is true even if the two droplets are not initially in the same vorticity plane (case 2,3,5,6,9), or if the second droplet is in the lower hemisphere relative to the first one (case 7,8,9). Particularly, in cases 8 and 9, the droplet pair first rotates clockwise, then slides along the wall, before finally reaching the stable orientation (see ESI Video 1). The anomalous trajectory is a clear evidence of the influence of the walls, which, together with the attractive depletion force, break the symmetry of the droplet binary interactions.

The above results suggest that, for two droplets subject to an attractive depletion force in strongly confined simple shear flows, only one configuration is dynamically stable. It further implies that, for multiple droplets ( $N > 2$ ) traveling in a pressure-driven channel with  $H/D < 4$  ( $H$  being the channel height, see Sec. 3.3), a chain-like structure oriented in the flow direction is expected. We remark that the precise configuration of the droplet cluster may depend on the flow conditions and the level of confinement (see Appendix B for further discussion); however, the *qualitative* picture of the pairwise interaction shall remain unchanged, provided that the number of contact is  $N - 1$ . As this is often the case before a compact cluster is formed, we proceed to examine the droplet self-assembly in pressure-driven flows.

### 3.3. Droplet clusters in pressure-driven channel flows

In the following, clusters of three or four droplets are initialized to be in contact ( $N - 1$  contacts for  $N$  droplets) and are released into different regions of a microfluidic channel to study their transport behavior. The production of these droplets is omitted, as the step-emulsifier is typically much smaller than the size of the channel, allowing for separation of the two processes (Shen 2014; Chakraborty *et al.* 2017). We note that, although the droplets are already in a

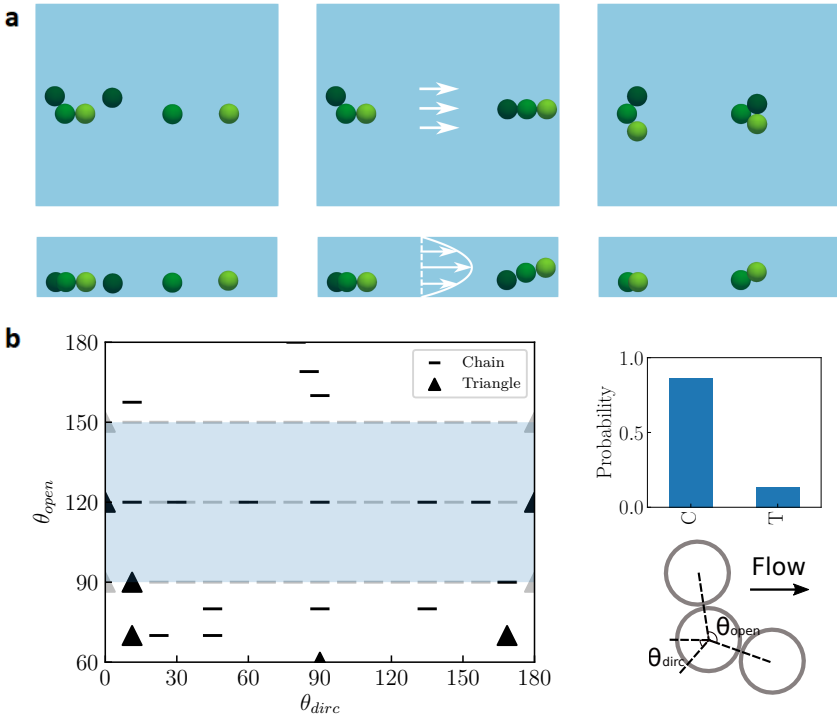


Figure 7: Three droplets in the Poiseuille flow. (a) Top (upper panels) and side (lower panels) views of the droplet positions. The droplets are colored differently only for visualization purposes. Left: without any depletion force (scattered droplets). Middle: with depletion force (forming a chain). Right: with depletion force (forming a triangle due to a different initial configuration). (b) Phase diagram showing the final configuration of three droplets under depletion force.  $\theta_{open}$  and  $\theta_{dirc}$  denote the initial opening and the direction angles (see inset for illustration). Interpolating the results for  $\theta_{open} \in [90, 150]$  (shaded region), chain is clearly the predominant structure as shown in the probability distribution.

cluster initially, their relative rearrangement is still important as it determines the cluster morphology in the final state. The latter results primarily from the droplet-flow interaction and has direct consequence on the photonic properties of the droplet lattice, as we will discuss in details below.

### 3.3.1. Uniform region (the Poiseuille flow)

First, we consider droplet clusters in a Poiseuille flow; that is, we place the droplets in a channel whose undisturbed velocity is given as  $(u, v, w) = (0, 6z/H(1 - z/H), 0)$ , with the channel height  $H = 3D$ . As in the simple

shear flow, the droplets are neutrally buoyant, and  $x, y, z$  denote the spanwise, streamwise, and wall-normal directions, respectively. Enforcing periodic boundary conditions in both  $x$  and  $y$  directions, the flow can be computed efficiently using FFT, approximating the flow field far from the edges of the Hele-Shaw channel (see Fig. 1b).

As a control case, we simulate three droplets initially located near the bottom of the channel without any depletion forces. This is shown in the first column of Fig. 7a, where the top and bottom panels illustrate the top and side views of the channel (see Fig. 1). The two snapshots are separated by 13.5 convection time units (i.e.  $\tilde{\tau}$ ). Clearly, the droplets quickly scatter as carried by the flow. In a previous work, we theoretically predicted the emergence of singlets and pairs of a dilute particle suspension due to weak particle-particle interactions (Fouxon *et al.* 2017). This example illustrates the separation of a droplet cluster, enhanced by their initial proximity already at  $N = 3$ , supporting our theoretical predictions.

In contrast, when the droplets are bound by a strong depletion force, the same initial condition can lead to a chain structure oriented in the flow direction, see the second column of Fig. 7a. Inspection of the side view reveals the apparent reason: the leading droplets migrate towards the middle of the channel due to the shear, thus experiencing faster flows; the attractive depletion force prevents the cluster from separating into singlets and pairs, yielding the eventual droplet string parallel to the stream. We propose that this shear-induced alignment mechanism is fundamentally due to the confinement-mediated pairwise interaction discussed in the previous section. The difference is that the Poiseuille flow has no simple analytical solution in the presence of droplets (hence the two cannot be compared exactly), and the confinement requirement is halved due to the symmetry of the parabolic velocity profile.

To further test the robustness of the shear-alignment mechanism, we consider multiple initial configurations of the triplet in the same flow. As sketched in Fig. 7b, three touching droplets whose centers are in the same  $xy$  plane can be completely described by two angles:  $\theta_{open}$ , denoting the opening angle of the triplet, and  $\theta_{dir_c}$ , denoting the angle between the bisector of the triplet and the direction of the undisturbed flow. For identical droplets, admissible angles are  $\theta_{open} \in [60, 180]$  deg., and  $\theta_{dir_c} \in [0, 180]$  deg. Extensive tests show that the chain structure is far more favorable than the closed triangular cluster in Poiseuille flows (see Fig. 7b). One case of the triangle cluster is visualized in the third column of Fig. 7a, where two droplets initially on the sides migrate towards the center, eventually leading to the closure of the open chain. In the vast majority of the cases, however, a straight droplet string aligned with the flow is observed, even if they are close to a triangle initially (note the small  $\theta_{open}$  cases in Fig. 7b).

The above results confirm that the chain-like structure is indeed the predominant configuration of droplets bound by short-range depletion forces in the Poiseuille flow. Experimentally, this corresponds to strong diluting flows at the

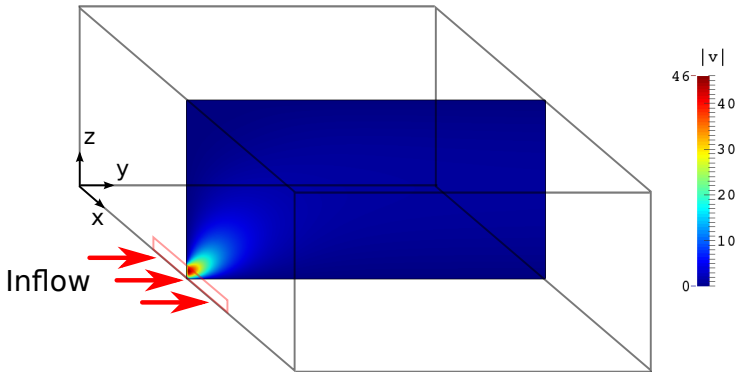


Figure 8: Cross-section of the channel inlet and magnitude of the initial velocity field at the central plane without droplets. The flow is injected from the step-emulsifier (red rectangle), where the droplets (not shown) are produced, into the channel (cf. Fig. 1b). The velocity is normalized such that  $|v| = 1$  corresponds to the bulk flow velocity averaged over the entire channel.

channel inlet, where long droplet strings are also observed further downstream (see Shen (2014), p137). More importantly, our simulations suggest that aligning of the droplets is a 3D shear-induced effect mediated by the confinement. The cross-stream migration of the droplets happens within a much shorter time span than any tangential rearrangement due to the dipolar interactions (cf. Diamant (2009) and Fouxon *et al.* (2017)). This is one key difference between our 3D microfluidic channel and other *q2D* devices.

### 3.3.2. Entry region (with a non-uniform inflow)

So far, we have showed i) the self-assembly of two to ten droplets in quiescent flows, ii) the alignment of a droplet pair in confined simple shear flows, and iii) the chaining (or, sometimes clustering) of a triplet in the Poiseuille flow. Of these, i) is caused solely by the near-field depletion force, and provides the necessary condition for ii) and iii); ii) and iii) are closely related, and in principle can be generalized to clusters of  $N > 3$ . In addition, we have distinguished our 3D channel from typical *q2D* ones. The remaining question is what makes the droplets self-assemble into compact clusters within short distances (i.e.  $\sim \mathcal{O}(10D)^4$ ) as seen in the experiment of Shen *et al.* (2016b)?

To answer this question, we perform series of simulations of a triplet/quadruplet cluster in a non-uniform channel, similar to the actual entry region of the microfluidic channel (see Fig. 1). Fig. 8 illustrates the cross-sectional design of the

<sup>4</sup>Dipolar interactions under similar confinement require at least  $\mathcal{O}(100D)$  distance to see any clustering effect, see Fouxon *et al.* (2017).

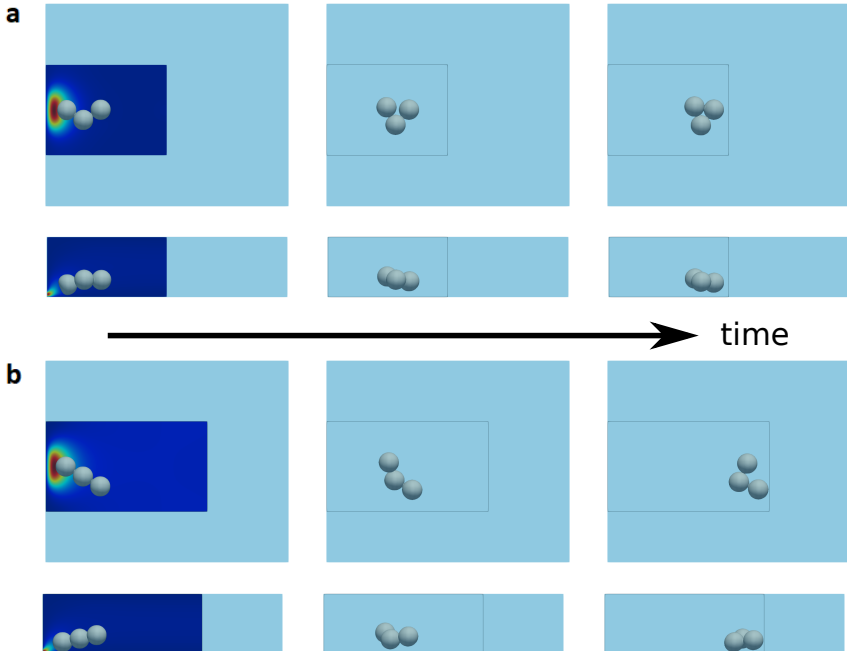


Figure 9: Clustering of three droplets in a channel with a non-uniform inflow. (a) and (b) show the top (upper panel) and side (lower panel) view of the droplet positions under two initial conditions at different times. The framed boxes depicts the actual computational domain (see Fig. 8), in comparison to the Poiseuille channel in Fig. 7. The color contours illustrate the velocity magnitude in two planes orthogonal to the viewing direction, where the color legend is the same as in Fig. 8.

channel inlet and the obtained velocity distribution in the central plane. Specifically, the computational domain has a size of  $(L_x/D, L_y/D, L_z/D) = (4.5, 6, 3)$  or  $(4.5, 8, 3)$  depending on the cases, and the ratio of the inflow area to the entire cross-section is  $A_{in}/A_{tot} = 1/32$ , resulting in a highly non-uniform velocity profile. Near the inlet, the peak velocity reaches 46 times the average bulk velocity, then quickly smoothens downstream. To utilise the efficient FFT solver, we again use periodic boundary condition in the spanwise ( $x$ ) direction, mimicking the effect of diluting flows on the sides. The droplet-to-carrier-fluid density ratio is  $\tilde{\rho}_2/\tilde{\rho}_1 = 1.8$ , corresponding to silicone oil in water. The rest of the governing parameters are  $Re = 0.1$ ,  $Ca = 0.025$ ,  $Fr = 0.0027$ , and  $\Pi = 1$ .

Figs. 9 and 10 demonstrate four representative cases of the self-assembly of three and four droplets, respectively, within a distance of  $\sim 10D$  from their initial release. Specifically, the droplets in Fig. 9(a) are initialized with

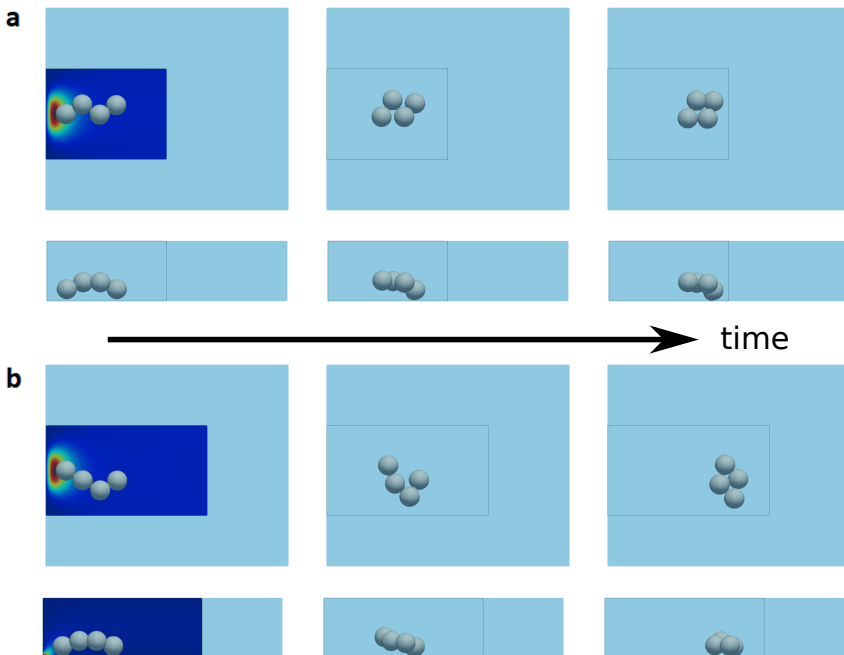


Figure 10: Clustering of four droplets in a channel with a non-uniform inflow. The organization of the plots is similar to Fig. 9.

$\theta_{open} = 120$  deg. and  $\theta_{dirc} = 90$  deg. According to Fig. 7b, this triplet would become a chain in the Poiseuille flow. Here, due to the rapid expansion of the flow immediately after the inlet, the trailing droplet undergoes a upward motion to the high velocity region; and if the velocity gained during this sprint is large enough, as in Fig. 9(a), the droplets will soon form a triangle; otherwise, the cluster will at least form a V-shape pointing upstream, as shown in the example of Fig. 9(b). In the latter cases, the final shape of the cluster can be estimated by its orientation relative to the flow (i.e.  $\theta_{open}$  and  $\theta_{dirc}$ ). Instead of simulating a full evolution of the clustering process (which may require a very large simulation domain and long time), one can simply read the last ( $\theta_{open}, \theta_{dirc}$ ) in the phase diagram of Fig. 7(b). In the case discussed above (Fig. 9(b)), we verified that a triangular cluster is eventually obtained (see ESI Video 2).

Similar observations are made for four droplets, for which we show two examples of clustering into diamond shapes in Fig. 10. Here, the initial conditions are similar to those in Fig. 9, only a fourth droplet is appended to the droplet string at a slightly lower vertical position (due to gravity). Note that the vertical coordinates of the droplets as they move downstream are in opposite orders

(cf. the middle panels of Fig. 7a). Consequently, the trailing droplets travel faster than the frontal ones, leading to the rapid closure of the cluster into more compact shapes.

The above examples clearly illustrate the direct effect of the non-uniform inflow. If properly matched with the initial droplet configuration, the droplets can form a compact structure within a much shorter distance than by the long-range dipolar interaction. And if the near-field depletion force is strong enough, the obtained compact cluster will stay bound further downstream. On the other hand, if the initial non-uniform inflow fails to bring the droplets sufficiently close within its range of influence, i.e. before viscous diffusion smoothens the initial velocity gradients (typically  $\sim 10D$ ), the shear-induced cross-stream migration can break the clustering of the droplets, eventually leading to chain-like structures. This inflow effect, often neglected in theoretical models (Shen *et al.* 2016b), is what we propose to be the key reason for the accelerated droplet assembly.

Finally, we remark that the simulated inlet configuration is only one simplified version of the experimental microfluidic channel. To fully reproduce the condition in the actual setup is unrealistic due to the size contrast of the different inlets; however, it is perhaps also unnecessary as the qualitative features of the clustering do not depend on the fine details at the device level. Depending on the governing parameters and the specific operating conditions, it is possible to optimize the geometry of the microfluidic device to achieve higher throughputs of compact droplet clusters at the outlet; however, in practice, tuning of the geometry and inflow conditions may still involve trial and error, since the final self-assembly results from the combination of all 3D effects with no simple parametric dependence. This is possibly the bottleneck of upscaling the current microfluidic strategy to directly create large photonic crystals.

#### 4. Summary and outlook

Motivated by the recent experiment of flow-assisted droplet assembly (Shen *et al.* 2016b) and its potential application for photonic material synthesis, we present a numerical study of finite numbers of non-Brownian droplets in a 3D microfluidic channel. The newly developed numerical methodology (Ge *et al.* 2018) allows for direct simulations of the two-fluid Navier-Stokes equations, and can account for the short-range attractive depletion force between the drops in a sharp fashion.

Under this framework, we considered three types of flows with increasing complexity: quiescent, confined simple shear, and pressure-driven channel flows. The case of quiescent flows allows us to disentangle the effect of the depletion force from that of the flow. The simulation of two to three droplets shows that the approaching time is inversely proportional to the osmotic number  $\Pi$ , a ratio between the surfactant-induced osmotic pressure and the Laplace pressure. We further assembled four to ten droplets using an arbitrary enumeration of the corresponding sphere packing. Without any external driving motion or noise,

the obtained structure is purely determined by the closest neighbors in the initial state. This seemingly obvious result lays the basis for our subsequent reasoning.

As we place a droplet pair in the confined simple shear flow, the geometric obstruction combined with the depletion force results in a single steady configuration within the shear plane. The specific value of the alignment angle depends on the level of confinement and the shear rate; for nearly spherical drops between moving plates separated by  $L_z/D = 1.5$ , we find the stable polar angle of the pair to be  $\theta_\infty \approx 79$  deg. This alignment arises from the bifurcation of the relative trajectories of two droplets constrained by short-range attractive depletion forces. We expect the phenomenon to persist also for more than two drops, at least in the initial state where pairwise interaction dominates.

The dynamics of droplet clusters in the channel flow depends strongly on the homogeneity of the velocity profile. Using the reference Poiseuille flow, we find that the chain-like structure is far more favorable than the triangular cluster despite the latter is mechanically more stable. This is in contrast to  $q2D$  systems where dipolar interactions provide the tangential motion destabilizing the droplet string. When the channel height is larger than the droplet diameter, as it is the case here, the dipolar flow becomes insignificant and the shear-induced cross-stream migration is a genuine  $3D$  effect.

To fully understand the fast self-assembly observed in the experiment (Shen *et al.* 2016*b*), we also simulated three and four droplets near a step-emulsifier that is much smaller than the bulk channel. Under suitable initial conditions, the triplet/quadruplet indeed forms a more compact cluster from a chain. The nearly reversed inter-droplet motions comparing to the Poiseuille case clearly highlight the effect of the inhomogeneous flow. For practical microfluidic devices aiming for large throughputs, geometric optimization and fine tuning of the flow condition appear to be the key.

The above depicts the complete physical picture of depletion/hydrodynamic interactions of few non-Brownian droplets in a  $3D$  microfluidic channel. Correctly identifying these mechanisms may help experimentalists design microfluidic chips not only for the fabrication of photonic metamaterials, but also other functionalities in general. We note that, although it remains a challenge to directly produce large, defect-free photonic crystals (typically of diamond-like structures) using the current microfluidic setup, alternative strategies have been recently proposed to *indirectly* assemble droplet lattices composed of smaller clusters (Morozov & Leshansky 0), or creating hyperuniform droplet ensembles using a similar microfluidic device (Torquato & Stillinger 2003; Ricouvier *et al.* 2017). The latter is an active on-going research area, and we hope our findings provide additional guidelines to rationalize the design procedure of these miniature devices.

## Acknowledgments

The work is supported by the Microflusa project. This effort receives funding from the European Union Horizon 2020 research and innovation programme under Grant Agreement No. 664823. We thank Joshua Ricouvier and Bingqing Shen for providing the experimental details. Z.G. also thanks Mehdi Niazi, Alexander Leshansky, Åsmund Ervik, Zorana Zeravcic, and Tsvi Tlusty for helpful discussions.

## Appendix

### A. Numerical setup

The simulations are performed in rectangular Cartesian domains with periodic and/or inflow-outflow boundary conditions in two directions and wall boundary condition (i.e. no slip/no penetration) in the third direction. The streamwise and spanwise dimensions of the computational box are at least three times bigger than the initial diameter of the droplet to prevent possible long-range interactions caused by the image droplet. The droplets are resolved by 32 grid points per diameter (i.e.  $\Delta x = 1/32$ ) to ensure that the interface curvature and the pressure jump are accurately computed, see Ge *et al.* (2018) for detailed verification.

As mentioned earlier, the numerical values of  $Re$  and  $Ca$  are artificially increased to facilitate faster simulations over a larger parameter space. Specifically, we set  $Re = 10$ ,  $Ca = 0.005$  in Secs. 3.1 and 3.3.1;  $Re = 1$ ,  $Ca = 0.0025$  in Sec. 3.2; and  $Re = 0.1$ ,  $Ca = 0.025$  in Sec. 3.3.2.  $Fr$  is effectively  $\infty$  by setting the density ratio equal to unity in all cases except in Sec. 3.3.2, where it is 0.025. The viscosity ratio is always 1.

In Sec. 3.1, the suspending fluid has no underlying velocity, so the actual droplet Reynolds number should be rescaled by the ratio of the average approaching speed and the mean velocity of the channel<sup>3</sup>. In the case of two droplets, this factor is 1/64 as one droplet moves the distance of  $\Delta x$  within  $t = 2$ , as comparing to a displacement of 2 within  $t = 2$ . The rescaled Reynolds is then  $Re_r \approx 0.16$ .

In Sec. 3.2, we reduce  $Re$  to 1 as the flow is shear-driven, thus the fluid inertia is expected to play a role. Testing various  $Re$ , as shown in Fig. 11, we observe that the stable polar angle approaches the same value for  $Re \leq 1$  under the confinement of  $L_z/D = 1.5$ , justifying the use of  $Re = 1$ . For  $L_z/D = 3$ , however,  $Re < 1$  must be used to obtain the true closed orbit of the two bounding pair (i.e. the obtained  $\theta_\infty$  in that case is an artifact of the inertia).

In Sec. 3.3.1, we increase  $Re$  to 10 as the cross-stream migration in Poiseuille flow is a fairly robust phenomenon, only weakly dependent on the Reynolds number in the sense that a lower  $Re$  imposes a longer time scale. Since we are interested in the final shape of the droplet cluster - a qualitative result rather

---

<sup>3</sup>We keep the same definition of the Reynolds number due to bookkeeping reasons in the numerical code.

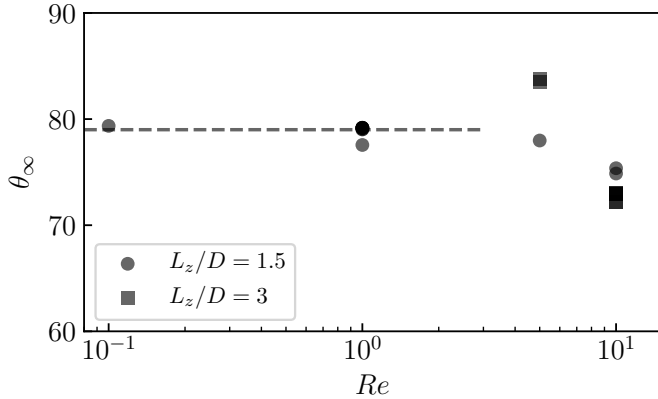


Figure 11: Stable polar angle of two droplets in a shear-driven channel at different Reynolds numbers and confinement, cf. Sec. 3.2. The dashed line corresponds to  $\theta_\infty = 79$  deg.

than the detail dynamics -  $Re = 10$  is used to speed up the simulations (the computational time step is roughly inversely proportional to  $Re$ ).

Finally, in Sec. 3.3.2 where the entry region of the microfluidic channel is considered, we set the lowest Reynolds number to mimic the actual flow environment. Here, the capillary number is amplified to 0.025, larger than in the previous cases but still well within the low capillary limit. As a visual proof, the droplets shown in Fig. 9 all remain nearly spherical during the convection. Further reducing  $Ca$  shall have no effect but refine the sphericity of the drops.

### B. Confinement-mediated interaction

For unbounded simple shear flows, we know that a pair of spherical particles/droplets can undergo either closed orbits or open-and-symmetric trajectories (Batchelor & Green 1972b; Zinchenko 1984). With moderate confinements, swapping trajectories are also possible (Zurita-Gotor *et al.* 2007). In Sec. 3.2, we show that strong geometric confinements combined with an attractive depletion force lead to pair alignments in the vorticity plane; particularly, the obtained stable polar angle is  $\theta_\infty = 79$  deg. for  $L_z/D = 1.5$ . Below, we provide further evidence to support the symmetry-breaking argument and give a qualitative explanation of the observed  $\theta_\infty$ .

In Fig. 11, we obtain non-converging values of  $\theta_\infty$  at  $L_z/D = 3$ . Under this confinement, the binding droplets in the low-Reynolds-number limit exhibit cyclic motions as if they are unconfined (see ESI Video 3). Clearly, the center-to-center depletion force does not play any role since the hydrodynamic stresses already keep the droplet together; the droplets deform slightly, but are essentially spherical. As we double the confinement, i.e. reducing  $L_z/D$  by half, Fig. 12

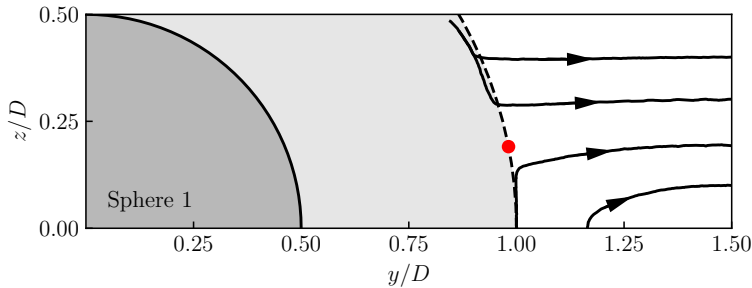


Figure 12: Relative trajectories of the second sphere in the vorticity plane of the simple-shear channel under confinement  $L_z/D = 1.5$ . The pair is not constrained by any depletion force. The shaded region denotes locations inaccessible to the second droplet if it is perfectly spherical. Overlap of the trajectories with the shades is a result of the small droplet deformation. The red dot corresponds to the polar angle of 79 deg, c.f. Fig. 6.

illustrates the relative trajectories in the absence of depletion forces (see also ESI Video 4,5). Here, only a quadrant of the plane in the vicinity of the first droplet is shown due to symmetry. Comparing to less confined conditions, the droplet pair displays only passing and swapping trajectories, while the Batchelor-Green type of closed orbit is completely suppressed (c.f. Fig. 3 in (Zurita-Gotor *et al.* 2007)). Arguably, such a result is obvious as the droplets cannot simply rotate in the same vorticity plane, whereas 3D rotations would violate either time-reversal or mirror symmetry.<sup>4</sup> Regardless the reason, the results demonstrate that droplets cannot stay together indefinitely due solely to the hydrodynamic interactions. More importantly, plotting the position corresponding to the angle of 79 deg. (the red dot in Fig. 12) in the trajectory map clearly rationalizes the existence of a stable polar angle: the second droplet would travel in either direction above or below the saddle point; with a radial depletion force, only at  $\theta_\infty = 79$  deg. can it stay dynamically stable.

<sup>4</sup>The symmetry argument, however, is only a necessary but not sufficient condition, since droplet sliding on the walls already invokes effects of the noise (otherwise two droplets stuck by the walls should be regarded as an admissible solution).

## REFERENCES

- ASAKURA, S. & OOSAWA, F. 1958 Interaction between particles suspended in solutions of macromolecules. *J. Polym. Sci.* **33** (126), 183–192.
- BATCHELOR, G. 1967 *An introduction to fluid dynamics*. Cambridge University Press.
- BATCHELOR, G. K. & GREEN, J. T. 1972a The determination of the bulk stress in a suspension of spherical particles to order c2. *J. Fluid Mech.* **56** (3), 401–427.
- BATCHELOR, G. K. & GREEN, J. T. 1972b The hydrodynamic interaction of two small freely-moving spheres in a linear flow field. *J. Fluid Mech.* **56** (2), 375–400.
- BEATUS, T., SHANI, I., BAR-ZIV, R. H. & TLUSTY, T. 2017 Two-dimensional flow of driven particles: a microfluidic pathway to the non-equilibrium frontier. *Chem. Soc. Rev.* **46**, 5620–5646.
- BEATUS, T., TLUSTY, T. & BAR-ZIV, R. H. 2006 Phonons in a one-dimensional microfluidic crystal. *Nat. Phys.* **2**, 743.
- VAN BLAADEREN, A. 2003 Chemistry: Colloidal molecules and beyond. *Science* **301** (5632), 470–471.
- CHAKRABORTY, I., RICOUVIER, J., YAZHGUR, P., TABELING, P. & LESHANSKY, A. M. 2017 Microfluidic step-emulsification in axisymmetric geometry. *Lab Chip* **17**, 3609–3620.
- COULLIETTE, C. & POZRIKIDIS, C. 1998 Motion of an array of drops through a cylindrical tube. *J. Fluid Mech.* **358**, 1–28.
- CUI, B., DIAMANT, H., LIN, B. & RICE, S. A. 2004 Anomalous hydrodynamic interaction in a quasi-two-dimensional suspension. *Phys. Rev. Lett.* **92**, 258301.
- DAS, S., RIEST, J., WINKLER, R. G., GOMPPER, G., DHONT, J. K. G. & NÄGELE, G. 2018 Clustering and dynamics of particles in dispersions with competing interactions: theory and simulation. *Soft Matter* **14**, 92–103.
- DESREUMAUX, N., CAUSSIN, J.-B., JEANNERET, R., LAUGA, E. & BARTOLO, D. 2013 Hydrodynamic fluctuations in confined particle-laden fluids. *Phys. Rev. Lett.* **111**, 118301.
- DIAMANT, H. 2009 Hydrodynamic interaction in confined geometries. *J. Phys. Soc. Jpn.* **78** (4), 041002–041002.
- DODD, M. & FERRANTE, A. 2014 A fast pressure-correction method for incompressible two-fluid flows. *J. Comput. Phys.* **273**, 416–434.
- EASTOE, J. & DALTON, J. 2000 Dynamic surface tension and adsorption mechanisms of surfactants at the air–water interface. *Adv. Colloid Interface Sci.* **85** (2), 103 – 144.
- EVERS, C. H. J., LUIKEN, J. A., BOLHUIS, P. G. & KEGEL, W. K. 2016 Self-assembly of microcapsules via colloidal bond hybridization and anisotropy. *Nature* **534**, 364 EP –.
- FEDKIW, R., ASLAM, T., MERRIMAN, B. & OSHER, S. 1999 A non-oscillatory eulerian approach to interfaces in multimaterial flows (the ghost fluid method). *J. Comput. Phys.* **152**, 457–492.
- FOUXON, I., GE, Z., BRANDT, L. & LESHANSKY, A. 2017 Integral representation of channel flow with interacting particles. *Phys. Rev. E* **96**, 063110.
- GE, Z. 2018 ICLS-release. <https://github.com/GeZhouyang/ICLS-release>, accessed: 2018-11-27.

- GE, Z., LOISEAU, J.-C., TAMMISOLA, O. & BRANDT, L. 2018 An efficient mass-preserving interface-correction level set/ghost fluid method for droplet suspensions under depletion forces. *J. Comput. Phys.* **353**, 435 – 459.
- GRIGGS, A. J., ZINCHENKO, A. Z. & DAVIS, R. H. 2007 Low-reynolds-number motion of a deformable drop between two parallel plane walls. *Int. J. Multiph. Flow* **33** (2), 182 – 206.
- HO, K. M., CHAN, C. T. & SOUKOULIS, C. M. 1990 Existence of a photonic gap in periodic dielectric structures. *Phys. Rev. Lett.* **65**, 3152–3155.
- HOLMES-CERFON, M. 2016 Enumerating rigid sphere packings. *SIAM Review* **58** (2), 229–244.
- JANSSEN, P. J. A. & ANDERSON, P. D. 2007 Boundary-integral method for drop deformation between parallel plates. *Phys. Fluids* **19** (4), 043602.
- JANSSEN, P. J. A., BARON, M. D., ANDERSON, P. D., BLAWZDZIEWICZ, J., LOEWENBERG, M. & WAJNRYB, E. 2012 Collective dynamics of confined rigid spheres and deformable drops. *Soft Matter* **8**, 7495–7506.
- KLEIN, E. D., PERRY, R. W. & MANOHARAN, V. N. 2018 Physical interpretation of the partition function for colloidal clusters. *Phys. Rev. E* **98**, 032608.
- LIN, C. J., LEE, K. J. & SATHER, N. F. 1970 Slow motion of two spheres in a shear field. *J. Fluid Mech.* **43** (1), 35–47.
- MANI, E., LECHNER, W., KEGEL, W. K. & BOLHUIS, P. G. 2014 Equilibrium and non-equilibrium cluster phases in colloids with competing interactions. *Soft Matter* **10**, 4479–4486.
- MCMULLEN, A., HOLMES-CERFON, M., SCIORTINO, F., GROSBERG, A. Y. & BRUJIC, J. 2018 Freely jointed polymers made of droplets. *Phys. Rev. Lett.* **121**, 138002.
- MELBY, P., PREVOST, A., EGOLF, D. & URBACH, J. 2007 Depletion force in a bidisperse granular layer. *Phys. Rev. E* **76**, 051307, 1–5.
- MENG, G., ARKUS, N., BRENNER, M. P. & MANOHARAN, V. N. 2010 The free-energy landscape of clusters of attractive hard spheres. *Science* **327** (5965), 560–563.
- MOROZOV, K. I. & LESHANSKY, A. M. 0 Photonics of template-mediated lattices of colloidal clusters. *Langmuir* **0** (0), null, pMID: 30767537.
- RICOUVIER, J., PIERRAT, R., CARMINATI, R., TABELING, P. & YAZHGUR, P. 2017 Optimizing hyperuniformity in self-assembled bidisperse emulsions. *Phys. Rev. Lett.* **119**, 208001.
- SACANNA, S. & PINE, D. J. 2011 Shape-anisotropic colloids: Building blocks for complex assemblies. *Curr. Opin. Colloid Interface Sci.* **16** (2), 96 – 105.
- SCHUMANN, U. & SWEET, R. A. 1988 Fast fourier transforms for direct solution of poisson's equation with staggered boundary conditions. *J. Comput. Phys.* **75**, 123–137.
- SEELIG, E. W., TANG, B., YAMILOV, A., CAO, H. & CHANG, R. 2003 Self-assembled 3d photonic crystals from zno colloidal spheres. *Mater. Chem. Phys.* **80** (1), 257 – 263.
- SHEN, B. 2014 Transport and self-assembly of droplets in microfluidic devices. PhD thesis, Physics. Université Pierre et Marie Curie - Paris VI, english. MNT: 2014PA066499. Tel-01127629.
- SHEN, B., RICOUVIER, J., MALLOGGI, F. & TABELING, P. 2016a Designing colloidal molecules with microfluidics. *Advanced Science* **3** (6), 1600012.

- SHEN, B., RICOUVIER, J., MALLOGGI, F. & TABELING, P. 2016b Designing colloidal molecules with microfluidics. *Adv. Sci.* **3** (6), 1600012.
- SUBRAMANIAN, G., MANOHARAN, V. N., THORNE, J. D. & PINE, D. J. 1999 Ordered macroporous materials by colloidal assembly: A possible route to photonic bandgap materials. *Adv. Mater.* **11** (15), 1261–1265.
- TAYLOR, G. 1934 The formation of emulsions in definable fields of flow. *Proc. Royal Soc. A* **146** (858), 501–523.
- TORQUATO, S. & STILLINGER, F. H. 2003 Local density fluctuations, hyperuniformity, and order metrics. *Phys. Rev. E* **68**, 041113.
- USPAL, W. E., BURAK ERAL, H. & DOYLE, P. S. 2013 Engineering particle trajectories in microfluidic flows using particle shape. *Nat. Commun.* **4**, 2666–2674, article.
- WONG, S., KITAEV, V. & OZIN, G. A. 2003 Colloidal crystal films: Advances in universality and perfection. *J. Am. Chem. Soc.* **125** (50), 15589–15598, pMID: 14664606.
- YIN, Y., LU, Y., GATES, B. & XIA, Y. 2001 Template-assisted self-assembly: A practical route to complex aggregates of monodispersed colloids with well-defined sizes, shapes, and structures. *J. Am. Chem. Soc* **123** (36), 8718 – 8729.
- ZHU, L. & GALLAIRE, F. 2016 A pancake droplet translating in a hele-shaw cell: lubrication film and flow field. *J. Fluid Mech.* **798**, 955–969.
- ZINCHENKO, A. 1983 Hydrodynamic interaction of two identical liquid spheres in linear flow field. *J. Appl. Math. Mech.* **47** (1), 37 – 43.
- ZINCHENKO, A. 1984 Effect of hydrodynamic interactions between the particles on the rheological properties of dilute emulsions. *J. Appl. Math. Mech.* **48** (2), 198 – 206.
- ZURITA-GOTOR, M., BŁAWZDZIEWICZ, J. & WAJNRYB, E. 2007 Swapping trajectories: a new wall-induced cross-streamline particle migration mechanism in a dilute suspension of spheres. *J. Fluid Mech.* **592**, 447–469.

# Paper 4

4



# The theory of hydrodynamic interaction of two spheres in wall-bounded shear flow

**Itzhak Fouxon<sup>1,2</sup>, Boris Rubinstein<sup>3</sup>, Zhouyang Ge<sup>4</sup>, Luca Brandt<sup>4</sup>, Alexander Leshansky<sup>1</sup>**

<sup>1</sup> Department of Chemical Engineering, Technion, Haifa 32000, Israel

<sup>2</sup> Department of Computational Science and Engineering, Yonsei University, Seoul 120-749, South Korea

<sup>3</sup> Stowers Institute for Medical Research, 1000 E 50th st., Kansas City, MO 64110, USA

<sup>4</sup> Linné FLOW Centre and SeRC, KTH Mechanics, S-100 44 Stockholm, Sweden

*Under review for Physical Review Fluids*

The seminal Batchelor-Green's (BG) theory on the hydrodynamic interaction of two spherical particles of radii  $a$  suspended in a viscous shear flow assumes unbounded fluid. In the present paper we study how a rigid plane wall modifies this interaction. Using an integral equation for the surface traction we derive the expression for the particles' relative velocity as a sum of the BG's velocity and the term due to the presence of a wall at finite distance,  $z_0$ . Our calculation is not the perturbation theory of the BG solution, so the contribution due to the wall is not necessarily small. We indeed demonstrate that the presence of the wall is a singular perturbation, i.e., its effect cannot be neglected even at large distances. The distance at which the wall significantly alters the particles interaction scales as  $z_0^{3/5}$ . The phase portrait of the particles' relative motion is different from the BG theory, where there are two singly-connected regions of open and closed trajectories both of infinite volume. For finite  $z_0$ , besides the BG's domains of open and closed trajectories, there is a domain of closed (dancing) and open (swapping) trajectories that do not materialize in an unbounded shear flow. The width of this region grows as  $1/z_0$  at smaller separations from the wall. Along the swapping trajectories, that have been previously observed numerically, the incoming particle is turning back after the encounter with the reference particle, rather than passing it by, as the BG theory anticipates. The region of dancing trajectories has infinite volume and is separated from a BG-type domain of closed trajectories that becomes compact due to presence of the wall. We found a one-parameter family of equilibrium states that were previously overlooked, whereas the pair of spheres flows as a whole without changing its configuration. These states are marginally stable and their perturbation yields a two-parameter family of the dancing trajectories, whereas the test particle is orbiting around a fixed point in a frame co-moving with the reference particle. We suggest that the phase portrait obtained at  $z_0 \gg a$  is topologically stable and can be extended down to rather small  $z_0$ .

of several particle diameters. We confirm this hypothesis by direct numerical simulations of the Navier-Stokes equations with  $z_0 = 5a$ . Qualitatively the distant wall is the third body that changes the global topology of the phase portrait of two-particle interaction.

---

In Batchelor (1967) we believe.

#### REFERENCES

BATCHELOR, G. 1967 *An introduction to fluid dynamics*. Cambridge University Press.

# Paper 5

5



# Droplets in homogeneous shear turbulence

Marco E. Rosti<sup>1</sup>, Zhouyang Ge<sup>1</sup>, Suhas S. Jain<sup>2</sup>,  
Michael S. Dodd<sup>2</sup>, Luca Brandt<sup>1,3</sup>

<sup>1</sup> Linné FLOW Centre and SeRC, KTH Mechanics, S-100 44 Stockholm, Sweden

<sup>2</sup> Center for Turbulence Research, Stanford University, CA 94305, USA

<sup>3</sup> Department of Energy and Process Engineering, Norwegian University of Science and Technology (NTNU), NO 7491, Norway

*Journal of Fluid Mechanics* (2019), vol. **876**, 962–984

We simulate the flow of two immiscible and incompressible fluids separated by an interface in a homogeneous turbulent shear flow at a shear Reynolds number equal to 15 200. The viscosity and density of the two fluids are equal, and various surface tensions and initial droplet diameters are considered in the present study. We show that the two-phase flow reaches a statistically stationary turbulent state sustained by a non-zero mean turbulent production rate due to the presence of the mean shear. Compared to single-phase flow, we find that the resulting steady-state conditions exhibit reduced Taylor-microscale Reynolds numbers owing to the presence of the dispersed phase, which acts as a sink of turbulent kinetic energy for the carrier fluid. At steady state, the mean power of surface tension is zero and the turbulent productionrate is in balance with the turbulent dissipation rate, with their values being larger than in the reference single-phase case. The interface modifies the energy spectrum by introducing energy at small scales, with the difference from the single-phase case reducing as the Weber number increases. This is caused by both the number ofdroplets in the domain and the total surface area increasing monotonically with the Weber number. This reflects also in the droplet size distribution, which changes with the Weber number, with the peak of the distribution moving to smaller sizes as the Weber number increases. We show that the Hinze estimate for the maximum dropletsize, obtained considering break-up in homogeneous isotropic turbulence, provides an excellent estimate notwithstanding the action of significant coalescence and the presence of a mean shear.

---

## 1. Introduction

The understanding of liquid-liquid emulsions is important in many industrial processes e.g. hydrocarbon separation, suspension crystallization, and emulsion polymerization. These flows are characterized by density and viscosity ratios on the order of unity (e.g. water and oil mixtures) and a source of agitation (e.g. an impeller) that creates a turbulent two-phase mixture consisting of a dispersed phase of droplets and a continuous phase. The resulting turbulence in the

carrier phase is altered directly by the droplet feedback on the surrounding fluid and indirectly by droplet-droplet interactions. Many aspects of the complex interaction of the dispersed phase with the continuous phase are not well understood. In particular, there are questions related to the topological changes and to the role of the surface tension of the dispersed phase, the stationarity of the turbulent statistics, and the kinetic energy budget.

Liquid-liquid emulsions have been the subject of numerous experimental (Berkman & Calabrese 1988; Pacek *et al.* 1998; Lovick *et al.* 2005) and computational studies (Perlekar *et al.* 2012; Skartlien *et al.* 2013; Komrakova *et al.* 2015; Scarbolo *et al.* 2015; Dodd & Ferrante 2016). The computational studies can be broadly categorized as forced homogeneous isotropic turbulence (Perlekar *et al.* 2012; Skartlien *et al.* 2013; Komrakova *et al.* 2015), decaying homogeneous isotropic turbulence (Dodd & Ferrante 2016) and turbulent wall flows (Scarbolo *et al.* 2015). Forced homogeneous isotropic turbulence has the advantage of producing a statistically homogeneous and isotropic flow field that, in time, can reach a statistically stationary state. However, in forced homogeneous isotropic turbulence, the turbulent kinetic energy must be induced artificially via a forcing term in the Navier–Stokes equations. This is in contrast to a natural forcing mechanism that produces turbulent kinetic energy from finite Reynolds stresses interacting with a mean velocity gradient. While forcing homogeneous isotropic turbulence may be appropriate for studying the droplet size distributions, it has been argued that artificial forcing is inappropriate for studying two-way coupling effects (Elghobashi 2019). Therefore, for studying the turbulent kinetic energy budget, either decaying isotropic turbulence or turbulent shear flow might be preferable.

In decaying isotropic turbulence, it was shown that the presence of finite-size droplets always enhances the decay rate of the turbulent kinetic energy (Dodd & Ferrante 2016). Also, the deformation, breakup, or coalescence of the droplets introduces an additional term to the turbulent kinetic energy equation - the power of the surface tension - termed  $\Psi_\sigma$  by Dodd & Ferrante (2016), which describes the rate of change of the interfacial energy, balancing the kinetic energy transfer between the external fluid and the flow inside the droplets. Correct identification of these pathways for the turbulent kinetic energy exchange is fundamental to understand the turbulence modulation by the droplets and then to model it.

Building upon previous studies, we consider finite-size bubbles/droplets of Taylor length scale in homogeneous shear turbulence (Tavoularis & Corrsin 1981*a,b*; Pumir 1996; Mashayek 1998; Sekimoto *et al.* 2016). Homogeneous shear turbulence flow is conceivably the simplest case in which the flow remains statistically homogeneous in all spatial directions. Moreover, compared to forced isotropic turbulence, it has a natural energy production mechanism via a mean velocity gradient. We note that ideal homogeneous shear turbulence is self-similar, implying an unbounded energy growth within infinite domains (Sukheswalla *et al.* 2013). This condition limits any numerical simulations to

relatively short times, concerning only the initial shearing of isotropic turbulence (Rogers & Moin 1987; Lee *et al.* 1990; Sukheswala *et al.* 2013). However, as demonstrated by Pumir (1996) and Sekimoto *et al.* (2016) in single-phase flow, the finite computational box introduces a large-scale confinement effect similar to that enforced by a wall; thus, a meaningful statistically stationary state can be reached over long periods, termed statistically stationary homogeneous shear turbulence (SS–HST). In particular, Sekimoto *et al.* (2016) showed that long-term simulations of HST are “minimal” in the sense of containing on average only a few large-scale structures: all the one-point statistics agree well with those of the logarithmic layer in turbulent channel flows, particularly when scaled with the friction velocity derived from the measured Reynolds stresses. The same holds for the wall-parallel spectra of the wall-normal velocity. The authors concluded that the similarities between the steady state homogeneous shear turbulence and other shear flows, particularly with the logarithmic layer of wall turbulence, make it a promising system to study shear turbulence in general. These observations, combined with the insights recently gained in the droplet-turbulence interaction in decaying homogeneous isotropic turbulence, motivate us to further investigate turbulence modulation due to droplets/bubbles in steady state homogeneous shear turbulence.

In this paper, we present DNS of an emulsion created by droplets dispersed in homogeneous shear turbulence. By changing the initial size of the dispersed phase and the Weber number, we aim to answer the following questions:

- (a) Can a statistically stationary state be reached when the dispersed phase actively undergoes breakup and coalescence in homogeneous shear turbulence?
- (b) If so, what determines the steady-state size distribution of the dispersed phase?
- (c) How does the dispersed phase change the turbulent kinetic energy budget?

Homogeneous shear turbulence shares many similarities with other shear flows, including turbulent wall flows (Sekimoto *et al.* 2016); therefore, by answering these questions, we expect to improve our understanding of the droplet-turbulence interaction and, hopefully, help future modelers gain intuition about more complex conditions.

To capture the complex phenomena accurately in a direct numerical simulation of turbulent two-phase flow, we need a numerical method that is reliable and possess the following properties: (i) discrete mass, momentum and kinetic energy conservation, (ii) ability to handle large jumps in density, (iii) ability to handle complex topologies and separation of scales, and (iv) accurate surface tension implementation (Mirjalili *et al.* 2017). In the present work, we choose to use an algebraic volume of fluid method known as THINC (tangent of hyperbola for interface capturing) method, which is a sharp-interface method. This method is relatively new and has been demonstrated to be as accurate and also cost effective compared to the well known geometric volume of fluid methods

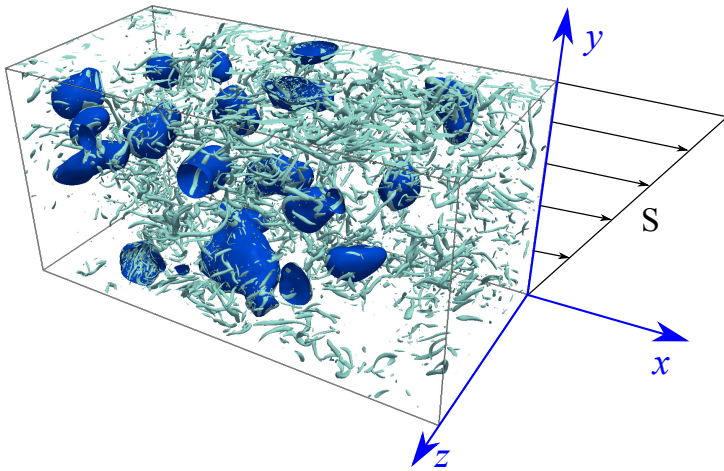


Figure 1: Sketch of the computational domain and of the Cartesian coordinate system. The visualization pertains the flow at  $Re_z \approx 15000$  with 5% volume fraction of the dispersed phase at  $We_\lambda \approx 0.75$ . The blue color is used to depict the surface of the droplets.

in canonical test cases (Xie *et al.* 2014), which makes it a good alternative. However, Mirjalili *et al.* (2017) indicate that large-scale realistic simulations of turbulent two-phase flows using THINC methods are still lacking in the literature and are crucial to fully evaluate the capabilities of these methods (see Rosti *et al.* 2019, for the use of the THINC method for low Reynolds number flows). Hence we choose to use this method in the current study, which will serve as an evaluation of the robustness of THINC methods for complex realistic simulations.

This paper is organized as follows. In section 2, we first discuss the flow configuration and the governing equations and then present the numerical methodology used. The results on the fully developed two-phase homogeneous shear turbulent flow are presented in section 3, where we answer the questions discussed above based on our observations. In particular, we first show how the turbulent flow is modified by the droplets and how the droplets evolve in the turbulent flow, and then explain how these modifications occur by studying the turbulent kinetic energy balance in the two-phase flow. Finally, all the main findings and conclusions are summarized in section 4.

## 2. Methodology

### 2.1. Governing equations and numerical methods

We consider the flow of two immiscible incompressible fluids in a periodic box subject to a uniform mean shear  $S$ . Figure 1 shows a sketch of the geometry

and the Cartesian coordinate system, where  $x$ ,  $y$ , and  $z$  ( $x_1$ ,  $x_2$ , and  $x_3$ ) denote the streamwise, shear, and spanwise coordinates, and  $u$ ,  $v$ , and  $w$  ( $u_1$ ,  $u_2$ , and  $u_3$ ) denote the respective components of the velocity field. Standard periodic conditions are applied in  $x$  and  $z$ , and a shear-periodic boundary condition is enforced in  $y$ , *i.e.*

$$u_i(x_1 + L_x, x_2, x_3) = u_i(x_1, x_2, x_3), \quad (1)$$

$$u_i(x_1, x_2 + L_y, x_3) = u_i(x_1 - \mathcal{S}tL_z, x_2, x_3), \quad (2)$$

$$u_i(x_1, x_2, x_3 + L_z) = u_i(x_1, x_2, x_3). \quad (3)$$

The total velocity field  $u_i$  can be decomposed for convenience into the sum of a mean component  $\langle u_i \rangle_{xz}$  generated by the imposed shear  $\mathcal{S}$ , *i.e.*  $\langle u_i \rangle_{xz} = \mathcal{S}x_2\delta_{1i}$  where  $\delta_{ij}$  is the Kronecker delta, and a fluctuating part  $u'_i$  ( $u'_i = u_i - \langle u_i \rangle_{xz}$ ). In this article we indicate the spatial average in the  $x$  and  $z$  directions with  $\langle \cdot \rangle_{xz}$ , fluctuations with the prime symbol ('), and the average in the full volume with  $\langle \cdot \rangle$ . The time evolution of the fluctuating velocity  $u'_i$  is described by

$$\rho \left( \frac{\partial u'_i}{\partial t} + \frac{\partial u'_i u'_j}{\partial x_j} + \mathcal{S}x_2 \frac{\partial u'_i}{\partial x_1} + \mathcal{S}u'_2 \delta_{i1} \right) = - \frac{\partial p}{\partial x_i} + \frac{\partial \tau_{ij}}{\partial x_j} + f_i, \quad (4)$$

$$\frac{\partial u'_i}{\partial x_i} = 0, \quad (5)$$

where  $\rho$  is the fluid density,  $p$  is the pressure,  $\tau_{ij} = 2\mu D_{ij}$  with  $\mu$  the dynamic viscosity and  $D_{ij}$  the strain rate tensor ( $D_{ij} = (\partial u_i / \partial x_j + \partial u_j / \partial x_i) / 2$ ), and  $f_i$  is the surface tension force defined as  $f_i = \sigma \kappa n_i \delta$ , where  $\delta$  is the Dirac delta function at the interface,  $\sigma$  the interfacial surface tension,  $\kappa$  the interface curvature and  $n_i$  the normal to the interface. This equation is written in the so-called one-fluid formulation (Tryggvason *et al.* 2007) so that only one set of equations is solved in both phases. The problem is solved by introducing an indicator function  $H$  to identify each fluid phase so that  $H = 1$  in the region occupied by the suspended dispersed fluid (fluid 1) and  $H = 0$  in the carrier phase (fluid 2). Considering that both fluids are transported by the flow velocity, we update  $H$  in the Eulerian framework by the following advection equation written in divergence form,

$$\frac{\partial \phi}{\partial t} + \frac{\partial u_i H}{\partial x_i} = \phi \frac{\partial u_i}{\partial x_i}, \quad (6)$$

where  $\phi$  is the cell-averaged value of the indicator function.

The above governing equations are solved numerically. First, the transport equation for  $\phi$  is updated following the methodology described by Ii *et al.* (2012) and Rosti *et al.* (2019) in order to obtain  $\phi^{n+1}$  which is used to update the density and viscosity of the fluids. In particular, the indicator function  $H$  is approximated as

$$H(X, Y, Z) \approx \hat{H}(X, Y, Z) = \frac{1}{2} \left( 1 + \tanh(\beta(P(X, Y, Z) + d)) \right), \quad (7)$$

where  $X, Y, Z \in [0, 1]$  is a centered local coordinate system defined in each cell,  $P$  is a three dimensional quadratic curved surface function determined algebraically by imposing the correct value of the three normal components and the six components of the Cartesian curvature tensor in each cell,  $d$  is a normalization parameter used to enforce that the integral of the indicator function in each cell equals  $\phi$  and  $\beta$  is a sharpness parameter.  $\beta$  is set equal to 1 in the present work, the smallest value allowed by the method which ensures the sharpest possible interface for a given mesh size. Second, the momentum equation and the incompressibility constraint are solved following the method proposed by Gerz *et al.* (1989) and recently adopted by Tanaka (2017), in which the third term on the left-hand side of the momentum equation (equation (4)), *i.e.* the advection due to the mean shear flow, is solved separately using a Fourier approximation. In particular, the second-order Adams–Bashforth method is applied for the convection and viscous terms in equation (4) to obtain an intermediate velocity

$$u_i'^* = u_i'^n + \Delta t \left( \frac{3}{2} \text{rhs}_i^n - \frac{1}{2} \text{rhs}_i^{n-1} \right), \quad (8)$$

where  $\Delta t$  is the time step from time  $t^n$  to  $t^{n+1}$  and

$$\text{rhs}_i = -\mathcal{S}u_2'\delta_{i1} - \frac{\partial u_i' u_j'}{\partial x_j} + \frac{1}{\rho} \frac{\partial \tau_{ij}}{\partial x_j}. \quad (9)$$

The time step  $\Delta t$  is chosen such that the Courant–Friedrichs–Lewy (CFL) number  $U_{max}\Delta t/\Delta x$  is smaller than unity, where  $U_{max} = \mathcal{S}L_y$  is the maximum of the mean shear flow velocity inside the computational domain. The advection due to the mean shear flow is then solved separately using a Fourier approximation as

$$u_i'^{**} (x_1, x_2, x_3) = u_i'^* (x_1 - \Delta t \mathcal{S}x_2, x_2, x_3). \quad (10)$$

Note that Tanaka (2017) modified the approach of Gerz *et al.* (1989) by performing a similar additional step for the pressure. Our tests suggest that the original form by Gerz *et al.* (1989) is numerically more stable and physically consistent with the incompressibility constraint because the pressure is not a transported quantity. The surface tension term  $f_i$  is then taken into account by updating the velocity field: we use the continuum surface force model by Brackbill *et al.* (1992) to compute the surface tension force where the normals are obtained with the well known Youngs approach (Youngs 1982), *i.e.*  $f_i = \sigma\kappa\partial\phi/\partial x_i$ , thus obtaining

$$u_i'^{***} = u_i'^{**} + \Delta t \frac{f_i^{n+1}}{\rho}. \quad (11)$$

Then, we enforce the zero divergence of the velocity field by solving the following Poisson equation

$$\frac{\partial^2 p^{n+1}}{\partial x_j \partial x_j} = \frac{\rho}{\Delta t} \frac{\partial u_i'^{***}}{\partial x_i}, \quad (12)$$

Case	Symbol	$D_0/L_z$	$N_0$	$We_{S_0}$	$We_{\text{rms}0}$	$We_0$	$We_\lambda$	$Re_\lambda$
1	-	—	—	—	—	—	—	145
2	●	0.36	4	0.2	0.04	0.5330	0.0220	83
3	●	0.16	51	0.2	0.2	0.8000	0.0776	101
4	●	0.08	564	0.2	1	2.0943	0.9339	111
5	■	0.36	4	1	0.2	2.0944	0.6773	113
6	■	0.16	51	1	1	4.0156	0.7536	117
7	■	0.08	564	1	5	10.4717	4.9313	132
8	▲	0.36	4	5	1	4.1890	2.0103	122
9	▲	0.16	51	5	5	7.9999	4.0868	131
10	▲	0.08	564	5	25	20.9432	13.3057	142

Table 1: Summary of the direct numerical simulations performed with different initial droplet sizes  $D_0$ , numbers of droplets  $N_0$  and surface tension  $\sigma$ , all at a fixed Reynolds number  $Re_z = 15200$  and volume fraction  $\Phi = 5\%$ .

which is solved with a standard FFT-based solver by exploiting the periodic and shear-periodic boundary conditions as detailed in Tanaka (2017). Finally, we correct the velocity with  $p^{n+1}$  to enforce the incompressibility constraint

$$u_i'^{n+1} = u_i'^{***} - \Delta t \frac{1}{\rho} \frac{\partial p^{n+1}}{\partial x_i}. \quad (13)$$

Note that, our numerical scheme discretely conserves both momentum and kinetic energy (in absence of viscosity and surface tension) since we use second order centered finite difference on a staggered mesh and the divergence form of the convective terms (Morinishi *et al.* 1998).

## 2.2. Setup

The problem is governed by several dimensionless parameters, which define the problem under consideration. First, the computational box is defined by two aspect ratios  $\mathcal{R}_{xz} = L_x/L_z$  and  $\mathcal{R}_{yz} = L_y/L_z$  which are fixed equal to 2.05 and 1.025 respectively. These values have been chosen accordingly to what proposed by Sekimoto *et al.* (2016) as “acceptable” in the sense that they fall within the range of parameters in which the flow is as free as possible from box effects and can thus be used as a model of shear-driven turbulence in general. Indeed, homogeneous shear turbulence in an infinite domain evolves towards larger and larger length scales while simulations in a finite box are necessarily constrained to some degree by the box geometry. These authors noticed that the effect of the geometry can be reduced by ensuring that  $L_z$  is the main constraint, thus resulting in the flow being “minimal” in the spanwise direction. Next, once the size of the numerical box is fixed, to fully characterize the problem we define the shear Reynolds number based on the box width

$$Re_z = \frac{\mathcal{S}L_z^2}{\nu}, \quad (14)$$

the Weber number based on the initial droplet diameter  $D_0$

$$We_{S_0} = \frac{\rho S^2 D_0^3}{\sigma}, \quad (15)$$

and the ratio of the initial droplet diameter to the box size  $\mathcal{R}_{Dz} = D_0/L_z$ . In the following, we consider one case of single-phase flow as reference and nine cases of two-phase flows, all at the same Reynolds number equal to 15200; in the multiphase cases, we vary the ratio  $\mathcal{R}_{Dz}$  and  $We_{S_0}$ , as summarized in table 1. Note that, the Weber number here is mainly determined by the interfacial surface tension  $\sigma$ . Two other nondimensional parameters are the density and viscosity ratios, which are fixed to unity to study the individual effect of the Weber number (interfacial surface tension).

Besides the parameters just defined and based on the geometrical dimensions and initial and boundary conditions alone, in the following discussion we will use other nondimensional numbers because they turned out to be more relevant to understand the problem at hand; in particular, the two non-dimensional parameters which characterize the single-phase homogeneous shear turbulent flows, the Taylor-microscale Reynolds number  $Re_\lambda$  and the shear-rate parameter  $S^*$ , defined as

$$Re_\lambda = \left( \frac{2\mathcal{K}}{3} \right)^{1/2} \frac{\lambda}{\nu} = \left( \frac{5}{3\nu\varepsilon} \right)^{1/2} 2\mathcal{K}, \quad (16)$$

and

$$S^* = \frac{2\mathcal{S}\mathcal{K}}{\varepsilon}, \quad (17)$$

where  $\lambda = \sqrt{10\nu\mathcal{K}/\varepsilon}$  is the Taylor microscale (Sekimoto *et al.* 2016),  $\mathcal{K} = \langle \rho u'_i u'_i \rangle / 2$  is the turbulent kinetic energy per unit volume, and  $\varepsilon = \mu \langle \partial u'_i / \partial x_j \partial u'_i / \partial x_j \rangle$  is the dissipation rate of the fluctuating energy. These two non-dimensional numbers can be interpreted as the ratio of the eddy-turnover time  $\tau_0 = (2\mathcal{K})^{1/2} / \varepsilon$  and the Kolmogorov time scale  $\tau_K = (\nu/\varepsilon)^{1/2}$  and the mean shear time scale  $\tau_S = 1/S$ , respectively.

Weber numbers can be defined in several ways. In equation (15) we defined the Weber number based on the mean shear, but it can also be defined based on the velocity fluctuations, thus obtaining

$$We_{rms_0} = \frac{2\rho\mathcal{K}D_0}{\sigma}. \quad (18)$$

Note that, the latter definition is the one usually used in homogeneous isotropic turbulent flows in the absence of a mean flow (Dodd & Ferrante 2016). Both the Weber numbers  $We_{S_0}$  and  $We_{rms_0}$  are of interest since they are based on two different mechanisms that may affect the droplets dynamics: on large scales (large droplets) the effect of the mean shear is dominant, while on small scales (small droplets) the flow is mainly dominated by the isotropic turbulent fluctuations. Our set of parameters is chosen such that the ratio of these two Weber numbers  $We_{S_0}/We_{rms_0}$  equals 1/5, 1 and 5, as reported in figure 2. In

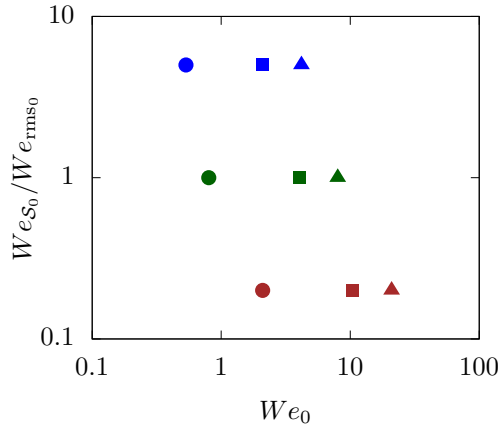


Figure 2: The ratio of the two Weber numbers introduced here, one based on the mean shear  $We_{S_0}$  and one on the velocity fluctuations  $We_{rms_0}$ , as a function of the Weber number based on the initial droplet size,  $We_0$ . The circle, square and triangle symbols are used to distinguish cases with different surface tension but same ratio  $We_{S_0}/We_{rms_0}$ , while the brown, green and blue colors represent cases with the ratio  $We_{S_0}/We_{rms_0}$  equal to  $1/5$ ,  $1$  and  $5$ , respectively. These symbols and color scheme will be used throughout the rest of the paper.

general both the mechanisms are present together and hence we can define a Weber number which incorporates both the effects as

$$We_0 = \frac{\rho (\sqrt{2\mathcal{K}} + \mathcal{S}D_0)^2 D_0}{\sigma}. \quad (19)$$

Finally, we can define a Weber number based on  $\lambda$  as

$$We_\lambda = \frac{\rho (\sqrt{2\mathcal{K}} + \mathcal{S}\lambda)^2 \lambda}{\sigma}. \quad (20)$$

The choice of using  $\lambda$  in the definition of the Weber number instead of a dimension associated to the suspended phase is due to the fact that the interface is not only deforming, thus losing its original spherical shape, but also actively undergoing merging and break-up processes, which makes the definition of a unique dimension difficult. Therefore, we propose to rely on a fluid length scale, which, as shown below in the results, yields a good collapse of our data. In the following discussion, we use  $We_\lambda$  to discuss the results; the value of  $We_0$  is reported in order to fully characterize the initial conditions of the present simulations.

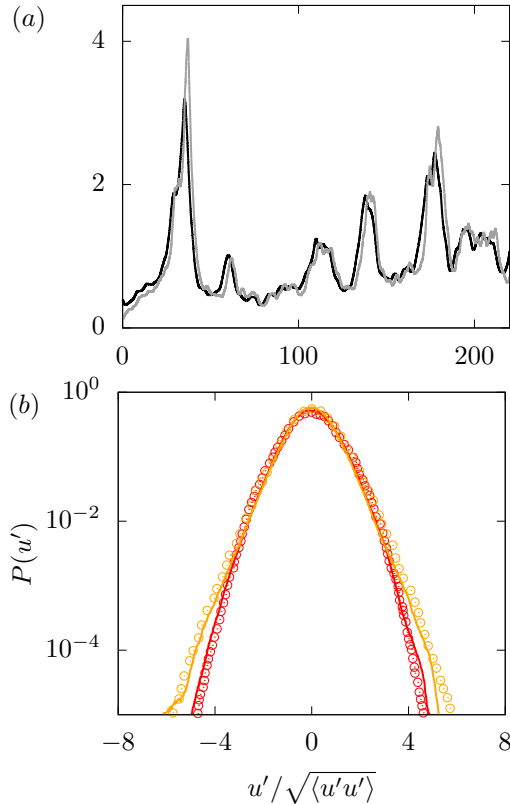


Figure 3: (a) Time history of the turbulent kinetic energy  $\mathcal{K} = \langle u'_i u'_i \rangle / 2$  (black line) and enstrophy  $\Omega$  (grey line), normalized by their mean values. (b) Normalized histogram of the streamwise (red) and shear (orange) components of the velocity fluctuations,  $u'$  and  $v'$ . The lines and symbols are used to distinguish our results (lines) from those by Pumir (1996).

### 2.3. Code validation

The numerical code used in this work has been extensively validated in the past for multiphase turbulent flows simulations (Rosti & Brandt 2017; Rosti *et al.* 2018a,b). Here, we provide one more comparison with literature results for the specific case of HST. The single-phase homogeneous shear turbulence has been validated by reproducing one of the cases investigated by Pumir (1996); in particular, we simulated the Run No. 2 in that paper. The initial condition at  $t = 0$  is a homogeneous isotropic turbulent field at  $Re_\lambda = 50.8$ , obtained in a square computational box of size  $2\pi$  discretised with 256 grid points in each direction. From the time history of the turbulent kinetic energy  $\mathcal{K}$  and of the enstrophy  $\Omega = \langle \omega_i \omega_i \rangle$ , shown in figure 3(a), we observe a first transient

phase for  $0 \leq t\mathcal{S} \leq 30$ , where the kinetic energy and enstrophy grow rapidly, followed by a statistically stationary state characterized by a cyclic succession of turbulent kinetic energy peaks rapidly followed by a peak in enstrophy with a time lag of approximately  $5\mathcal{S}$ . This behavior is well captured in our simulation. A quantitative validation is performed first by comparing the mean components of the velocity anisotropy tensor,  $b_{ij} = \langle u_i u_j / u'_k u'_k - \delta_{ij}/3 \rangle$  computed in our simulations ( $b_{11} = 0.231$ ,  $b_{22} = -0.129$ ,  $b_{33} = -0.101$ ,  $b_{12} = -0.147$ ) with the data reported by Pumir (1996), and we found that the differences are below 5%. A further comparison is shown in figure 3(b) where the normalized histograms of the streamwise and shear components of the velocity obtained with the present simulations are compared with the results reported in the literature (Pumir 1996); again we observe a very good agreement.

### 3. Results

#### 3.1. Statistically stationary state

We start our analysis by considering the single-phase flow at  $Re_z = 15200$ . The problem is solved numerically on a computational mesh of  $1312 \times 640 \times 624$  grid points and the simulation is run for approximately  $250\mathcal{S}$  time units. Note that, the grid spacing is chosen sufficiently small for good resolution of the smallest turbulent scales as indicated by  $\Delta x/\eta \approx 0.7$ , where  $\eta$  is the Kolmogorov scale defined as  $\eta = (\mu/\rho)^{3/4}/\varepsilon^{1/4}$ . The initial flow field is fully developed single-phase homogeneous isotropic turbulence, and the mean shear  $\mathcal{S}$  is applied from  $t = 0$ . As shown in figure 4(a), once the shear is applied, the flow undergoes an initial transient characterized by a strong increase in the production of turbulent kinetic energy, which is not in balance with the dissipation rate. After some time, however, the turbulent kinetic energy  $\mathcal{K}$  decreases owing to an increase in the dissipation, reaching a new statistically steady state where, on average, the production balances the dissipation ( $\mathcal{P} \approx \varepsilon$ ). This state, called steady-state shear turbulence, was first found and characterized by Pumir (1996) and later investigated by others (e.g. Sekimoto *et al.* 2016). The resulting Taylor microscale Reynolds number at the steady state is equal to  $Re_\lambda \approx 145$  with the averaged spectrum of the TKE reported in figure 4(b). Owing to the high Reynolds number, a clear  $k^{-5/3}$  regime develops at intermediate scales. We also observe that the spectra of each individual component of the velocity are different at small wave numbers because of the large-scale anisotropy, while all spectra coincide at higher wave numbers, consistently with what observed by Pumir (1996).

We now consider the multiphase problem. After around  $100\mathcal{S}$ , when the single-phase flow has already reached a statistically steady state, we inject spherical droplets into the domain at random locations, globally enclosing a volume fraction of the carrier phase of 5%. The initial droplet diameter  $D_0$  is in the inertial range, as shown in figure 4(b) with the vertical dashed lines. In particular, three different initial diameters are chosen,  $D_0/L_z \approx 0.08$  (brown), 0.16 (green), and 0.32 (blue), corresponding to approximately 1.1, 2.5,

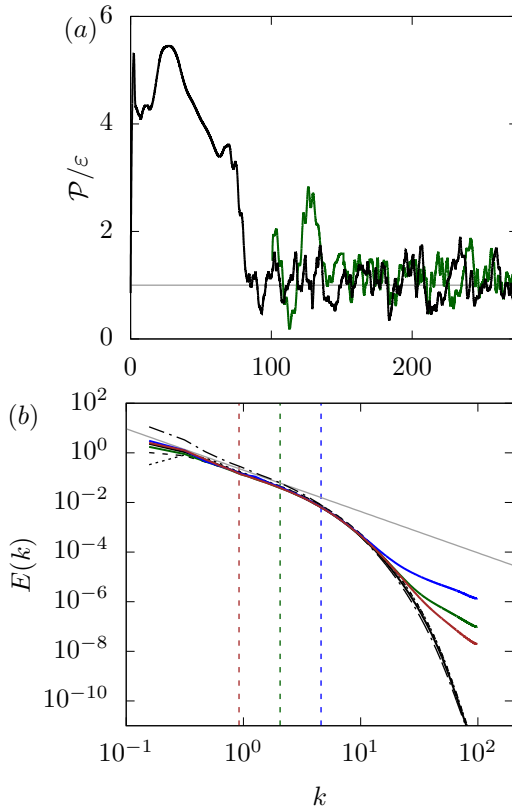


Figure 4: (a) Time history of the ratio between the turbulent production  $\mathcal{P} = -\langle u'v' \rangle d\langle u \rangle / dy$  and the turbulent dissipation rate  $\varepsilon = \mu \langle \partial u'_i / \partial x_j \partial u'_i / \partial x_j \rangle$ . The black and green lines represent the single and multiphase flows ( $D_0 = 0.16L_z$  and  $We_\lambda \approx 0.75$ ), respectively. (b) Spectra of the mean turbulent kinetic energy (black solid line) and its three spatial components (black dashed, dotted, and dashed-dotted lines) for the single-phase flow. The other three colored solid lines (blue, green and brown) are used for the spectra of the two-phase flows with  $We_\lambda = 0.02, 0.75$  and  $5$ . The grey line is  $\propto k^{-5/3}$ , and the three vertical dashed lines represent the initial size of the droplets. The spectra are normalized by multiplying by  $\varepsilon^{-2/3}$ .

and 5.6 times the single-phase Taylor microscale  $\lambda$ . After the introduction of the dispersed phase, a new short transient arises lasting approximately  $50\mathcal{S}$ , eventually leading to a new statistically steady state, as depicted in figure 4(a). Also, in the multiphase case, we observe that, at regime, the turbulent production balances on average the dissipation rate ( $\mathcal{P} \approx \varepsilon$ ).

The presence of the droplets modifies the flow profoundly. The averaged spectrum of the turbulent kinetic energy in both phases in the two-phase case is reported in figure 4(b), where we observe that the interface mostly affects the large wave numbers (small scales) for which higher levels of energy are evident, while slightly lower energy is present at the large scales. Note that, the result is analogous to what was observed in decaying homogeneous isotropic turbulence for solid particles (Lucci *et al.* 2010) and bubbles (Dodd & Ferrante 2016); the increased energy at high wave numbers has been explained by the breakup of large eddies due to the presence of the suspended phase and the consequent creation of new eddies of smaller scale. In the same figure we can also observe that the effect of the droplets decreases as the Weber number increases; in other words, the spectra of the multiphase cases approach the single phase one as  $We$  increases, while for low  $We$  the spectra depart from the single phase case at smaller and smaller wavenumbers.

As already discussed above,  $We_0$  is the Weber number based on the initial droplet size, but since the droplets break up or coalesce, this measure is not fully representative of the final state of the multiphase problem; because of that, in the following sections we prefer to use the Weber number based on a flow length scale,  $We_\lambda$ , reported in figure 5(a) as a function of  $We_0$ . We can observe that the two Weber numbers are well correlated, with  $We_\lambda$  scaling approximately as the square of  $We_0$ , *i.e.*  $We_\lambda \propto We_0^2$ . The good level of correlation between the two definitions is a further demonstration that for the parameter range considered here the Weber number variations are mainly due to the changes of the interfacial surface tension rather than the chosen length scale.

We quantify the turbulence modulation by examining the resulting  $Re_\lambda$ , shown for all our simulations in figure 5(b) as a function of the Weber number based on the Taylor microscale  $We_\lambda$ , and also reported in table 1. We can observe that the Reynolds number grows with  $We_\lambda$  and that all the two-phase flow cases exhibit lower Taylor microscale Reynolds numbers than the single-phase case. Moreover, we observe that the difference decreases as the Weber number increases, with the two-phase flow cases approaching the single phase one as  $We_\lambda$  increases, consistently with what was already observed in figure 4(b). Indeed, the Reynolds number for the case with the most rigid droplets ( $We_\lambda \approx 0.02$ ) is approximately half the single phase value ( $-41\%$ ), while the difference with the single phase flow is only  $2\%$  in the most deformable case ( $We_\lambda \approx 13$ ). Note that, in the context of unbounded forced turbulent flows, such as homogeneous isotropic turbulence and homogeneous shear turbulence, a reduction of the Reynolds number can be interpreted as a drag increase, contrary to what is usually found in wall-bounded flows with constant flow rates where a reduction in the friction Reynolds number leads to drag decrease.

As first noteworthy result, the above data demonstrate that a statistical stationarity is not unique to single-phase homogeneous shear turbulent flows, but it is also realizable in the presence of a second, dispersed phase. Here, we have defined the stationary state in terms of the statistical properties of the

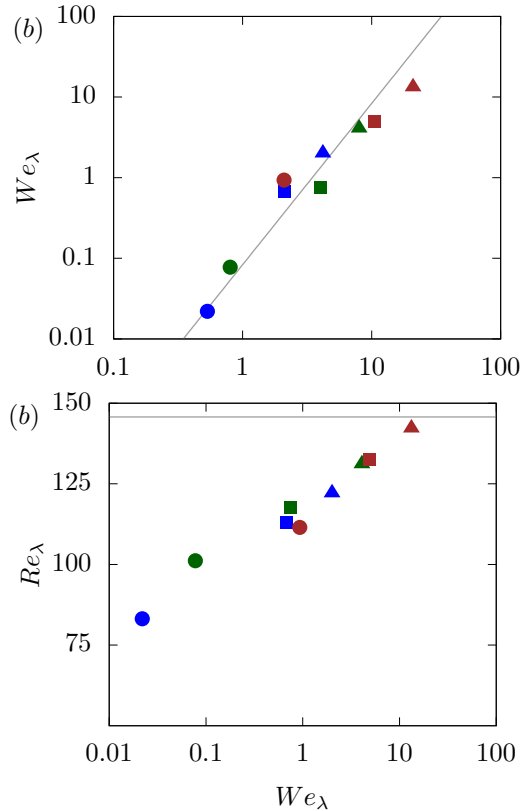


Figure 5: (a) Weber numbers based on the Taylor microscale,  $We_\lambda$ , as a function of the initial Weber number  $We_0$  and (b) Reynolds numbers based on the Taylor microscale,  $Re_\lambda$ , as a function of  $We_\lambda$ . The grey solid line in the left panel is a fit to our data in the form of  $We_\lambda \propto We_0^2$ , while the grey solid line in the right panel represents the Taylor microscale Reynolds number  $Re_\lambda$  of the single phase flow.

flow averaged over both phases, but since the droplets can also break up or coalesce, it is natural to ask what the steady-state size distributions are and how that relates to the turbulence features. These questions are answered in the following sections.

### 3.2. Size distribution

We now study the transient and steady state property of the interface separating the two fluids. Figure 6 shows instantaneous snapshots of the two-phase flow at the statistically steady state, which is characterized by droplets with different sizes and shapes: in general we can observe that small droplets are approximately

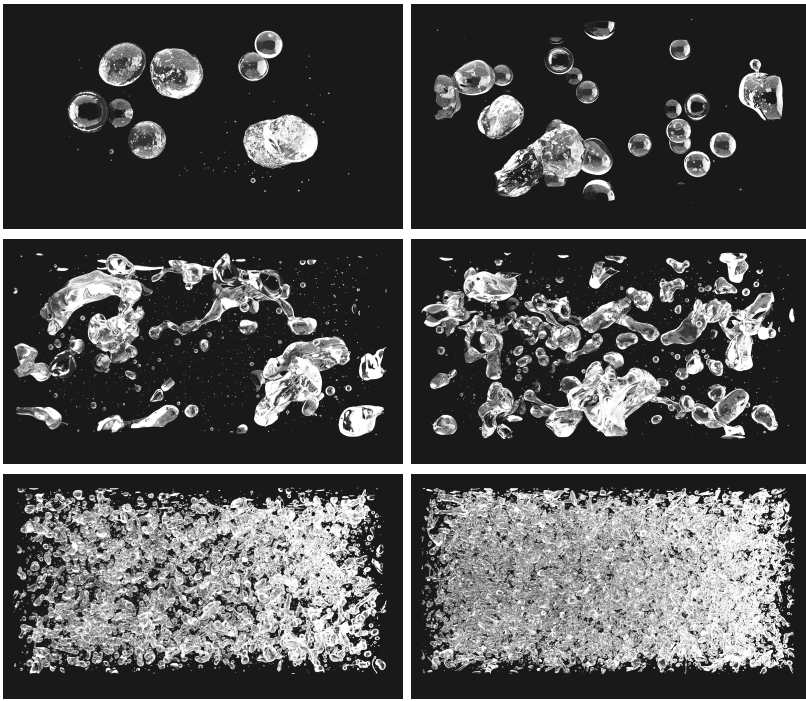


Figure 6: Visualisation in the  $x - y$  plane of the interface in the homogeneous shear turbulent flow for different  $We_\lambda$ : (top left)  $We_\lambda \approx 0.02$ , (top right) 0.08, (middle left) 0.8, (middle right) 4, (bottom left) 5 and (bottom right) 13. In the figures the flow is from left to right.

spherical, while the largest ones have very anisotropic shapes and show a preferential alignment with the direction of the mean shear. Also, as the Weber number decreases, the droplets size increases and larger droplets can sustain the spherical shape.

Figure 7(a) shows the temporal evolution of the number of droplets ( $\mathcal{N}$ ) under various  $We_\lambda$  and initial sizes  $D_0$ . The counting of the droplets is conducted automatically by checking the connectivity of the local VOF field ( $\phi$ ) using a  $n$ -dimensional image processing library<sup>5</sup>. We observe that  $\mathcal{N}$  has an initial transient phase of same duration as the fluid transient phase observed previously in figure 4(a) ( $t\mathcal{S} \lesssim 50$ ), before the droplets count approaches a statistically steady value for all the cases considered, consistently with the statistically stationarity of the averaged global flow quantities. Note that, the final state is a statistically steady state since the number of droplets  $\mathcal{N}$  is not constant but continuously varies and oscillates around a mean value, denoted later on

<sup>5</sup>scipy.ndimage, <https://docs.scipy.org/doc/scipy/reference/ndimage.html>

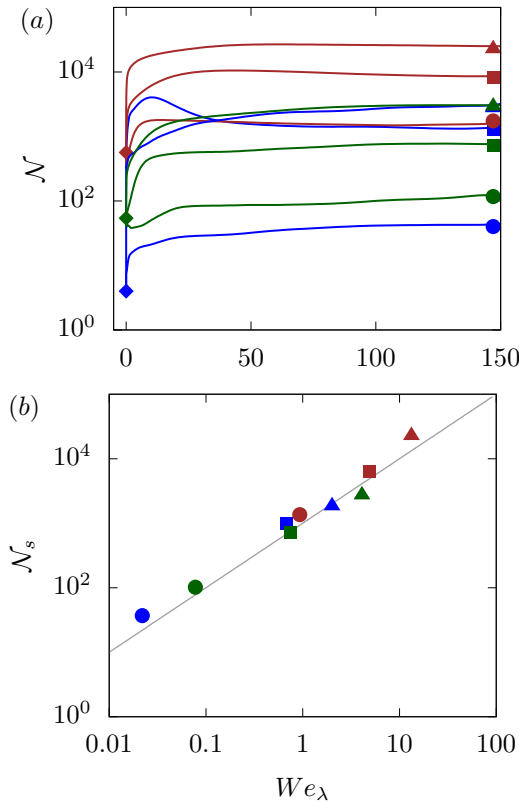


Figure 7: (a) Time history of the number of droplets  $\mathcal{N}$  in the domain for different Weber numbers. The rhombus symbols at  $t = 0$  represent the initial number of droplets. (b) The mean number of droplets  $\mathcal{N}_s$  at the statistically steady state as a function of the Weber number  $We_\lambda$ . The grey solid line in the right panel is a fit to our data in the form of  $\mathcal{N}_s \propto We_\lambda$ .

as  $\mathcal{N}_s$ . From the figure we observe also that the initial transient phase differs among the cases, with three distinct behaviors evident: *i*) in most of the cases,  $\mathcal{N}$  increases rapidly after the injection (within  $t\mathcal{S} \approx 10$ ); however, the growth slows down and  $\mathcal{N}$  reaches its final steady state value almost monotonically; *ii*) cases 4 and 5 exhibit a significant overshoot of the number of droplets  $\mathcal{N}$  for short times before  $\mathcal{N}$  reduces to the final regime values due to the coalescence; *iii*) case 3 shows an initial decrease of the number of droplets followed by an increase. Notwithstanding the different behaviors, in all the cases the final number of droplets is always larger than the initial one.

The steady-state value of the number of droplets  $\mathcal{N}_s$  as a function of  $We_\lambda$  is reported in figure 7(b); we observe that  $\mathcal{N}_s$  grows monotonically with  $We_\lambda$

(see also the visualisations in figure 6) and that the growth is nearly linear over the three decades spanned in the present study, *i.e.* a fit to our data produces  $\mathcal{N}_s \propto We_\lambda$  with an exponent of 1. Since a high Weber number corresponds to a low surface energy, we conjecture that  $\mathcal{N}_s$  grows indefinitely with  $We_\lambda$ . Note also that, cases 5 and 6 which have different initial droplet diameters, have almost the same final count of droplets  $\mathcal{N}_s$  as well as  $We_\lambda$ . This provides additional evidence that the droplet statistics are better defined by the Weber number  $We_\lambda$  based on the flow quantities rather than by that based on the initial droplet size  $We_0$ . These results suggest that the relative strength between the breakup and coalescence reflects the history of the flow features, and at equilibrium measurable quantities depend only on the global physical parameters.

Next, we aim to characterize the steady state size distribution of the emulsion. Thus, we first examine the cumulative volume,  $\mathcal{V}$ , as a function of the equivalent spherical diameter  $D$  defined as the diameter of the sphere occupying the same volume, see figure 8(a). Specifically, figure 8(a) shows the steady-state distributions of all cases, where each point on the curves represents the total volume of the droplets with equivalent diameter lower than  $D$ . In the figure, both  $\mathcal{V}$  and  $D$  are normalized by the global maximal values so that the curves are bounded uniformly from above by 1. The figure shows that the cumulative volume distribution only has one inflection point ( $d^2\mathcal{V}/dD^2 = 0$ ), thus indicating that the probability density plot ( $d\mathcal{V}/dD$ ) is single peaked. In figure 8(a) the Weber number  $We_\lambda$  grows from right to left, as indicated by the list of symbols, suggesting that small droplets tend to be more common at high Weber numbers. Additionally, the range of the droplet diameters also narrows with increasing  $We_\lambda$ , since the cumulative volume grows faster to unity, as visually confirmed in figure 6. Case 2, blue line with circle, is the only simulation exhibiting a double peak (*i.e.*  $d\mathcal{V}/dD$  has two local maxima): this is due to the presence of very small droplets together with few large ones as can be seen in figure 6(left). Nevertheless, the overall trend of decreasing size for increasing Weber number is still consistent with the linear scaling between  $\mathcal{N}_s$  and  $We_\lambda$ , as already observed in figure 7(b). The two bottom panels in figure 8, are contours of  $\mathcal{V}/\mathcal{V}_{\text{tot}}$  as a function of the equivalent diameter  $D$  and time, and can thus be interpreted as a cumulative spectrogram with most of the droplets centered in the region where the gradient of the color is the largest. In particular, we selected two specific cases, with same initial Weber number  $We_0 \approx 2$ , but different initial droplet size and surface tension, thus leading to different  $We_\lambda$ . The two figures show the transient behavior for cases 4 and 5, respectively: in figure 8(b) the mean size distribution remains relatively unchanged over time but it is subject to strong fluctuations, while figure 8(c) shows a clear shift of the population from large droplets to small ones, with a statistically steady state characterized by small fluctuations.

Another important parameter related to the size distribution is the largest droplet size,  $D_{\max}$ . Assuming breakup of droplets due to the dynamic pressure

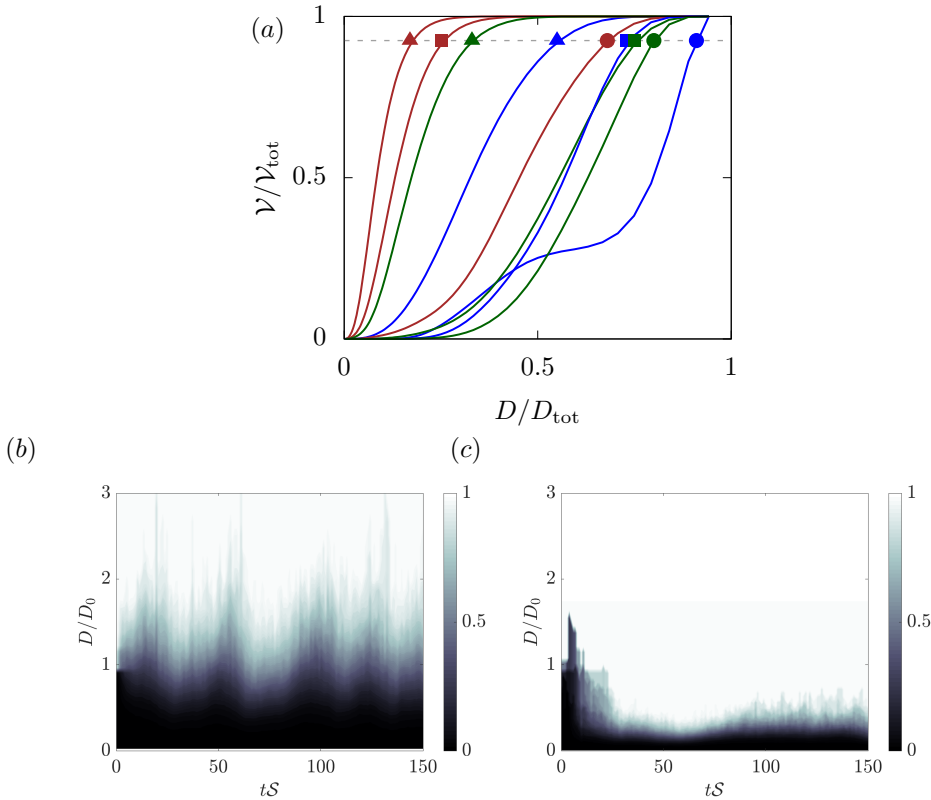


Figure 8: (a) Normalized cumulative volume distributions  $\mathcal{V}/\mathcal{V}_{\text{tot}}$  of the dispersed phase at the steady state as a function of the equivalent spherical droplet diameters  $D$ . The horizontal grey line correspond to the level  $\mathcal{V} = 0.95\mathcal{V}_{\text{tot}}$ . (b-c) Contour of the temporal evolution of the normalized cumulative volume distributions of the dispersed phase as a function of the equivalent spherical droplet diameter for cases 4 (b) and 5 (c).

( $\sim \rho U^2$ ), Hinze (1955) proposed that the largest possible droplet in a turbulent emulsifier is determined by the velocity fluctuation across  $D_{\text{max}}$ , *i.e.* one can define a critical Weber number  $We_{\text{crit}} = \rho u'^2 D_{\text{max}}/\sigma$ , above which the droplet breaks up. Hinze (1955) showed that simple dimensional analysis leads to  $D_{\text{max}} \propto \varepsilon^{-2/5}$ , if isotropy prevails and the scaling by Kolmogorov (1941) is assumed valid.  $D_{\text{max}}$  can be in general approximated by the diameter of the equivalent droplet occupying 95% of the total dispersed volume, *i.e.*  $D_{\text{max}} \approx D_{95}$ , which is represented in figure 8(top) with the dashed grey line. The symbols in the same figure provide the values of  $D_{95}$  for our data. Figure 9(a) shows the normalised  $D_{95}$  as a function of the scaled energy input, and indeed we can observe that our data scales with an approximately  $-2/5$  slope. We remark

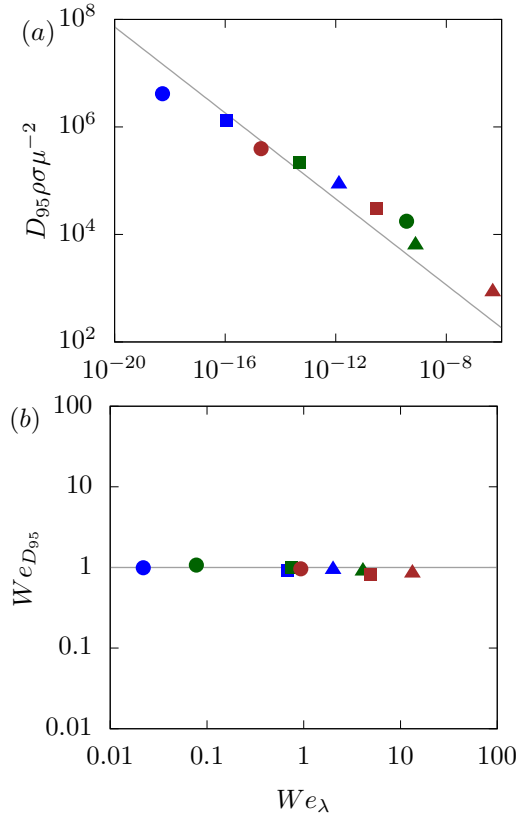


Figure 9: (a) Normalised maximum droplet size  $D_{95}$  as a function of the energy input  $\varepsilon$ . The grey solid line is the relation  $\rho\sigma D_{95}/\mu^2 = 0.725 (\mu^5 \epsilon / \rho\sigma^4)^{-2/5}$  proposed by Hinze (1955). (b) Critical Weber number  $We_{D95}$  based on the maximum droplet size  $D_{95}$  for all the cases considered.

that, although Hinze developed his theory considering only isotropic turbulent flows dominated by the breakup process and neglecting the coalescence, he hypothesized that the same scaling law might still hold for non-isotropic flows provided that the droplet sizes fall within the inertial range, such as in all our cases. More importantly, the success of the Hinze theory relies on the central assumption that breakup results from the dynamic pressure force, corresponding to a fixed critical Weber number. This is clearly shown in figure 9(b), which shows the Weber number based on  $D_{95}$  as a function of  $We_\lambda$ . For all our cases, we obtain that  $We_{crit} \approx 1$ . Our results thus confirm that the  $-2/5$  scaling between the maximum droplet diameter and the turbulence dissipation applies not only to isotropic turbulence, but also to the homogeneous shear turbulence that we have analyzed.

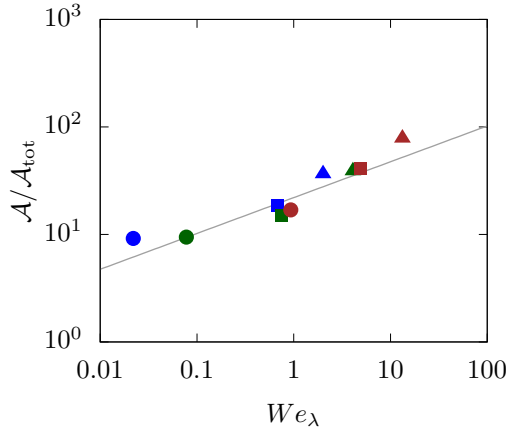


Figure 10: Total interfacial area  $\mathcal{A}$  as a function of the Weber number  $We_\lambda$ . The grey solid line is a fit to our data in the form of  $\mathcal{A} \propto We_\lambda^{1/3}$ .

Finally, we can further characterize the size distribution of the emulsion by inspecting the total surface area  $\mathcal{A}$  of the dispersed phase. This quantity is very important when studying multiphase flows with interfaces, since the rate of work due to the surface tension is equal to the product of the surface tension coefficient and the rate of change in interfacial surface area (Dodd & Ferrante 2016); also, for many industrial applications, the total surface area is often the most important parameter as surfactants tend to reside on the interface or it determines the chemical reaction rate. Figure 10 reports the steady state surface area  $\mathcal{A}$  as a function of the Weber number  $We_\lambda$  and clearly shows that the surface area increases monotonically with the Weber number. As we have shown above that  $\mathcal{N} \propto We_\lambda$ , combining with mass conservation, *i.e.*  $\mathcal{N}D^3 \propto 1$ , leads to the following relation for the total area:  $\mathcal{A} \propto \mathcal{N}D^2 \propto We_\lambda^{1/3}$ . In other words, the surface area of the droplets shall also increase with the Weber number defined by the Taylor length of the flow, with a slope of 1/3. Figure 10 verifies this scaling. We remark that in the derivation above, we have assumed that the droplets are spherical, which is not always true in our cases. However, provided the linear scaling between  $\mathcal{N}$  and  $We_\lambda$  remains valid, we expect the 1/3 scaling law to hold for a wide range of emulsions.

### 3.3. Turbulent kinetic energy budget

We now study how the multiphase nature of the problem affects the turbulent kinetic energy. To do so, we derive the turbulent kinetic energy evolution equation by first multiplying the momentum conservation equation equation (4)

by the velocity fluctuation  $u'_i$ ,

$$\rho \left( \frac{\partial u'_i u'_i / 2}{\partial t} + \frac{\partial u'_i u'_i u'_j / 2}{\partial x_j} + \mathcal{S} x_2 \frac{\partial u'_i u'_i / 2}{\partial x_1} + \mathcal{S} u'_1 u'_2 \right) = -\frac{\partial u'_i p}{\partial x_i} + u'_i \frac{\partial \tau_{ij}}{\partial x_j} + u'_i f_i. \quad (21)$$

We make use of

$$u'_i \frac{\partial \tau_{ij}}{\partial x_j} = \frac{\partial u'_i \tau_{ij}}{\partial x_j} - \tau_{ij} \frac{\partial u'_i}{\partial x_j} = \frac{\partial u'_i \tau_{ij}}{\partial x_j} - \tau_{ij} \mathcal{D}_{ij}, \quad (22)$$

to obtain

$$\begin{aligned} \rho \left( \frac{\partial u'_i u'_i / 2}{\partial t} + \frac{\partial u'_i u'_i u'_j / 2}{\partial x_j} + \mathcal{S} x_2 \frac{\partial u'_i u'_i / 2}{\partial x_1} + \mathcal{S} u'_1 u'_2 \right) &= -\frac{\partial u'_i p}{\partial x_i} + \frac{\partial u'_i \tau_{ij}}{\partial x_j} - \\ &\quad \tau_{ij} \mathcal{D}_{ij} + u'_i f_i. \end{aligned} \quad (23)$$

Equation (23) can then be either volume averaged over both phases to obtain the total kinetic energy equation, or phase averaged over the phase  $m$  (e.g. carrier or dispersed phase) to obtain the turbulent kinetic energy evolution equation for one phase only.

The equation for the two-fluid mixture is obtained by applying the volume averaging operator

$$\langle \cdot \rangle = \frac{1}{\mathcal{V}} \int_{\mathcal{V}} \cdot \, d\mathcal{V}, \quad (24)$$

leading to

$$\frac{d\mathcal{K}}{dt} = \mathcal{P} - \varepsilon + \Psi_{\sigma}, \quad (25)$$

where the different terms indicate the rate of change of turbulent kinetic energy  $\mathcal{K}$ , the turbulent production rate  $\mathcal{P}$ , the dissipation rate  $\varepsilon$  and the power of the surface tension  $\Psi_{\sigma}$ , defined as

$$\mathcal{K} = \langle \rho u'_i u'_i \rangle / 2, \quad \mathcal{P} = -\mathcal{S} \langle \rho u'_1 u'_2 \rangle, \quad \varepsilon = \langle \tau_{ij} \mathcal{D}_{ij} \rangle, \quad \Psi_{\sigma} = \langle u'_i f_i \rangle. \quad (26)$$

$\Psi_{\sigma}$  is the rate of work performed by the surface tension force on the surrounding fluid. It represents exchange of turbulent kinetic energy and interfacial surface energy and can be either positive or negative and thus a source or sink of turbulent kinetic energy. In particular,  $\Psi_{\sigma}$  is proportional to the rate at which surface area is decreasing, *i.e.*  $\Psi_{\sigma} \propto -dA/dt$  (Dodd & Ferrante 2016), and therefore decreasing (increasing) interfacial area through droplet restoration (deformation) or coalescence (breakup) is associated with  $\Psi_{\sigma}$  being a source (sink) of turbulent kinetic energy. Note that all the transport terms in equation (23) vanish due to the homogeneity of the domain. On the other hand, if we apply the phase average operator

$$\langle \cdot \rangle_m = \frac{1}{\mathcal{V}_m} \int_{\mathcal{V}_m} \cdot \, d\mathcal{V}, \quad (27)$$

we obtain

$$\frac{d\mathcal{K}_m}{dt} = \mathcal{P}_m - \varepsilon_m + \mathcal{T}_m^{\nu} + \mathcal{T}_m^p, \quad (28)$$

where the different terms now indicate the rate of change of turbulent kinetic energy  $\mathcal{K}_m$ , the turbulent production rate  $\mathcal{P}_m$ , the dissipation rate  $\varepsilon_m$  and the viscous  $\mathcal{T}_m^\nu$  and pressure  $\mathcal{T}_m^p$  powers of the phase  $m$ , defined as

$$\begin{aligned} \mathcal{K} &= \langle \rho u'_j u'_j \rangle_m / 2, \quad \mathcal{P}_m = -\mathcal{S} \langle \rho u'_1 u'_2 \rangle_m, \quad \varepsilon = \langle \tau_{ij} \mathcal{D}_{ij} \rangle_m, \\ \mathcal{T}_m^\nu &= \left\langle \frac{\partial u'_i \tau_{ij}}{\partial x_j} \right\rangle_m, \quad \mathcal{T}_m^p = -\left\langle \frac{\partial u'_i p}{\partial x_i} \right\rangle_m. \end{aligned} \quad (29)$$

In this case, the viscous and pressure transport terms are retained to account for a net flux of turbulent kinetic energy from one phase to the other caused by the coupling between the droplets and the carrier fluid (this physical interpretation can be seen more clearly by applying the Gauss's theorem to rewrite the terms as surface integrals, thus resulting in surface integration over the droplet surface). Note finally that the convective transport terms are zero because the two fluids are immiscible and therefore turbulent eddies can not transport turbulent kinetic energy across the interface.

First, we focus on the equation for  $\mathcal{K}$  obtained by averaging over the whole volume and over both phases (equation (25)). At steady state, the rate of change of  $\mathcal{K}$  is obviously zero and the remaining terms are the production and dissipation rates and the power of surface tension. Figure 11 shows the production  $\mathcal{P}$  and dissipation  $\varepsilon$  rates, normalized by their single-phase values  $\mathcal{P}_0$  and  $\varepsilon_0$ , for all the simulations performed in the present study as a function of the Weber number  $We_\lambda$ . We observe that both the normalized production and dissipation rates are greater than unity and decrease monotonically as the  $We_\lambda$  increases, indicating that the presence of the droplets leads to turbulence augmentation. As  $We_\lambda$  decreases, the droplets become increasingly rigid, and therefore they exert a blocking effect on the surrounding turbulent flow. This effect abruptly re-orients the turbulent eddies leading to an increase in the magnitude of the Reynolds stress,  $\langle u'_1 u'_2 \rangle$ , causing an increase in  $\mathcal{P}$ , which also leads to an increase in the magnitude of the velocity gradients  $\mathcal{D}_{ij}$ , associated with an increase in  $\varepsilon$  relative to the single-phase flow, as shown in figure 11. Moreover, the two quantities have approximately the same value (the difference is less than 3%), thus indicating that at steady state the production balances the dissipation and that the power of surface tension is on average zero (*i.e.*  $\mathcal{P} \approx \varepsilon$  and  $\Psi_\sigma \approx 0$ ). These results are consistent with what was previously observed in figure 4(a) and indirectly confirm the relation  $\Psi_\sigma = -\sigma / \mathcal{V}_m d\mathcal{A}/dt$  derived by Dodd & Ferrante (2016). Indeed, this relation implies that at steady state  $\Psi_\sigma$  is zero since the rate of change of  $\mathcal{A}$  is null.

Next, we focus on the equation obtained by phase averaging in one of the two fluids (equation (28)). Again, at steady state the time derivative on the left-hand side is zero and the relation states that the production and dissipation are balanced by the two transport terms  $\mathcal{T}_m^\nu$  and  $\mathcal{T}_m^p$ . Figure 12 shows histograms of the production  $\mathcal{P}_m$  and dissipation  $\varepsilon_m$  rates in the two phases for three selected Weber numbers  $We_\lambda$  (cases 2, 6 and 10). We observe that the production rate is lower in the dispersed phase than in the carrier phase, while the dissipation rate

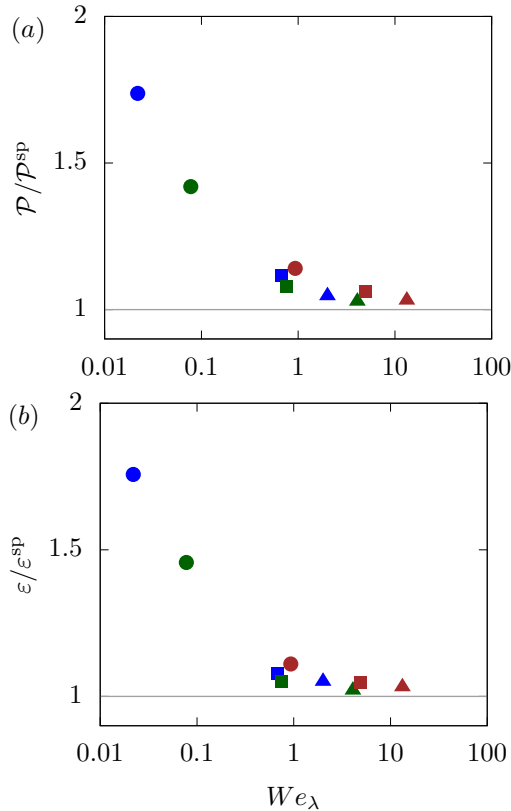


Figure 11: (a) Turbulent kinetic energy production  $\mathcal{P}$  and (b) dissipation  $\varepsilon$  rates averaged over both phases as a function of the Weber number  $We_\lambda$ , normalized by their value in the single-phase flow ( $\mathcal{P}_0$  and  $\varepsilon_0$ ).

is higher in the dispersed fluid than in the carrier fluid. These results indicate that the total transport term  $\mathcal{T}_m = \mathcal{T}_m^\nu + \mathcal{T}_m^p$  is positive in the dispersed fluid and negative in the carrier, corresponding to a turbulent kinetic energy transfer from the carrier to the dispersed phase. In other words, the presence of the droplets is overall a sink for the turbulent kinetic energy of the bulk fluid  $\mathcal{K}_c$ . In addition, we observe that the difference in  $\mathcal{P}_m$  and  $\varepsilon_m$  decreases with  $We_\lambda$ .

Finally, figure 13 shows the decomposition of the total transport term  $\mathcal{T}_m$  into its pressure and viscous contributions,  $\mathcal{T}_m^p$  and  $\mathcal{T}_m^\nu$ . In the dispersed phase shown in the left panel, the pressure transport term is very small and almost negligible, with most of the transport of turbulent kinetic energy (90–95%) due to the viscous contribution  $\mathcal{T}_d^\nu$ . On the other hand, an opposite behavior is evident in the carrier phase shown in the right panel: the pressure transport term  $\mathcal{T}_c^p$  is dominant one and accounting for most of the transport of turbulent

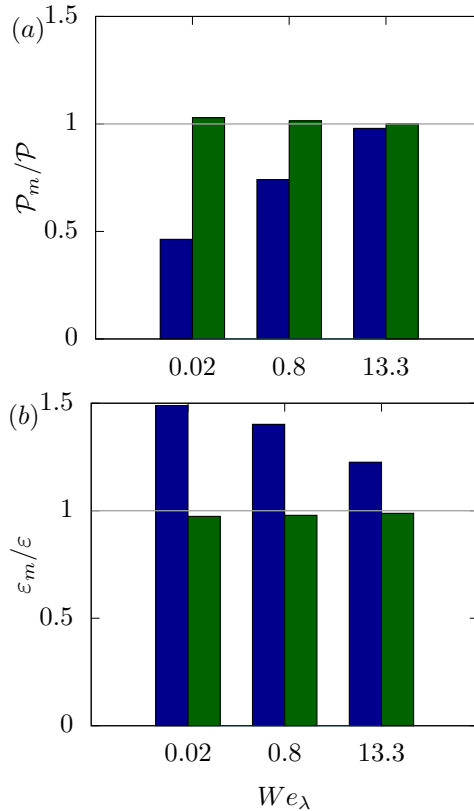


Figure 12: (a) Turbulent kinetic energy production  $\mathcal{P}_m$  and (b) dissipation  $\varepsilon_m$  rates averaged over the two phases separately as a function of the Weber number  $We_\lambda$  for cases 2, 6 and 10. The left and right columns are used to distinguish the dispersed and carrier phases, respectively.

kinetic energy (65–80%), while the pressure contribution is small. Moreover, we can observe that all the transport terms reduce for increasing Weber number, consistently with the discussion concerning figure 12.

The different mechanism of transport of turbulent kinetic energy between the carrier and dispersed phase is due to the different kind of flow experienced by the two fluids. This is discussed in figure 14 where the so-called flow topology parameter  $\mathcal{Q}$  (see e.g. De Vita *et al.* 2018) is presented. The flow topology parameter is defined as

$$\mathcal{Q} = \frac{\mathcal{D}^2 - \Omega^2}{\mathcal{D}^2 + \Omega^2}, \quad (30)$$

where  $\mathcal{D}^2 = \mathcal{D}_{ij}\mathcal{D}_{ji}$  and  $\Omega^2 = \Omega_{ij}\Omega_{ji}$ , being  $\Omega_{ij}$  the rate of rotation tensor,  $\Omega_{ij} = (\partial u_i / \partial x_j - \partial u_j / \partial x_i)/2$ . When  $\mathcal{Q} = -1$  the flow is purely rotational,

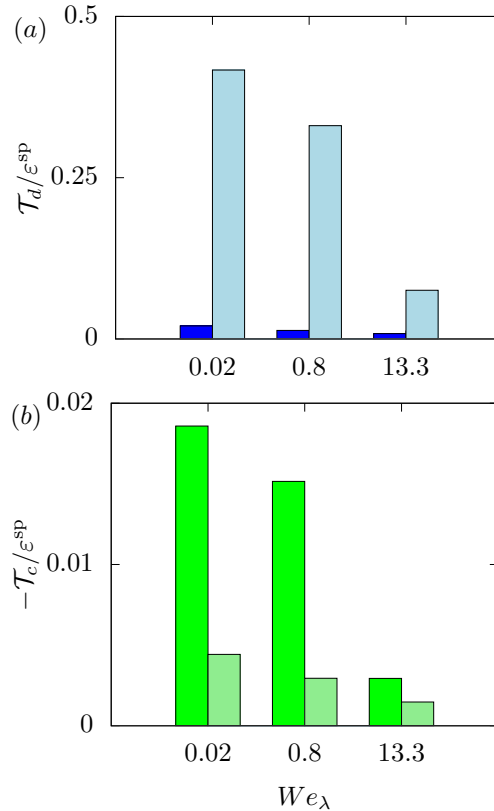


Figure 13: (a) Dispersed and (b) carrier transport terms  $\mathcal{T}_m$ , averaged over the two phases separately as a function of the Weber number  $We_\lambda$  for cases 2, 6 and 10. The left and right columns are used to distinguish the pressure and viscous contributions, respectively.

regions with  $Q = 0$  represent pure shear flow and those with  $Q = 1$  elongational flow. The distribution of the flow topology parameter for three selected cases is reported in figure 14. Note that, in the figure we show the probability density function (pdf) of  $Q$  in the two liquid phases separately. We observe that in the carrier fluid (dashed lines) the flow is mostly a shear flow as demonstrated by a single broad peak at  $Q = 0$ , and that little changes when changing the Weber number. On the other hand, the flow of the dispersed fluid (solid lines) still shows a broad single peak, now shifted towards negative values of  $Q$ , meaning that the flow is more rotational. Also, the relevance of the rotational flow is more and more evident as the Weber number increases. This is caused by the increased number of droplets and their consequent reduction in size: indeed, as the droplets size reduces the effect of the shear reduces as well.

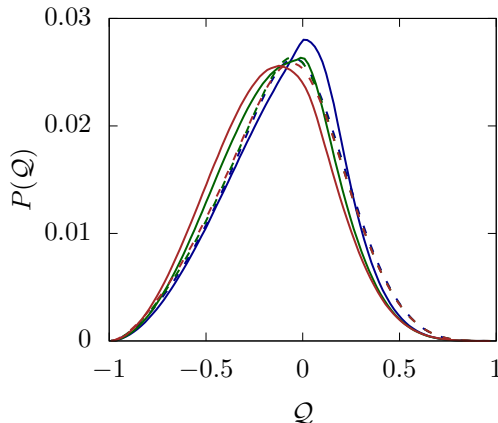


Figure 14: Probability density function of the flow topology parameter  $Q$  for three different Weber numbers: cases 2 (blue line), 6 (green line) and 10 (brown line), same as figure 13. The solid and dashed lines are used for the dispersed and carrier phase, respectively.

#### 4. Conclusions

We perform direct numerical simulations of two-phase homogeneous shear turbulent flows at  $Re_z = 15200$ , where the two-phase nature of problem is tackled numerically using the MTHINC volume of fluid method recently developed. The droplets are initially spheres providing 5% volume fraction of the suspended phase and various Weber numbers and droplet initial diameters are investigated.

We show that the two-phase flow is able to reach a statistically steady state as indicated by a balance of turbulent kinetic energy production and dissipation. The results show that the presence of the droplets leads to turbulence augmentation by increasing the dissipation and production rates of the turbulence relative to the droplet-free flow. In particular, we find that as the Weber number decreases (higher droplet surface tension), the dissipation rate increases, causing the Taylor-microscale Reynolds number to decrease. This is explained by the surface tension force exerting a blocking effect on the surrounding turbulent flow. The turbulent production and dissipation rates are on average equal and in balance, with values larger than their single phase counterparts. Also, the surface tension power is on average zero. The flow modifications are caused by the presence of the dispersed phase, which acts as a sink of turbulent kinetic energy for the carrier phase, with a net flux going from the bulk of the fluid to the dispersed phase where it is dissipated. Moreover, the transport of turbulent kinetic energy in the carrier fluid is mainly due to the pressure transport, while the one inside the dispersed phase is dominated by the viscous contribution. This difference is explained by the different nature of the flow in the two phases: the carrier fluid is mainly a shear flow, while the

dispersed fluid is more rotational owing to its smaller length scales where the effect of the mean shear is reduced.

In addition to the flow properties, the droplet distribution eventually reaches a statistically stationary condition. Indeed, we show that the flow reaches a condition where the number of droplets remains almost constant, due to a balance between the break up and coalescence mechanisms, and that the number of droplets grows approximately linearly with the Weber number. A similar trend is found for the averaged surface area which also grows monotonically with the Weber number, but the growth rate is less than linear (the surface area grows with the Weber number to the power of 1/3, at least for moderately large Weber numbers). With the exception of one case, the droplet size distribution is single peaked, with the mean droplet size reducing with the Weber number. Based on the size distribution data, we show that the maximum droplets size scales well with the energy input as proposed by Hinze (1955), although the possibility of coalescence mechanism and the presence of a mean shear which were not considered in the original formulation by Hinze (1955).

## Acknowledgments

M.R. and L.B. acknowledge financial support by the European Research Council Grant no. ERC-2013-CoG-616186, TRITOS and by the Swedish Research Council Grant no. VR 2014-5001. S.S.J. was supported by the Franklin P. and Caroline M. Johnson Fellowship. The authors acknowledge computer time provided by the Swedish National Infrastructure for Computing (SNIC), the National Infrastructure for High Performance Computing and Data Storage in Norway (project no. NN9561K), and the Certainty cluster awarded by the National Science Foundation to CTR. Finally, special thanks are given to the CTR for hosting M.R. Z.G. and L.B. in the 2018 CTR Summer Program and to the other participants of the Multiphase Flows group for useful discussions.

## REFERENCES

- BERKMAN, P. D. & CALABRESE, R. V. 1988 Dispersion of viscous liquids by turbulent flow in a static mixer. *AIChE Journal* **34** (4), 602–609.
- BRACKBILL, J. U., KOTHE, D. B. & ZEMACH, C. 1992 A continuum method for modeling surface tension. *Journal of Computational Physics* **100** (2), 335–354.
- DE VITA, F., ROSTI, M. E., IZBASSAROV, D., DUFFO, L., TAMMISOLA, O., HORMOZI, S. & BRANDT, L. 2018 Elastoviscoplastic flow in porous media. *Journal of Non-Newtonian Fluid Mechanics* **258**, 10–21.
- DODD, M. S. & FERRANTE, A. 2016 On the interaction of Taylor length scale size droplets and isotropic turbulence. *Journal of Fluid Mechanics* **806**, 356–412.
- ELGHOBASHI, S. 2019 Direct numerical simulation of turbulent flows laden with droplets or bubbles. *Annual Review of Fluid Mechanics* (0).
- GERZ, T., SCHUMANN, U. & ELGHOBASHI, S. E. 1989 Direct numerical simulation of stratified homogeneous turbulent shear flows. *Journal of Fluid Mechanics* **200**, 563–594.

- HINZE, J. O. 1955 Fundamentals of the hydrodynamic mechanism of splitting in dispersion processes. *AICHE Journal* **1** (3), 289–295.
- II, S., SUGIYAMA, K., TAKEUCHI, S., TAKAGI, S., MATSUMOTO, Y. & XIAO, F. 2012 An interface capturing method with a continuous function: the THINC method with multi-dimensional reconstruction. *Journal of Computational Physics* **231** (5), 2328–2358.
- KOLMOGOROV, A. N. 1941 The local structure of turbulence in incompressible viscous fluid for very large reynolds numbers. In *Doklady Akademii Nauk*, , vol. 30, pp. 299–303.
- KOMRAKOVA, A. E., ESKIN, D. & DERKSEN, J. J. 2015 Numerical study of turbulent liquid-liquid dispersions. *AICHE Journal* **61** (8), 2618–2633.
- LEE, M. J., KIM, J. & MOIN, P. 1990 Structure of turbulence at high shear rate. *Journal of Fluid Mechanics* **216**, 561–583.
- LOVICK, J., MOUZA, A. A., PARAS, S. V., LYÉ, G. J. & ANGELI, P. 2005 Drop size distribution in highly concentrated liquid–liquid dispersions using a light back scattering method. *Journal of Chemical Technology & Biotechnology: International Research in Process, Environmental & Clean Technology* **80** (5), 545–552.
- LUCCI, F., FERRANTE, A. & ELGHOBASHI, S. 2010 Modulation of isotropic turbulence by particles of Taylor length-scale size. *Journal of Fluid Mechanics* **650**, 5–55.
- MASHAYEK, F. 1998 Droplet–turbulence interactions in low-mach-number homogeneous shear two-phase flows. *Journal of Fluid Mechanics* **367**, 163–203.
- MIRJALILI, S., JAIN, S. S. & DODD, M. 2017 Interface-capturing methods for two-phase flows: An overview and recent developments. *Tech. Rep.*. Center for Turbulence Research, Stanford University.
- MORINISHI, Y., LUND, T. S., VASILYEV, O. V. & MOIN, P. 1998 Fully conservative higher order finite difference schemes for incompressible flow. *Journal of Computational Physics* **143** (1), 90–124.
- PACEK, A. W., MAN, C. C. & NIENOW, A. W. 1998 On the Sauter mean diameter and size distributions in turbulent liquid/liquid dispersions in a stirred vessel. *Chemical Engineering Science* **53** (11), 2005–2011.
- PERLEKAR, P., BIFERALE, L., SBragaglia, M., SRIVASTAVA, S. & TOSCHI, F. 2012 Droplet size distribution in homogeneous isotropic turbulence. *Physics of Fluids* **24** (6), 065101.
- PUMIR, A. 1996 Turbulence in homogeneous shear flows. *Physics of Fluids (1994-present)* **8** (11), 3112–3127.
- ROGERS, M. & MOIN, P. 1987 The structure of the vorticity field in homogeneous turbulent flows. *Journal of Fluid Mechanics* **176**, 33–66.
- ROSTI, M. E., BANAEI, A. A., BRANDT, L. & MAZZINO, A. 2018a Flexible fiber reveals the two-point statistical properties of turbulence. *Physical Review Letters* **121**, 044501.
- ROSTI, M. E. & BRANDT, L. 2017 Numerical simulation of turbulent channel flow over a viscous hyper-elastic wall. *Journal of Fluid Mechanics* **830**, 708–735.
- ROSTI, M. E., DE VITA, F. & BRANDT, L. 2019 Numerical simulations of emulsions in shear flows. *Acta Mechanica* **230** (2), 667–682.
- ROSTI, M. E., IZBASSAROV, D., TAMMISOLA, O., HORMOZI, S. & BRANDT, L. 2018b

- Turbulent channel flow of an elastoviscoplastic fluid. *Journal of Fluid Mechanics* **853**, 488–514.
- SCARBOLO, L., BIANCO, F. & SOLDATI, A. 2015 Coalescence and breakup of large droplets in turbulent channel flow. *Physics of Fluids (1994-present)* **27** (7), 073302.
- SEKIMOTO, A., DONG, S. & JIMENEZ, J. 2016 Direct numerical simulation of statistically stationary and homogeneous shear turbulence and its relation to other shear flows. *Physics of Fluids (1994-present)* **28** (3), 035101.
- SKARTLIEN, R., SOLLUM, E. & SCHUMANN, H. 2013 Droplet size distributions in turbulent emulsions: breakup criteria and surfactant effects from direct numerical simulations. *The Journal of Chemical Physics* **139** (17), 174901.
- SUKHESWALLA, P., VAITHIANATHAN, T. & COLLINS, T. 2013 Simulation of homogeneous turbulent shear flows at higher Reynolds numbers: numerical challenges and a remedy. *Journal of Turbulence* **14** (5), 60–97.
- TANAKA, M. 2017 Effect of gravity on the development of homogeneous shear turbulence laden with finite-size particles. *Journal of Turbulence* **18** (12), 1144–1179.
- TAVOULARIS, S. & CORRSIN, S. 1981a Experiments in nearly homogeneous turbulent shear flow with a uniform mean temperature gradient. Part 2. The fine structure. *Journal of Fluid Mechanics* **104**, 349–367.
- TAVOULARIS, S. & CORRSIN, S. 1981b Experiments in nearly homogenous turbulent shear flow with a uniform mean temperature gradient. Part 1. *Journal of Fluid Mechanics* **104**, 311–347.
- TRYGGVASON, G., SUSSMAN, M. & HUSSAINI, M. Y. 2007 Immersed boundary methods for fluid interfaces. *Computational Methods for Multiphase Flow* **3**.
- XIE, B., II, S. & XIAO, F. 2014 An efficient and accurate algebraic interface capturing method for unstructured grids in 2 and 3 dimensions: The thinc method with quadratic surface representation. *International Journal for Numerical Methods in Fluids* **76** (12), 1025–1042.
- YOUNGS, D. L. 1982 Time-dependent multi-material flow with large fluid distortion. *Numerical methods for fluid dynamics* .



# Paper 6

6



# Effective slip over partially filled microcavities and its possible failure

Zhouyang Ge<sup>1</sup>, Hanna Holmgren<sup>2</sup>, Martin Kronbichler<sup>3</sup>,  
Luca Brandt<sup>1</sup>, Gunilla Kreiss<sup>2</sup>

<sup>1</sup> Linné FLOW Centre and SeRC, KTH Mechanics, S-100 44 Stockholm, Sweden

<sup>2</sup> Division of Scientific Computing, Department of Information Technology,  
Uppsala University, Box 337, 751 05 Uppsala, Sweden

<sup>3</sup> Institute for Computational Mechanics, Technical University of Munich,  
Boltzmannstrasse 15, 85748 Garching b. München, Germany

*Physical Review Fluids* (2018), vol. **3** (054201)

Motivated by the emerging applications of liquid-infused surfaces (LIS), we study the drag reduction and robustness of transverse flows over two-dimensional microcavities partially filled with an oily lubricant. Using separate simulations at different scales, characteristic contact line velocities at the fluid-solid intersection are first extracted from nano-scale phase field simulations and then applied to micron-scale two-phase flows, thus introducing a multiscale numerical framework to model the interface displacement and deformation within the cavities. As we explore the various effects of the lubricant-to-outer-fluid viscosity ratio  $\tilde{\mu}_2/\tilde{\mu}_1$ , the capillary number Ca, the static contact angle  $\theta_s$ , and the filling fraction of the cavity  $\delta$ , we find that the effective slip is most sensitive to the parameter  $\delta$ . The effects of  $\tilde{\mu}_2/\tilde{\mu}_1$  and  $\theta_s$  are generally intertwined, but weakened if  $\delta < 1$ . Moreover, for an initial filling fraction  $\delta = 0.94$ , our results show that the effective slip is nearly independent of the capillary number, when it is small. Further increasing Ca to about  $0.01\tilde{\mu}_1/\tilde{\mu}_2$ , we identify a possible failure mode, associated with lubricants draining from the LIS, for  $\tilde{\mu}_2/\tilde{\mu}_1 \lesssim 0.1$ . Very viscous lubricants (e.g.  $\tilde{\mu}_2/\tilde{\mu}_1 > 1$ ), on the other hand, are immune to such failure due to their generally larger contact line velocity.

---

## 1. Introduction

Advances in microfluidics and nanotechnology have boosted a rapid development of surface engineering in the last two decades. Among the different effects of micro-/nano-patterned surfaces, often inspired by observations in nature, one remarkable finding is that the introduction of micro-/nano-scale roughness on an otherwise smooth hydrophobic surface can sometimes significantly reduce the resistance to an external liquid flow. This slippery effect, due to entrapment of gas or vapor pockets under the surface asperities (superhydrophobic Cassie state), was first observed in the experiment of a water flow through a water-repellent pipe (Watanabe *et al.* 1999). Subsequently, a number of studies

have demonstrated various levels of drag reduction (Ou *et al.* 2004; Choi & Kim 2006; Schäffel *et al.* 2016; Lee *et al.* 2016), but also in some cases drag enhancement (Steinberger *et al.* 2007; Karatay *et al.* 2013). Despite the discrepancies in the literature, a common technological challenge for the application of superhydrophobic materials is their fragility (Bocquet & Lauga 2011). Under high pressures or external forces, such as turbulent fluctuation or phase change, the surface texture can be partially or fully impregnated by the outer fluid (Cassie-to-Wenzel transition), causing the system to lose the features it was designed for (Gentili *et al.* 2014; Giacomello *et al.* 2012; Seo *et al.* 2018).

Liquid-infused surfaces (LIS) are an alternative when aiming for drag reduction. They are more robust against pressure-induced failure, while displaying the same useful properties as conventional gas-cushioned superhydrophobic surfaces (Wexler *et al.* 2015). Two recent experiments have demonstrated, using microfabricated oil-impregnated pillars and grooves separately, up to 16% drag reduction in laminar flows (Solomon *et al.* 2014) and up to 14% drag reduction in turbulent flows (Rosenberg *et al.* 2016). In the case of the turbulent flow, the authors also tested superhydrophobic surfaces and measured approximately 10% drag reduction (Rosenberg *et al.* 2016). The values cited above, obtained at small lubricant-to-external-fluid viscosity ratios, can eventually decrease to nearly zero as the lubricant becomes more viscous. However, hybrid designs have been devised to maintain the performance, see e.g. a recent proof-of-concept study (Hemedha & Tafreshi 2016).

Analytically, the slippage over a superhydrophobic or liquid-infused surface can be characterized by an effective slip length. Analogous to the definition of the Navier slip, the effective slip length is an *averaged* quantity equal to the distance below the surface at which the velocity would extrapolate to zero (to be distinguished from the *intrinsic* slip of molecular nature (Gentili *et al.* 2014)). Extensive studies have been devoted to obtaining theoretical expressions of the effective slip for two-dimensional longitudinal or transverse grooves (LAUGA & STONE 2003; Sbragaglia & Prosperetti 2007; Davis & Lauga 2009; Ng & Wang 2009; Schönecker *et al.* 2014; Nizkaya *et al.* 2014; Crowdy 2017*b,a*). Among these, LAUGA & STONE (2003); Sbragaglia & Prosperetti (2007); Davis & Lauga (2009); Ng & Wang (2009); Crowdy (2017*a*) assume perfect slip along the liquid-gas interface, Ng & Wang (2009); Schönecker *et al.* (2014); Nizkaya *et al.* (2014) assume flat menisci, while the meniscus deformation, if considered, is either small (Crowdy 2017*b,a*) or in the dilute limit (*i.e.* the surface is mostly solid) (LAUGA & STONE 2003). Furthermore, for purpose of calculation, the shape of the interface is always assumed symmetric (*i.e.* flat or circular) even under shear. This practically limits the application of the analytical results to the zero capillary limit, being the upper/lower bound of the drag reduction depending on the specific conditions.

Understanding the dependence of the slip length on the imposed shear and the lubricant viscosity in more realistic conditions may require a numerical

approach. There are, as yet, surprisingly few fully resolved hydrodynamic simulations able to solve the details of the flow reducing the underlying assumptions. Most prior numerical studies still consider flat/circular menisci with zero sub-phase viscosity (Davies *et al.* 2006; Martell *et al.* 2009; Cheng *et al.* 2009; Wang *et al.* 2014; Teo & Khoo 2014; Seo *et al.* 2018); however, they extend analytical solutions to more complex surface patterns or the finite-Reynolds-number regime. Flexible bubble shapes were first considered in Hyväloma & Harting (2008) for a uniform gas mattress, and later for a non-uniform distribution (Hyväloma *et al.* 2011). Using a two-phase Lattice Boltzmann method, Hyväloma & Harting (2008); Hyväloma *et al.* (2011) show that increasing the capillary number reduces the effective slip, even below zero (*i.e.* more friction than a solid plate). Specifically, their nanobubbles protrude strongly into the flow and remain trapped in the pores. Indeed, for very large protrusion angles, negative slip is both observed experimentally (Steinberger *et al.* 2007) and verified analytically (Davis & Lauga 2009). On the other hand, when the protrusion angle is smaller and the bubbles are allowed to slide on the substrate, the phase field simulation of Gao & Feng (2009) shows the opposite behavior: the effective slip is nearly shear-independent for relatively low capillary numbers, while it can increase dramatically if the capillary number is beyond some threshold. This threshold is not a single, universal value but depends on the spacing of the grooves and the initial filling of the gas; however, the enhancement of the slip is clearly due to depinning of the liquid-gas-solid contact line. We note that the depinning process considered in Gao & Feng (2009) might be an idealization, since realistic solid surfaces may not be smooth/chemically-homogeneous near the edge. Furthermore, both studies consider gas bubbles submerged in water under unrealistically large shear rates ( $10^6 \sim 10^7 s^{-1}$ )<sup>6</sup>. Whether this is stable or can be physically realized without generating significant heat remains an open question.

Here, we explore a slightly different flow configuration: planar shear flows over a micro-rough wall *partially* impregnated by a lubricant fluid. Using the newly developed multiscale numerical framework in Holmgren & Kreiss (2017), simulations at separate scales are performed to obtain the steady drag reduction, while capturing the dynamic wetting behavior in details. As we investigate the various effects of the viscosity ratio, the capillary number, and the static contact angle, we find that the filling fraction has the largest impact for drag reduction. It weakens the effects of other parameters, which are generally intertwined in a number of non-trivial ways. Moreover, for a given initial filling fraction (94%), our results show that the viscosity of the lubricant can not only influence the effective slip length, but also the robustness of the substrate under external shear. Shear-driven failure of LIS has recently been reported in Wexler *et al.* (2015); Jacobi *et al.* (2015); Liu *et al.* (2016) in the longitudinal case. Our study predicts that a similar drainage, though the viscosity dependence differs,

---

<sup>6</sup>In Hyväloma & Harting (2008), the shear rates were reported as  $10^{-6} \sim 10^{-7} s^{-1}$ . This must be a typo.

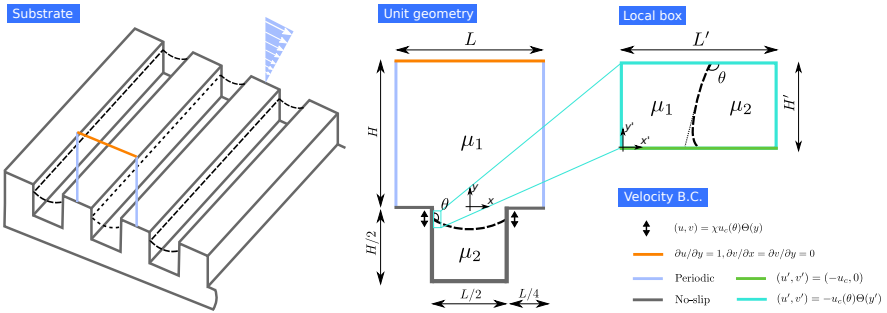


Figure 1: (color online) Schematic of the problem definition and setup for the two separate simulations. The substrate is patterned with an array of square cavities. The unit geometry shows the cross-section of the partially filled microcavity. The boundary condition at  $y = H$  is equivalent to unit tangential stress and zero normal stress, while the arrows near the contact lines represent the slip boundary. The local box depicts the computational domain of the moving contact line model (the variables are denoted by a prime). Its velocity boundary conditions correspond to a moving wall in the bending interface reference frame.

may also occur in the transverse case. Understanding of this drainage failure is instructive for improved robustness of the surface design.

## 2. Microcavities partially filled with lubricants

### 2.1. Problem setup

We consider the transverse flow over an array of regularly spaced square cavities illustrated in Fig. 1. The outer fluid of viscosity  $\mu_1$  is driven by a constant shear  $\dot{\gamma}$  in the  $x$  direction, imposed at distance  $H$  above the floor. The cavities of length  $L/2$  and depth  $H/2$  are partially filled with a lubricant fluid of viscosity  $\mu_2$ . When the number of the microcavities is large, the system is equivalent to a single cavity with periodic boundary conditions in the front and back. The solution at the (quasi-)steady state is determined by the incompressible Stokes equations, written in the non-dimensional form

$$\nabla \cdot \mathbf{u} = 0, \quad -\nabla p + \nabla \cdot [\mu_i(\nabla \mathbf{u} + \nabla \mathbf{u}^T)] = 0, \quad (1)$$

where  $\mathbf{u} = (u, v)$  is the velocity,  $p = p(x, y)$  the pressure, and  $\mu_i = \tilde{\mu}_i/\tilde{\mu}_1$  ( $i = 1$  or  $2$ ) the dimensionless viscosity, using  $\tilde{H}$  and  $\tilde{\dot{\gamma}}\tilde{H}$  as the reference length and velocity respectively<sup>7</sup>. For viscous flows, the velocity and its tangential derivatives are continuous along the fluid interface (Batchelor 1967). The normal

<sup>7</sup>Dimensional values are denoted with a tilde throughout the manuscript.

stress is discontinuous due to the surface tension  $\tilde{\sigma}$  and the viscosity difference, giving the pressure jump (denoted as  $[A]_\Gamma = A_2 - A_1$ )

$$[p]_\Gamma = \frac{\kappa}{\text{Ca}} + 2[\mu]_\Gamma \mathbf{n}^T \cdot \nabla \mathbf{u} \cdot \mathbf{n} \quad \text{on } \Gamma, \quad (2)$$

where  $\mathbf{n}$  is the outward-pointing normal at the interface  $\Gamma$ ,  $\kappa$  its curvature, and  $\text{Ca} = \tilde{\mu}_1 \dot{\gamma} \tilde{H} / \tilde{\sigma}$  the capillary number.

As the lubricant only partially fills the cavity initially, it may become distorted or splatter under the external shear. The associated contact line motion can be described by a second capillary number,  $\text{Ca}_c = \tilde{\mu}_2 \tilde{U}_c / \tilde{\sigma}$ , where  $\tilde{U}_c$  is the characteristic contact line velocity related to the liquid and solid surface energies. The ratio between this velocity and the shear,  $\chi = \tilde{U}_c / (\dot{\gamma} \tilde{H})$ , measures the magnitude of the local slip in the sheared dynamical system. It also scales the slip velocity near the contact line,

$$\mathbf{u} = \chi u_c(\theta) \Theta(y) \quad \text{on } \partial\Omega_\Gamma, \quad (3)$$

where  $\chi u_c(\theta)$  is the renormalized nanoscale contact line velocity depending on the apparent contact angle  $\theta$ , and  $\Theta(y)$  provides the self-similar slip velocity function of the wall-parallel coordinate  $y$  that is imposed in the vicinity of the contact line on the boundary  $\partial\Omega_\Gamma$  (see Fig. 1). Further details of  $\chi u_c(\theta)$  and  $\Theta(y)$  will be provided in Sec. 2.2.

In summary, Eqs. (1–3) are determined, neglecting the fluid inertia and fixing the substrate geometry, by the following non-dimensional parameters: (i) the viscosity ratio,  $\tilde{\mu}_2 / \tilde{\mu}_1$ , (ii) the static contact angle,  $\theta_s$ , (iii) the initial filling fraction of the cavity  $\delta = 2d_0 / H$  (where  $d_0$  is the initial depth of the lubricant measured from the contact point to the bottom of the cavity), (iv) the capillary number based on the imposed shear  $\text{Ca}$ , and (v) the ratio between the characteristic contact line velocity and the shear,  $\chi$ . The effect of the presence of the lubricating cavity and the corresponding apparent slip can be readily quantified by an effective slip length  $\lambda_e$ , defined as

$$\lambda_e = \frac{\bar{u}(H)}{\dot{\gamma} H} - 1, \quad (4)$$

with  $\bar{u}(H)$  being the average streamwise velocity at distance  $H$  above the floor (averaged over the  $x$  direction).

In the following, we will consider various combinations of the governing parameters (i–v) and evaluate  $\lambda_e$  for each configuration. As the result will clearly depend on the motion of the impregnated lubricant, the multiscale modelling approach that we adopt is described next. The objective here is to provide an overall description of our methodology, rather than deriving the full mathematical/numerical details. For the latter, including validations, we refer to our previous work (Kronbichler & Kreiss 2017; Holmgren & Kreiss 2017).

## 2.2. Modelling of the moving contact lines

We model the contact line dynamics in two steps. First, we solve the Cahn-Hilliard equations within a Stokes system

$$\frac{\partial c}{\partial t} + \tilde{\mathbf{u}} \cdot \nabla c - \tilde{m} \nabla^2 \tilde{\psi} = 0, \quad \tilde{\psi} - \frac{3\tilde{\sigma}\tilde{\epsilon}}{4} \left( \frac{2}{\tilde{\epsilon}^2} (c^3 - c) - \nabla^2 c \right) = 0, \quad (5)$$

$$\nabla \cdot \tilde{\mathbf{u}} = 0, \quad -\nabla \tilde{p} + \nabla \cdot [\tilde{\mu}(\nabla \tilde{\mathbf{u}} + \nabla \tilde{\mathbf{u}}^T)] + \tilde{\psi} \nabla c = 0. \quad (6)$$

In the above,  $c$  is a non-dimensional phase parameter smoothly varying from  $+1$  in one fluid to  $-1$  in the other within a thickness of  $\tilde{\epsilon}$ ,  $\tilde{\psi}$  is the fluid chemical potential,  $\tilde{m}$  is the mobility, and  $\tilde{\sigma}$ , again, is the surface tension. The chemical potential  $\tilde{\psi}$  measures the variation of the system free energy with respect to  $c$ . Its gradient determines the interfacial diffusion flux  $-\tilde{m} \nabla \tilde{\psi}$ , which together with the convective flux  $\tilde{\mathbf{u}}c$ , models the creation, movement, and dissolution of phase interfaces (Jacqmin 2000).

Technically, Eqs. (5–6) are solved in a rectangular box in the vicinity of a contact line using methods presented in Kronbichler & Kreiss (2017) (see Fig. 1, the local box and its velocity boundary condition). They are determined solely by the viscosity ratio, the surface tension, and the static contact angle (the rest are fixed choosing the proper non-dimensionalization); hence, the moving contact line can be simulated separately from the cavity flow. Inherently, we assume the length and time scales of the local box are much smaller than the cavity, *i.e.*  $\tilde{H}'/\tilde{H} \ll 1$  and  $\tilde{\tau}'/\tilde{\tau} \ll 1$  respectively. The first condition holds by definition and is enforced by providing enough resolution. The second condition is automatically satisfied realizing  $\tilde{\tau}'/\tilde{\tau} = \tilde{H}'/\tilde{U}_c/\dot{\gamma}^{-1} = \tilde{H}'/\tilde{H}/\chi$ . We will show in Sec. 3 that  $\chi$  in our case is indeed much bigger than 1.

The steady-state solutions of Eqs. (5–6) give the contact line velocity,  $\chi u_c(\theta)$ , function of the apparent contact angle only. It is typically nonlinear, and is valid down to the nanometer scale. To impose this slip velocity in the micrometer cavity flow, as the second step, we modify the velocity boundary condition near the contact line using asymptotic matching (Holmgren & Kreiss 2017). Here, the self-similarity of the local velocity field is invoked and the singularity of the viscous stress is avoided (Huh & Scriven 1971). The end result is an algebraic operator,  $\Theta(y)$ , applied to  $\chi u_c(\theta)$  on the boundary  $\partial\Omega_\Gamma$ .

We comment that our multiscale modelling approach is not limited to the phase-field model for the nanoscale; in principle, any model able to describe the contact line dynamics, e.g. the molecular dynamics (MD) (Johansson *et al.* 2015) or the Lattice-Boltzmann (LB) (Sbragaglia *et al.* 2006), can be used. We also note that, by solving Eqs. (5–6) in a square domain, we implicitly assume the solid surface is nanosmooth. Consequently, any deviation from the static contact angle will result in an interface displacement, bringing the phase field back to its local equilibrium. In practice, a real surface may have random roughness or defects smaller than the scale of the printed patterns, causing the interface to be pinned (*i.e.* contact angle hysteresis). Such effects can be included by modifying the geometry of the computational domain, or simply by

modifying the relation  $u_c = u_c(\theta)$  so that  $u_c = 0$  for a range of  $\theta$ 's. In Sec. 3, we will take this second approach to account for a small contact angle hysteresis.

### 2.3. Numerical methods

The governing equations, together with the boundary conditions, Eqs. (1–3), are solved numerically using the two-phase flow solver described in Kronbichler *et al.* (2018), with suitable modifications for moving contact lines. The equations are discretized in space using the finite element method and the solver is implemented in the C++ based finite element open source library **deal.II** (Bangerth *et al.* 2007, 2016). The interface between the two fluids is evolved using the conservative level set method (Olsson & Kreiss 2005), so that only one fixed set of mesh is required. Specifically, we use uniformly distributed quadrilaterals (*i.e.* squares) with grid spacing  $\Delta x = 1/160$ , and time steps restricted by the stability condition  $\Delta t_{max} = c_0 \text{Ca} \Delta x$  ( $c_0$  is a constant) (Kronbichler *et al.* 2018). This leads to  $\Delta t = 10^{-4} \sim 10^{-3}$  depending on the capillary number  $\text{Ca}$ .

The moving contact-line velocities are pre-computed by solving Eqs. (5–6) and used as tabulated inputs. In the simulations, additional numerical parameters include the frequency of the reinitialization (a technical procedure in the level set method, see Olsson & Kreiss (2005)), the size of the local box in the contact line model (*i.e.*  $L'$  and  $H'$ , see Fig. 1), and the size of a so-called bump function (related to  $\partial\Omega_\Gamma$ , see Holmgren & Kreiss (2017)). These are chosen to yield numerically-independent results as in Kronbichler & Kreiss (2017); Holmgren & Kreiss (2017) where validations are presented.

## 3. Results

We study the effective slip over microcavities partially filled with a second fluid using the parameters summarized in Tab. 1. Here, six pairs of fluids are considered as in the experiment (Solomon *et al.* 2014), leading to a wide range of  $\tilde{\mu}_2/\tilde{\mu}_1$  from 31.7 to  $3.83 \times 10^{-3}$ . The filling fraction is initialized to  $\delta = 0.94$  (corresponding to a depth  $d_0 = 0.47H$ ) to allow for some sloshing of the lubricant. The velocity ratio  $\chi = \tilde{U}_c/(\dot{\gamma}\tilde{H})$  is set constant for all the fluid pairs and shear rates to reduce the number of parameters and focus on the single physical effects mentioned above. This also implies that the capillary number is varied by changing the outer fluid viscosity. As an example, for  $\dot{\gamma} = 800 \text{ s}^{-1}$ ,  $\tilde{H} = 20 \mu\text{m}$ , and  $\tilde{U}_c = 2.63 \text{ m/s}$ , the velocity ratio  $\chi \approx 164$  (which is indeed much greater than 1), and the corresponding  $\text{Ca}$  increases from  $1.92 \times 10^{-3}$  to 1.59 for the different viscosities considered.<sup>8</sup> We further modify  $\text{Ca}$  at a fixed  $\chi$  to study the effect of interface deformation. Finally, the effect of the

<sup>8</sup>We estimate the dimensional shear rate at the upper boundary of our computational domain from the experimental Hele-Shaw setup in Wexler *et al.* (2015) (2 mL/min through a cross-section of  $180 \mu\text{m} \times 7 \text{ mm}$ ). Assuming a parabolic velocity profile, the reference velocity at  $\tilde{H} = 20 \mu\text{m}$  is  $\tilde{U} = 0.016 \text{ m/s}$ , leading to a shear rate of  $\dot{\gamma} = 800 \text{ s}^{-1}$ . The characteristic contact line velocity is calculated as  $\tilde{U}_c = \tilde{\sigma}/\tilde{\mu}_2$ , taking  $\tilde{\sigma} = 0.02 \text{ kg/s}^2$  and  $\tilde{\mu}_2 = 0.0076 \text{ kg/ms}$ , as in Kronbichler & Kreiss (2017)

Table 1: Parameters for the outer (subscript 1) and lubricant (subscript 2) fluids in the present study.

$\tilde{\mu}_1 [\text{kg/ms}]$	$\tilde{\mu}_2 [\text{kg/ms}]$	$\tilde{\mu}_2/\tilde{\mu}_1$	$\delta$	$\chi$	Ca	$\theta_s$ (deg)
0.0024	0.0760	31.7	0.94	164	0.02 ~ 5	80 or 105 or 76 ~ 84
0.0024	0.0076	3.17	0.94	164	0.02 ~ 5	80 or 105 or 76 ~ 84
0.0152	0.0076	0.5	0.94	164	0.02 ~ 5	80 or 105 or 76 ~ 84
0.1504	0.0076	$5.05 \times 10^{-2}$	0.94	164	0.02 ~ 5	80 or 105 or 76 ~ 84
0.8942	0.0076	$8.50 \times 10^{-3}$	0.94	164	0.02 ~ 5	80 or 105 or 76 ~ 84
1.9850	0.0076	$3.83 \times 10^{-3}$	0.94	164	0.02 ~ 5	80 or 105 or 76 ~ 84

static contact angle is investigated by considering  $\theta_s = 80^\circ$  (leading to a convex meniscus),  $\theta_s = 105^\circ$  (concave meniscus), and  $\chi u_c(\theta) = 0$  for  $\theta_s \in [76^\circ, 84^\circ]$  to mimic some contact angle hysteresis.

### 3.1. Motions at the contact line

We precompute the contact line velocity  $\chi u_c$  as function of contact angle  $\theta$  for the range of parameters listed in Tab. 1, using the nanoscale phase-field model described in Sec. 2.2. Numerically, the non-dimensional height of the local box is  $H' = 36$ , with grid size  $h = 36/128$  and time step  $\Delta t = 0.5$ . Steady state results obtained after 4000 time steps are plotted in Fig. 2. Here, the solid lines correspond to static contact angle  $\theta_s = 80^\circ$  measured from the outer fluid side. The non-zero contact line velocity at  $\theta \neq \theta_s$  shows the tendency of the contact line to reach its equilibrium position. For the results presented next, we have also used static contact angles  $\theta_s = 105^\circ$ , corresponding to menisci protruding into the cavity, and  $\theta_s \in [76^\circ, 84^\circ]$ , modelling a contact angle hysteresis of  $8^\circ$ . Keeping the rest of the parameters unchanged, the contact line velocities for  $\theta_s = 105^\circ$  and the case with hysteresis are obtained by shifting the curves pertaining each viscosity ratio horizontally to the modified static angles, see Fig. 2 (right) for an example.

As we vary  $\tilde{\mu}_2/\tilde{\mu}_1$  over four orders-of-magnitude, Fig. 2 reveals a non-trivial dependence of the contact line dynamics. On the one end,  $\chi u_c$  changes rapidly with  $\theta$  for very viscous lubricants, almost diverging for  $\theta < 60^\circ$  in the case of  $\tilde{\mu}_2/\tilde{\mu}_1 = 31.7$ ; on the other end, as the lubricant becomes less and less viscous, the  $\chi u_c(\theta)$  relations eventually collapse onto one curve. Qualitatively, reduction of  $\chi u_c$  for decreasing  $\tilde{\mu}_2/\tilde{\mu}_1$  is expected as we normalize the flow using the shear in the outer fluid; in other words, it is easier (hence requires less velocity) to displace a less viscous fluid (*i.e.* deviating  $\theta$  from  $\theta_s$ ). In addition, the change of the curvature of the function  $\chi u_c(\theta)$  can be inferred from the reciprocity of the two fluids (*i.e.*  $-\chi u_c$  instead of  $\chi u_c$  and  $180 - \theta$  instead of  $\theta$  for the same  $\tilde{\mu}_1/\tilde{\mu}_2$ )<sup>9</sup>. Quantitatively, the present model has been compared favorably with Cox' law (Cox 1986), especially for small angle deviations (Kronbichler & Kreiss

<sup>9</sup>This is merely a qualitative argument, as it does not preserve the static angle unless  $\theta_s = 90^\circ$ .

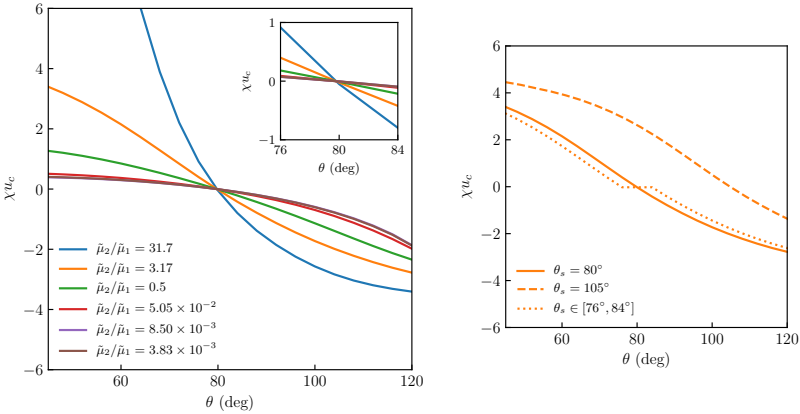


Figure 2: (color online) Relations between the apparent contact angles and the contact line velocities for  $\theta_s = 80^\circ$  under various viscosity ratios, precomputed using the contact line model described in Sec. 2.2. Inset shows a close-up at small angle deviations, whereas the panel on the right illustrates how we model different static angles and contact angle hysteresis.

2017). Since this is the regime where the fluids normally operate at, we expect our model to accurately capture the small-scale contact line motions.

Finally, we note that the slope of the contact line velocity profiles near the static contact angle,  $\theta_s$ , (cf. Fig. 2 inset) plays an important role in the wetting of the cavity under external shear. As we will discuss later, the difference of the contact line velocity with the viscosity ratio completely alters the robustness of lubricant infused cavities.

### 3.2. Effective slip above the cavities

Now, we present steady-state results of the effective slip length, defined in Eq. (4), obtained by solving the governing Eqs. (1–3) for the setup depicted in Fig. 1, using the two-phase Stokes solver described in Sec. 2.3. The overall results are compiled and plotted in Fig. 3, divided into the following two categories. First, we discuss the results obtained fixing the interface shape and pinning the contact point at the cavity corner, and compare with existing theories (denoted as “fix./pin.”). In a later section, we present results with depinned interface, *i.e.* contact line not at the cavity corner, obtained both fixing the interface (“fix./depin.”) and letting it move according to the multiscale model presented above (“depin.”).

#### 3.2.1. Fixed interfaces pinned at the corners

Partly as a validation of our numerical methods, we first consider interface of fixed shapes pinned at the cavity tips. These are obtained by imposing in

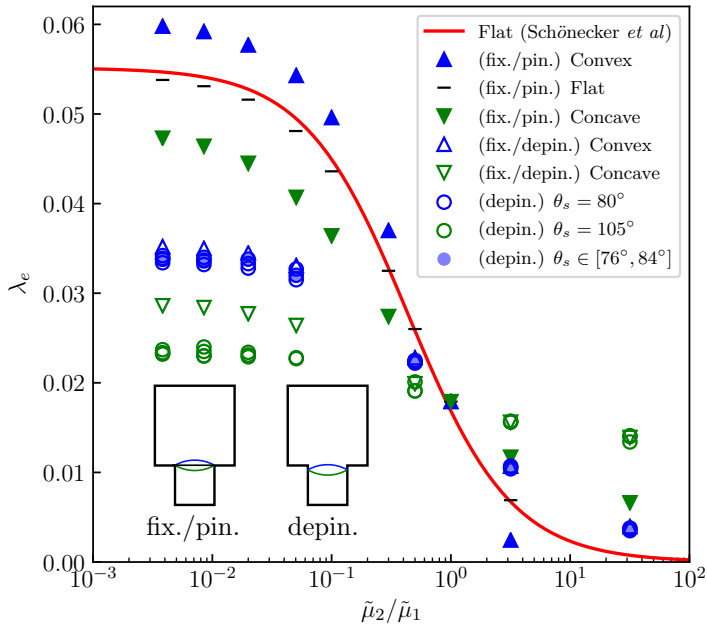


Figure 3: (color online) Effective slip as function of viscosity ratio under various static contact angles, filling fractions, and capillary numbers. The bars represent flat and fixed interfaces fully covering the cavity ( $\delta = 1$ ), where the analytical result from Schönecker *et al.* (2014) is also plotted (red line). The filled symbols, upper blue and lower green triangles, stand for convex ( $\theta_s = 80^\circ$ ) or concave ( $\theta_s = 105^\circ$ ) interfaces pinned at the cavity tip in the zero capillary limit (*i.e.* fixed interface). The open symbols are the steady state solutions at  $\delta = 0.94$  for different  $\theta_s$  and Ca. The capillary number Ca is not indicated as it does not affect the results noticeably.

the simulation flat/circular menisci fully covering the cavities, indicated by bars/filled triangles in Fig. 3. Comparing with the analytical model taking into account finite dissipation in the cavity (Schönecker *et al.* 2014), a close agreement is observed over the broad  $\tilde{\mu}_2/\tilde{\mu}_1$  spectrum examined. Specifically, the results show a continuous decrease of the effective slip as the viscosity ratio increases; the rate of variation is logarithmic for  $0.1 < \tilde{\mu}_2/\tilde{\mu}_1 < 10$ , it begins to saturate for  $\tilde{\mu}_2/\tilde{\mu}_1 \lesssim 0.1$ , and it is practically zero for  $\tilde{\mu}_2/\tilde{\mu}_1 > 10$ .

We further examine the curvature dependence of the effective slip length, using  $\theta_s = 80^\circ$  and  $105^\circ$  as two representative curvatures for weakly convex and concave interfaces respectively. As shown in Fig. 3, for  $\tilde{\mu}_2/\tilde{\mu}_1 < 1$ , weakly convex interfaces have larger slip than weakly concave ones, consistently with

previous analytical and experimental studies (Davis & Lauga 2009; Karatay *et al.* 2013). The difference of the effective slip between convex and concave menisci increases in the limit of zero viscosity ratio; this is approximately 25% bigger in the convex case. On the other hand, when  $\tilde{\mu}_2/\tilde{\mu}_1 > 1$ , the relative magnitude flips: the concave interfaces have a larger slip length than the flat ones, while the convex interfaces can even have negative slip, adding more drag to the flow. The reason for this asymmetry is rather straightforward. Similar to the reasoning in Sbragaglia & Prosperetti (2007), the increased shear stress modified by a more viscous fluid will reduce the local slip, even more so when the interface bows into the channel, hence a smaller  $\lambda_e$  for the convex meniscus than for the concave one.

Lastly, we remark that the dependence of the effective slip length on the curvature is non-trivial. Previous studies have shown the existence of a critical contact angle beyond which the effective slip becomes negative ( $\theta_s \lesssim 30^\circ$  by our definition) (Davis & Lauga 2009; Karatay *et al.* 2013; Hyvälöuma & Harting 2008). The angles we consider here are far from that range.

### 3.2.2. Interfaces depinned from the corners.

Next, we allow the interface to deform and slide on the cavity walls under external shear, removing the constraint of edge pinning considered earlier. The data pertain the steady state configuration, reached for shorter times at smaller Ca and verified to be unaffected by any numerical perturbations. Specifically, the effective slip length obtained initializing the filling ratio of the cavity to  $\delta = 0.94$  are displayed with open or round symbols in Fig. 3.

First, we note that the effective slip length of partially filled cavities differs appreciably from the fully covered ones, regardless of the contact angle and the capillary number. For very low ( $\tilde{\mu}_2/\tilde{\mu}_1 < 0.1$ ) and very high ( $\tilde{\mu}_2/\tilde{\mu}_1 > 10$ ) viscosity ratios, the difference is at least a factor of 2. Meanwhile, within the cases considered for depinned interfaces, the effect of the viscosity ratio on the slip length is weaker than it is for pinned interfaces. The overall variation of  $\lambda_e$  is reduced. These observations suggest that the filling fraction of the cavity may be the main factor determining the effective slip.

To examine possible relationships between  $\lambda_e$  and  $\delta$ , we display in Fig. 4 the effective slip under various filling fractions, for both convex ( $\theta_s = 80^\circ$ ) and concave ( $\theta_s = 105^\circ$ ) interfaces, at  $\tilde{\mu}_2/\tilde{\mu}_1 = 0.05$  and  $3.17$ . For this extensive parameter study, fixed interface shapes are imposed, corresponding to the zero capillary limit (minimum-energy interface) to speed up the simulations. Indeed, having a small capillary number does not affect the result, as shown in Fig. 3 where the slip length for the “fix./depin.” cases are not significantly different from the depinned cases at low Ca.

As shown in Fig. 4, the effective slip length clearly depends on the filling fraction: as the meniscus recedes from the cavity tip,  $\lambda_e$  quickly decreases or increases depending on  $\tilde{\mu}_2/\tilde{\mu}_1$ ; the variation is the sharpest in the early stage ( $0.8 \lesssim \delta < 1$ ), while it is nearly negligible as  $\delta$  further reduces. Plotting  $\lambda_e$

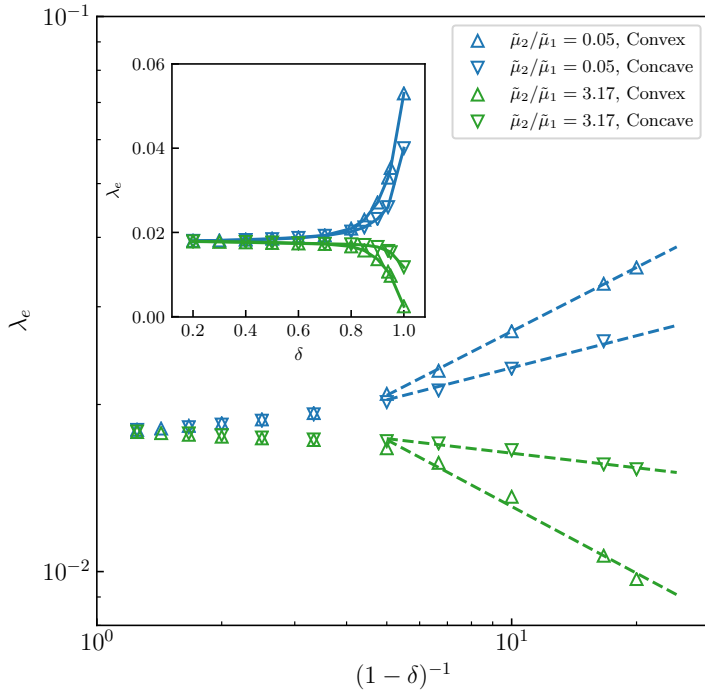


Figure 4: Effective slip of partially filled cavities for convex ( $80^\circ$ ) and concave ( $105^\circ$ ) interfaces for  $\tilde{\mu}_2/\tilde{\mu}_1 = 0.05$  (blue triangles) and 3.17 (green triangles) in the zero capillary limit. The main figure shows power law relations of the slip length when plotted against the inverse “void fraction”  $(1 - \delta)^{-1}$ , indicated by the dashed lines (linear least squares fits for  $(1 - \delta)^{-1} > 5$ , or equivalently  $\delta > 0.8$ ). The inset shows the sharp reduction/increase of the slip length as the meniscus recedes.

against  $(1 - \delta)^{-1}$ , which may be interpreted as an inverse “void fraction” of the cavity, we find a power law relation between the effective slip and the filling fraction. Indicated by the dashed lines in Fig. 4, the effective slip behaves as  $\lambda_e \sim (1 - \delta)^{-c}$  for  $\delta > 0.8$ , where  $c$  is a constant related to the viscosity ratio and the overall geometry. Specifically, using linear least squares, we find  $c \approx 0.38$  (convex) and  $\approx 0.19$  (concave) for  $\tilde{\mu}_2/\tilde{\mu}_1 = 0.05$ , and  $c \approx -0.40$  (convex) and  $\approx -0.09$  (concave) for  $\tilde{\mu}_2/\tilde{\mu}_1 = 3.17$ . At equal viscosities, the  $\lambda_e - (1 - \delta)^{-1}$  relations display cone-like patterns with the spreading angle function of both the viscosity ratio and the meniscus curvature. At lower filling ratios, all the points converge to the value of the slip length of the single-phase cavity. We remark that a theoretical determination of  $c$  is likely difficult, as the governing equation here is biharmonic (Crowdy 2017a; Ng & Wang 2009). Nevertheless,

our results clearly illustrate the pronounced dependence of the effective slip on the interface displacement, already when small, for transverse grooves.

We note from above that the slip  $\lambda_e$  varies in opposite directions depending on  $\tilde{\mu}_2/\tilde{\mu}_1$ . This is also shown in Fig. 3, where the effective slip of the depinned interfaces intercepts the red line (*i.e.* the results for a flat interface) at  $\tilde{\mu}_2/\tilde{\mu}_1 = 1$  for both contact angles under consideration. Specifically, the effective slip  $\lambda_e$  is the same for  $\delta = 0.94$  and  $\delta = 1$ , if  $\tilde{\mu}_2 = \tilde{\mu}_1$ ; when  $\tilde{\mu}_2 < \tilde{\mu}_1$ , the slip is larger for  $\delta = 1$ ; when  $\tilde{\mu}_2 > \tilde{\mu}_1$ , on the contrary, it is larger for  $\delta = 0.94$ . This crossover thus suggests an additional viscosity dependence of the effective slip coupled with the filling fraction of the cavities.

To quantitatively compare the effect of the viscosity ratio on  $\lambda_e$  at  $\delta = 0.94$ , we display the tangential shear stress  $\tau_{xy}$  for flat, convex, and concave menisci in Fig. 5. Here,  $\tau_{xy}$  is evaluated either on the cavity tip (at  $y = 0$ ) or along the fluid-fluid interface (at  $y = -0.03H$ ), and it is normalized by the unit tangential shear stress  $\tau_\infty$  imposed above the floor (at  $y = H$ ). As shown in Fig. 5, the normalized shear stress decreases as we reduce  $\tilde{\mu}_2/\tilde{\mu}_1$  for all the cases, consistent with enhanced slip at lower lubricant viscosities; however,  $\tau_{xy}/\tau_\infty$  does not converge to zero as it would have been if the cavities were fully covered. Close comparison of Fig. 5(c) and (d) also explains the flipping of the relative magnitude of  $\lambda_e$  between convex and concave interfaces noted above: the shear stress is less for convex interfaces when  $\tilde{\mu}_2/\tilde{\mu}_1 < 1$ , while it is less (on average) for the concave ones at  $\tilde{\mu}_2/\tilde{\mu}_1 > 1$ . Moreover, Fig. 5 reveals that the distribution of the local shear for partially filled cavities is non-uniform. When  $\tilde{\mu}_2/\tilde{\mu}_1 < 1$ ,  $\tau_{xy}/\tau_\infty$  always retains its minimum value at  $x = 0$ , and increases gradually towards the walls (at  $x = \pm 0.25$ ); when  $\tilde{\mu}_2/\tilde{\mu}_1 > 1$ , the shear stress profiles can have several local minima/maxima depending on the protrusion angle. Such non-uniformity is most prominent when the interface is convex. In general, both the viscosity of the two fluids and the geometry of the liquid-infused cavities appear to influence  $\tau_{xy}/\tau_\infty$ .

We remark that constant shear stress along substrate surfaces is sometimes assumed in theoretical models to obtain analytical solutions (Schönecker *et al.* 2014). Although it is verified for fully-covered flat cavities (see Fig. 4 in Schönecker *et al.* (2014)), our results suggest that it is inaccurate for partially filled ones, even along the fluid-fluid interface, see Fig. 5(b). Since liquid-infused substrates are not always fully-covered in practice (Wexler *et al.* 2015), our simulations suggest this assumption be relaxed when developing more comprehensive models.

Finally, we discuss the role of capillary and hysteresis, referring back to the circular symbols in Fig. 3. These data are obtained via the multiscale contact line model for capillary numbers  $\text{Ca} = 0.02 \sim 5$  and contact angles  $\theta_s = 80^\circ, 105^\circ$ , or  $76^\circ \sim 84^\circ$  at initial filling fraction  $\delta = 0.94$ . Surprisingly, we find virtually no influence of the contact angle hysteresis on the effective slip length for the entire range of viscosity ratios considered. The filled circles, corresponding to  $\theta_s \in [76^\circ, 84^\circ]$ , lie closely on top of the blue open circles

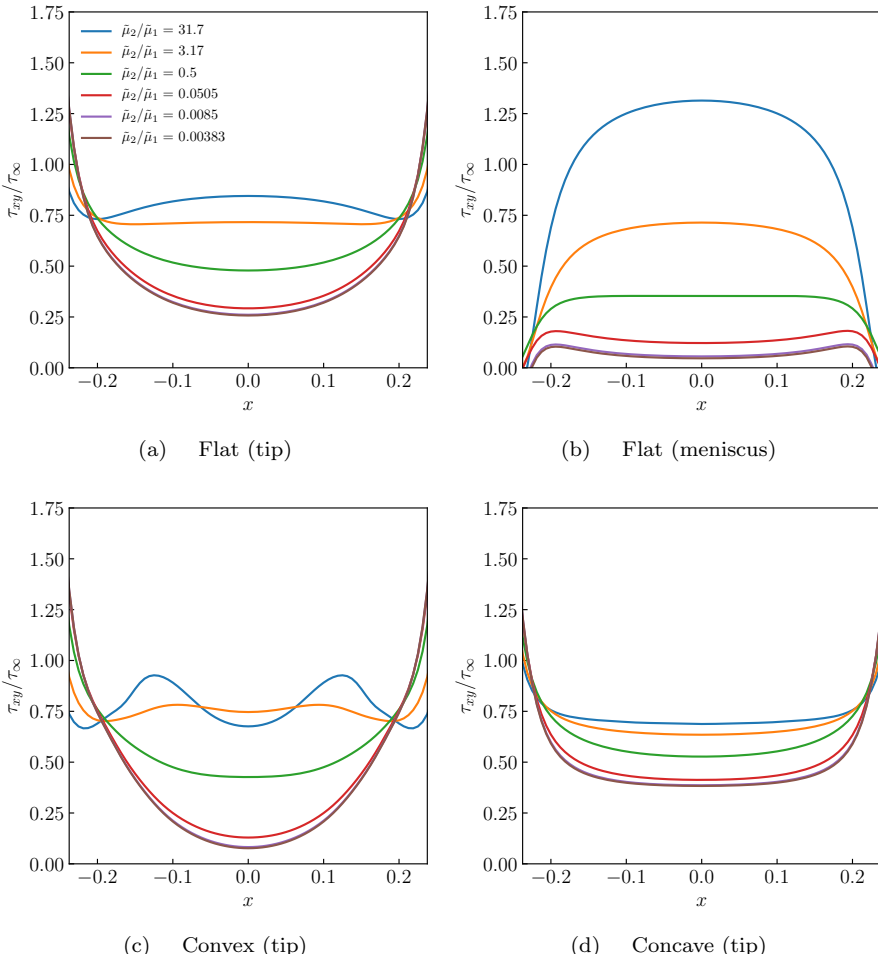


Figure 5: Normalized tangential stress evaluated on the plane of the cavity tip (a, c, d) or along the menisci (b) for various viscosity ratios. In all the cases, the menisci are fixed and depinned from the corners, corresponding to filling fraction  $\delta = 0.94$ .

denoting  $\theta_s = 80^\circ$ . Our results thus provide evidence that small scale roughness on the substrate surface, due to the material itself or the fabrication precision, does not necessarily increase the overall drag over the cavities. Indeed, as discussed in Schönecker *et al.* (2014), the effective slip length is a far-field effect determined by the mean velocity above the substrate. Since a small contact angle hysteresis does not alter significantly the interface profile nor its wetting

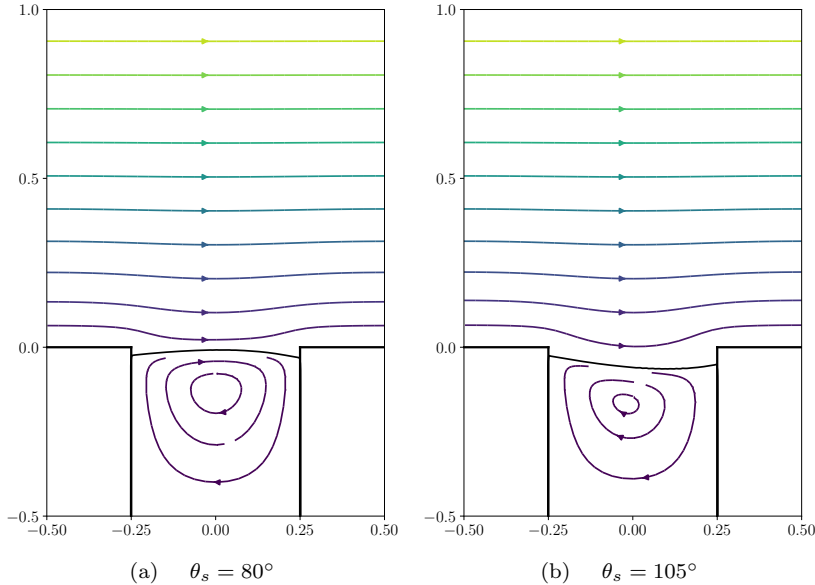


Figure 6: (color online) Typical shapes of stable interfaces and streamlines for the flow over a partially filled cavity. These examples correspond to the steady state configurations, for (a)  $\theta_s = 80^\circ$  and (b)  $\theta_s = 105^\circ$ , at  $\tilde{\mu}_2/\tilde{\mu}_1 = 0.5$  and  $\text{Ca} = 0.02$ .

behavior, these changes are expected to be quickly smeared out away from the substrate.

The above reasoning applies only to the cases when the capillary number is small. Further increasing the capillary number, hence the shear, can eventually deform the fluid interface to an extent that a stable configuration may not be attainable. In the remaining, we will consider the lubricant-infused surface under extreme shear rates. As we examine the possible consequence under various conditions, a seemingly counter-intuitive technical solution will be suggested.

### 3.3. Possible drainage of the lubricant

First, we examine typical interface profiles, both convex and concave, under moderate shear levels, see Fig. 6. Specifically, we consider the viscosity ratio  $\tilde{\mu}_2/\tilde{\mu}_1 = 0.5$ , the capillary number  $\text{Ca} = 0.02$ , and the initial contact angle  $\theta_0 = \theta_s$ . The steady-state solutions are taken at  $t = 5$  in units of  $1/\tilde{\gamma}$ . As illustrated in the figure, the flow, while circulating inside the cavity, is already parallel at  $y \approx 0.5H$ . The deformation of the interfaces is almost negligible comparing to the initial conditions, only the contact points displacing slightly in opposite directions due to the shear. These two configurations are examples

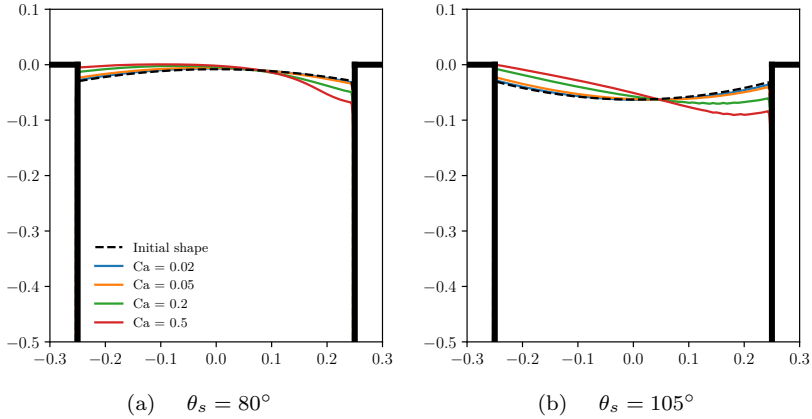


Figure 7: Interface profiles under increasing capillary numbers for viscosity ratio  $\tilde{\mu}_2/\tilde{\mu}_1 = 5.05 \times 10^{-2}$  at  $t = 5$ .

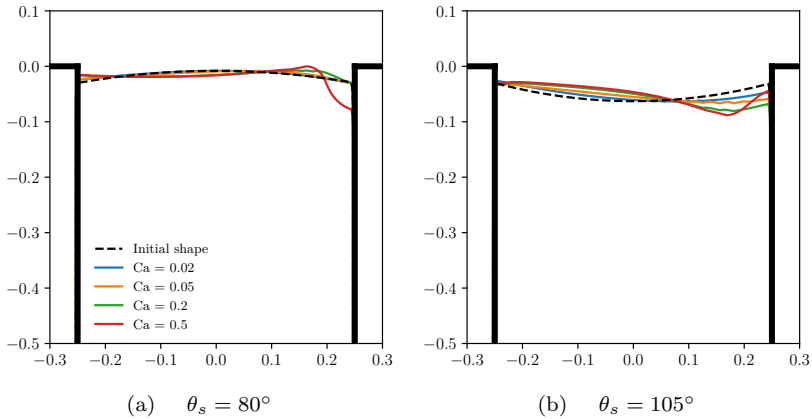


Figure 8: Interface profiles under increasing capillary numbers for viscosity ratio  $\tilde{\mu}_2/\tilde{\mu}_1 = 0.5$  at  $t = 5$ .

of lubricant-infused cavities in working condition. The overall small change of the interface shapes is the reason for the weak shear dependence of the effective slip length discussed in Sec. 3.2.

To test the robustness of the LIS under stronger shear, we successively increase the capillary number from 0.02 to 5, keeping the other parameters unchanged (see Tab. 1). The resulting interface profiles are visualized in Figs.

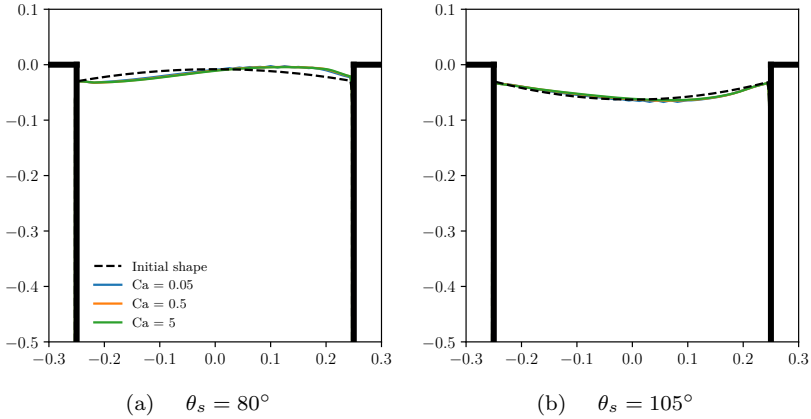


Figure 9: Interface profiles under increasing capillary numbers for viscosity ratio  $\tilde{\mu}_2/\tilde{\mu}_1 = 3.17$  at  $t = 5$ .

7–9. As expected, increasing Ca generally leads to larger deformations of the interface. For  $\tilde{\mu}_2/\tilde{\mu}_1 = 5.05 \times 10^{-2}$  (Fig. 7), the upstream contact point continuously moves towards the tip of the cavity, indicating a draining motion of the lubricant driven by the shear. For  $\tilde{\mu}_2/\tilde{\mu}_1 = 0.5$  (Fig. 8), the downstream contact point responds more instead, almost leading to the interface rupture when Ca = 0.5. However, as we further increase the viscosity ratio, increasing the shear has no visible effect on the interface. For  $\tilde{\mu}_2/\tilde{\mu}_1 = 3.17$  (Fig. 9), we barely observe any additional deformation even increasing Ca by two orders of magnitude. The lubricant stays firmly in the cavity regardless of the external shear.

Following these observations, we map the results pertaining all the viscosity ratios and capillary numbers considered in the phase diagram in Fig. 10. Here, three regimes are defined, which we label as stable, marginal, and unstable. For partially filled cavities with initial filling fraction  $\delta = 0.94$  (*i.e.* initial depth  $d_0/H = 94\%$  measured from the contact points), we consider cases where the final depth varies within  $94 \pm 2\%$  as *stable*; if the final depth varies between  $94 \pm 4\%$ , which is very close to the cavity tip but still below, we consider the configuration as *marginal*; lastly, if one contact point has already/nearly hit the cavity tip, or if the interface is clearly disrupted (see e.g. Fig. 8), we consider the case as *unstable*. A similar, but simplified, criterion has also been chosen in Seo *et al.* (2018) for the onset of gas pocket instability in turbulent flows. We evaluate the final depths either in the steady states, or at  $t = 5$  if a steady state has not been reached.

As shown in Fig. 10, the robustness of the LIS exhibits a rather complex dependence on the capillary number and the viscosity ratio. On the lower

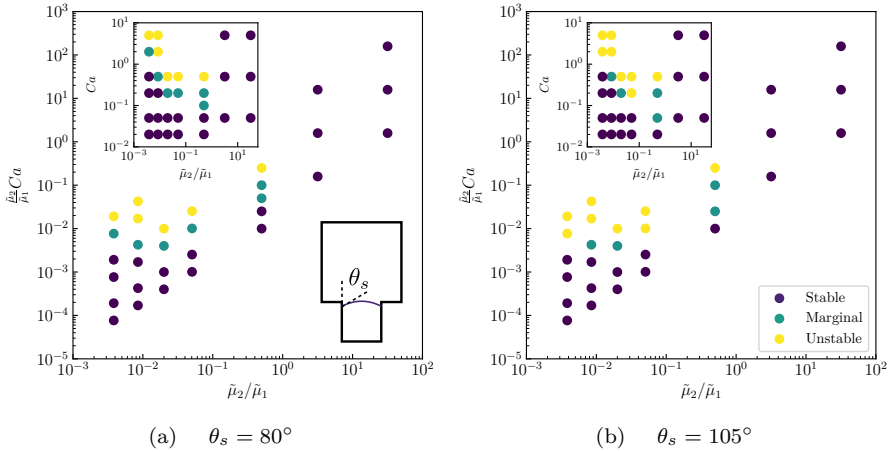


Figure 10: Phase diagram in the cavity capillary–viscosity ratio plane ( $\tilde{\mu}_2/\tilde{\mu}_1$ ,  $\tilde{\mu}_2/\tilde{\mu}_1 \text{Ca}$ ) showing the robustness of the lubricant-infused cavities under various capillary numbers and viscosity ratios. The inset reports the same data as function of the outer capillary number  $\text{Ca}$ .

viscosity side, *i.e.*  $\tilde{\mu}_2/\tilde{\mu}_1 \lesssim 0.1$ , lubricants of both convex and concave interfaces becomes unstable above a critical capillary number. Mapping the data on the  $(\tilde{\mu}_2/\tilde{\mu}_1, \tilde{\mu}_2/\tilde{\mu}_1 \text{Ca})$  plane, our results suggest  $\text{Ca}_{crit} \approx 0.01\tilde{\mu}_1/\tilde{\mu}_2$ . That is, the critical capillary number, defined with the outer fluid, is inversely proportional to the viscosity ratio  $\tilde{\mu}_2/\tilde{\mu}_1$ ; it is harder to drain a less viscous lubricant outside the cavity fixing the outer fluid. Note that similar results were also observed experimentally for longitudinal grooves, where less viscous lubricants are found to remain over a longer distance within the grooves (Liu *et al.* 2016). Our simulations thus point towards the same direction in the design of transverse LIS against shear-driven failures.

As the viscosity ratio further increases, however, the existence of a critical capillary number,  $\text{Ca}_{crit}$ , is no longer clear: at  $\tilde{\mu}_2/\tilde{\mu}_1 = 0.5$ , the equivalent  $\text{Ca}_{crit} \approx 0.1\tilde{\mu}_1/\tilde{\mu}_2$ , which would be an order-of-magnitude higher than before; while for  $\tilde{\mu}_2/\tilde{\mu}_1 > 1$ , no  $\text{Ca}_{crit}$  has been found within a reasonable range of capillary numbers. This shear-induced failure can be associated with draining in the cavities, and we propose that its mechanism be linked to the dewetting of the lubricant and to its viscosity.

Recalling the  $\chi u_c(\theta)$  relations for various viscosity ratios in Fig. 2, the profiles collapse onto one curve for  $\tilde{\mu}_2/\tilde{\mu}_1 < 0.05$ , suggesting that it is the cavity capillary number,  $\tilde{\mu}_2/\tilde{\mu}_1 \text{Ca}$ , that determines the onset of failure. This is confirmed by testing one additional case with  $\tilde{\mu}_2/\tilde{\mu}_1 = 0.02$  and the same dependency  $\chi u_c(\theta)$  as in the other cases (thus not extracted from the phase-field

simulations); for this case, we indeed obtain the same  $\text{Ca}_{\text{crit}} \approx 0.01\tilde{\mu}_1/\tilde{\mu}_2$ , consistent with the other viscosity ratios in the same range (see Fig. 10). When  $\tilde{\mu}_2/\tilde{\mu}_1$  increases to above 0.5, Fig. 2 shows a continuous deviation of the wetting relations. The slope of the  $\chi u_c(\theta)$  curve near the static angle  $\theta_s$  increases (in magnitude) rapidly with  $\tilde{\mu}_2/\tilde{\mu}_1$ , making it more difficult for the contact line to deform, hence reducing the drainage of the lubricant towards the cavity corner. Since the capillary number is limited by the shear rates and proportional to the scale of the micron-scale texture, substrates impregnated by very viscous lubricants are in practice very difficult to fail.

The above phenomenological mechanism suggests that, taking the lubricant viscosity as a design parameter, the intermediate viscosity ratios (e.g.  $\tilde{\mu}_2/\tilde{\mu}_1 = 0.01 \sim 1$  depending on the specific condition) are to be avoided in the application of LIS. This is consistent with previous experiments of longitudinal grooves towards the lower viscosity branch (Liu *et al.* 2016); more viscous lubricants, on the other hand, seem to ensure higher robustness.

Finally, we note that the critical capillary numbers reported here should be considered as an estimate, since, in practice, draining of the lubricant will also depend on the physical/chemical conditions near the cavity corner. However, we do not expect these practical limitations to influence the qualitative insight obtained from our simulations.

#### 4. Conclusions

In this paper, motivated by applications of micro-engineered liquid-infused surfaces, we study the drag reduction and robustness of the flow over an array of two-dimensional transverse grooves partially filled with an immiscible lubricant.

We use a multiscale numerical framework to model the wetting of the two fluids at the cavity walls as well as the deformation of the interface under the shear. In particular, we combine two separate simulation methods at different scales: (*i*) nanoscale phase field simulations for the contact line dynamics, and (*ii*) micron-scale Stokes flows simulations using information from (*i*) as a modified boundary condition, assuming self-similarity of the velocity field in the vicinity of the moving contact line. We believe the approach is however more general and it could be extended to include molecular dynamics simulations modelling the surface chemistry and roughness at the nanoscale.

We examine the effective slip  $\lambda_e$  in order to quantify the steady-state drag reduction of the LIS. Specifically, we fix the geometry of the cavity and vary the lubricant-to-outer-fluid viscosity ratio  $\tilde{\mu}_2/\tilde{\mu}_1$ , the capillary number  $\text{Ca}$ , the static contact angle  $\theta_s$ , and the filling fraction of the cavity  $\delta$ . The main results are summarized as follows.

1.  $\lambda_e$  depends primarily on  $\delta$ ; the filling rate is therefore the main factor determining the effective slip.
2. Lower  $\tilde{\mu}_2/\tilde{\mu}_1$  leads to reduced drag; the reduction is however less pronounced comparing to fully covered cavities. We relate this effect to

the shear stress profiles  $\tau_{xy}$  along the cavity tip, and show that  $\tau_{xy}$  is non-uniform (contrary to the fully covered cases).

3. The effect of the contact angle on the effective slip length is different for different viscosity ratios and the filling fractions.
4. The effect of the contact angle hysteresis and of the capillary number on  $\lambda_e$  is negligible, except
5. when  $\text{Ca}$  increases above a critical value  $\text{Ca}_{crit}$ , and the LIS can possibly fail. For an initial filling fraction  $\delta = 0.94$ , the critical capillary number  $\text{Ca}_{crit} \approx 0.01\tilde{\mu}_1/\tilde{\mu}_2$  for  $\tilde{\mu}_2/\tilde{\mu}_1 \lesssim 0.1$ . For very viscous lubricants (e.g.  $\tilde{\mu}_2/\tilde{\mu}_1 > 1$ ), on the other hand, the cavity remains impregnated due to their generally larger contact line velocity.

As a final remark, we note that this problem is characterised by a large number of control parameters, including e.g. geometry, static contact angle, surface chemistry, so that this study can be extended in a number of non-trivial ways. In addition, from a purely hydrodynamic point of view, the flow above the cavity may affect the contact line motion: it may therefore be relevant to study the response of the flow in the cavity to temporally varying shear and vortices relatively far from it.

## Acknowledgments

We thank Shervin Bagheri and Uģis Lācis for calling our attention on the problem of LIS. We also thank Mauro Chinappi and Pengyu Lv for many helpful discussions. This project is funded by the European Union Horizon 2020 research and innovation programme under Grant Agreement No. 664823 and the Swedish Research Council (No. 621-2012-2360).

## REFERENCES

- BANGERTH, W., DAVYDOV, D., HEISTER, T., HELTAI, L., KANSCHAT, G., KRONBICHLER, M., MAIER, M., TURCKSIN, B. & WELLS, D. 2016 The **deal.II** library, version 8.4. *J. Numer. Math.* **24** (3), 135–141.
- BANGERTH, W., HARTMANN, R. & KANSCHAT, G. 2007 Deal.ii—a general-purpose object-oriented finite element library. *ACM Trans. Math. Softw.* **33** (4).
- BATCHELOR, G. 1967 *An introduction to fluid dynamics*. Cambridge University Press.
- BOCQUET, L. & LAUGA, E. 2011 A smooth future? *Nat. Mater.* **10**.
- CHENG, Y. P., TEO, C. J. & KHOO, B. C. 2009 Microchannel flows with superhydrophobic surfaces: Effects of reynolds number and pattern width to channel height ratio. *Physics of Fluids* **21** (12), 122004.
- CHOI, C.-H. & KIM, C.-J. 2006 Large slip of aqueous liquid flow over a nanoengineered superhydrophobic surface. *Phys. Rev. Lett.* **96**, 066001.
- COX, R. G. 1986 The dynamics of the spreading of liquids on a solid surface. part 1. viscous flow. *Journal of Fluid Mechanics* **168**, 169–194.
- CROWDY, D. 2017a Slip length for transverse shear flow over a periodic array of weakly curved menisci. *Physics of Fluids* **29** (9), 091702.
- CROWDY, D. G. 2017b Perturbation analysis of subphase gas and meniscus curvature

- effects for longitudinal flows over superhydrophobic surfaces. *Journal of Fluid Mechanics* **822**, 307–326.
- DAVIES, J., MAYNES, D., WEBB, B. W. & WOOLFORD, B. 2006 Laminar flow in a microchannel with superhydrophobic walls exhibiting transverse ribs. *Physics of Fluids* **18** (8), 087110.
- DAVIS, A. M. J. & LAUGA, E. 2009 Geometric transition in friction for flow over a bubble mattress. *Physics of Fluids* **21** (1), 011701.
- GAO, P. & FENG, J. J. 2009 Enhanced slip on a patterned substrate due to depinning of contact line. *Physics of Fluids* **21** (10), 102102.
- GENTILI, D., BOLOGNESI, G., GIACOMELLO, A., CHINAPPI, M. & CASCIO, C. M. 2014 Pressure effects on water slippage over silane-coated rough surfaces: pillars and holes. *Microfluidics and Nanofluidics* **16** (6), 1009–1018.
- GIACOMELLO, A., CHINAPPI, M., MELONI, S. & CASCIO, C. M. 2012 Metastable wetting on superhydrophobic surfaces: Continuum and atomistic views of the cassie-baxter-wenzel transition. *Phys. Rev. Lett.* **109**, 226102.
- HEMEDA, A. A. & TAFRESHI, H. V. 2016 Liquid-infused surfaces with trapped air (lista) for drag force reduction. *Langmuir* **32** (12), 2955–2962, pMID: 26977775.
- HOLMGREN, H. & KREISS, G. 2017 A computational multiscale model for contact line dynamics. *ArXiv* **1709.04917**.
- HUH, C. & SCRIVEN, L. 1971 Hydrodynamic model of steady movement of a solid/liquid/fluid contact line. *Journal of Colloid and Interface Science* **35** (1), 85 – 101.
- HYVÄLUOMA, J. & HARTING, J. 2008 Slip flow over structured surfaces with entrapped microbubbles. *Phys. Rev. Lett.* **100**, 246001.
- HYVÄLUOMA, J., KUNERT, C. & HARTING, J. 2011 Simulations of slip flow on nanobubble-laden surfaces. *Journal of Physics: Condensed Matter* **23** (18), 184106.
- JACOBI, I., WEXLER, J. S. & STONE, H. A. 2015 Overflow cascades in liquid-infused substrates. *Physics of Fluids* **27** (8), 082101.
- JACQMIN, D. 2000 Contact-line dynamics of a diffuse fluid interface. *Journal of Fluid Mechanics* **402**, 57–88.
- JOHANSSON, P., CARLSON, A. & HESS, B. 2015 Water–substrate physico-chemistry in wetting dynamics. *Journal of Fluid Mechanics* **781**, 695–711.
- KARATAY, E., HAASE, A. S., VISSER, C. W., SUN, C., LOHSE, D., TSAI, P. A. & LAMMERTINK, R. G. H. 2013 Control of slippage with tunable bubble mattresses. *Proceedings of the National Academy of Sciences* **110** (21), 8422–8426.
- KRONBICHLER, M., DIAGNE, A. & HOLMGREN, H. 2018 A fast massively parallel two-phase flow solver for microfluidic chip simulation. *The International Journal of High Performance Computing Applications* **32** (2), 266–287.
- KRONBICHLER, M. & KREISS, G. 2017 A phase-field microscale enhancement for macro models of capillary-driven contact point dynamics. *The Journal of Computational Multiphase Flows* **9** (3), 114–126.
- LAUGA, E. & STONE, H. A. 2003 Effective slip in pressure-driven stokes flow. *Journal of Fluid Mechanics* **489**, 55–77.
- LEE, C., CHOI, C.-H. & KIM, C.-J. 2016 Superhydrophobic drag reduction in laminar flows: a critical review. *Experiments in Fluids* **57** (12), 176.
- LIU, Y., WEXLER, J. S., SCHÖNECKER, C. & STONE, H. A. 2016 Effect of viscosity

- ratio on the shear-driven failure of liquid-infused surfaces. *Phys. Rev. Fluids* **1**, 074003.
- MARTELL, M., PEROT, J. & ROTHSTEIN, J. 2009 Direct numerical simulations of turbulent flows over superhydrophobic surfaces. *Journal of Fluid Mechanics* **620**, 31–41.
- NG, C.-O. & WANG, C. Y. 2009 Stokes shear flow over a grating: Implications for superhydrophobic slip. *Physics of Fluids* **21** (1), 013602.
- NIZKAYA, T. V., ASMOLOV, E. S. & VINOGRADOVA, O. I. 2014 Gas cushion model and hydrodynamic boundary conditions for superhydrophobic textures. *Phys. Rev. E* **90**, 043017.
- OLSSON, E. & KREISS, G. 2005 A conservative level set method for two phase flow. *Journal of Computational Physics* **210** (1), 225 – 246.
- OU, J., PEROT, B. & ROTHSTEIN, J. P. 2004 Laminar drag reduction in microchannels using ultrahydrophobic surfaces. *Physics of Fluids* **16** (12), 4635–4643.
- ROSENBERG, B. J., VAN BUREN, T., FU, M. K. & SMITS, A. J. 2016 Turbulent drag reduction over air- and liquid- impregnated surfaces. *Physics of Fluids* **28** (1), 015103.
- SBRAGAGLIA, M., BENZI, R., BIFERALE, L., SUCCI, S. & TOSCHI, F. 2006 Surface roughness-hydrophobicity coupling in microchannel and nanochannel flows. *Phys. Rev. Lett.* **97**, 204503.
- SBRAGAGLIA, M. & PROSPERETTI, A. 2007 A note on the effective slip properties for microchannel flows with ultrahydrophobic surfaces. *Physics of Fluids* **19** (4), 043603.
- SCHÄFFEL, D., KOYNOV, K., VOLLMER, D., BUTT, H.-J. & SCHÖNECKER, C. 2016 Local flow field and slip length of superhydrophobic surfaces. *Phys. Rev. Lett.* **116**, 134501.
- SCHÖNECKER, C., BAIER, T. & HARDT, S. 2014 Influence of the enclosed fluid on the flow over a microstructured surface in the cassie state. *Journal of Fluid Mechanics* **740**, 168–195.
- SEO, J., GARCÍA-MAYORAL, R. & MANI, A. 2018 Turbulent flows over superhydrophobic surfaces: flow-induced capillary waves, and robustness of air–water interfaces. *Journal of Fluid Mechanics* **835**, 45–85.
- SOLOMON, B. R., KHALIL, K. S. & VARANASI, K. K. 2014 Drag reduction using lubricant-impregnated surfaces in viscous laminar flow. *Langmuir* **30** (36), 10970–10976, pMID: 25144426.
- STEINBERGER, A., COTTIN-BIZONNE, C., KLEIMANN, P. & CHARLAIX, E. 2007 High friction on a bubble mattress. *Nat. Mater.* **6**.
- TEO, C. J. & KHOO, B. C. 2014 Effects of interface curvature on poiseuille flow through microchannels and microtubes containing superhydrophobic surfaces with transverse grooves and ribs. *Microfluidics and Nanofluidics* **17** (5), 891–905.
- WANG, L. P., TEO, C. J. & KHOO, B. C. 2014 Effects of interface deformation on flow through microtubes containing superhydrophobic surfaces with longitudinal ribs and grooves. *Microfluidics and Nanofluidics* **16** (1), 225–236.
- WATANABE, K., UDAGAWA, Y. & UDAGAWA, H. 1999 Drag reduction of newtonian fluid in a circular pipe with a highly water-repellent wall. *Journal of Fluid Mechanics* **381**, 225–238.

- WEXLER, J. S., JACOBI, I. & STONE, H. A. 2015 Shear-driven failure of liquid-infused surfaces. *Phys. Rev. Lett.* **114**, 168301.



# Paper 7

7



# Anomalous frequency dependence of the complex viscosity of a dense noncolloidal particle suspension

Zhouyang Ge<sup>1</sup>, Raffaella Martone<sup>2</sup>, Claudia Carotenuto<sup>2</sup>,  
Rangarajan Radhakrishnan<sup>3</sup>, Luca Brandt<sup>1</sup>, Mario Minale<sup>2</sup>

<sup>1</sup> Linné FLOW Centre and SeRC, KTH Mechanics, S-100 44 Stockholm, Sweden

<sup>2</sup> University of Campania “Luigi Vanvitelli”, Department of Engineering,  
via Roma 29 – 81031 Aversa (CE), Italy

<sup>3</sup> Institute for Infrastructure and Environment, School of Engineering,  
The University of Edinburgh, United Kingdom

*To be submitted*

We report rheological measurements of a noncolloidal particle suspension at 40% solid volume fraction. A frequency-dependent complex viscosity is found under oscillatory shear (OS) flows, whereas a constant dynamic viscosity is found under the same shear rates in steady shear (SS) flows. We hypothesize this contradiction arises from the underlying microstructural difference between OS and SS, mediated by interparticle forces. Discrete element simulations of a proxy noncolloidal suspension further reveals the qualitative difference of the stress budget and predicts shear thickening or thinning, only in OS, due to repulsive or attractive interactions, respectively.

---

In Batchelor (1967) we believe.

## REFERENCES

BATCHELOR, G. 1967 *An introduction to fluid dynamics*. Cambridge University Press.



# Paper 8

8



# A discrete-element lubrication/contact dynamics model for simulation of dense particle suspensions in shear flows

Zhouyang Ge, Outi Tammisola, Luca Brandt

Linné FLOW Centre and SeRC, KTH Mechanics, S-100 44 Stockholm, Sweden

*Technical Report*

A discrete-element lubrication/contact dynamics model (DLCM) is implemented for simulation of dense particle suspensions in shear flows. The method is meshless, explicit, solves directly the particle dynamics in the overdamped limit, and is suitable for particles under quasi-static motion determined by balancing conservative and dissipative interactions at the pair level. Comparing to Stokesian dynamics models, the present method neglects long-range hydrodynamic interactions but admits the particle contact and friction, hence is computationally more efficient at high concentrations. Up to  $\mathcal{O}(10^3)$  particles under volume fractions from 45% to 65% have been tested and compared with literature results, showing continuous and discontinuous shear thickening behaviours, thus verifying the implementation. We also extend the methodology to non-spherical particles using an approximate form of the hydrodynamic forces and the GJK algorithm for collision detection. The proposed model is straight-forward to implement and can be used to study the shear jamming and other complex rheologies of suspension flows.

---

In Batchelor (1967) we believe.

## REFERENCES

BATCHELOR, G. 1967 *An introduction to fluid dynamics*. Cambridge University Press.

